HIGH SPEED FORMING 2004

PROCEEDINGS OF THE 1st INTERNATIONAL CONFERENCE

MARCH 31 / APRIL 1, 2004

DORTMUND, GERMANY

Edited by:

Prof. Dr.-Ing. M. Kleiner
Lehrstuhl für Umformtechnik,
Universität Dortmund

In corporation with:

Deutsche Forschungsgemeinschaft DFG

For 443 EMB Elektromagnetische Blechumformung

Scientific Committee:

T. Altan	Ohio State University (USA)
N. Asnafi	Volvo Body Car Components (Sweden)
Y. Batygin	National Technical University, Kharkov (Ukraine)
J.-C. Gelin	University of Franche-Comte' (France)
S. Golovashchenko	Ford (USA)
H. Hoffmann	Technical University of Munich (Germany)
F. Hollmann	DFG German Science Foundation (Germany)
M. Kleiner	University of Dortmund (Germany)
A. Kost	Brandenburg Technical University of Cottbus (Germany)
E. Lugscheider	RWTH Aachen University (Germany)
R. Neugebauer	Technical University of Chemnitz (Germany)
K. Roll	DaimlerChrysler (Germany)
A. E. Tekkaya	Middle East Technical University (Turkey)
F. Vollertsen	University of Bremen (Germany)

LEHRSTUHL FÜR UMFORMTECHNIK
Universität Dortmund
Baroper Str. 301
D-44227 Dortmund
Germany

Edited by:

Chair of Forming Technology
University of Dortmund
Prof. Dr.-Ing. M. Kleiner

ISBN 3-00-012970-7

Table of Contents

Preface

Forming materials of low ductility, like e.g. aluminum alloys relevant for light weight construction, not only requires an optimisation of conventional methods, but also the invention and further development of alternative forming processes.

The implementation of high speed forming processes, including electromagnetic forming in particular, represents an exceptionally promising approach.

The First International Conference on High Speed Forming (ICHSF 2004) at the University of Dortmund will serve as a forum for the presentation of the current research and development status and for an intensive professional exchange.

Research results regarding subjects as workpiece and material behaviour, modelling, and simulation as well as process design will be presented and discussed in a range of selected scientific lectures.

Dortmund, March 2004 Matthias Kleiner

SESSION 1

MATERIALS & TESTING

High Speed Forming of the Light-Weight Wrought Alloys

E. El-Magd, M. Abouridouane

Department of Materials Science (LFW), Aachen University, Germany

Abstract

The deformation and fracture behaviour of the Al-alloy AA7075, Mg-alloy AZ80, and Ti-alloy Ti-6Al-4V were investigated in quasi-static and dynamic uniaxial compression and tension tests at strain rates in the range of 0.001 $s^{-1} \leq \dot{\varepsilon} \leq 5000\ s^{-1}$ and temperatures between 20°C and 500°C. Shear tests with hat shaped specimens of AZ80 were carried out by quasi-static and dynamic loading in the shear rate range of $0.01\,\mathrm{s}^{-1} \leq \dot{\gamma} \leq 116000\,\mathrm{s}^{-1}$ *at a temperature of 20°C.*

For strain rates of $\dot{\varepsilon} \leq 10\ s^{-1}$, the tests were carried out using a computer numerical controlled hydraulic testing machine. High strain rate experiments with $\dot{\varepsilon} \geq 1000\ s^{-1}$ were performed on a Split Hopkinson Pressure Bar. Using the experimentally determined flow curves, the effect of strain rate and temperature on the compressive deformation at fracture was determined, showing that the forces required for forming as well as the limits of the possible deformation are controlled by strain rate und temperature. Under dynamic loading, both AA7075 and AZ80 show an increase of the deformation degree at fracture with increasing strain rate, whereas the Ti-6Al-4V shows a decrease of it. The investigated mechanical material behaviour (strain hardening, strain rate sensitivity, and thermal softening) and metallographic investigations of the deformed specimens in dynamic compression tests allow an explanation for character, formation, and evolution of damage in the deformed material. Constitutive material laws, whose parameters are determined from the experimental data, can be applied to describe the influence of strain rate and temperature on the mechanical material behaviour in compression, tension and shear tests. These material laws are to be implemented into the FE simulation, in order to determine the local state of stress and strain at time of the fracture. Through combination of experiment and simulation, a failure criterion for ductile fracture could be determined for AA7075 under quasi-static and dynamic tensile loading.

Keywords:

Flow behaviour, High strain rates, Constitutive material law

1 Introduction

Forming and machining of brittle materials such as Magnesium alloys with conventional methods is limited, so that an intermediate treatment of the work piece should be necessary. Under dynamic loading, metallic materials exhibit an increase of flow stress and ductility with increasing deformation rate [1]. Consequently, materials of lower ductility can be deformed to higher strains using high strain rate deformation processes such as magnetic or explosive forming [2]. Therefore, adequate knowledge is needed. Furthermore, constitutive material laws are necessary to describe the material behaviour in simulation of high strain rate deformation processes as crash test and high speed cutting.

The strain rate and temperature considerably influence the material flow behaviour in deformation processes. Under quasi-static loading, strain hardening causes an increase of force and acts stabilising on the deformation process. In case of dynamic loading, additional influences on the flow stress and the ductility of the material have to be taken into consideration. With increasing deformation rate, the strain rate sensitivity increases, leading to a higher local value of flow stress and stabilises the deformation. On the other hand, the adiabatic character of the deformation process reduces the flow stress and promotes instability. Furthermore, the deformation process is influenced by inertia [3] and mechanical wave propagation effects [4]. The aim of this work is to characterise, model, and simulate the mechanical material behaviour of the light-weight wrought alloys, AA7075, AZ80, and TiAl6V4 subjected to high strain rates compression, tension, and shear loading.

2 Experimental results

Quasi-static and dynamic compression tests were carried out on cylindrical specimens of Al-alloy AA7075 in the T7351 condition as well as Mg-alloy AZ80 and Ti-alloy Ti-6Al-4V in the as extruded condition. The tests were conducted at strain rates in the range of $0{,}001\ s^{-1} \leq \dot{\varepsilon} \leq 5000\ s^{-1}$ and temperatures between $20\ °C \leq \vartheta \leq 500\ °C$. Experimentally determined flow curves of the investigated materials are represented in Figure 1. The stress of the quasi-static flow curves increases continuously with increasing strain due to strain hardening. With higher strain rates $\dot{\varepsilon} \geq 1000\ s^{-1}$, the flow curves show an increase of flow stress at lower strains, on the other hand a decrease of stress beyond a stress maximum due to thermal softening caused by the adiabatic character of the deformation process resulting in a temperature increase in the specimen at high strains. Under dynamic loading, both AA7075 and AZ80 show an increase of the deformation at fracture with increasing strain rate, whereas the Ti-6Al-4V shows a decrease of it. Furthermore, the higher the temperature the lower the 0.2% proof stress and the higher the ductility of the tested materials.

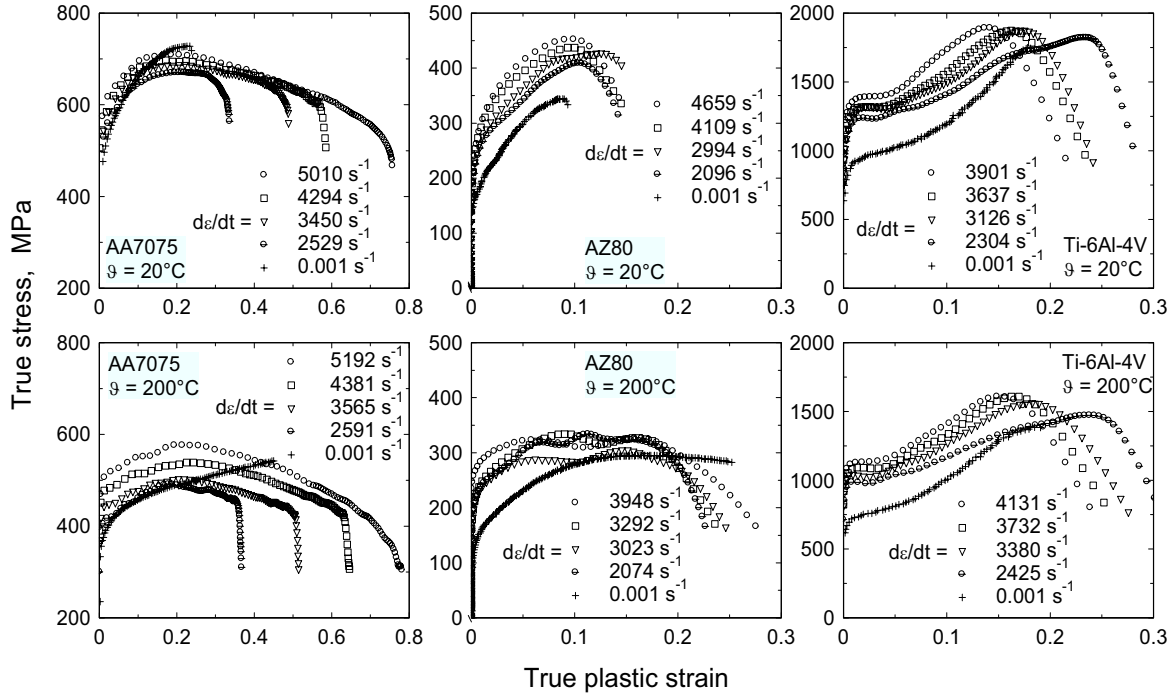

***Figure 1**: Flow curves of AA7075, AZ80 and Ti-6Al-4V from compression tests at different stain rates and temperatures*

The experimental results of the tensile and shear tests at room temperature on AA7075 and AZ80 respectively are illustrated in Figure 2. In both cases the influence of the strain rate on the flow stress and deformation at fracture is obvious. Under dynamic loading, the stress-strain curves show a maximum at lower strains due to contrary effects of the strain rate sensitivity and thermal softening on the stress. Furthermore, the ductility of the tested alloys is controlled by these effects.

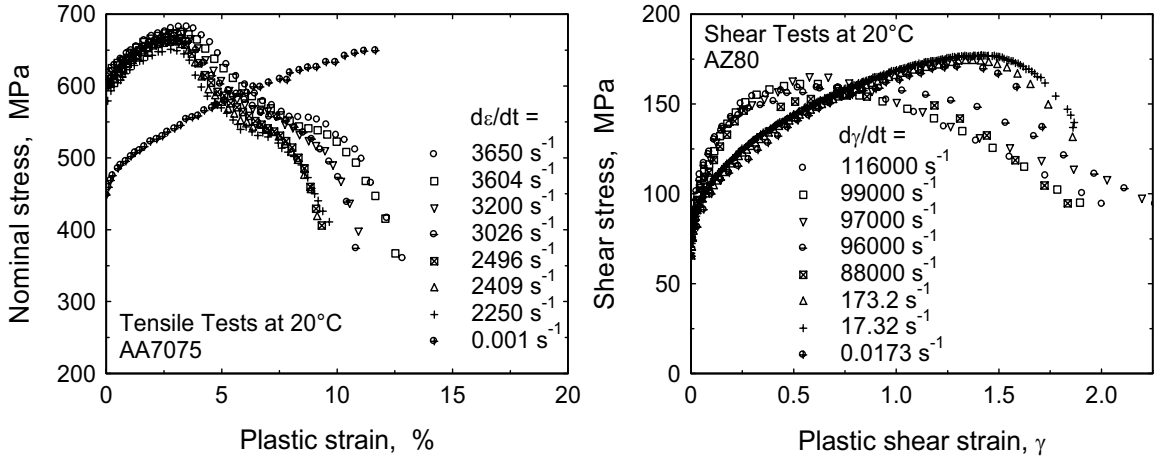

***Figure 2:** Stress-strain curves of AA7075 in tension and of AZ80 in shear tests at different strain rate and 20°C*

2.1 Effect of strain rate and temperature on deformation degree at fracture

The deformation degree at fracture, defined as the relative reduction of the height $(-\Delta H / H_0)f$ of the cylindrical compression specimen at fracture, is considered as a measure for the compressive ductility of the material. The deformation degree at fracture was determined as a function of the strain rate for different temperatures as represented in Figure 3. At room temperature with increasing strain rate in the range of $0{,}001\ s^{-1} \leq \dot{\varepsilon} \leq 1\ s^{-1}$, the deformation degree at fracture shows an increase due to the stabilising effect of the strain rate sensitivity for all tested materials. Under impact loading with strain rates higher than $1000\ s^{-1}$, the ductility of AA7075 and AZ80 increases sharply with the strain rates due to higher strain rate sensitivity, while it decreases for Ti-6Al-4V because of the dominating influence of strain rate on the damage process. Under quasi-static loading with $\dot{\varepsilon} = 0{,}001\ s^{-1}$, the fracture strain increases with the temperature. No fracture was detected at temperatures of 150°C, 200°C, 450°C and higher for AA7075, AZ80, and Ti-6Al-4V respectively up to values of $(-\Delta H / H_0) = 80\%$. In case of dynamic loading the ductility of AZ80 and Ti-6Al-4V were clearly influenced by temperature, while AA7075 shows a little temperature dependence.

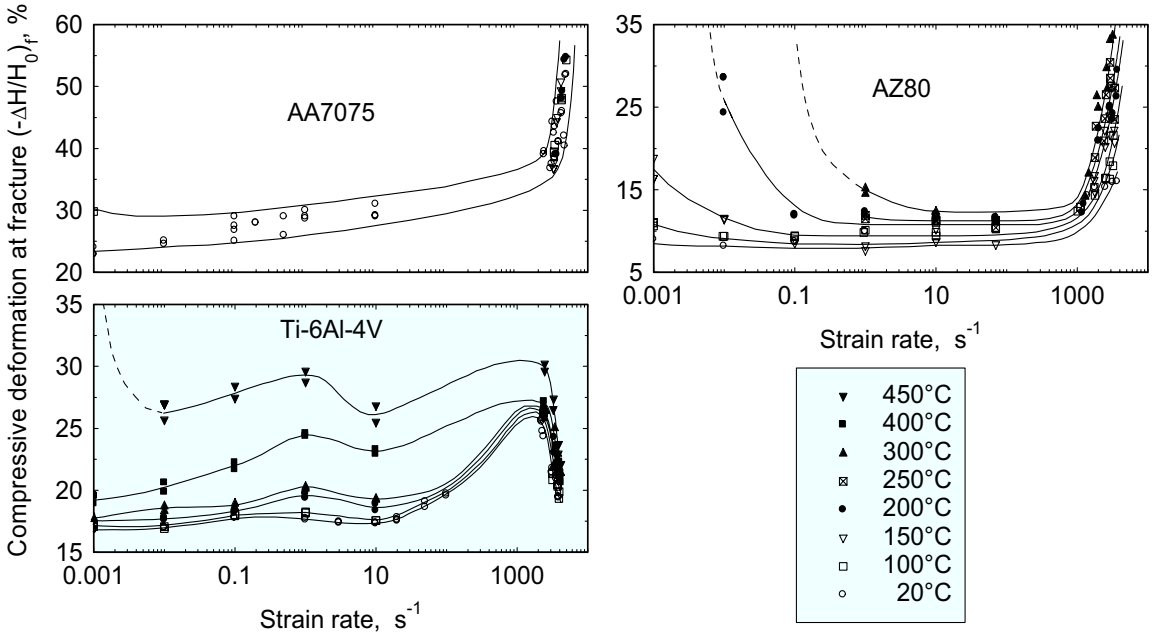

***Figure 3**: Deformation degree at fracture as a function of the strain rate and temperature (AA7075, AZ80 and Ti-6Al-4V)*

2.2 Damage by dynamic adiabatic shear bands

In order to examine the failure behaviour of the tested materials, metallographic investigations were accomplished on compressed specimens from AA7075 at test conditions $\dot{\varepsilon} = 4000\ s^{-1}$, $\vartheta = 20°C$ up to a pre-defined deformation $(-\Delta H/H_0) = 50\%$ for both of AZ80 and Ti-6Al-4V at $\dot{\varepsilon} = 2000\ s^{-1}$, $\vartheta = 20°C$ and $(-\Delta H/H_0) = 18\%$. Longitudinal sections of the impacted specimens are represented in Figure 4. The deformed specimens come to ductile shear fracture which localised along the surface of the compression cone. Compression cone usually causes by the friction between the sample and upsetting bars. This effect of friction increases in dynamic compression tests due to wave reflection from the output bar. The damage initiates from the contact surfaces where the friction constrains

the radial deformation of the specimen. A higher magnification of the longitudinal section in AA7075 and Ti-6Al-4V shows a creation of shear bands. In case of AZ80, the deformation localisation was detected along the compression cone, but has not led to shear band formation.

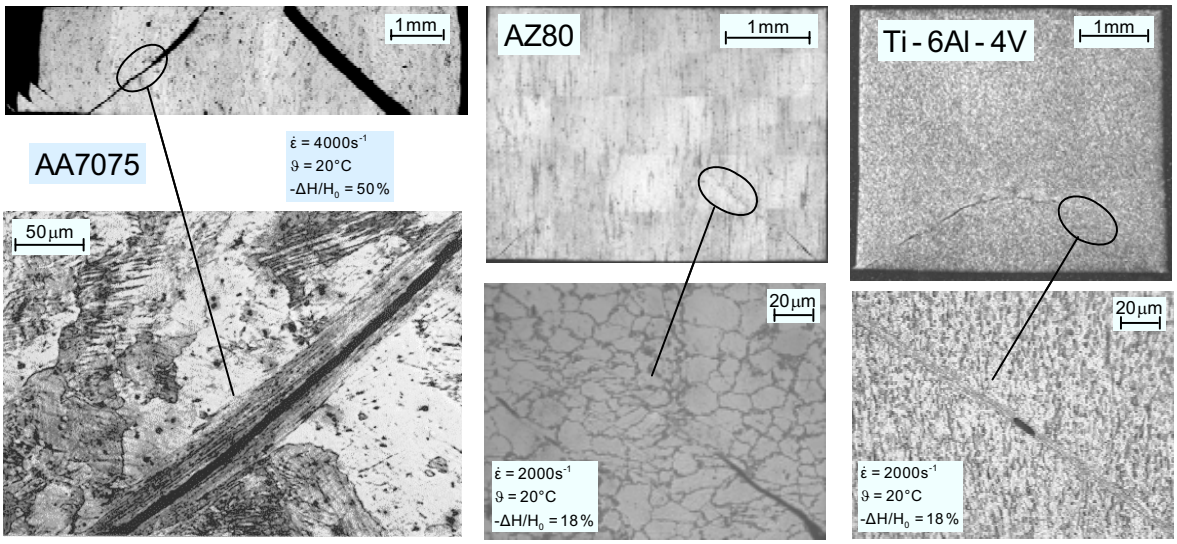

Figure 4: *Deformation localization and damage within specimens of AA7075, AZ80 and Ti-6Al-4V, deformed under impact loading at room temperature*

3 Constitutive modelling for material flow curves

3.1 Material law for impact loading

In case of dynamic loading with strain rates higher than 1000 s^{-1}, the influence of the strain rate can be represented by a linear relation $\sigma = \sigma + \eta\dot{\varepsilon}$ according to the damping mechanism as it was confirmed e.g. in [5]. The parameter σ_h signifies the stress extrapolated from the range of high strain rates down to $\dot{\varepsilon} = 0\,s^{-1}$; η is the damping parameter. The influence of the temperature increase on the flow stress can be considered by a multiplicative function, so that the material behaviour can be described by [6]:

$$\sigma = \left[K(B+\varepsilon)^n + \eta\dot{\varepsilon}\right] exp\left[-\beta\frac{T-T_0}{T_m}\right] \tag{1}$$

where *B*, *K*, and n are material constants. T_m, T_0, and *T* are the absolute melting point, room temperature, and actual temperature respectively. β is a material constant which can be set to 3 for several materials [6]. Assuming that the major part of deformation energy is transferred to heat during a dynamic deformation process and that the remaining part is consumed by an internal energy increase e.g. due to dislocation multiplication. The temperature increase can be determined by $\overline{\rho}\,\overline{c}\,dT = \kappa\,\sigma\,d\varepsilon$. In this equation $\kappa = 0.9$ [7] represents the fraction of energy transferred to heat, ρ and *c* are the density and the specific heat capacity of the material. With the relation between flow stress and temperature according to Equation (1), the increase of temperature can be determined as a function of strain by integration. The stress-strain relation under consideration of the two contrary influences of strain rate sensitivity and thermal softening results from the substitution of temperature in Equation (1):

$$\sigma = \frac{K(B+\varepsilon)^n + \eta\dot{\varepsilon}}{exp\left[\beta(T_S - T_0)/T_m\right] + a\int\left[K(B+\varepsilon)^n + \eta\dot{\varepsilon}\right]\dot{\varepsilon}dt} \tag{2}$$

with T_S is the test start temperature and $a = \kappa\beta/(T_m\overline{\rho c})$.

Figure 5 shows a comparison between computational results following Equation (2) (continuous curves) and experimental results from dynamic compression tests (markers) for AA7075-T7351, AZ80, and Ti-6Al-4V at different strain rates and 20°C. The parameters determined for AA7075 and AZ80 are given in Figure 5. In the case of the Ti-alloy, Equation (2) do not well describe the flow curves in the range of small strains $\varepsilon < 0.04$. In this range, the flow stress is approximately constant and equal to the 0.2% proof stress given by $R_{p0,2}=1026 + 0.092\,\dot{\varepsilon}$ where $R_{p0,2}$ in MPa and $\dot{\varepsilon}$ in s^{-1}. If the stress value calculated by Equation (2) is less than $R_{p0,2}$ it is to be replaced by this value.

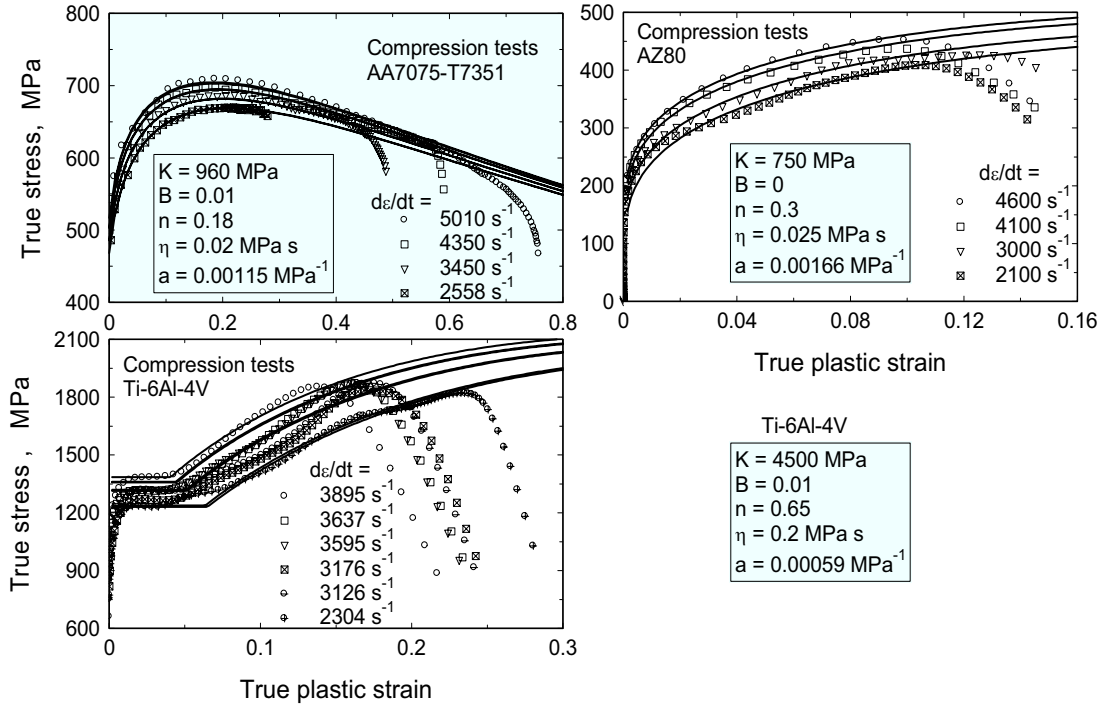

Figure 5: *Experimental and computational results of dynamic compression tests for AA7075, AZ80 and Ti-6Al-4V*

3.2 Material law for the whole range of strain rate and temperature

If the material behaviour is to be described in a larger range of strain rate and temperature, different physical influences must be combined. At lower strain rates the deformation is controlled by a combination of creep processes and plastic flow. In the range of high speed deformation the mechanical behaviour can be described with damping controlled gliding. So the complete strain rate range can be described as follows:

$$\dot{\varepsilon} = (1-M)\left(\left(\frac{\sigma}{\sigma_0(T,\varepsilon)}\right)^{N(T)} + \left(\frac{\sigma}{\sigma_H(T,\varepsilon)}\right)^{\frac{1}{m(T)}}\right) + M\left(\frac{\sigma - \sigma_G(T,\varepsilon)}{\eta} + \dot{\varepsilon}_G\right) \tag{3}$$

where $M = (T, \varepsilon, \dot{\varepsilon})$ is a transition function between dynamic strain rates and lower strain rates. The stress and strain rate for the transition point is given by:

$$\sigma_G(T,\varepsilon) = \sigma_H(T,\varepsilon)\dot{\varepsilon}_G^{\,m(T)} \text{ and } \dot{\varepsilon}_G = \left(m(T)\cdot\sigma_H(T,\varepsilon)/\eta\right)^{\frac{1}{(1-m(T))}} \quad (4)$$

With fitted values for the parameters $\sigma_0(T,\varepsilon)$, $\sigma_H(T,\varepsilon)$, $m(T)$, and $N(T)$ the full range of strain rates and temperatures can be described (Figure 6).

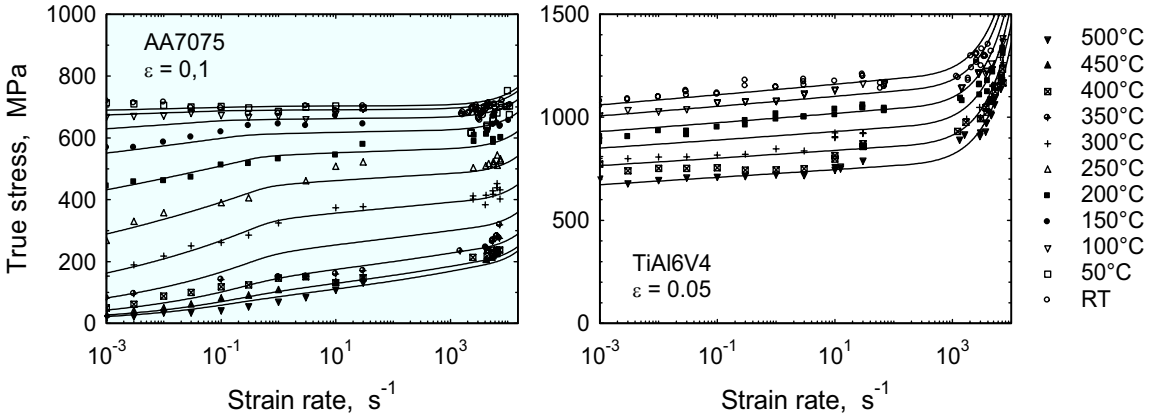

Figure 6: *Description of the material behaviour of AA7075 and Ti-6Al-4V in a wide range of strain rate and temperature [8]*

4 Computational results

4.1 Simulation of compression and shear tests

Compression and shear tests on the investigated materials at room temperature were simulated by the finite element method. The material behaviour in the quasi-static (ABAQUS\Standard, axisymmetrical), and the dynamic (ABAQUS\Explicit, axisymmetrical) simulations was described by the constitutive material law Equation (2). In both cases the numerical simulation was calculated up to the experimentally determined global deformation at fracture considering Coulomb friction with a coefficient μ=0.1. In Figure 7 the experimental and computation results at the fracture are plotted for the quasi-static isothermal ($\dot{\varepsilon}$ = 0,001 s^{-1}, Figure 7 a-d) and dynamic adiabatic ($\dot{\varepsilon}$ = 5010 s^{-1}, Figure 7 e-k) compression tests on AA7075. Under quasi-static loading the local distributions of the equivalent strain and stress have the same tendency and symmetry along the compression cones (Figure 7c, d). Oppositely, asymmetrical distribution (Figure 7g, k) was obtained in the dynamic case due to the effect of wave reflection from the output bar, which is consent with the experimental results shown in Figure 7f. The highest values of local plastic strain correspond to the lowest values of local stress (Figure 7g, k) due to decreasing of the adiabatic flow curve after reaching to maximum value as represented in Figure 7e. The ratio between maximum local deformation $\hat{\varepsilon}_{fr}$ and global deformation $\overline{\varepsilon}_{fr}$ reaches a value of 1.36 in case of quasi-static loading. In case of dynamic loading this ratio increases up to a value of 1.61 due to deformation localisation in the adiabatic shear bands.

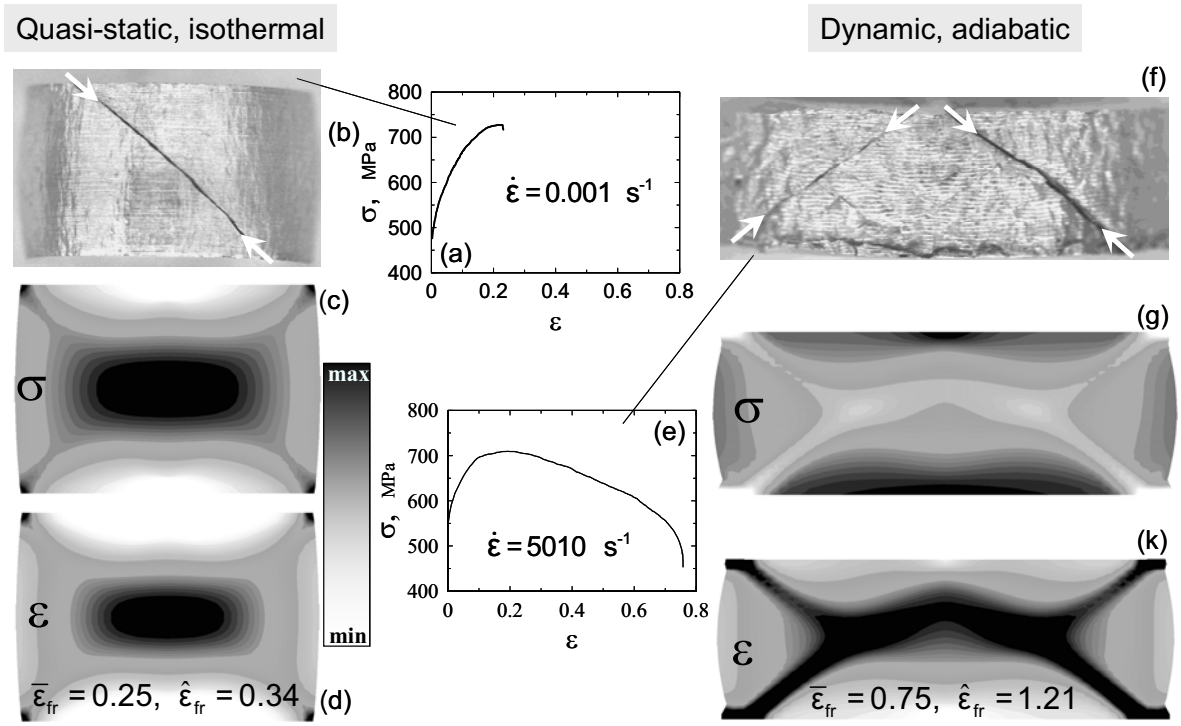

Figure 7: *Experimental and simulation results of compression test for quasi-static and dynamic loading on AA7075*

Figure 8 represents optical micrograph (Longitudinal sections) of hat shaped specimens of AZ80 deformed up to the fracture under quasi-static ($\dot{\gamma} = 0.0173\,s^{-1}, \vartheta = 20°C$) and impact ($\dot{\gamma} = 116000\,s^{-1}, \vartheta = 20°C$) loading as well as the results of its numerical simulations (local shear stress and shear strain distributions). In both cases the investigated specimens come to ductile shear fracture, whereby shear localisation was observed by dynamic loading, Figure 8f. In quasi-static simulation, the failure zone of the specimen exhibits relatively diffuse shear strain distribution and does not appear to localise, Figure 8d. Oppositely, by dynamic loading the deformation is localised due to thermal softening of the material and higher values of shear strain are reached (Figure 8h), which is in agreement with the experimental results.

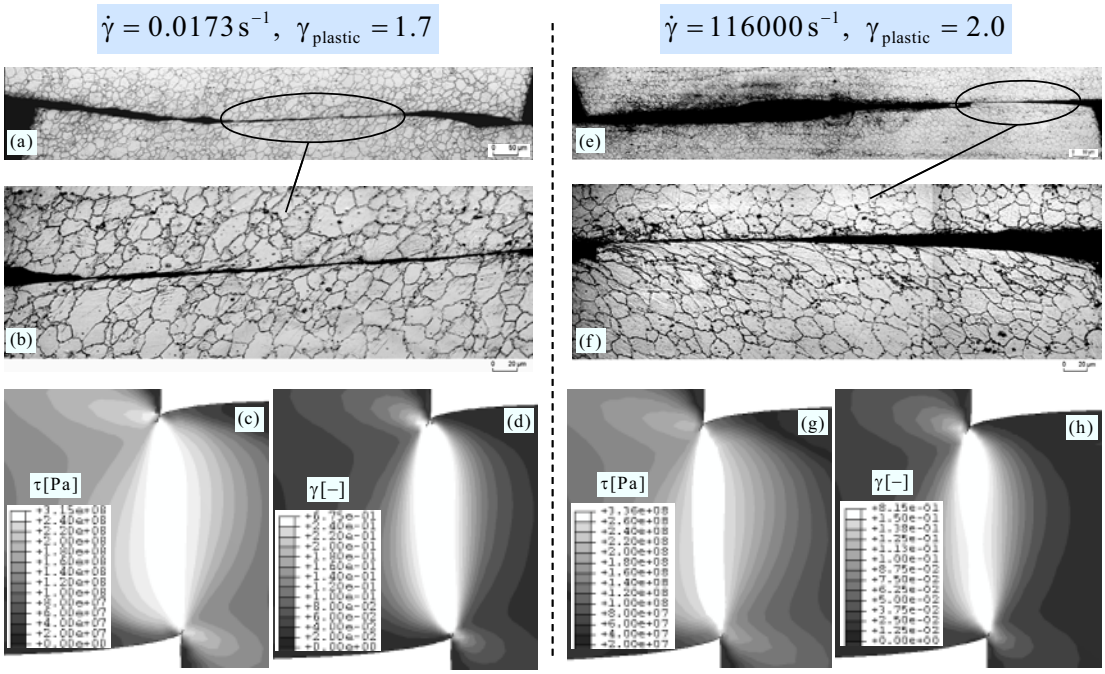

Figure 8: *Shear strain localization by impact shear test on AZ80 (ϑ = 20°C)*

4.2 Failure criterion for ductile fracture

Figure 9 shows the results of the FE-Simulations of smooth tensile specimens and differently notched bars of Al-alloy AA7075 T7351.

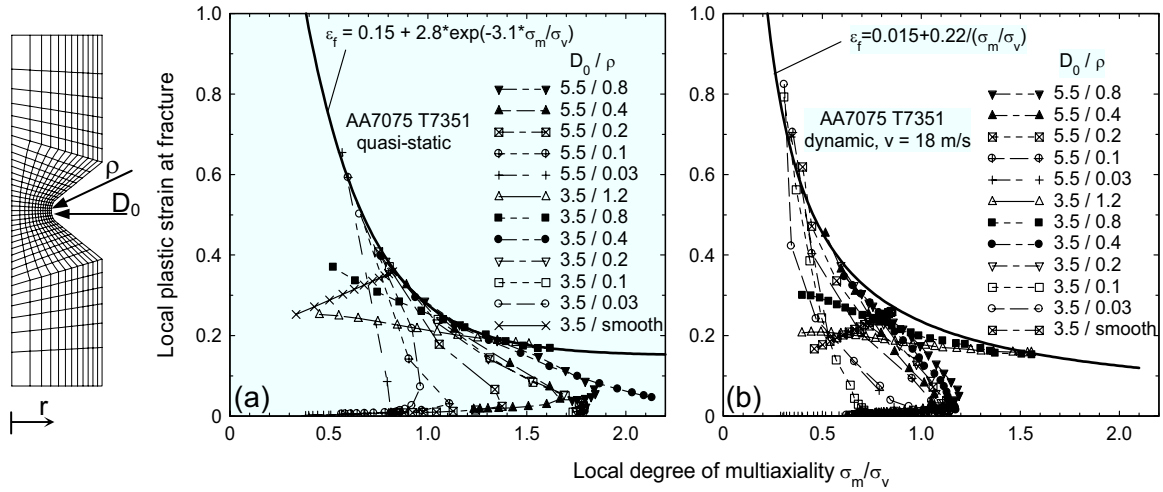

Figure 9: *Local equivalent plastic strain at fracture as a function of the degree of multiaxiality (σ_m/σ_v) along the specimen radius at the narrowest cross-section of differently notched specimen of aluminium AA7075 T7351 under (a) quasi-static (ABAQUS/Standard) and (b) dynamic loading (ABAQUS/Explicit) [9]*

The failure criterion for AA7075 was defined by the local failure strain $\overline{\varepsilon}_f$ as a function of the ratio between local mean stress σ_m and local equivalent stress σ_v. Such a criterion was deduced considering that ductile fracture occurs due to nucleation, growth, and coalescence of micro-cavities. The experimental specimen elongation at fracture was used as

a termination time point for the FE-Simulation. The corresponding values of the local equivalent plastic strain $\bar{\varepsilon}(r)$ and degree of multiaxiality were computed for the different notch geometries at the different Gauss-integration points along the radius r of the specimen in the narrowest cross-section D_0. The results are represented by a continuous curve for each geometry. Each point of the curve represents a location r along the radius in the smallest cross-section. Only one point of each curve fulfils the failure criterion, so that the envelope of all curves represents the failure criterion. For quasi-static loading, the envelope is described by the Hancock/Mackenzie relation [10], and for dynamic loading by [11]. Under quasi-static loading, the local effective plastic strain for a given degree of multiaxiality is higher than in the case of dynamic loading.

5 Conclusions

- The mechanical behaviour of materials at high strain rates is mainly characterised by increased strain rate sensitivity and the adiabatic character of the deformation process
- Under impact loading the ductility of AA7075 and AZ80 increases sharply with strain rate due to the higher strain rate sensitivity, while it decreases for Ti-6Al-4V due to the dominating rate dependence of the damage process
- Deformation localisation and shear band cause the damage in AA7075, AZ80, and Ti-6Al-4V under dynamic compression loading
- The mechanical flow behaviour of the investigated alloys was characterised with adequate constitutive material laws
- In order to validate the used constitutive material laws, compression, tension and shear tests were simulated by the finite element method.

References

[1] *Lips, H.; Brodmann, M.; El-Magd, E.*: J. Phys. IV 10 (2000) 371.
[2] *Neubauer, A.; Stroppe, H.; Wolf, H.*: Verlag Technik, Berlin 1988.
[3] *El-Magd, E.; Treppmann, C.; Weisshaupt, H.*: J. Phys. IV, suppl. III, 1997, 511.
[4] *Lippmann, H.*: Springer Verlag, Berlin, 1981, 210.
[5] *Sakino, K.; Shiori, J.*: J. Physique. IV, suppl. III, 1991, 1, C3.
[6] *El-Magd, E.*: J. Phys. IV, suppl. J. Phys. III 1994, 4, 149.
[7] *Taylor, G.I.; Quinney, H.*: Proc. R. Soc. A413 (1934) 307.
[8] *Treppmann, C.*: PhD-Thesis, RWTH Aachen, Germany, 2001.
[9] *Brodmann, M.*: PhD-Thesis, RWTH Aachen, Germany, 2001.
[10] *Hancock, J.W.; Mackenzie, A.Z.*: J. Mech. Phys. Solids 24 1976, 147.
[11] *El-Magd, E.*: Steel Res. 68 2 1997, 67.

Determination of Material Characteristics using Electromagnetic Forming and Weak Coupled Finite Element Simulations*

A. Brosius, M. Kleiner

Chair of Forming Technology, University of Dortmund, Germany

Abstract

The aim of this approach is to determine material characteristics of aluminium alloys (in the present case: AA5747) at very high strain rates, more precisely the relationship between yield stress, plastic strain and strain rate is figured out. To achieve high strain rates up to 10^4 s^{-1} the electromagnetic forming process (EMF) is applied, where a pulsed magnetic field is used to form materials with a high electrical conductivity during a process time between 10µs - 50µs. The advantage that EMF is a non-contact forming process can be used to determine material characteristics without any influence of friction. Additionally, in contrast to other testing methods the assumption of a mean strain rate over the process time is not needed, because the evaluation is done by finite element simulations.

To compute the associated flow curve array, where the strain rate is the third dimension, a method will be proposed combining an on-line measurement technique and iterative finite element simulations. During EMF of the tube specimen, the radial displacement of at least one significant point at the tube surface is measured on-line. These data are used as reference values for the iteration scheme. The iteration starts with the material data of a quasi-static tensile test. In order to minimise the deviations between on-line measurement and simulation result an automated data modification scheme is implemented.

The kernel of this scheme consists of an optimisation algorithm and two finite element codes. The first one is used to compute the deformation process of the specimen in a conventional transient way. The second code is implemented to calculate the body force distribution by a harmonic electromagnetic analysis. These two codes are coupled in a weak staggered approach.

Keywords:

Parameter identification, Finite Element Method, Electromagnetic Forming

---

* This work is based on the result of a research project form the DFG-SPP 1046 – The authors would like to thank the Deutsche Forschungsgemeinschaft DFG for its financial support

1 Introduction

For the description and analysis of high speed forming processes by means of finite element simulations a certain amount of knowledge about the qualitative and quantitative material behaviour during the forming process is essential. The intention of the present work is to determine yield curves at high strain rates using an iterative finite element simulation procedure. For this purpose the electromagnetic Forming (EMF) is used as a typical high speed forming process, where the energy density of a pulsed magnetic field is used for a contact less forming of metals with high electrical conductivity, such as copper or aluminium. The work-piece to be deformed will be located within the effective area of the tool coil, so that the resulting type of stress during the forming process is determined by the type of coil used and its arrangement as related to the component. Tubular components can be narrowed by means of compression coils or widened by means of expansions coils (see Figure 1).

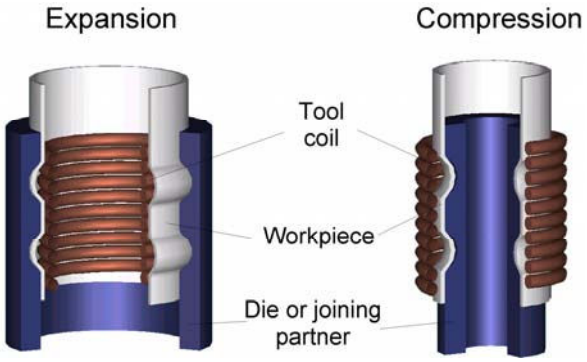

Figure 1: *Electromagnetic forming – Type of coils*

The basic idea for the determination of the dynamic material behaviour is to vary the strain rate dependent yield curves used as input for a finite element simulation (as a part from the optimisation strategy) until the calculated deformations match the measured ones. To evaluate the simulation results a comparison between the calculated radius and the experimentally determined radius is done in order to minimise the resulting difference.

In the present work the compression and expansion of a tube will be observed. At first, the important characteristics of the process serving as input for a mechanical finite element model will be determined. These will be the accurate geometrical dimensions of tool coil and work-piece, the acting body force depending on the time as well as the deformation of a significant point during the process.

2 On-line Measurement

For the comparison of experimentally obtained deformations and simulated deformations in the considered axial cross section (Figure 2a) the inner and outer contours will be measured off-line with a coordinate measurement machine (CMM) before and after the forming operation. As the geometrical data shall serve as reference values for the mechanical finite element simulation the obtained geometry at the end of the deformation is not sufficient to allow assumptions about the behaviour during the forming process. There-

fore, in addition to the off-line measurement a determination of reference data for an unambiguous description of the deformation would be useful. For this purpose an on-line measurement system based on a laser optical principle has been developed [1].

Because the forming process usually ends after a few ten microseconds, a very high time resolution had to be realised. The set-up of the developed measuring device for tube compression is shown in Figure 1a. As source of light a laser diode with line generator is used. The amount of parallel light shining through the sample is detected by a PSD (position sensitive detector) and depends on the actual inner radius of the sample. The output voltage of the PSD is proportional to the displacement of point A, in which the maximum deformation occurs. The same principle is used for the tube expansion (Figure 2b).

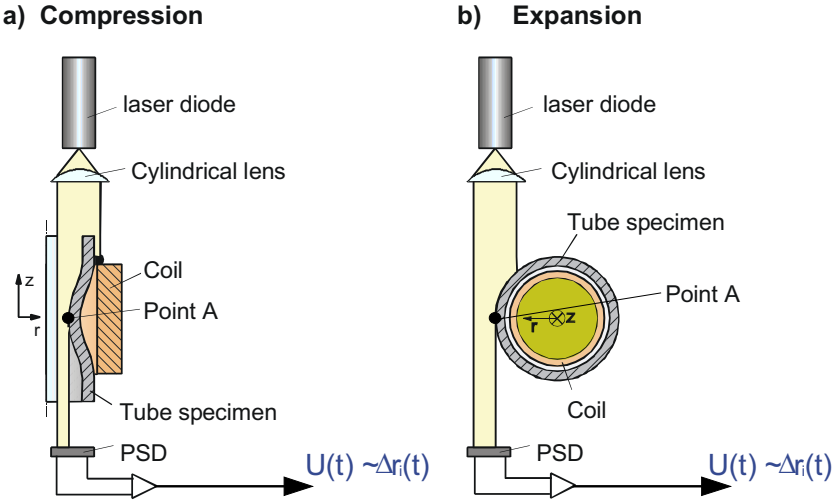

Figure 2: *On-line measurement system for radial displacement*

3 Finite Element Modelling

The finite element model consists of two different domains that are coupled in a staggered approach (see Figure 3).

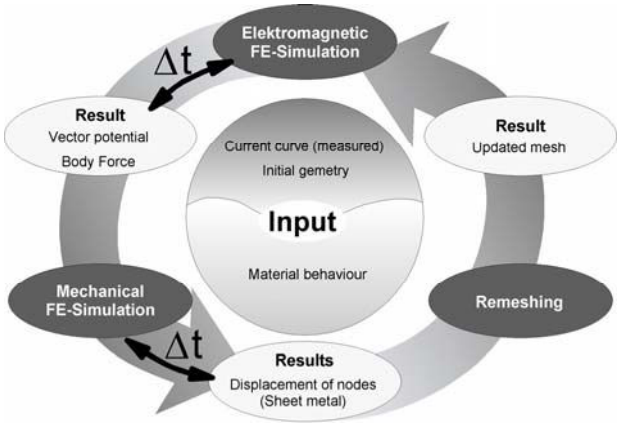

Figure 3: *Weak Coupling Procedure*

The mechanical sub-system allows the structure-dynamic simulation of the forming process. For this purpose the general-purpose-program MARC (version 2003) combined with user-subroutines is used. Contrary, the electromagnetic field simulation is done by a self developed FE-Code to determine the acting body forces inside the tube specimen.

The used weak coupling procedure is shown in Figure 3. Starting with an initial mesh in the electromagnetic domain, the body force distribution is calculated assuming a harmonic oscillating coil current with amplitude of 1kA. These force distribution is scaled with the measured coil current for a defined time interval Δt to ensure a transient evolution of acting forces during the mechanical analysis with Marc. The calculated deformation requires the update of the mesh for the surrounding air. Therefore a re-meshing algorithm is implemented based on a delauney triangulation to ensure the automated mesh generation during the coupled simulation. After finishing this, a new electromagnetic simulation will be carried out to update the body force distribution with respect to the actual geometry. In the following chapters the mentioned modules will be described.

3.1 Mechanical Model

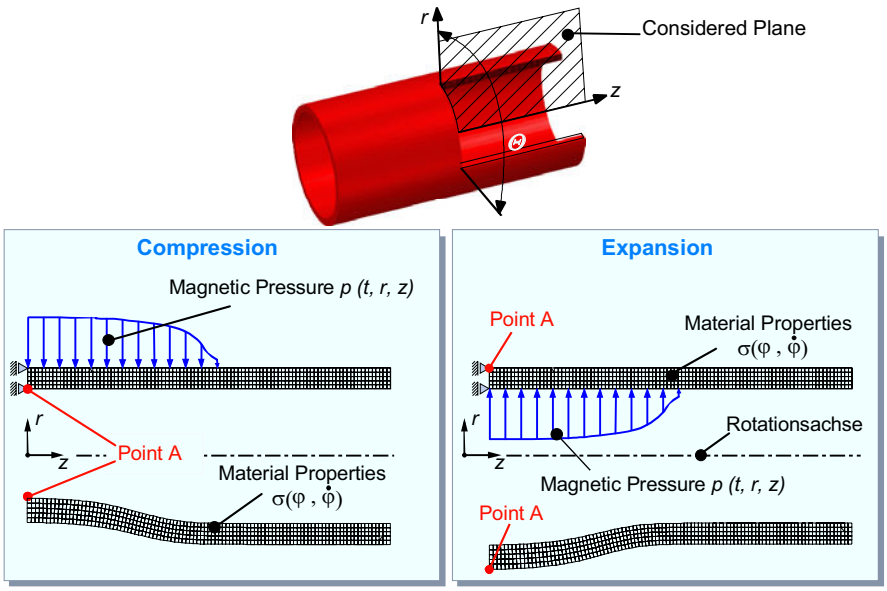

Figure 4: *Mechanical finite element model for tube compression and expansion*

The mechanical as well as the electromagnetic finite element model, makes use of the rotational symmetry of tool and work-piece. This simplification is possible, because the symmetrical pressure distribution causes a symmetrical deformation with very good concentricity of the sample even after the forming process. By utilising the symmetry of the tube, only half the geometry has to be considered. To ensure the consideration of inertia effects during the process an implicit time integration scheme (Newmark) has been applied to solve the equations of motion. The mechanical mesh was build up with approximately 400 iso-parametric four-node 2-½ D elements with bilinear shape function. Figure 4 shows the mesh of the modelled half with the applied load distribution depending from the chosen arrangement. The displayed load type (magnetic pressure as a surface load) is only for simplification because the body force is considered. The calculation of this load is done by a self-developed FE-Code, which is implemented via user-subroutines.

3.2 Electromagnetic Model

To simplify the time intensive transient calculation of the electromagnetic field, the following harmonic system will be solved.

$$\left(\left[K\right] - \Omega \cdot \left[C\right]\right) \cdot \left(\left\{u_1\right\} + i \cdot \left\{u_2\right\}\right) = \left\{F_1 + i \cdot F_2\right\} \tag{1}$$

K:	Stiffness matrix	Ω:	Imposed circular frequency
C:	"Damping" matrix	A_e:	Magnetic vector potential
u_1, u_2:	Real and imaginary part of the DOF	ν_e:	time integrated electric scalar potential
F_1, F_2:	Real and imaginary part of the force	i:	Square root of -1

The vector potential A_e as well as the electric scalar potential ν_e are considered as a degree of freedom (DOF). This kind of modelling is necessary to ensure the capability of a massive conductor simulation with an appropriate current density calculation inside the windings. A detailed description of the implemented Matrices is given in [2].

Despite a typical number of 10,000 nodes, which are necessary to model the electromagnetic domain, short simulation times are required to reduce the over-all simulation time for the material determination. To ensure this, an iterative conjugate gradient sparse matrix solver is implemented to solve Equation (1). Beside the advantage of getting a fast solution, less memory storage is needed compared to conventional frontal solvers.

3.3 Re-meshing algorithm

Similar to the mentioned different simulation domains, two different finite element meshes are in usage. The first one is the mechanical mesh, shown in Figure 4. The element connectivity is unchanged over the whole calculation, but the nodal coordinates are changing because of the transient mechanical simulation.

The second mesh regards the electromagnetic field simulation. It has to be updated for each harmonic simulation. To reduce the time effort for the re-meshing procedure during the staggered simulation this area is subdivided into two parts: On the one hand a fixed mesh is used, which is unchanged during the whole simulation. This part includes the windings and the areas far away from the region where the deformation occurs. On the other hand, the region nearby the deformation area has to be re-meshed with respect to the tube contour. This is done automatically by a delauney triangulation.

4 Material behaviour and its description

The material behaviour is modelled as a function of plastic strain as well as from plastic strain rate. Despite the fact that EMF is nearly an adiabatic process, finite element simulations of the tube compression have shown a maximal temperature rise of approximately 20 K [3]. Therefore temperature effects on the yield stress are neglected.

With the aim using an optimisation algorithm for the automated modification of the material parameters, the mathematical description of the material must fulfil several demands. On the one hand the chosen parameters have to be suitable for modelling the material behaviour with respect to the physics and do not constrain it in an unrealistic

manner (e.g. by a insufficient number of parameters). On the other hand the number of parameters must be limited to apply an optimisation algorithm in a reasonable way with respect to the computational effort.

To overcome this conflict of aims a Bezier-Surface is used to approximate the flow curve array (see Figure 6). 16 control points are necessary to define the surface; each of them consists of 3 coordinates which over-all generates 48 independent parameters. By definition of reasonable restrictions (the quasi-static yield curve remains and upper boundaries for the strain and strain rate) the number of parameters can be reduced to 26.

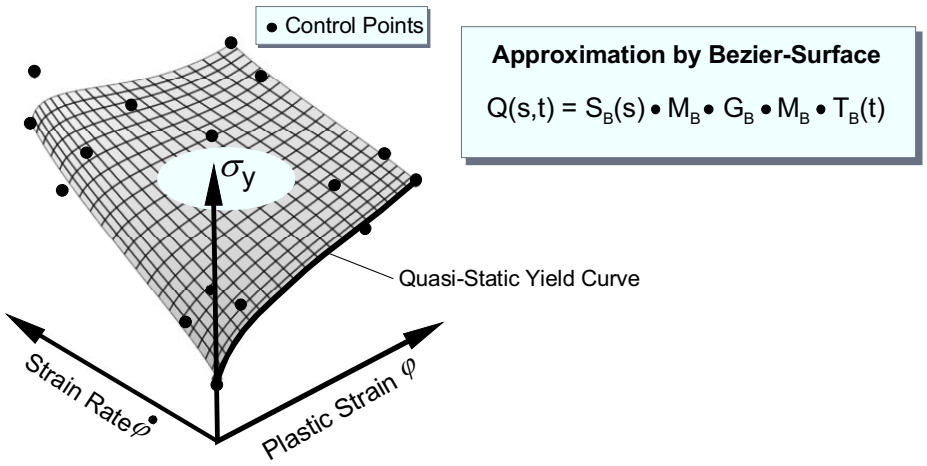

Figure 6: *Approximation of strain rate dependency via Bezier-Surface*

5 Optimisation algorithm

Searching for an optimum can be very time consuming. Especially, if it is completely unknown where the optimum is located. Independent from the used optimisation tool, it is necessary to define a point where the algorithm starts. In the present case, at least 26 parameters have to be defined with values, which are still unidentified. To overcome this problem, two optimisation strategies are applied. First, a physical based strategy will be used to determine starting parameters, which are located in the area of the optimum. These parameters are used by the second strategy to initialise the starting point and proceed with the optimisation process immediately.

5.1 Physical based optimisation

The basic idea of this pre-optimisation is the assumption of a constant amount of dissipated energy due to plastic deformation, independent from the hardening behaviour of the material. This assumption is not in accordance with the physical behaviour of the material, but it can be used as a rough estimation for the first optimisation stage.

The requirement for starting the optimisation is the knowledge about the quasi-static yield curve $\sigma_v(\varphi_v)$ of the tube specimen. During the forming process energy dissipates due to plastic deformation regarding Equation 2 (specific work is used for a simpler notification).

$$w = \int_0^{\varphi_v} \sigma_v \cdot d\varphi_v \tag{2}$$

A first simulation with the quasi-static yield curve is carried out and the radial displacement will be measured by the system described in chapter 2. The logarithmic tangential strain $\varphi_{33,\,\mathrm{exp}}$ is calculated from the on-line measurement using Equation 3 (Δr: radial displacement; r_0: initial radius). A scale factor f is defined by dividing the maximal tangential strain from the experiment by the one calculated during the finite element simulation (Equation 4).

$$\varphi_{33,\,\mathrm{exp}} = \ln\left(1 + \frac{\Delta r}{r_0}\right) \tag{3}$$

$$f = \frac{\max\left(\varphi_{33,\mathrm{exp}}\right)}{\max\left(\varphi_{33,\mathrm{sim}}\right)} \tag{4}$$

This factor is applied to the simulated equivalent plastic strain, which is considered as a function of time [$\varphi_v = \mathrm{f}(t)$]. Remembering the basic assumption of this procedure regarding a constant amount of work independent from the hardening behaviour, it is obvious that an unbalanced system is generated (Equation 5 and 6).

$$w_{sim} \neq w_{sim,scale} \tag{5}$$

$$\int_0^{\varphi_v} \sigma_v \cdot d\varphi_v \neq \int_0^{\varphi_{v,scale}} \sigma_v \cdot d\varphi_{v,scale} \tag{6}$$

To get a balanced system, the yield stress has to be modified by a correction term $\Delta\sigma_v$ which can be seen as a function of the strain rate [$\Delta\sigma_v = f(\dot{\varphi}_v)$].

$$\int_0^{\varphi_v} \sigma_v \cdot d\varphi_v = \int_0^{\varphi_{v,scale}} (\sigma_v + \Delta\sigma_v) \cdot d\varphi_{v,scale} \tag{7}$$

Applying Equation 7 during the whole simulation procedure, the correction term $\Delta\sigma_v = f(\dot{\varphi}_v)$ can be determined for every increment directly. By updating the initially used quasi-static yield curve, the hardening behaviour becomes also a function from the strain rate $\sigma_v = f(\varphi_v, \dot{\varphi}_v)$. The described steps will be repeated until a) a rough agreement between simulation and experiment is achieved and b) the starting point of the subsequent optimisation strategy is well defined. In the present case 27 simulations has to be done to initialise the subsequent optimisation algorithm.

5.2 Numerical based optimisation

In the present case a “Downhill-Simplex” algorithm is used, which is not related to the simplex method of linear programming [4]. The method needs only function evaluations and requires no derivatives. Unfortunately it converges very slowly, because no information about a preferable direction like in a gradient-based optimisation strategy is given. But this disadvantage will be compensated by the algorithms robustness.

Using the simulation results from the previous optimisation stage, the initial simplex can be initialised with a suitable starting position and the optimisation can proceed. The function to be minimised is the deviation between simulated and measured radial displacement over the whole process time. If the obtained solution between two iterations remains static, the optimisation procedure will stop and the material description is found.

The described combination of the two strategies ensures a fast convergence for the determination of material parameters. A typical number of necessary iterations are about 120.

6 Determined material characteristic

Figure 7 shows the comparison between the measured and simulated tube narrowing (Figure 7a) and tube expanding (Figure 7b) by means of two different loading energies for each arrangement.

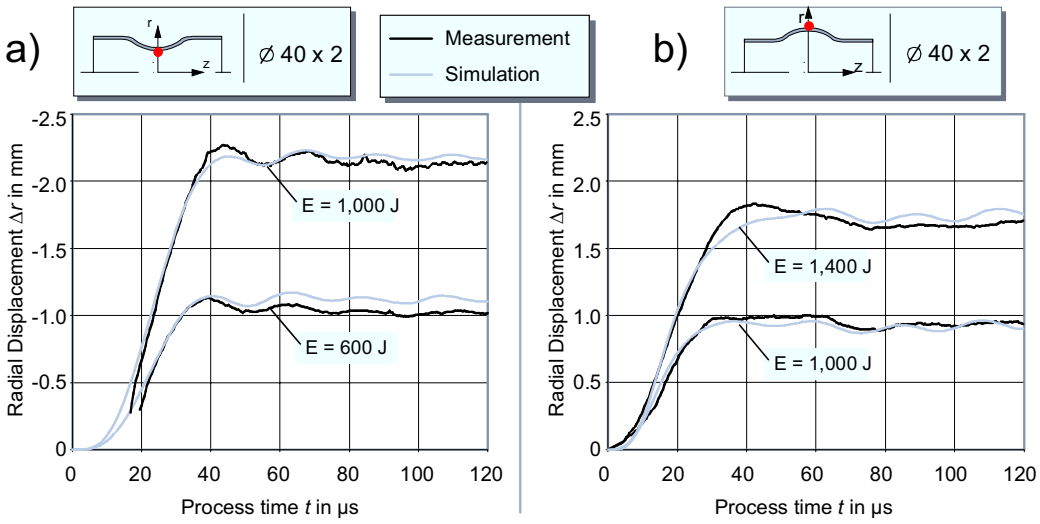

Figure 7: *Measured and simulated radial displacement*

Because of a measurement inaccuracy of approximately 0.1 mm an exclusive evaluation of the displacement deviations between the corresponding curves isn't meaningful. An additional check of the relevant eigenfrequencies is also advisable. Doing this, it can be seen that the simulation results are in good agreement with the experiment, except the tube expansion with a charging energy of 1,400 J. The experimental curve shows the typical "overshooting" of the displacement, followed by an untypical low frequent oscillation. This measured curve wasn't reached by any simulation result. A reason could be an insufficient roundness of the initial tube specimen. Spot tests have shown maximal deviations of about ± 0.2 mm. The influence of this has to be quantified by a 3-dimensional simulation with an accordant wall thickness distribution.

Figure 8 shows the corresponding yield curve array as a Bezier-Surface for the relevant strain and strain rate area for tube compression (Figure 8a) as well as for tube expansion (Figure 8b). Both yield curve arrays show a distinct hardening due to the achieved strain rate during the forming process, but the materials gets a higher strength in case of tube expansion. Reasons for this phenomenon could be the different hardening behaviour for tensile and compressive stressing, known from the literature as Bausch-

inger-effect. If this will become dominant for aluminium alloys to be formed with this process, the assumption of an isotropic material behaviour must be dropped. Instead of this, an initial anisotropy must be included and experiments for tube compression as well as for tube expansion has to be done for a complete material characterisation.

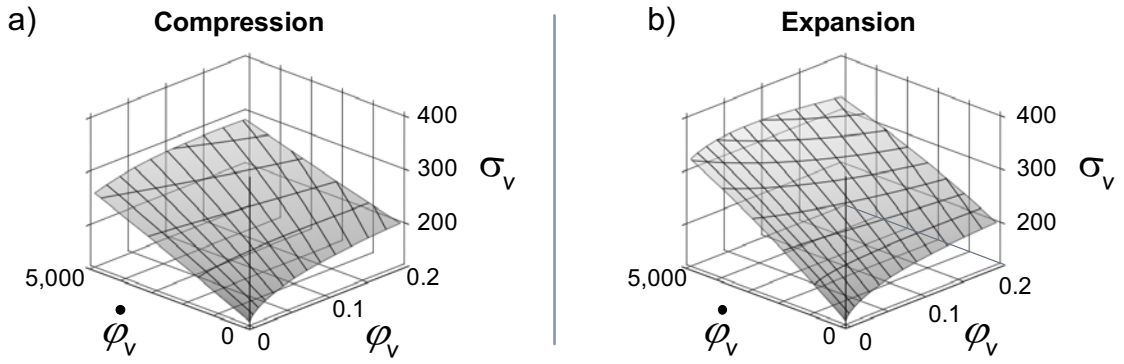

Figure 8: *Determined flow curve arrays*

7 Summary and Outlook

The present article describes the possibility to determine material characteristics by using the electromagnetic forming process for tube compression and tube expansion and an iterative weak coupled finite element simulation procedure. The experimental set-up is capable to achieve strain rates up to 10,000 s^{-1} where other techniques will start to fail. The simulation procedure allows a very fast simulation of the coupled field problem with a sufficient accuracy, which is essential for the determination of material parameters.

The presented results show a dependency on the direction of stressing. Therefore an initial anisotropic material behaviour inside the simulation has to be implemented and the effect on the determined material parameters has to be quantified. This approach is directly transferable to the material determination using the electromagnetic sheet metal forming process where effects of cinematic hardening can be expected.

References

[1] *Bauer, D.:* Der Einfluß hoher Formänderungsgeschwindigkeiten auf die Kaltumformung von Stahl Kupfer und Alumumium, Fortschrittberichte der VDI-Zeitschriften; Reihe 2, Nr. 26.

[2] SAS IP, Inc: Ansys Theory Reference, 11th edition, V5.6, 1999.

[3] *Brosius, A.; Kleiner, M.:* Ermittlung Gescgwindigkeitsabhängiger Fließkurven mittels Elektromagnetischer Umformung, Oral Presentation at 2. Kolloq. Elektromagnetische Umformung, 28. Mai 2003, Dortmund.

[4] *Nelder, J.A., and Mead, R.* 1965, Computer Journal, Vol. 7, pp. 308–313.

Stress-Strain Curves of Sheet Material in High-Rate Forming Processes

S.Golovashchenko[1], V.Mamutov[2]

[1] Manufacturing & Processes Department, Ford Research & Advanced Engineering, USA
[2] Chair of Machines & Technology of Metal Forming, St.Petersburg Politechnical University, Russia

Abstract

Electromagnetic forming technologies are based on high-voltage discharge of capacitors through the conductive coil. Two methods of testing and the results of dynamic coefficient kd for aluminum alloys, copper, brass, steel, and some other materials are presented. The first method is based on expansion of rings machined from tubular blanks, which are designated for further stamping operations. The displacement of the ring was registered by using the light shading method. Parameters of the discharge electric current running through the electromagnetic coil were measured with a Rogowski gauge. The acceleration stage of the ring expansion process was used for more accurate calibration of the inductive gauge defining the parameters of electromagnetic pressure. Registering the kinematics of the ring during the inertial stage of the deformation process provided the information on dynamic behavior of the studied material.

The second method employed in this paper for dynamic yield stress measurement was based on transverse pulsed loading of a sheet sample clamped by its ends. Shapes of the samples during their deformation were photographed using a high-speed camera. The specifics of the sheet sample deformation under the pulsed transverse load are the following: the sample has near-trapezoidal shape; the middle part of the sample has almost the same velocity υ_0 through the whole process; the angle between two inclined parts of the sample and the horizontal middle area γ has minor variation during the deformation process. In some cases, hybrid stamping processes including conventional forming on the press and final shape calibrating with pulsed forming technique require additional information about the influence of the static preliminary deformation of the sheet on dynamic yield stress. Experiments with different levels of material prestrain were conducted for this purpose.

Keywords:

Forming, Sheet, High Strain-Rate

1 Introduction

Electropulsed forming technologies are based on high-voltage discharge of capacitors through the conductive coil or between the electrodes in water. These processes generate high pressure on a sheet or tubular blank being formed, calibrated or assembled with other parts. The important benefits of pulsed technologies include low investment in one-sided dies [1], increased formability [2], reduced wrinkling and springback [3]. Material properties under high strain-rate deformation are the necessary input to analyze all pulsed stamping and joining operations.

Strain rates in pulsed electromagnetic forming and electrohydraulic forming of sheet material are usually within the following range $\dot{\varepsilon} \in [10^2\text{-}10^3]\ s^{-1}$. This range significantly exceeds conventional tensile test conditions of $\dot{\varepsilon}_0 = 10^{-4}\ s^{-1}$. Approximate information on dynamic stress-strain curves is especially important regarding the design stage of pulsed stamping processes. For example, for calibration of parts stamped from sheet metal or tubular blanks we need to estimate the required energy, choose the right duration of the pressure pulse, and design the calibration die appropriately to provide its sufficient durability. Each of these tasks requires preliminary data on material behavior under high strain rates. Later on this information can be corrected after conducting additional experiments with existing tools.

One of the possible approaches to this problem is based on the assumption that the average strain rate of the stamping process $\dot{\varepsilon}$ significantly exceeds the strain rate of the static test $\dot{\varepsilon}_0$. If this assumption is valid it is possible to represent the stress-strain rate function with reasonable accuracy based on the static curve $\sigma_s(\varepsilon_i, \dot{\varepsilon}_0)$ multiplied by some dynamic functional $k(\varepsilon_i, \dot{\varepsilon})$:

$$\sigma_s = k(\varepsilon_i, \dot{\varepsilon})\, \sigma_s(\varepsilon_i, \dot{\varepsilon}_0) \tag{1}$$

For simplicity the functional can be replaced by some dynamic coefficient k^d valid in a certain range of strain rates. The dynamic coefficient can be represented as a power function

$$k = \left(\frac{\dot{\varepsilon}}{\dot{\varepsilon}_0} \right)^m \tag{2}$$

If the strain rate value $\dot{\varepsilon}$ exceeds the value of $\dot{\varepsilon}_0$ in several orders of magnitude, the functional $k(\varepsilon_i, \dot{\varepsilon})$ can be replaced by the integral dynamic coefficient k^d [4]. Variation of the dynamic coefficient for most part of some high-rate stamping process can be relatively small. Usually the strain rate of the high-speed stamping processes varies within one or two orders of magnitude.

$$\frac{1}{T} \int_0^T \varepsilon_i(t)\, dt \in \left[\dot{\varepsilon}_{max}, \dot{\varepsilon}_{min} \right],\ \frac{\dot{\varepsilon}_{max}}{\dot{\varepsilon}_{min}} < 10^1 \ldots 10^2 \tag{3}$$

where T is duration of the stamping process. Taking into account that the parameter m in (2) for majority of metals is a small value, an average dynamic coefficient can be used instead of the function of strain-rate hardening for each material in some limited interval of strain rates.

$$k^d = \left[\frac{\left(\dot{\varepsilon}_{min} + \dot{\varepsilon}_{max}\right)}{\left(2\dot{\varepsilon}_0\right)}\right]^m \in \left[k^d_{min}, k^d_{max}\right] \tag{4}$$

On a design stage of the stamping processes such simplification is valid because for the majority of experimental methods defining the parameters of a dynamic stress-strain curve the following inequity is valid:

$$2\frac{\left(k^d_{max} - k^d_{min}\right)}{\left(k^d_{max} - k^d_{min}\right)} < \gamma \tag{5}$$

where γ is the relative error of the experimental results.

Several methods of defining dynamic stress-strain curves of metals are known in the literature. One of the simplest is the method of expansion of rings, which allows to create the stress state in the sample close to the uniaxial tension similar to a standard test [3,5]. Effects of waves propagation do not create significant distortions; therefore, the stress and strain distributions are close to being uniform. The other well-known method is based on the transverse impact on the sheet metal, where the speed of the plastic wave propagation is the most important factor defining the dynamic yield stress [6,7,8]. In many cases, high-speed forming is used after the conventional forming. Therefore, some adjustments of this method allowing the study of the effect of preliminary deformation on the dynamic yield stress [9] are beneficial. Employment of various methods for the same material provides more reliable data as to their dynamic behavior. It also helps to calibrate the technique of measurements and data processing.

2 Study of dynamic behavior of metals using expansion of rings

The schematic of the experimental technique used in this paragraph is shown in Figure 1.

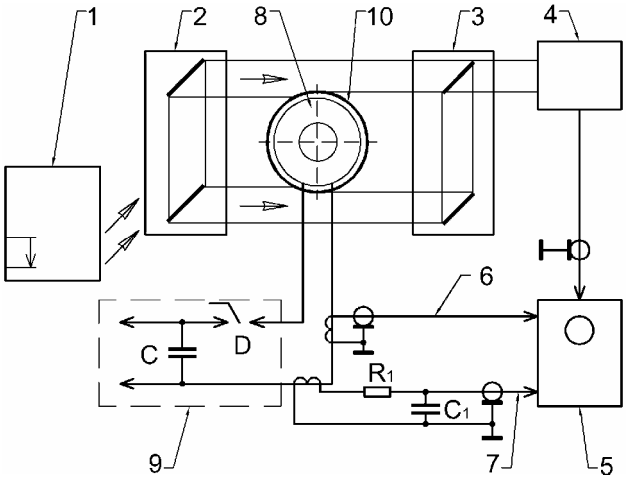

Figure 1: *Schematic of the experimental device to study the dynamic yield stress by registering the dynamics of the ring expansion: 1 - optical laser, 2 - block of beams formation, 3 - summation block, 4 - receiver based upon the photo-electronic multiplier, 5 - oscilloscope, 6 - Rogowski gauge, triggering the oscilloscope, 7 - Rogowski gauge with integration RC contour for measurement of the discharge current, 8 - coil, 9 - electromagnetic forming machine, 10 - ring to be expanded*

A beam from the optical laser 1 is transformed into two identical parallel beams of rectangular cross-section and rather uniform distribution of light intensity using the block of beams formation 2 The thickness and width of the beam as well as the distance between two beams can be tuned according to the dimensions of the ring used in experimental studies. The summation block 3 adds both beams and directs them to a receiver 4 based on a photo electronic multiplier. The receiver is equipped with the narrow range light filters, which allow to separate the actual signal from the general light. The receiver was mounted inside the metal box in order to protect it from the electromagnetic noise. The electromagnetic coil 8 is positioned inside the ring 10, which is being accelerated during the high-voltage discharge of electric capacitors of the electromagnetic forming machine 9 through the coil. During the expansion of the ring driven by internal electromagnetic pressure, the wall of the ring is shading the beams of the laser. This results in a changing of the luminous flux coming to the receiver and registered by the oscilloscope 5. The initiation of the oscilloscope was carried out by a signal from Rogowski gauge 6. The signal from the other Rogowski gauge 7 was integrated using a R-C contour and also registered by the oscilloscope. This signal was necessary to define the moment when the discharge of the electromagnetic forming machine is completed. From that moment on, further deformation of the ring is purely inertial.

The experiments were conducted using an electromagnetic forming machine with the following parameters: capacitance - 215 μF, maximum charging voltage - 20 kV; frequency of the machine dictated by its L-C combination - 24 kHz. The rings had the following dimensions: external diameter - 44 mm; width - 3 mm; thickness - 1 mm. Copper samples were annealed in vacuum at a temperature of 560°C for one hour. The multi-turn coil machined from a brass bar was press-fit over the micarta internal mandrel. The absence of error signals was checked by discharging capacitors through the coil without placing a ring and having the signal from the light receiver constant during the discharge process and also by switching on and off the light in the laboratory.

The simplest static linearity of the displacement measuring system can be checked by placing a ring of a larger diameter than the samples used in the expansion experiment and then moving this larger ring to different sides as a rigid body, shading different light beams. If the system is linear the signal of the ring displacement, corresponding to the ring outer diameter, should be the same. The dynamic linearity of the system was checked by an optical chopper disc rotated at a high speed. In order to make the pressure pulse shorter, the additional active resistance was connected in series with the coil. The value of this resistance was adjusted to provide an aperiodic discharge of capacitors. The example of oscillograms from the photo electronic multiplier, proportional to the radial displacement of the ring, and from the Rogowski gauge, proportional to the discharge electric current, are shown in Figure 2.

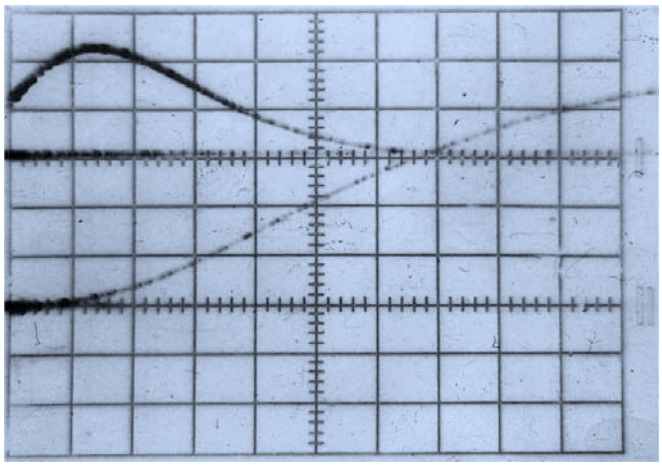

Figure 2: *Example of the oscillogram combining the radial displacement of the ring during its expansion combined with discharge current vs time. The scale along the horizontal axis was 10 μsec. Maximum displacement of the ring was 3.4 mm*

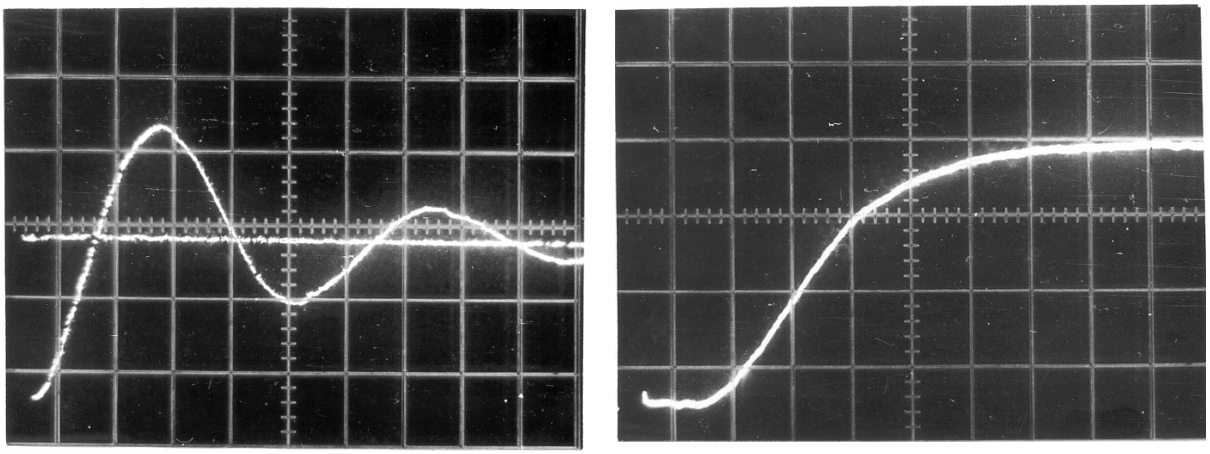

a b

Figure.3: *Examples of oscillograms of the induced electromotive force in the inductive gauge (a) and displacement of the ring being expanded (b). The scale along the horizontal axis is 20 μsec*

In order to define the dynamic behavior of studied materials, we used the integral energy conservation law. The dynamic coefficient k^d was defined by the following relationship:

$$k^d = \frac{\sigma_s^d}{\sigma_s^s} = \frac{\int_{\varepsilon_i \in [\varepsilon_{i1}, \varepsilon_{i2}]} \sigma_s^d(\varepsilon_i) d\varepsilon_i}{\int_{\varepsilon_i \in [\varepsilon_{i1}, \varepsilon_{i2}]} \sigma_s^s(\varepsilon_i) d\varepsilon_i} \tag{6}$$

Where σ_s^d and σ_s^s are the average values of dynamic and static yield stresses in the given interval of strain intensity variation $[\varepsilon_{i1}, \varepsilon_{i2}]$ corresponding to the conditions of the experiment. For the ring expansion process, the circumferential deformation is equal to the strain intensity and can be defined as:

$$\varepsilon_1 = \varepsilon_i = ln\left(\frac{r}{r_0}\right) \tag{7}$$

where r_0 and r are the original and current radii of the ring during the deformation process. The data from the oscillograms were processed during the interval of time $t \in [t_1, t_2]$ after the discharge of capacitors was completed and no electromagnetic pressure was applied to the ring. During this interval the ring is moving due to its mass inertia. The interval boundaries are defined in the following way: $t_1 > t_p$, where t_p is time when the pressure pulse was completed; $t_2 < t_{end}$, where t_{end} is the time when the plastic deformation process was completed and the ring stopped. For this interval, the energy conservation law can be used in the following form:

$$\frac{\rho\left[\dot{r}^2(t_1) - \dot{r}^2(t_2)\right]}{2} = \int_{\varepsilon_i(t_1)}^{\varepsilon_i(t_2)} \sigma_s^d(\varepsilon_i)\, d\varepsilon_i \tag{8}$$

where ρ is the mass density of the ring material; $\dot{r}^2(t_1)$, $\dot{r}^2(t_2)$ - radial velocity of the ring corresponding to the moments t_1 and t_2. Having known the parameters of the static stress-strain curve, the dynamic coefficient can be estimated from the following equation:

$$k^d = \frac{\rho\left[\dot{r}^2(t_1) - \dot{r}^2(t_2)\right]}{2\int_{\varepsilon_i(t_1)}^{\varepsilon_i(t_2)} \sigma_s^d(\varepsilon_i)\, d\varepsilon_i} \tag{9}$$

The values of velocities $\dot{r}(t_1)$ and $\dot{r}(t_2)$ were defined by numerical differentiation of the curve of radial displacement of the ring.

For the annealed copper M1 the average dynamic coefficient was obtained as $k^d = 1.35 \pm 0.20$. The averaging was conducted in the interval of strain rates of $\varepsilon \in [0.8, 1.6]\cdot 10^3 s^{-1}$ and the range of strains $\varepsilon_i \in [0.05, 0.20]$.

The described approach offers the very important advantage of excluding the uncertainty of registration of the pulsed load. This solution may not be feasible for materials with low ductility where the expansion of the ring is limited by its splitting, or in case of using the medium voltage electromagnetic forming machines (up to 5 - 6 kV of charging limit) and the coil with multiple turns with rather slow pressure pulse. In both of these cases, the electromagnetic pressure affects the deformation of the ring almost through the whole deformation process and equation (8) is not valid. The employment of the Rogowski gauge can also bring some averaging of the electromagnetic pressure along the coil axis. In this case a possible solution lies in installing the inductive gauge in the space between the coil and the ring, so we can register the applied pressure more accurately. It should be specified that the gauge has to be electrically insulated from both the coil and the ring. To satisfy this requirement, we mounted the inductive gauge outside the multiturn cylindrical coil in between the layers of the glass tape, covered by epoxy. After solidification the external surface of such an insulation was machined to fit accurately inside the ring. The inductive gauge was positioned approximately in the middle of the coil along its z-axis in order to get a uniform distribution of the electromagnetic pressure. The electromotive force $E(t)$ generated inside the inductive gauge was registered by the oscilloscope parallel to the radial displacement of the ring. According to [10] it can be represented as

$$E(t) = \frac{d\Phi}{dt} = -\mu_0 S_{effective} \frac{dH(t)}{dt} \tag{10}$$

where $H(t) = H_0 e^{-\delta t} \sin \omega t$ t – time; μ_0 - magnetic permeability of vacuum; δ, ω - the damping coefficient and circular frequency; Seffective is the geometric characteristic of the inductive gauge, which was defined by a separate test of the ring expansion made from annealed aluminum. The deformation of the thin ring driven by pulsed electromagnetic pressure can be defined by a simple equation:

$$p_0 e^{-2\delta t} \sin^2 \omega t = \frac{\sigma_s^s}{R} + \rho s \frac{d^2 R}{dt^2} \tag{11}$$

where p_0 is the pressure amplitude at t = 0; σ_s is current material yield stress; ρ is material density; s and R are current thickness and radius of the ring, changing during the deformation process.

In the beginning of the process, during the ring quick acceleration stage, the first term in the right part of the equation can be found using a dynamic stress-strain curve of a known material or known dynamic coefficient and static curve. During this stage, the second term in the right side of the equation (11) clearly dominates over the first term, representing the energy dissipation through plastic deformation. Based on this consideration, the inductive gauge was calibrated during this stage and then used for further analysis of the material behavior. It was conducted by solving the equation (11) relatively the unknown value of σ_s at every time step. From the first glance, it looks very attractive to differentiate twice the function R(t) known from the experiment and find the unknown σ_s. However, some errors of registration R(t) can make the result inaccurate. Instead of that, we used the implicit procedure of integration adjusting σ_s to satisfy the R(t) curve and then smoothing the obtained results.

The technique described in this paragraph has some drawbacks including rather difficult tuning of the measuring system. It also has some limitation regarding electrical conductivity of the material being tested. For these reasons, the data obtained with this method was mostly used for an estimation of the results obtained with the transverse impact method.

3 Study of the dynamic behavior of metals using the transverse impact method

The method of transverse impact is based upon the specifics of the plastic waves propagation inside thin strip of metal sheet clamped by its edges. During the deformation process the strip has the shape of trapezoid, while both the velocity υ_0 of the central part of the strip and the angle γ between inclined and horizontal parts of the strip are almost constant through the whole process. Experimental data on υ_0 and γ allows the calculation of the dynamic yield stress [8]

$$\sigma_s^d = \rho \left[\frac{\upsilon_0}{tg(\gamma)} \right]^2 \tag{12}$$

Having defined the values of both dynamic and static yield stresses σ_s^d and σ_s^s, it is easy to find the dynamic coefficient k^d. The schematic of the measuring device is shown in Figure 4.

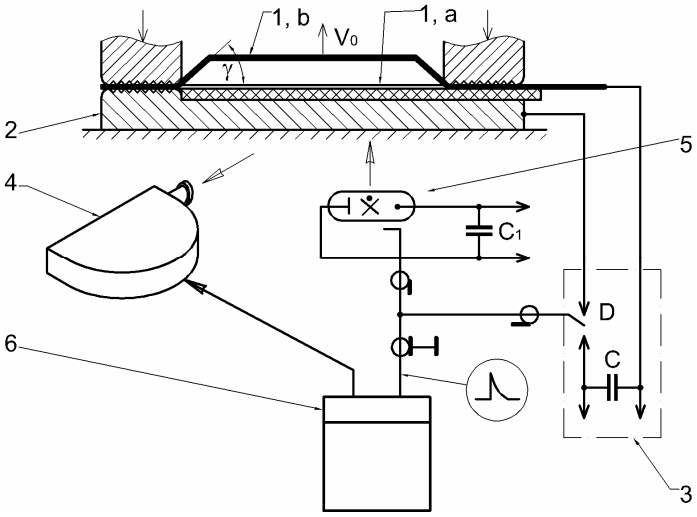

Figure 4: *Schematic of measurement of the strip kinematics after transverse pulsed loading with electromagnetic field (1 – sample being tested, a – in original position; b – during the deformation process; 2 – fixture for clamping the sample; 3 – electromagnetic forming machine; 4 – high-rate photo camera; 5 – block of pulsed light generation; 6 – control desk of the high-rate camera)*

The discharge current from the electromagnetic forming machine 3 is running through the supporting copper plate 2 and then through the sample 1, clamped by its edges. Driven by the pulse of electromagnetic pressure, the sample 1 quickly gains its initial speed and then goes through the deformation process. Photographing of the sample deformation history was conducted by a high-speed photo-registrator in reflected light of the flash lamp 5. Synchronization of the flash light, the deformation process, and its photo registration was conducted employing the special synchronization pulse from photo-registrator 6.

The samples for testing were fabricated from metal sheets 0.5 – 0.8 mm thick, 10 mm wide, and 160 mm long. The pulsed load generated by a pulsed electromagnetic field has some limitations mostly related to material electric conductivity. Due to this fact, copper, aluminum and their alloys are good candidates for such type of loading. In order to test samples from materials with significantly lower conductivity, the samples were coated by a layer of copper having the thickness of 0.003 – 0.05 mm. The described coating significantly improves the conditions for using pulsed electromagnetic fields as a source of impact transverse loads without adding any significant distortion into the experimental data. The examples of pictures illustrating the sample shape during the deformation process are shown in Figure 4.

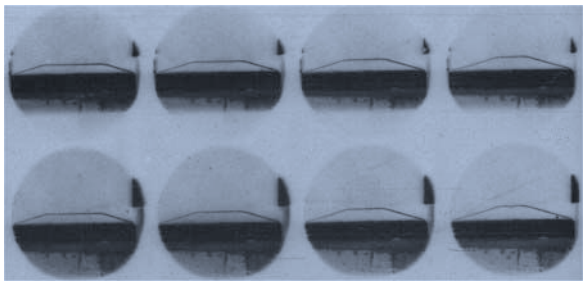

Figure 5: *Example of high-rate photo registration of sheet samples after the transverse pulsed loading (the rate of photographing is 62500 pictures/ second; the pictures are organized in a way that the top row includes odd numbers and the bottom row includes even numbers of pictures; the material of samples is copper M1)*

In order to study the effect of preliminary deformation and work hardening on the dynamic yield stress of tested metal, a special device was employed enabling the variation of the preliminary deformation.

4 Experimental results

The experimental data on testing the variety of metals is listed in Table 1. Each set of parameters was repeated from seven to ten times. Rounded up to the second digit, the number of trust interval was defined using the Student criterion and 95% of trust probability.

N	Material	Method of testing[1]	Preliminary deformation	Static yield stress, MPa	Dynamic coefficient k^d
1	Duralumin D16AM	2	0	127	1.65±0.15
2	Aluminum alloy, AMnM	2	0	56	1.30±0.20
3	Aluminum, AD1	2	0	90	1.35±0.10
4	Nickel	2	0	180	1.40±0.15
5	Molybdenum	2	0	1040	1.10±0.10
6	Niobium	2	0	416	1.10±0.05
7	Stainless steel	2	0	233	1.10±0.10
8	High Strength Steel	2	0	290	1.25±0.10
9	Brass	2	0	110	1.25±0.10
10	Copper, M1	1	0	102	1.35±0.20
11	Copper, M1	2,3	0	102	1.40±0.20
12	Copper, M1	3	0.09	183	1.30±0.15
13	Copper, M1	3	0.17	222	1.25±0.20
14	Mild steel, 08	2,3	0	185	1.30±0.15
15	Mild steel, 08	3	0.065	260	1.20±0.15
16	Mild steel, 08	3	0.125	310	1.15±0.10
17	Mild steel, 08	3	0.185	342	1.10±0.10

[1] 1 = pulsed expansion of rings; 2 = transverse impact; 3 = transverse impact with possible variation of the prestrain deformation

Table 1

5 Conclusions

Analysis of experimental data indicates that for testing samples of copper the method of ring expansion and the method of transverse impact provide sufficiently close results within the range of statistical deviation.

The increase of yield stress due to high strain-rate of testing for the majority of metals used in stamping can vary from several percents to 65%, which has to be considered on the design stage of the technological process of high-speed stamping.

References

[1] *Wilson F.W., ed.:* American Society of Tool and Manufacturing Engineers: High Velocity Forming of Metals (Prentice-Hall, Inc, Englewood Cliffs, N.J. 1964).

[2] *Golovashchenko, S.; Mamutov, V.; Dmitriev, V.; Sherman, A.:* Formability of sheet metal with pulsed electromagnetic and electrohydraulic technologies, Proceedings of TMS symposium "Aluminum-2003," San-Diego, 2003, p.99-110.

[3] *Golovashchenko S.:* Numerical and experimental results on pulsed tubes calibration, Proceedings of a 1999 TMS Symposium "Sheet Metal Forming Technology", San-Diego,1999, p.117-127.

[4] *Vagin, V.; Zdor G.; Mamutov V.*: Methods of analysis of high-rate deforming of metals, Minsk, 1990, 207p. –In Russian.

[5] *Lopatin, A.:* Development of dynamic stress-strain diagrams by using tubular samples," Pulsed Forming of Metals. Issue N2, Charkov, 1970, p.128-136. –In Russian.

[6] *Rahmatulin, H; Demyanov, Yu:* Strength under Intensive Short-Duration Loads, Moscow, 1961, 399 p. - In Russian.

[7] *Shcheglov, B.; Vlasov B.:* Study of Plastic Deformation of Thin Sheets under Dynamic Loading, Mechanical Engineering, 1972, N6, p.85-90. -In Russian.

[8] *Grushevskiy, A.:* Propagation of waves in Thin Strip and Study of Dynamic Yield Stress of Sheet Metals in Pulsed Stamping, Forging and Stamping Production, 1967, N8, p.21-25. – In Russian.

[9] *USSR Patent 926567: Bogoyavlenskiy, K.; Mamutov, V., Oreshenkov, A.; Perezhogin, A.:* The Device for Study of Dynamic Yield Stress for Sheet Metals. - In Russian.

[10] *Piekara, A.; Malecki, J.:* On a method of producing strong magnetic fields of short duration, Acta Physica Polonica. - 1956.-V.15, N4.-p.381-388.

A Review of the Techniques Available for Obtaining the Mechanical Properties of Materials at High Rates of Strain*

S.M. Walley, J.E. Field, W.G. Proud

Physics and Chemistry of Solids (PCS), Cavendish Laboratory, University of Cambridge, United Kingdom

Abstract

A variety of techniques used to obtain the mechanical properties of materials at high rates of strain (≥ 10 s^{-1}) are discussed. These include dropweight machines, split Hopkinson pressure bars (SHPBs), Taylor impact, and shockloading by plate impact. Their limitations as well as their advantages are outlined.

Keywords:

Dynamic, Strength, Deformation

1 Introduction

Figure 1 presents a schematic diagram of the range of strain rates (in reciprocal seconds) that are typically of interest to materials scientists. They span 16 orders of magnitude from creep (over periods of years) to shock (nanoseconds). Conventional commercial mechanical testing machines cover the low strain rate range up to around 10 s^{-1}. Dropweight machines are also available commercially and standards have been written covering their design and use in the strain rate range 10 - 1000 s^{-1}. Historically, machines for obtaining mechanical data at higher rates of deformation have tended to be confined to government or university laboratories, but recently some companies have been 'spun-off' to market items such as split Hopkinson pressure bars (SHPBs) and plate impact facilities.

The authors would like to thank EPSRC, [dstl], QinetiQ, AWE, and the US Office of European Research (London) for support in this area.

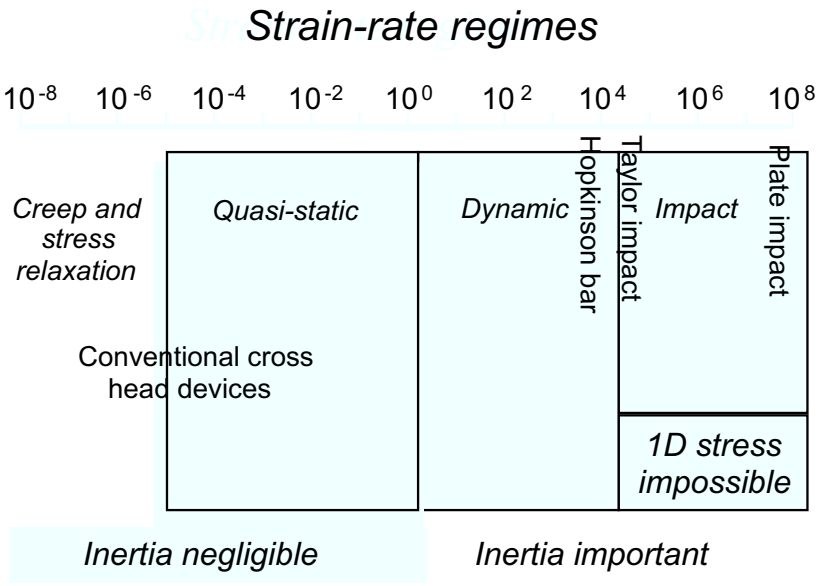

Figure 1: *Schematic diagram of strain rate regimes (in reciprocal seconds) and the techniques that have been developed for obtaining them*

One very important transition that this figure shows is that from a state of 1D stress to 1D strain. The strain rate at which this occurs depends on the density of the material being investigated and the size of the specimen: the larger the specimen and the higher its density, the lower the transitional strain rate [1,2]. Examples of the effect of strain rate on mechanical properties combined with the transition from 1D stress to 1D strain are given in Figure 2.

Because it is necessary to have about 1000 grains or crystals in a specimen for it to be mechanically representative of the bulk [5,6], the coarser the microstructure, the larger the specimen has to be to fulfil this condition and hence the lower the maximum strain rate that can be accessed in 1D stress. Hence, for investigating concrete, for example, very large Hopkinson bars have had to be constructed [7]. By contrast, very fine-grained metals can be deformed in 1D stress at strain rates close to 10^5 s^{-1} using miniaturised Hopkinson bars (3 mm diameter) and 1mm sized specimens [8].

Fuller historical surveys of the development of high strain rate techniques may be found in refs. [9,10]. Recent reviews of the techniques outlined in this paper may be found in ref. [11]. In addition, the DYMAT Association is in the process of publishing test recommendations. Those for compression Hopkinson bars [12] and Taylor impact [13] are already available; that for shockloading by plate impact will be published soon (see the website www.dymat.org).

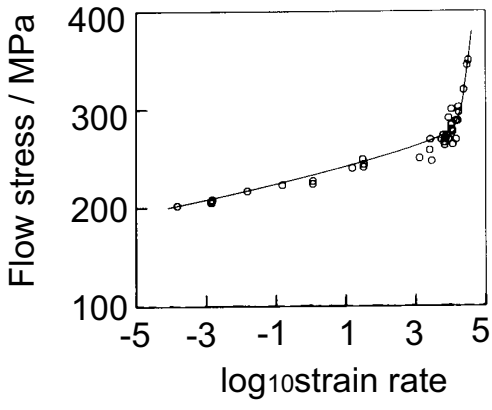

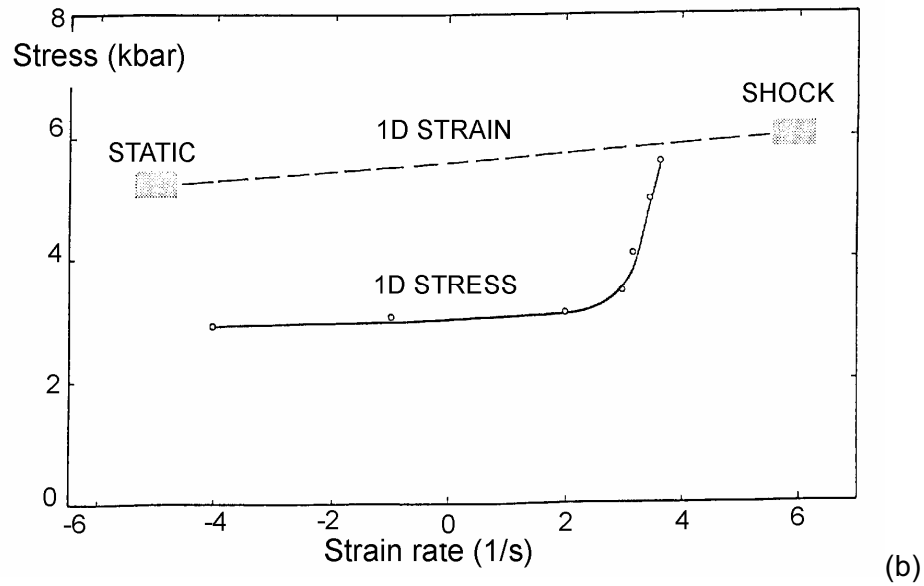

Figure 2: *(a) Plot of flow stress of copper as a function of log10(strain rate); from ref. [3]. (b) Failure stress of limestone as a function both of strain rate and loading state; from ref. [4]*

2 Dropweights

Machines where a falling weight is used to strike a plaque or a structure are widely used in industry both in research and in quality control. The weight is often used to carry darts of various shapes (sharp, rounded) to impact the target. ASTM Standards have been written governing the performance of such tests on sheet materials (ASTM D5420-98a, ASTM F736-95(2001)) and pipes (ASTM G14-88(1996)e1, ASTM D2444-99) (see their website www.astm.org). Dropweights are also used in explosives safety qualification: the higher a standard dropweight has to be dropped onto an energetic formulation before half the drops produce ignition, the safer that formulation is assumed to be.

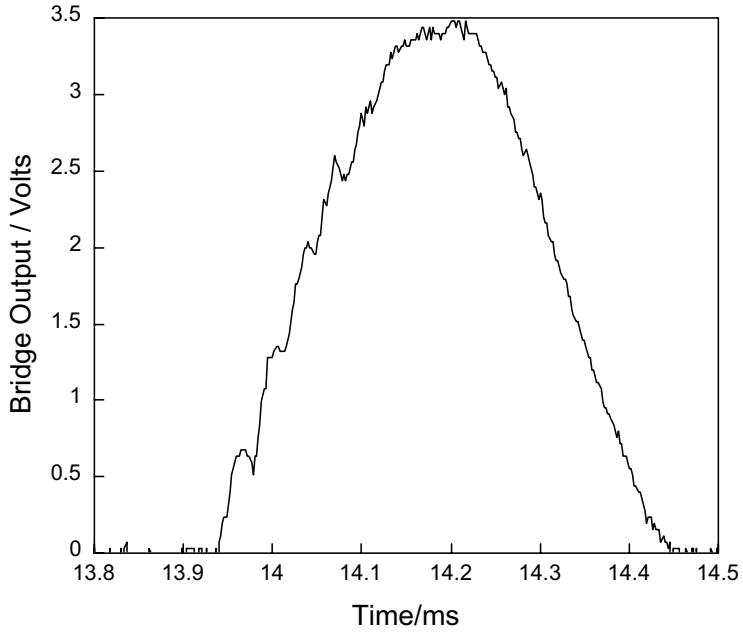

Figure 3: *Output of the strain gauge bridge for a dropweight force transducer calibration experiment*

The standard way of analysing the output of a dropweight machine assumes the weight behaves as a rigid body and hence that one can simply apply Newton's laws of motion. Thus, in determining the calibration factor k (N/V) of a dropweight force transducer dynamically, we assume we can replace $\int Fdt$ by $m\Delta v$. Thus:

$$k = \int Fdt \,/\, \int Vdt = m\Delta v \,/\, \int Vdt \qquad (1)$$

where m is the mass of the dropweight, $\int Vdt$ is the integral of the strain gauge bridge output voltage signal, and Δv is the change of velocity of the weight produced by impact on the force transducer (remembering, of course, that velocity is a vector, so that the magnitudes of the impact and rebound speeds must be added). A typical calibration signal is presented in Figure 3. Dynamic calibration has been found to agree well with that performed statically in a calibrated commercial testing machine [14].

In practice, the output signal from a dropweight machine often has oscillations comparable in size to the signal produced by the mechanical resistance of the specimen. This is particularly true if the dropweight itself is instrumented e.g. with accelerometers. The reason is that impact excites the weight below its resonance frequency [15]. Elastic waves therefore reverberate around inside until the momenta of the constituent parts of the weight have been reversed. Rebound then occurs and the specimen is unloaded. Recent work has demonstrated that it is possible to obtain high quality data from such machines (at least for simple specimen geometries) either by the use of a momentum trap in the weight if the weight itself has to be instrumented [16] or by careful design of a separate force transducer placed below the specimen [14]

3 Split Hopkinson Pressure Bars (SHPBs)

Three researchers had the idea of using two Hopkinson pressure bars [17] to measure the dynamic properties of materials in compression [18-20]. Methods of obtaining high rate mechanical properties of materials in tension and torsion had previously been invented [21-24]. However, SHPBs were not widely used until the 1970s (Figure 4). Instead, alternatives such as the propagation of plasticity down rods or the cam plastometer [25] were used for obtaining dynamic mechanical properties in compression. As SHPBs increasingly became the standard method of measuring material dynamic mechanical properties in the strain rate range 103 – 104 s^{-1}, tension [26] and torsion [27] versions were developed.

The basic idea of the SHPB is that the specimen is deformed between two bars excited above their resonant frequency (Figure 5). Note in comparing Figures (3) and (5) the very different shapes and durations of the loading pulses. The material of the bars is chosen so that they remain elastic (small strains) even though the specimen itself may be taken to large strains. This means that strain gauges can be used repeatedly to measure the signals in the bars (strain gauges normally have small failure strains). Dynamic loading is produced either by striking one end of one of the bars (the input bar) or by statically loading a section of the input bar held at some point by a clamp and then releasing the clamp, so that the load propagates to the specimen. Compression bars are nearly all of the dynamically loaded type (though there is no reason in principle why a 'statically' loaded compression SHPB could not be built). Tension SHPBs have been designed of both types [28]. Torsion SHPBs are nearly always statically loaded [29].

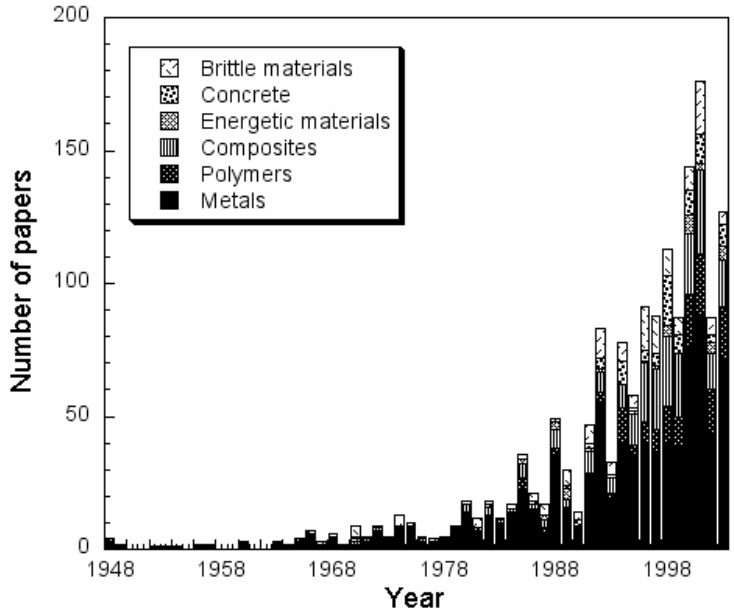

Figure 4: *Histogram of the number of papers published in any given year where an SHPB was used to obtain the high rate mechanical properties of various materials*

The classic elastic wave analysis of the SHPB assumes that the rods are one-dimensional objects (their true three dimensional nature is demonstrated by the oscillations on the recorded signals; see Figure (5)). The aim of the analysis is to relate the elastic strains in the rods (measured by, for example, strain gauges) to the force applied to and the defor-

mation of the specimen sandwiched between them. The full analysis may be found in ref. [30] and results in two equations:

$$\sigma(t) = \frac{AE\varepsilon_t}{A_s} \tag{2}$$

$$\frac{\partial \varepsilon}{\partial t} = \frac{2c_b\varepsilon_r}{l_s} \tag{3}$$

where $\sigma(t)$ is the stress in the specimen, A is the cross-sectional area of the bar, E is the Young's modulus of the bar material, ε_t is the strain pulse measured in the output bar (transmitted pulse), ε_r is the strain pulse reflected from the specimen and measured in the input bar, $\partial\varepsilon/\partial t$ is the specimen strain rate, c_b is the elastic wave speed of the bar material, and l_s is the current specimen length (thickness). The stress-strain curve of the specimen can be found from equations (2) and (3) by eliminating time as a variable. Similar analyses exist for tension and torsion systems. Note that two major assumptions were made in deriving these equations: (i) the forces on the two ends of the specimen are the same, and (ii) the specimen deforms at constant volume. If either of these assumptions are false, the equations are invalid. However, the force-time data obtained may still be used for checking material models.

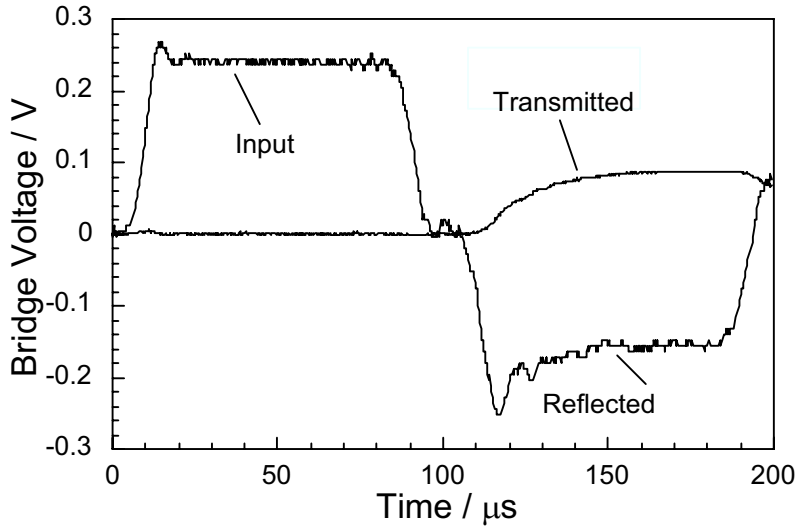

Figure 5: *Input (loading), reflected and transmitted pulses in a dural compression SHPB for a 4mm thick, 5mm diameter polycarbonate specimen (courtesy of C.R. Siviour)*

4 Taylor Impact

The Taylor test was developed by G.I. Taylor and co-workers during the 1930s [18, 31-33] as a method of estimating the dynamic strength of ductile materials in compression. The technique consists of firing a cylinder of the material of interest against a massive, rigid target. The dynamic flow stress can then be found by recovering the deformed cylinder and measuring its change of shape. However, this lacks the accuracy of deforming a disc of material and so Taylor impact is now rarely used for its original purpose.

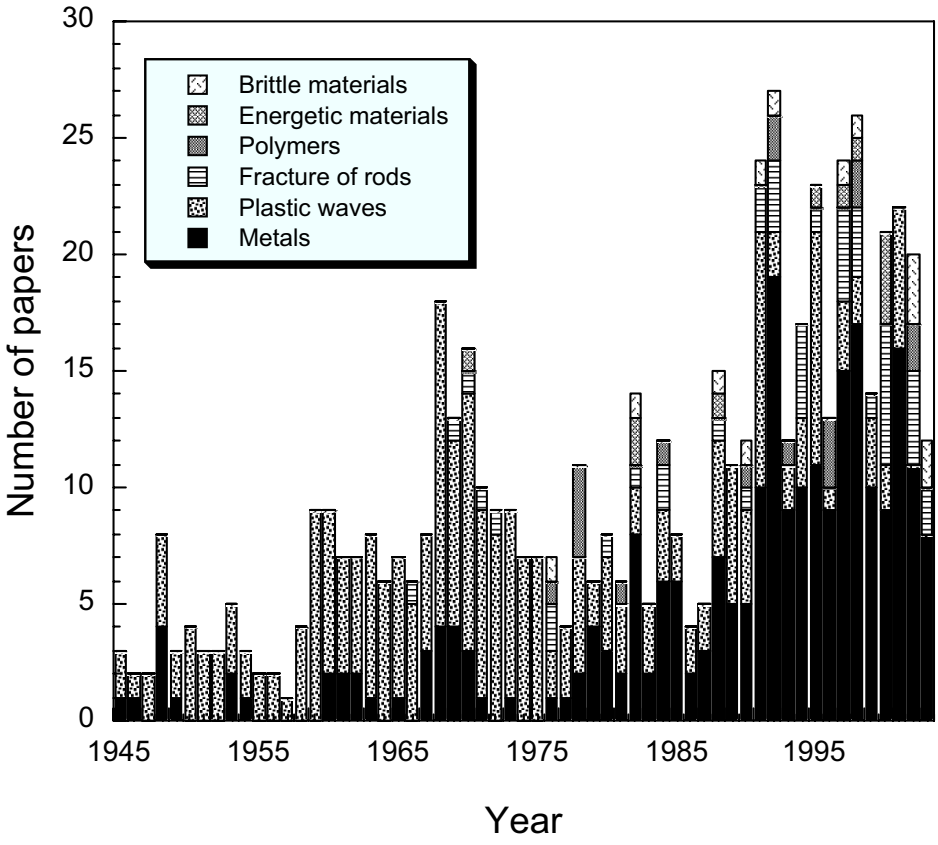

Figure 6: *Histogram of the number of publications published in any given year where Taylor impact or plastic wave propagation was used to investigate various materials*

As mentioned before, a technique that is in some sense intermediate between Taylor impact and the SHPB was popular for about 25 years, namely the study of the propagation of plastic waves along rods e.g. ref. [34]. However, recently there has been renewed interest in Taylor impact or its variants (such as rod-on-rod impact [35]) as a method of 'exercising' constitutive relations [36,37] for a wide range of materials (see Figure (6)). High-speed photography is invaluable in these modern studies and is essential for both brittle [38,39] and viscoelastic materials [40]. One reason this technique is so useful in exercising constitutive models is the wide range of strain rates it covers in one experiment from shockloading at the impact face to quasistatic loading at the rear [39, 41]. It also produces large strains.

5 Shockloading by plate impact

The planar impact of a disc of material onto a target specimen (Figure 7) produces shock waves in both target and impactor materials. The strain rates within the shock are typically in the range 106 to 108 s^{-1}. These are the highest rates of deformation that can be achieved in the laboratory by mechanical means. Higher rates and higher shock pressures can be achieved by, for example, nuclear bombs [42], high intensity lasers [43], and particle beams [44], but these techniques will not be considered further in this review. A fuller review of plate impact techniques may be found in ref. [45].

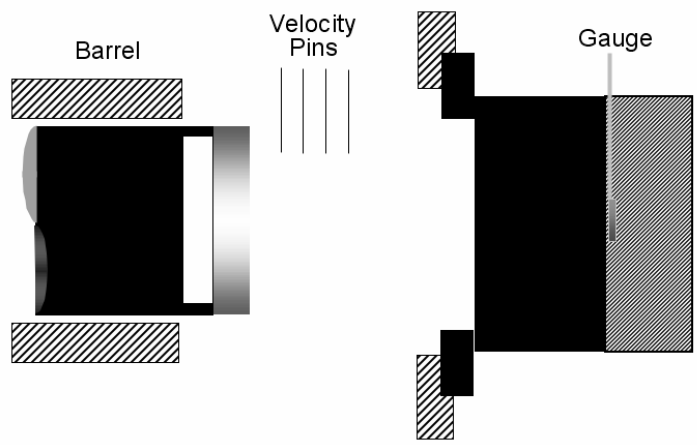

Figure 7: *Schematic diagram of the 'business end' of a plate impact shockloading gun*

As Figure 1 indicates, deformation takes place at these strain rates under 1D strain. This is because the inertia of the material involved in the collision acts (for a period of a few microseconds) to rigidly constrain the material in the centre of the colliding discs. Deformation therefore takes place only in the direction of impact. This state of affairs lasts until release waves reach the centre of the discs i.e. for a time given by r/cs where r is the radius of the disc and cs is the appropriate wavespeed in the shocked (and hense densified) material. Hence, the larger the diameter of the impactor/target, the longer the state of 1D shock strain lasts. However, the costs of manufacture and operation of a laboratory gun increase rapidly with the bore size. So most plate impact facilities use guns in the range 50-75 mm bore. Single stage guns operated with compressed gas have a typical upper impact speed of around 1.2 km/s if helium is used as the propellant. Higher velocities can be achieved with single stage guns using solid propellants, but this has the disadvantage of producing a great deal of residue which has to be cleaned out each time the gun is fired. To achieve impact speeds typical, say, of the impact of space debris on an orbiting satellite requires two- or even three-stage guns [46, 47]. One disadvantage is that each successive stage is of smaller diameter than the one before. Hence, the final projectile is typically only a few millimetres in diameter. For the very highest speeds in such systems, hydrogen is used as the propellant.

Typical applications of the plate impact technique to materials include: (i) obtaining their Hugoniot curves (locus of possible shock states) [48]; (ii) measuring their dynamic spall (or tensile) strengths [49]; (iii) investigating high pressure phase changes [50]; (iv) study of shock-induced chemistry [51]. Evidently, all of these are of interest to the military in applications such as armour, penetrators, shaped charges, explosives etc., but there are many civilian applications as well, including quarrying/blasting [52], shielding of orbiting satellites [53], geophysics [54], explosive welding [55], novel materials synthesis [51] etc.

References

[1] *Gorham*, *D.A.*: The effect of specimen dimensions on high strain rate compression measurements of copper. J. Phys. D: Appl. Phys. 24 (1991) 1489-1492.

[2] *Gorham, D.A.; Pope, P.H.; Field, J.E.*: An improved method for compressive stress-strain measurements at very high strain rates. Proc. R. Soc. Lond. A 438 (1992) 153-170.
[3] *Follansbee, P.S.; Regazzoni, G.; Kocks, U.F.*: The transition to drag controlled deformation in copper at high strain rates. Inst. Phys. Conf. Ser. 70 (1984) 71-80.
[4] *Brace, W.F.; Jones, A.H.*: Comparison of uniaxial deformation in shock and static loading of three rocks. J. Geophys. Res. 76 (1971) 4913-4921.
[5] *Armstrong, R.W.*: On size effects in polycrystal plasticity. J. Mech. Phys. Solids 9 (1961) 196-199.
[6] *Armstrong, R.W.*: Plasticity: Grain size effects. Encyclopedia of Materials: Science and Technology, ed. K.H.J. Buschow; R.W. Cahn; M.C. Flemings; B. Illschner; E.J. Kramer; S. Mahajan, publ. Elsevier, Amsterdam, p. 7103-7114.
[7] *Albertini, C.; Cadoni, E.; Labibes, K.*: Study of the mechanical properties of plain concrete under dynamic loading. Exper. Mech. 39 (1999) 137-141.
[8] *Gorham, D.A.*: Measurement of stress-strain properties of strong metals at very high strain rates. Inst. Phys. Conf. Ser. 47 (1980) 16-24.
[9] *Bell, J.F.*: The Experimental Foundations of Solid Mechanics, publ. Springer Verlag, Berlin (1973).
[10] *Field, J.E.; Proud, W.G.; Walley, S.M.; Goldrein, H.T.*: Review of experimental techniques for high rate deformation and shock studies. New Experimental Methods in Material Dynamics and Impact, ed. W.K. Nowacki; J.R. Klepaczko, publ. Institute of Fundamental Technological Research, Warsaw, Poland, p. 109-177.
[11] *Kuhn, H.; Medlin, D. (eds.)*: ASM Handbook. Vol. 8: Mechanical Testing and Evaluation, publ. ASM International, Materials Park, Ohio (2000).
[12] *Lichtenberger, A.; Gary, G.; Dodd, B.; Couque, H.; Kammerer, C.; Naulin, G.*: Test Recommendation: Dynamic Compression Testing using the Split Hopkinson Pressure Bar, publ. DYMAT, Saint-Louis, France (1999).
[13] *Couque, H.; Walley, S.; Lichtenberger, A.; Chartagnac, P.; Dormeval, R.; Petit, J.*: Test recommendation: Dynamic compression testing using the Taylor test, publ. DYMAT, Arcueil, France (2001).
[14] *Radford, D.D.; Walley, S.M.; Church, P.; Field, J.E.*: Dynamic upsetting and failure of metal cylinders: Experiments and analysis. J. Phys. IV France 110 (2003) 263-268.
[15] *Pope, P.H.*: Dynamic compression of metals and explosives. PhD thesis, Univ. of Cambridge (1985).
[16] *Swallowe, G.M.; Lee, S.F.*: A study of the mechanical properties of PMMA and PS at strain rates of 10-4 to 103 s-1 over the temperature range 293-363K. J. Phys. IV France 110 (2003) 33-38.
[17] *Hopkinson, B.*: A method of measuring the pressure produced in the detonation of high explosives or by the impact of bullets. Phil. Trans. R. Soc. Lond. A 213 (1914) 437-456.
[18] *Taylor, G.I.*: The testing of materials at high rates of loading. J. Inst. Civil Engrs 26 (1946) 486-519.
[19] *Volterra, E.*: Alcuni risultati di prove dinamichi sui materiali. Riv. Nuovo Cimento 4 (1948) 1-28.
[20] *Kolsky, H.*: An investigation of the mechanical properties of materials at very high rates of loading. Proc. Phys. Soc. Lond. B 62 (1949) 676-700.
[21] *Luerssen, G.V.; Greene, O.V.*: The torsion impact test. Proc. Amer. Soc. Testing Materials 33(2) (1933) 315-333.

[22] *Mason, W.*: The yield of steel wire under stresses of very small duration. Proc. Inst. Mech. Engrs 128 (1934) 409-438.
[23] *Mann, H.C.*: The relation between the tension static and dynamic tests. Proc. Amer. Soc. Testing Materials 35(2) (1935) 323-340.
[24] *Itihara, M.*: Impact torsion test. Technol. Rep. Tohoku Univ. 11 (1935) 16-50, 489-581; 12 (1936) 63-118.
[25] *Loizou, N.; Sims, R.B.*: The yield stress of pure lead in compression. J. Mech. Phys. Solids 1 (1953) 234-243.
[26] *Harding, J.; Wood, E.O.; Campbell, J.D.*: Tensile testing of materials at impact rates of strain. J. Mech. Engng Sci. 2 (1960) 88-96.
[27] *Duffy, J.; Campbell, J.D.; Hawley, R.H.*: On the use of a torsional split Hopkinson bar to study rate effects in 1100-0 aluminum. Trans. ASME: J. Appl. Mech. 38 (1971) 83-91.
[28] *Nemat-Nasser, S.*: Recovery Hopkinson bar technique. ASM Handbook. Vol. 8: Mechanical Testing and Evaluation, ed. H. Kuhn; D. Medlin, publ. ASM International, Materials Park, Ohio, p. 477-487.
[29] *Gilat, A.*: Torsional Kolsky bar testing. ASM Handbook. Vol. 8: Mechanical Testing and Evaluation, ed. H. Kuhn; D. Medlin, publ. ASM International, Materials Park, Ohio, p. 505-515.
[30] *Gray III, G.T.*: Classic split-Hopkinson pressure bar testing. ASM Handbook. Vol. 8: Mechanical Testing and Evaluation, ed. H. Kuhn; D. Medlin, publ. ASM International, Materials Park, Ohio, p. 462-476.
[31] *Taylor, G.I.*: The use of flat ended projectiles for determining yield stress. I: Theoretical considerations. Proc. R. Soc. Lond. A 194 (1948) 289-299.
[32] *Whiffin, A.C.*: The use of flat ended projectiles for determining yield stress. II: Tests on various metallic materials. Proc. R. Soc. Lond. A 194 (1948) 300-322.
[33] *Carrington, W.E.; Gayler, M.L.V.*: The use of flat ended projectiles for determining yield stress. III: Changes in microstructure caused by deformation at high striking velocities. Proc. R. Soc. Lond. A 194 (1948) 323-331.
[34] *Bell, J.F.*: An experimental study of instability phenomena in the initiation of plastic waves in long rods. Mechanical Behavior of Materials under Dynamic Loads, ed. U.S. Lindholm, publ. Springer-Verlag, Berlin, p. 10-20.
[35] *Erlich, D.C.*: Rod impact (Taylor) test. Metals Handbook vol. 8 (9th edn.), ed. publ. American Society of Metals, Metals Park, Ohio, p. 203-207.
[36] *Maudlin, P.J.; Gray III, G.T.; Cady, C.M.; Kaschner, G.C.*: High-rate material modelling and validation using the Taylor cylinder impact test. Phil. Trans. R. Soc. Lond. A 357 (1999) 1707-1729.
[37] *Walley, S.M.; Church, P.D.; Townsley, R.; Field, J.E.*: Validation of a path-dependent constitutive model for FCC and BCC metals using 'symmetric' Taylor impact. J. Phys. IV France 10 Pr. 9 (2000) 69-74.
[38] *Murray, N.H.; Bourne, N.K.; Field, J.E.; Rosenberg, Z.*: Symmetrical Taylor impact of glass bars. Shock Compression of Condensed Matter - 1997, ed. S.C. Schmidt; D.P. Dandekar; J.W. Forbes, publ. American Institute of Physics, Woodbury, New York, p. 533-536.
[39] *Radford, D.D.; Willmott, G.R.; Walley, S.M.; Field, J.E.*: Failure mechanisms in ductile and brittle materials during Taylor impact. J. Phys. IV France 110 (2003) 687-692.
[40] *Hutchings, I.M.*: Estimation of yield stress in polymers at high strain rates using G.I. Taylor's impact technique. J. Mech. Phys. Solids 26 (1978) 289-301.

[41] *Church, P.D.; Andrews, T.; Goldthorpe, B.*: A review of constitutive model development within DERA. Structures under Extreme Loading Conditions. PVP 394, ed. D.M. Jerome, publ. American Society of Mechanical Engineers, New York, p. 113-120.
[42] *Trunin, R.F.*: Shock Compression of Condensed Materials, publ. Cambridge University Press, Cambridge (1998).
[43] *Prat, C.; Autric, M.*: High power laser radiation induced shock waves in solids. Shock Waves @ Marseille III, ed. R. Brun; L.Z. Dumitrescu, publ. Springer, Berlin, p. 255-260.
[44] *Kanel, G.I.; Asay, J.R.; Baumung, K.; Bluhm, H.; Chhabildas, L.C.; Fortov, V.E.; Goel, B.; Hoppé, P.; Mehlhorn, T.; Razorenov, S.V.; Rusch, D.; Utkin, A.V.*: Applications of the ion beam technique for investigations of hypervelocity impacts. Int. J. Impact Engng 23 (1999) 421-430.
[45] *Gray III, G.T.*: Shock wave testing of ductile materials. ASM Handbook. Vol. 8: Mechanical Testing and Evaluation, ed. H. Kuhn; D. Medlin, publ. ASM International, Materials Park, Ohio, p. 530-538.
[46] *Munson, D.E.; May, R.P.*: Interior ballistics of a two-stage light gas gun using velocity interferometry. AIAA Journal 14 (1976) 235-242.
[47] *Kondo, K.; Hironaka, Y.; Ito, H.; Sugiura, H.; Ozaki, S.; Takeba, A.; Katayama, M.*: A trial of the three-stage light gas gun with a preheating stage. Shock Compression of Condensed Matter 1995, ed. S.C. Schmidt; W.C. Tao, publ. American Institute of Physics, Woodbury, New York, p. 1193-1196.
[48] *Marsh, S.P.*: LASL Shock Hugoniot Data, publ. University of California Press, Berkeley, California (1980).
[49] *Grady, D.E.*: The spall strength of condensed matter. J. Mech. Phys. Solids 36 (1988) 353-384.
[50] *Dunn, J.E.; Fosdick, R.; Slemrod, M.*: (eds.) Shock Induced Transitions and Phase Structures in General Media, publ. Springer, Berlin (1993).
[51] *Sekine, T.*: Shock wave chemical synthesis. Eur. J. Solid State Inorg. Chem. 34 (1997) 823-833.
[52] *Willmott, G.R.; Proud, W.G.; Field, J.E.*: Shock properties of diamond and kimberlite. J. Phys. IV France 110 (2003) 833-838.
[53] *Frey, J.D.; Janicot, F.; Garaud, X.; Groenenboom, P.; Lambert, M.*: The validation of hydrocodes for orbital debris impact simulation. Int. J. Impact Engng 14 (1993) 255-265.
[54] *Yoo, C.S.; Holmes, N.C.; Ross, M.; Webb, D.J.; Pike, C.*: Shock temperatures and melting of iron at Earth core conditions. Phys. Rev. Letts 70 (1993) 3931-3934.
[55] *Crossland, B.*: Explosive Welding of Metals and its Application, publ. Clarendon Press, Oxford (1982).

Material Behaviour at High Strain Rates*

L. W. Meyer

Chair Materials and Impact Engineering, Chemnitz University of Technology, Germany

Abstract

An overview is given of high rate mechanical testing procedures and the material behaviour under tensile, compression, and shear loading as well as under biaxial loading states tension/compression with torsion resp. shear.

Keywords:

Material, Strain rate, Behaviour

1 Introduction

For the characterisation of deformation processes of metallic materials the knowledge of flow and failure plays an essential role. But flow and failure are not independent material properties, they are influenced strongly by stress state, temperature and strain rate. Due to microstructural reasons combined with dislocation mechanics, the flow stresses, deformability, or toughness changes with strain rate. Most technical production methods like cutting, forging, stamping, or forming reach strain rates up to 10^2 to 10^4 s^{-1} which cover or overlap the high energy rate fabrication HERF-procedures. This gives reason and a strong need to explore the high rate material behaviour, because not only the strength, but the deformability is changed, too. The former named velocity embrittlement has disappeared nearly completely due to modern material production methods. Contrarily, the fracture strain of bcc - steels often is enhanced by 20 to 50% at strain rates at about $\dot{\varepsilon}$ = 10^3 s^{-1} [1]. The reasons are not fully understood, but twinning and adiabatic heating may play a role [2]. These differences to the quasistatic deformability are determined without any doubts, because the elongations are measured after the tests with arbitrary precision. The problems of force or stress measurement at higher strain rates arise when the weight of the load cell (adapted to the load capability of the testing machine) and the corresponding stiffness are leading to eigenfrequencies of some kHz or ringing periods of

*This work is based on the results of DFG and BMVg-public research; the author likes to thank for their financial support and interest

milliseconds or shorter. Only when the complete mechanical and electrical force measuring circuit exhibits bandwidths of 10 x more than the frequency response of the testing procedure contains, the basic requirements of measurement rules are fulfilled. This is easy and self-evident to demand, but not easy to fulfil. All known hydraulic driven testing machines are much quicker with the piston velocity than the load cell is able to follow. In a tensile test of a universal testing machine a third of the maximum piston velocity of v_{max} = 0.5 m/s with v = 0.15 m/s is used, Figure 1, and the original force-time-record, trace a), presents as expected yielding, strain hardening, maximum, reduction of area, and fracture, of course with some ringing. When this ringing of 400 kHz is smoothed out, and it is often claimed that this is allowed, then the following trace is found, trace b). In the same test another load cell with a higher eigenfrequency of 65 kHz was used, trace c), which is not affected or animated by the frequency spectrum of the testing event.

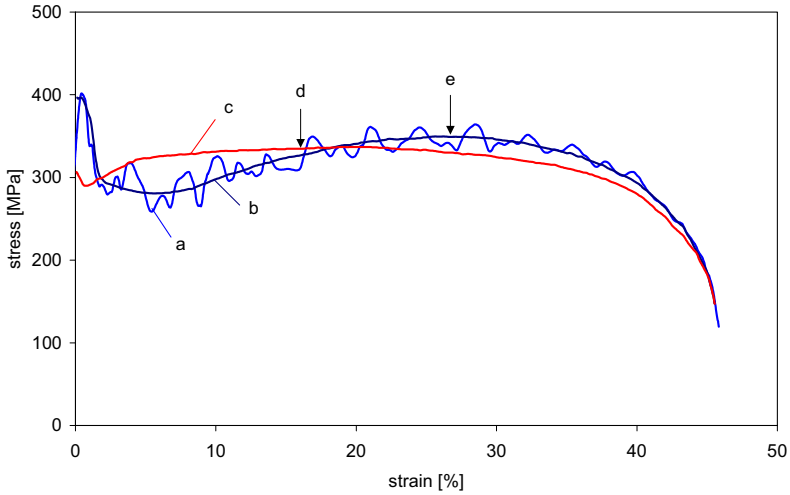

Figure 1: *Stress-strain traces of a tensile test in a hydraulic Universal testing machine with 150 mm/s piston velocity (max. possible is 500 mm/s) a) virgin stress trace of the original load cell; b) smoothed stress trace of the original load cell; c) stress trace of separate high eigenfrequency load cell; d) UTS and $\varepsilon_{uniform}$ with high bandwidth; e) UTS and $\varepsilon_{uniform}$ with original bandwidth*

The difference in strain hardening and homogenous strain determination is obvious. The reason for the deviations is that the observed frequency is not the base mode, but the second mode. The first mode is covered by the low fracture strain resp. the short testing time. If a longer specimen with a higher elongation would have to be used, than the first mode of ringing would appear with several full periods and not less than one, as shown here. The same principle is existing at higher strain rates. Therefore, for a satisfying reliability the original traces should be presentable.

2 Testing Procedures

2.1 Tensile Testing

To study the flow behaviour with strain rates above $\dot{\varepsilon} > 1\ s^{-1}$, the specimen are instrumented with strain gages in the gage length and on a cone with 8° just aside the

gage length, Figure 2. With l/d = 3 and d = 3,56 mm resp. a cross section of A = 10 mm^2 strain rates up to $\dot{\varepsilon}$ = 10^3 s^{-1} can be used without the necessity of curve smoothing.

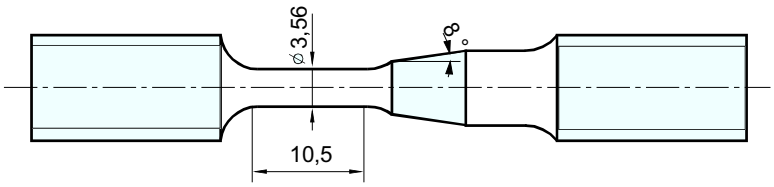

Figure 2: *Tensile specimen, optimised for high rate testing with l/d = 3, d = 3.56 mm, cone 8°, gages at cone and in the gage length*

With warm aging adhesives, the strain gages are usable to more than 6% plastic strain. With the known Youngs modul, the elastic strains at the cone are converted into stresses acting at the gage length. With recognising the wave speed and distance of less than 10 mm between gage length and gage area at the cone, a determination of the Youngs modul is possible in each test. This is a valuable control of the alignment of the specimen and the electronic set up. The high rate tensile deformation can be done by fast hydraulic, hopkinson, or rotating wheel devices set ups [3,4]. A careful alignment is necessary in each case. Because of wave reflections between specimen and hopkinson bars above $\dot{\varepsilon}$ = 10^3 s^{-1}, several methods of replacing the threads were tested, like e.g. brazing, gluing and, welding. The best results are reached with friction welding, which avoids differences of the acoustic impedance. The material to be tested is friction welded onto a 2 m long hopkinson bar and machined afterwards, Figure 3.

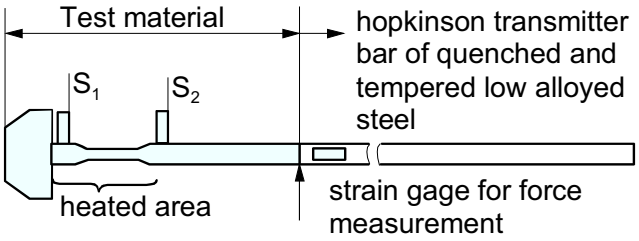

Figure 3: *High temperature, high rate tensile testing with direct hopkinson bar set up (DHB) S_1, S_2 = marker for touchless displacement measurement*

This procedure can lead to undisturbed records between $\dot{\varepsilon}$ = 10^3 and 10^4 s^{-1} and is, to our knowledge, the only way to reach clear results. Of course, strain rates of about 10^4 s^{-1} or 1% strain per microsecond force to use short, small specimen of 0.5 to 2 mm gage length and even then no $R_{p0.2}$, but only R_{p2} and higher can be determined accurately, because of the limited plastic wave speed and the requirement of stress balance along the length of the specimen. With the short specimen, the attachment of strain gages at the gage length becomes difficult or impossible. Instead, an electro-optical displacement transducer of Zimmer Ltd. gives a solution. The same procedure is needed for high rate, high temperature testing, e.g. of turbine blades, containment materials, or explosions of steam tubes, Figure 4, where for temperature reasons strain gages cannot be used. The left Figure 4 of the behaviour of a quenched and tempered steel presents a smooth transition between elastic and plastic elongation and nearly no ringing at $\dot{\varepsilon}$ = 10^3 s^{-1}. The right side Figure 4 of stress-time-curves of a 0.45% carbon-steel presents in an excellent manner

the high ability of this testing method of recording undisturbed measurements, even when a pronounced upper and lower yield stress by interstitials gives best conditions for initiating mechanical ringing. Such a material behaviour is exacting highest claims to the fidelity of the stress measurement.

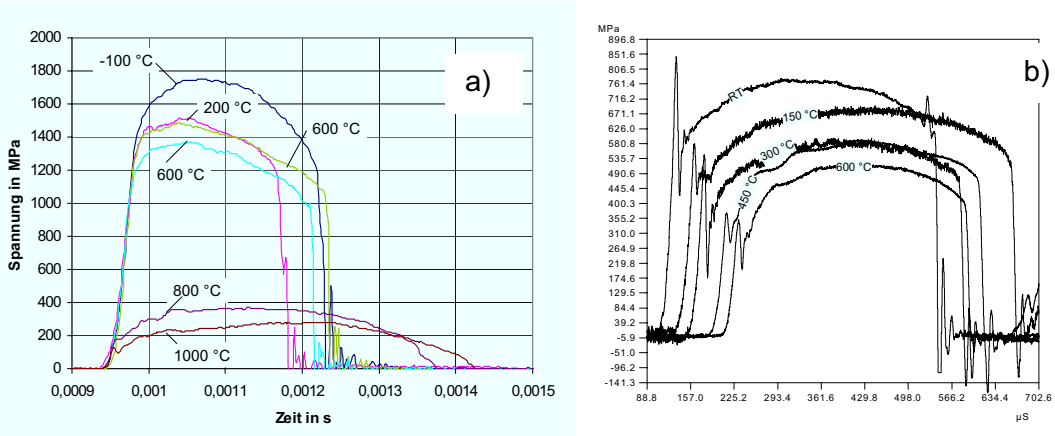

Figure 4: *Tensile results at $\dot{\varepsilon} = 10^3\ s^{-1}$ at room and elevated temperature of quenched and tempered steel, b) 0.45% carbon steel*

2.2 Testing Compression

Tensile testing of the amount at homogenous strain limits the flow curve to $0.05 < \varphi < 0.2$. Under compression, higher true strains are reachable until friction problems transfer the uniaxial stress state into a multiaxial one. Good lubrication and control are essential [5]. With a drop weight principle, high energies are available with strain rates between 10^2 and $5 \cdot 10^2\ s^{-1}$. The high energy ensures nearly a constant striking velocity up to the desired deformation, stopped by blocking.

Split hopkinson pressure bars (SHPB) are common, well understood [6]. The main advantage is the simple mechanical and electronic set up. Surely, for very high strain rates at $10^4\ s^{-1}$ again the specimen length has to be reduced to about 1 mm or less, which leads to the necessity of small diameters of the bars and the avoiding of buckling of the bar.

After regrinding the front surface of a meanwhile penny shaped deformed compression specimen and reheating, further compression deformation up to $\varphi = 1.5$ is possible under controlled friction conditions. These investigations revealed that the steady state of recrystallisation, which is known from high temperature medium velocity forging [7], is present, too, at low temperature high rate compression conditions, Figure 5.

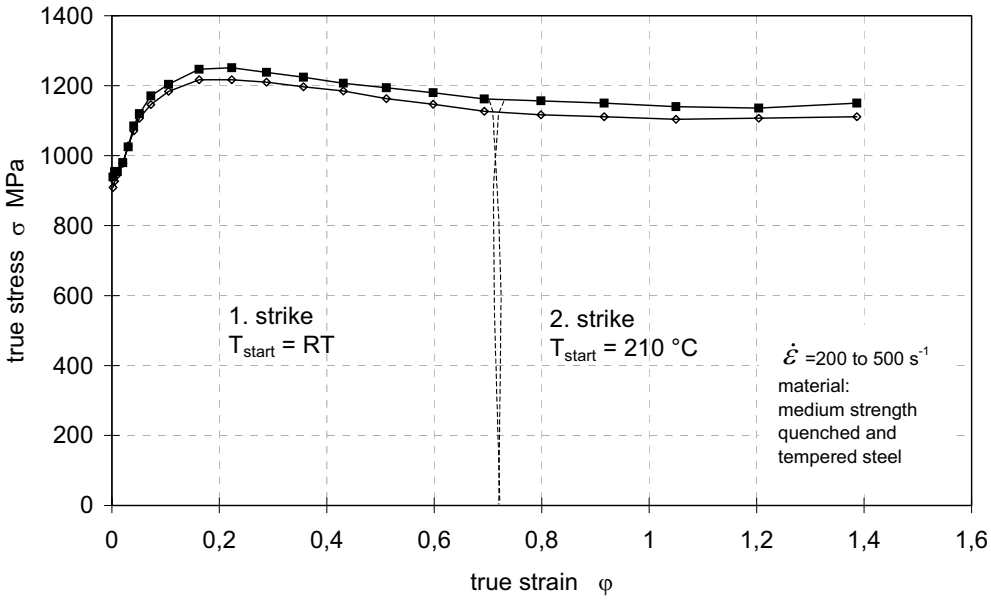

Figure 5: *Flow curve under compression loading, 2nd strike with two specimen as a block with enhanced starting temperature*

Such a behaviour is not easy to be described by constitutive equations of the Johnson-Cook-type, because the steady state (σ = const) is not considered.

The dropweight towers have further advantages with high rate bending or fracture toughness, both without ringing. A valuable testing possibility is the biaxial compression with shear component testing, figure 6.

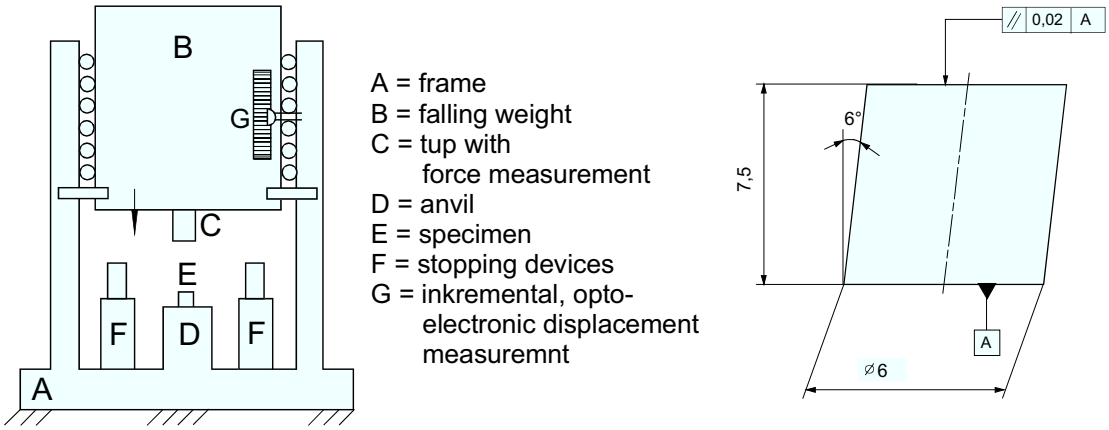

Figure 6: *Principle of drop weight machine with biaxial compression/shear specimen with h/d = 1.25, front faces need to be parallel to 0.01 mm*

Under pure compression, only a few materials like high strength steels or titanium alloys fail due to a adiabatic shear failure [8], Figure 7. With the aid of a few percent added shear stresses resp. with the transition to a slight biaxial stress state, many medium strength materials decide to fail under adiabatic conditions, too, Figure 8 [9].

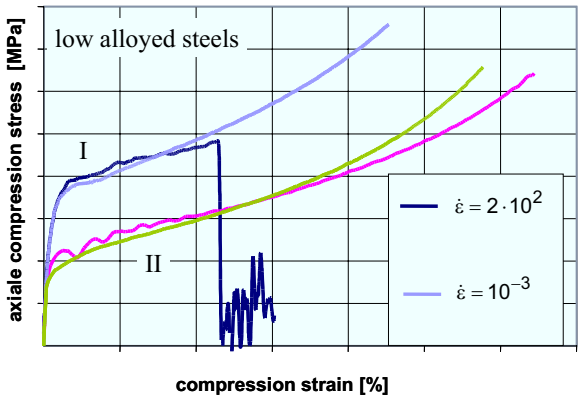

Figure 7: *Influence of hardness (I and II) and strain rate (10^{-3} and 10^2 s^{-1}) on deformability*

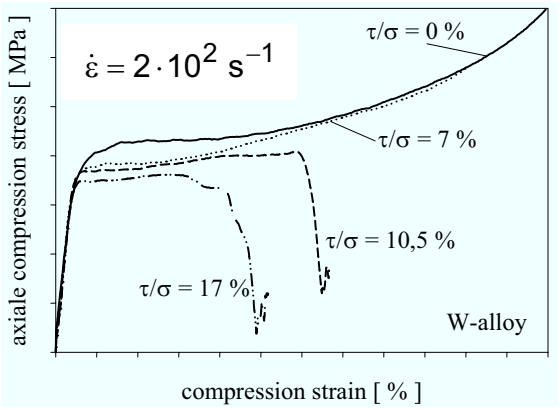

Figure 8: *Influence of biaxial loading at $\dot{\varepsilon} = 2 \cdot 10^2$ s^{-1} of W - alloy on deformability*

With using the “hat shaped” specimen [1], the material is forced to shear under adiabatic conditions, even when it is not prone to it [10]. The constraint character of the hat shaped specimen was changed into an “offer” of a biaxial stress state and the material is answering with different behaviour or failure occurrence: early, late, or not at all. This new compression-shear testing, Figure 6, as well as the hat shaped testing was accepted by the American Society of Metals and is included in the new handbook No. 8, 10th ed. [11], serving as a recommendation for a standard testing procedure.

2.3 Torsion testing

The industrial forming, not only the high rate forming often applies compression and shear loading states. This is due to the non activation or suppressing of tensile cracks. To explore the behaviour under this loading state, shear testing is needed. Nevertheless, generating exact shear or torsion loading states without additional bending is a difficult task. Therefore, hydraulic torsion machines or hopkinson torsion bars are not common. Stiebler created a modified tension-Torsion hopkinson set up [12]. In all cases the torsion angle is limited by the strength and length of specimen and bars. To reach, especially under torsion, the material limit of high shear straining at strain rates of 10^3 s^{-1} and higher, as well as with enhanced temperatures above 1000°C, a new kind of torsion testing device was developed in Chemnitz, namely a modified direct torsion hopkinson machine, Figure 9.

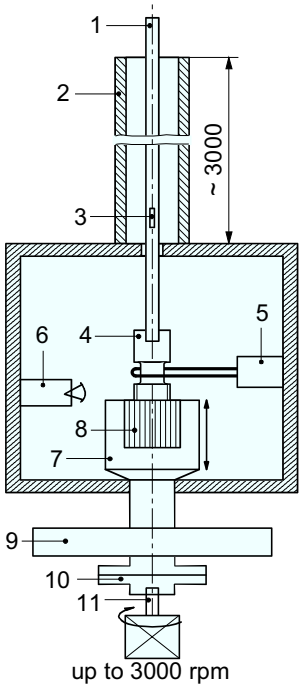

1 Torsion-Hopkinson bar
2 pipe with support
3 torque moment measurement
4 specimen with thread bedstop
5 induction heating device
6 contactless angle measurement
7 moveable coupling with thread
8 guideing bolt for center coupling
9 rotating wheel
10 flexible coupling
11 power transmission

$\dot{\varepsilon}_{max}$ ~ 2000 1/s depend on specimen geometry
ε_{max} ~ depend on material, no limit in angle
T_{max} ~ 1200 °C
Specimen: thin wall tubes with gauge length between 0.5 and 10 mm

Figure 9: *Principle of direct torsion hopkinson machine of LWM, Chemnitz University of Technology*

With a strong motor of a machine-tool from a few to 3000 rpm with a torque of 300 Nm, all continuous cyclic or incremental strain paths up to unlimited revolutions are available with the same specimen geometry.

3 Material Behaviour

The flow stress behaviour can be divided into two or three regimes, the non-velocity-sensitive so-called athermal behaviour (temperature, but not rate dependant), the mutual influence of temperature and strain rate (thermal activated, “linear” in temperature, logarithmic with strain rate), and the dislocation drag regime with a linear influence of strain rate, expected at strain rates above 10^3 s^{-1} [13]. Aluminium and aluminium alloys behave mostly athermal. Low alloyed steels , too, are rate insensitive up to 10^{-1} s^{-1}. Mild steel, sheet metals, carbon steels, austenitic steels, even maraging steels, are rate sensitive between 30 to 120 MPa per order of magnitude in strain rate [14]. The compression behaviour, even from the same batch and without texture influence, mostly is enhanced, compared to the tensile behaviour [15], Figure 9.

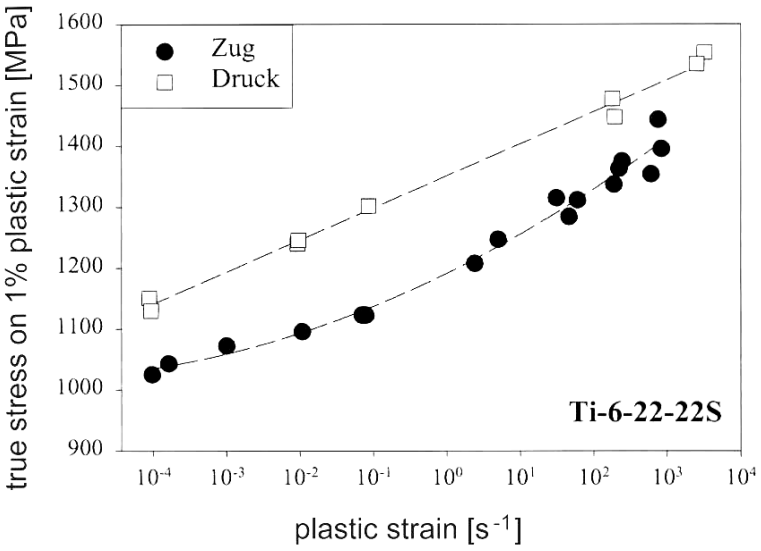

Figure 10: *1%-tensile yield stress and 1%-compression yield stress as a function of strain rate*

This is named strength differential effect or SD-effect. It varies with strain rate and strain, differences up to 18% are known [16]. The same Ti-6-22-22S of figure 10 was tested under flyer data conditions to reach $\dot{\varepsilon} = 10^5\ s^{-1}$. With the evaluation of uniaxial 0.2 – yield and 2% - flow stress of Kanel and Razorenov [17], a long missing connection between impact data and high rate uniaxial material properties is achieved. The result of Ti-6-22-22S indicates that the thermal activation rules the behaviour at low activation energies resp. at high strain rates up to $10^5\ s^{-1}$, Figure 11.

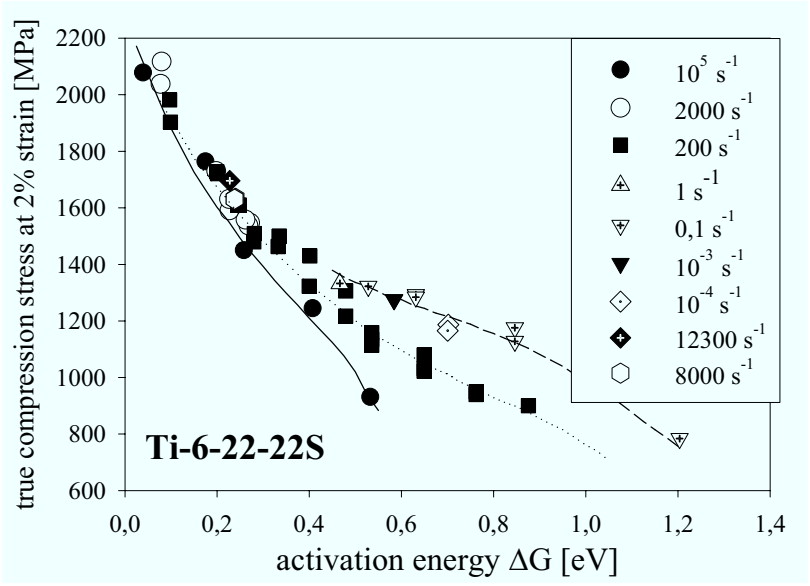

Figure 11: *2% true compression stress versus activation energy with temperature*

This is true for other materials, too. In figure 12 the 0.2 – flow stress versus the strain rate of a high annealed tool steel 40CrMnMo7 is continuously increasing without any sharp increase beyond $\dot{\varepsilon}$ = 10^3 and higher. There is no hint for a drag effect on the stress behaviour to be detected. The reasons for the detected stronger increase above $\dot{\varepsilon}$ = 10^3 s^{-1} at other materials are still under discussion. Additional proofs are necessary.

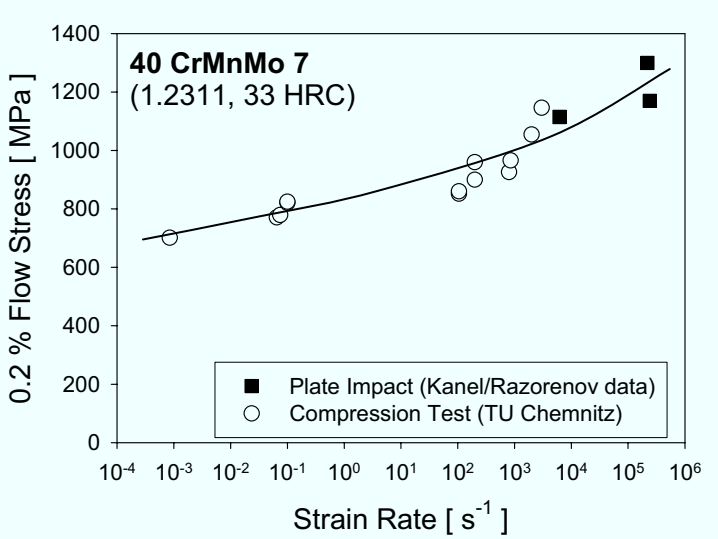

Figure 12: *0.2 yield stress versus strain rate $\dot{\varepsilon}$ from compression tests (4∅ and 2∅ mm specimen) and from plate impact test, conducted by Kanel and Razorenov from the same 1.2311 material*

Under multiaxial loading the material flows, when a certain critical stress is exceeded. This stress, equivalent to a uniaxial stress, is defined by mostly two theories, Tresca and v. Mises. For a biaxial loading of a normal and a shear stress, the equivalent stress and strain is defined by

$$\sigma_{eq} = \sqrt{\sigma^2 + a \cdot \tau^2} \qquad ; \qquad \varepsilon_{eq} = \sqrt{\varepsilon_{ax}{}^2 + \frac{1}{a}\gamma^2} \tag{1}$$

with a = 3 for v. Mises´s or a = 4 for Tresca´s theory.
Often, the reality can be described best with the adapting parameter a = 3.5, which is just between both theories, here for a HY80 steel [18], Figure 13 and 14.

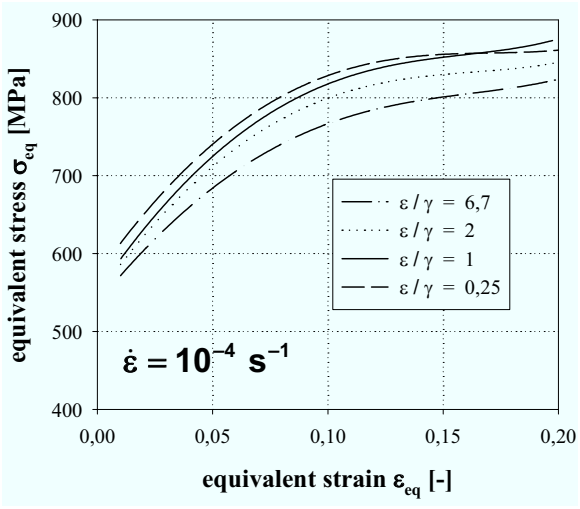

Figure 13: *Equivalent stress – equivalent strain curves of steel HY80 using the v. Mises criterion (a = 3)*

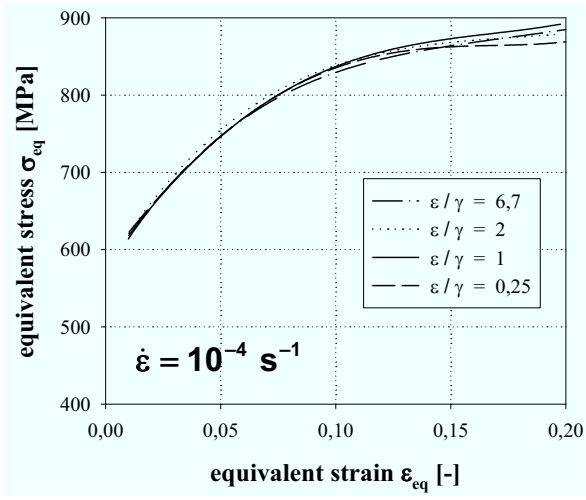

Figure 14: *Equivalent stress – equivalent strain curves of steel HY80 using the adapting parameter (a = 3.5)*

With increasing strain rate, a similar stress enhancement under the biaxial loading state takes place like under monoaxial loading, and the yield loci enlarge. In the first quadrant, the highest reached strain rate with a modified tension-torsion hopkinson bar yielded strain rates of $\dot{\varepsilon}_{eq}$ = 300 - 400 s^{-1}. The form of the 1% - yield loci tends to narrow v. Mises behaviour. These results are valid for the low alloyed tool steel 40CrMnMo7 [19], Figure 15.

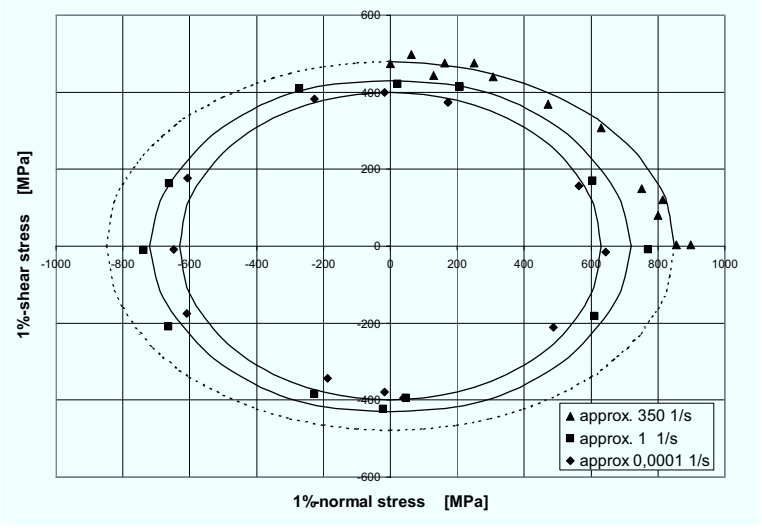

Figure 15: *Yield surface of 1.2311 (40CrMnMo7), quenched and tempered at 650°C at low and high strain rates*

4 Summary

The high rate material characterisation has made encouraging progress in the last decade, but further important tasks of e.g. dynamic multiaxial strength and failure behaviour in highspeed forming processes are waiting for deeper insight.

References

[1] *Hartmann, K.-H.; Kunze, H.-D. Meyer, L.W.:* Metallurgical Effects on Impact Materials. in: Shock Waves and High Strain Rate Phenomena in Metals, Hrsg. M.A. Meyers and L.E. Murr, Plenum Press, New York 1981, S. 325-337.

[2] *Reinders, B.-O.; Kunze, H.-D.:* Influence of Mechanical Twinning on the Deformation Behavior of Armco Iron. in: Shock Waves and High-Strain-Rate Phenomena in Materials Eds. M.A. Meyers, L.E. Murr, K.P. Staudhammer, M. Dekker, 1990, S. 127-136.

[3] *Nemat-Nasser,S.:* High Strain Rate Tests. in: ASM Handbook No. 8, 10th ed., Mechanical Testing and Evaluations, ASM International 2000, Materials Park, Ohio, p. 425 – 475.

[4] *Field, J.E.; Walley, S.M.; Bourne, N.K. and Huntley, J.M.:* Review of Experimental Techniques for High Rate Deformation Studies. Proc. Acoustics and Vibration Asia `98 (Singapore), 1998, p. 9-38.

[5] *Gorham, D.A.; Pope, P.H. and Cox, O.:* Sources of Error in Very High Strain Rate Compression Tests. Inst. Phys. Conf. Series, Vol. 70, 1984, p.151-158.

[6] *Gray III, G.T.:* Classic Split Hopkinson Pressure Bar Testing. Asm Handbook No. 8, Mechanical Testing and Evaluation, 10th ed. ASM International 2000, Materials Park, Ohio, USA, p. 462-476.

[7] *Weise, A.:* Entwicklung von Gefüge und Eigenspannungen bei der thermischen Behandlung von Stahl. PhD-Thesis, Chemnitz University of Technology, 1988.

[8] *Meyer, L.W.:* Dynamic Behaviour of Thermomechanically Treated Ultra High Strength Steel under Tensile and Compressive Loading. in: High Energy Rate Fabrication - 1984, Hrsg.: I. Berman and J. W. Schroeder, ASME, New York, S. 245-252.

[9] *Meyer, L.W.; Staskewitsch, E. Burblies, A.:* Adiabatic Shear Failure under Biaxial Dynamic Compression/Shear Loading. in: Mechanics of Materials 17, 1994, S. 203-214.

[10] *Hines, J.A. and Vecchio, K.S.:* Dynamic recrystallization in adiabatic shear bands in shock-loaded copper. Metallurgical and Material Applications of Shock-Wave and High-Strain-Rate Phenomena, eds. L.E. Murr, K.P. Staudhammer and M.A. Meyers, 1995, Elsevier Science B.V.

[11] *Meyer. L.W. and Krüger, L.:* Drop Weigth Compression Shear Testing. ASM Handbook No. 8, Mechanical Testing and Evaluation, 10th ed., ASM International 2000, S. 452-454.

[12] *Stiebler, K.; Kunze, H.-D. and El-Magd, E.:* Description of the Flow Behaviour of a High Strength Austenitic Steel under Biaxial Loading by a Constitutive Equation. Nuclear Engineering and Design, Vol. 127, 1991.

[13] *Campbell, J.D. and Ferguson, W.G.:* The Temperature and Strain Rate Dependence of Shear Strength of Mild Steel. Philos. Mag., Vol. 21, 1970, p. 63-82.

[14] *Kunze, H.-D.; Meyer, L.W.:* Materials for Extreme Dynamic Loads. in: Metallurgical Applications of Shock Waves and High-Strain-Rate Phenomena, Eds. L.E. Murr, K.P. Staudhammer, M.A. Meyers, Marcel Dekker, New York, Basel, 1986, S. 481-507.

[15] *Krüger, L.:* Untersuchungen zum Festigkeits-, Verformungs- und Versagensverhalten der Legierung Ti-622-22S in Abhängigkeit von der Temperatur, der Dehngeschwindigkeit und dem Spannungszustand, Dissertation TU Chemnitz, Lehrstuhl Werkstoffe des Maschinenbaus, 2001.

[16] *Meyer, L.W. and Abdel-Malek, S.:* Strain Rate Dependence of Strength-Differential Effect in Two Steels. in: J. de Physic IV, Vol. 10, 2000, p. 9-63.

[17] *Meyer, L. W.; Krüger, L.; Razorenov, S. V.; Kanel, G. I.:* Investigation of dynamic flow and Strength properties of Ti-6-22-22S at normal and elevated temperatures in: International Journal of Impact Engineering 28 (2003) S. 877-890.

[18] *Meyer, L.W. and Hahn, F.:* Dynamic Material Behaviour under Biaxial Loading. in: Schock-Wave and High-Strain-Rate Phenomena, eds. K. Staudhammer, L.E. Murr and M.A. Meyers, Elsevier, 2001, S. 11 – 24.

[19] *Halle, T.:* Untersuchungen zum mechanischen Werkstoffverhalten der Stähle C45E und 40CrMnMo7 und Korrelation mit HSC Spanergebnissen. Dissertation TU Chemnitz, Lehrstuhl Werkstoffe des Maschinenbaus, planed in 2004.

Effects of Electromagnetic and Hydraulic Forming Processes on the Microstructure of the Material *

Fr. W. Bach[1], L. Walden[1], M. Kleiner[2], D. Risch[2]

[1] Institute of Materials Science, University of Hannover, Germany
[2] Chair of Forming Technology, University of Dortmund, Germany

Abstract

Over the past few years, various papers have been published in the field of high speed forming processes. The focus was mainly on the technological aspects of metal forming, however. Therefore, the present contribution puts an emphasis on transmission electron microscopy analyses.

The present research work describes the effects of the two forming processes upon the aluminum microstructure and their influence on the material properties. The objective is to characterise the micro processes determining the plastic deformation with both forming velocities – the electromagnetic high speed forming process with strain rates of 10,000 s^{-1} and the bulge test, having deformation rates of less than 0.1 s^{-1} as a quasi-static process. In this article sheet metals out of technical pure aluminum 99.5% with a thickness of 1 mm were investigated. To this end, sample specimens were taken from manufactured workpieces along the radius at various distances from the center. Because of the similarity of the forming paths, two places on the specimens manufactured at different forming rates were evaluated and compared to each other: immediately next to the blankholder and from the area of maximum strain. Metallographic tests of the structures, the sheet thickness, and the micro hardness distribution of the initial state and the formed sheet metals were executed in advance.

Keywords:

Electromagnetic sheet metal forming, Bulge test, Microstructure, Dislocation

---

This work is based on the results of FOR443; the authors would like to thank DFG for its financial support

1 Introduction

Electromagnetic sheet metal forming (EMF) is a typical high speed forming process using the energy density of a pulsed magnetic field for a contactless forming of metals with high electrical conductivity, such as aluminum or copper. During this process maximum strain rates of 10,000 s^{-1} are achievable. As known from the literature, the material behavior at these high strain rates differs significantly from the one at quasi-static loading with deformation rates lesser than 0.1 s^{-1} [1]. Phenomenological observations during experiments indicate that the material seems to have a higher strength and greater formability under high speed forming conditions [2]. To evaluate the influence of the forming velocity, an investigation of two processes with different maximum strain rates was performed, especially to analyse the resulting material microstructure. The first process was the electromagnetic sheet metal forming as mentioned before. Secondly, the bulge test, using a pressurised fluid medium in order to obtain the deformation, was considered as a quasi-static process. The process principles and parameters are shown in Figure 1.

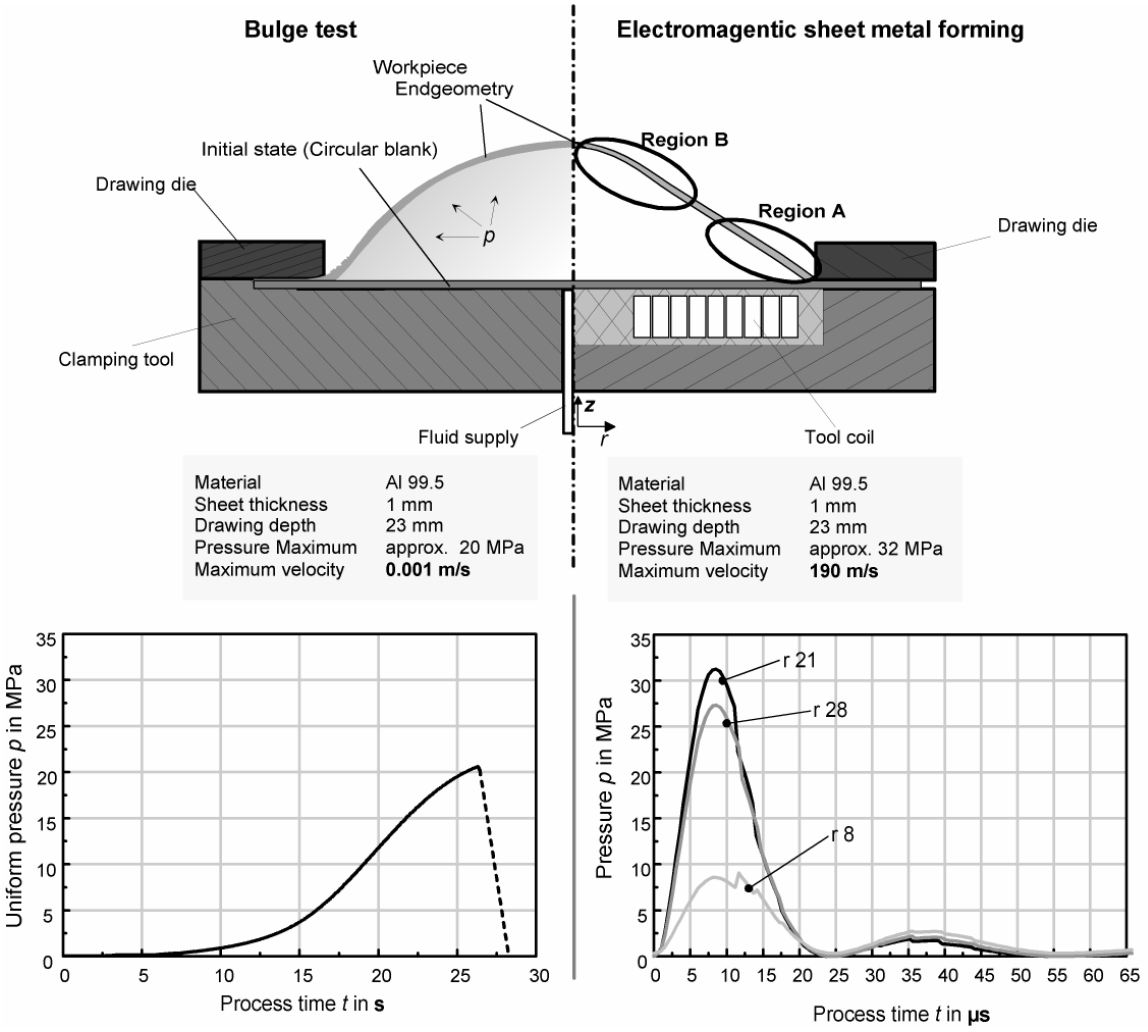

Figure 1: *Process principles and relevant parameters*

The pressure impulse in the electromagnetic sheet metal forming is very high and exists only in a short time slot. In contrast to this, the pressure impulse in the bulge test is long compared to the process time and has a smaller maximum. Furthermore, the pressure impulse in the EMF is a function over time and radius (see Figure 1), contrary to the pressure impulse in the bulge test which depends only on time. But both processes produce a similar final geometry. Only the deformation process differs significantly with respect to the occurring strain paths. Distinctive bending and unbending processes were present in area B during the EMF-process, whereas a constant stretch-forming condition exists during the bulge test. Comparable strain paths are observable only in region A for both processes. Despite of this, the whole developed lengths of the specimens was analysed in order to obtain information about the microstructure, because maximum strain rates occur in area A during the EMF-process.

If an external force is applied upon the workpiece the deformation of the material is caused by a slipping of atom layers in defined crystallographic directions and planes corresponding to the shear stress. Interaction between crystal defects, such as dislocations and the surrounding crystal lattice, are decisive for plastic deformation. Dislocations are linear lattice defects developing in slip planes and moving through the lattice driven by the outside force. According to the crystal plasticity theory, deformation takes place due to the migration of dislocations. This, in turn, increases the dislocation density depending on various mechanisms producing further dislocations. An increase of the yield stress because of intensified hardening at rising strain rates as well as a higher breaking elongation of the material are characteristic for the high speed forming process. On the microstructural level, aside from the thermally activatable deformation mechanisms, damping mechanisms occur at deformation rates of 10,000 s^{-1}. Slip obstacles are overcome non-thermally, without dwell time, too. Therefore, the decisive factor for the deformation based on these mechanisms is not the time needed for overcoming the obstacles, but the run time in between. The resulting greater plastic deformation of the material increases the possibility of the transformation of the microstructure due to the interaction of the dislocations with the grain boundaries, the precipitations, and other dislocations. The dislocation arrangement becomes inhomogeneous, cell structures are formed that change into subgrain boundaries. Only very few experimental studies of dislocation structures at very high strain rates using transmission electron microscopy (TEM) are available, therefore they are represented in detail here. For a complete characterisation of the material, the grain size, the stretching of the grain, the sheet thickness distribution as well as the micro hardness distribution in the initial state and along the radius of the formed specimens were determined. Corresponding specimens were analysed subsequently using the transmission electron microscope and were evaluated regarding their microstructure. In this work, a sheet metal of technically pure aluminum 99.5% with a thickness of 1 mm was analysed. The resultant different microstructure caused by the two considered processes will be analysed and discussed in the following chapters.

2 Metallographic and mechanical investigations

2.1 Microstructural investigations

In order to accomplish a complete analysis of the workpiece, the different laboratory analyses were conducted on different radiuses of the metal sheets in the shaped state. The labels of the inspected areas along the radius can be taken from Figure 2. The labels on the depicted specimen apply to both strain processes. They are adhered to for all subsequent analyses. The names “outer surface” and “inner surface” refer to the tool coil. The surface of the workpiece that faces the tool coil is called the inner surface, the outer surface is the opposite face.

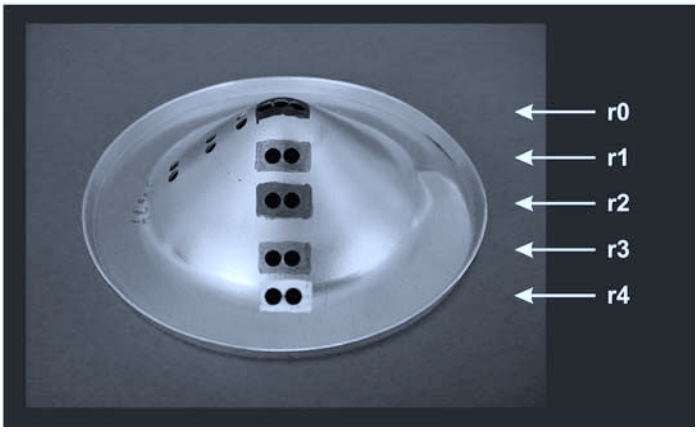

Figure 2: *Electromagnetically formed workpiece; region of interest*

Figure 3 summarises micrographs of the initial state and of the electro-magnetically shaped workpiece. Each depicts a transversal-section of the metal sheet, no particular differences between the surfaces, and the center of the specimen were apparent. Bach et. al describes already summarised analyses of the initial state as well as shaped specimens while varying the process parameters along the rolling direction (RD: rolling direction) [3]. Thus, this paper shows analyses along the transverse direction (TD: transverse direction) for comparison purposes. In the initial state the grains are less stretched in this direction, thus differences in the grain elongation become more obvious. For testing purposes, the electro-magnetically shaped workpiece was divided into two sub-divisions - in the immediate vicinity of the blankholder and from the center of the specimen. The metallographic analyses show a difference in the grain elongation between these areas (quantitatively, cf. chapter 2.2). The grain size remains constant, whereas the grain elongation continuously increases along the radius of the specimen towards the center of the specimen.

The micrographs of the hydraulically shaped specimen are shown in Figure 4. Just like the electro-magnetically shaped workpieces, no changes in the grain size are visible, but a grain elongation does occur. In the flange area (r4) a lower grain elongation than in the areas r3 to r0 occurs (quantitatively, cf. chapter 2.2). The grain elongation in the areas r3 to r0 remains constant as opposed to the electro-magnetically shaped workpiece.

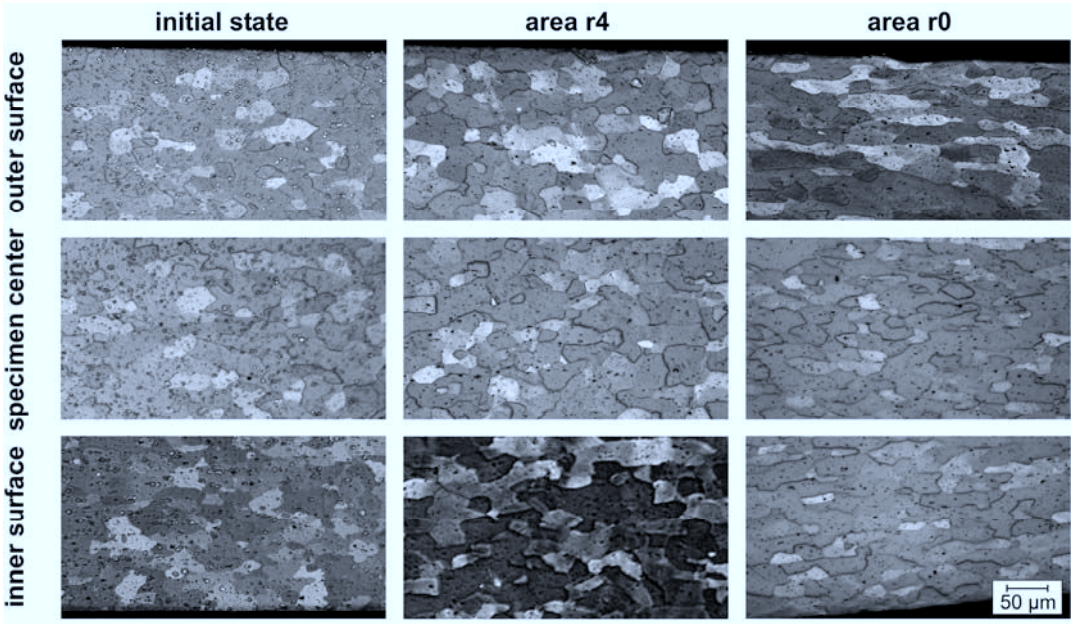

Figure 3: *Microstructure of the initial state and the electromagnetically formed workpiece in TD*

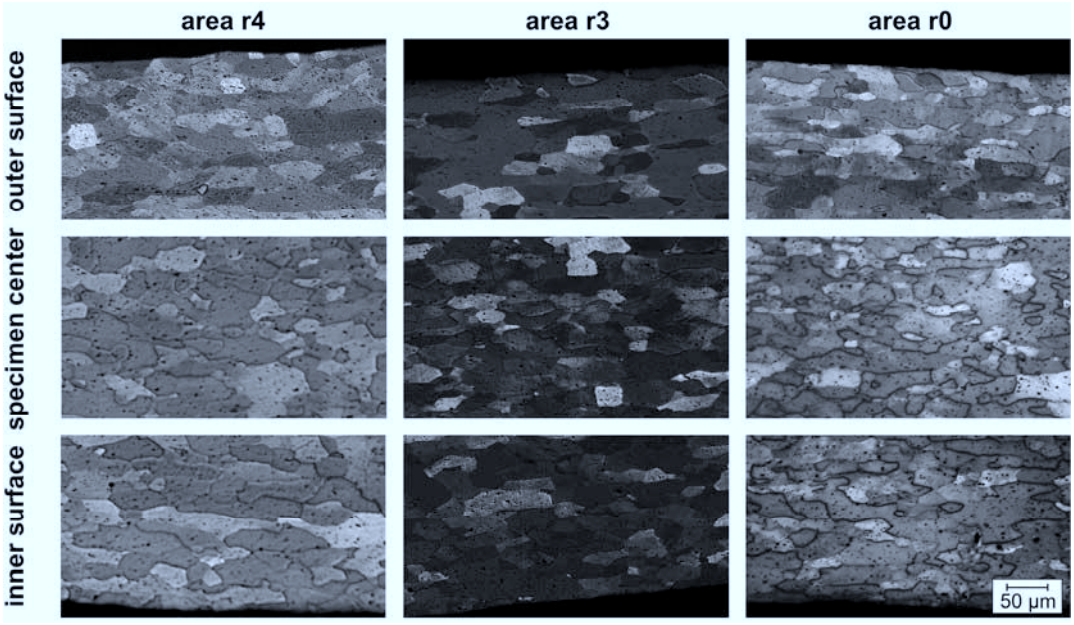

Figure 4: *Microstructure of the hydraulically formed workpiece in TD*

The accomplished metallographic investigations show that both processes cause relatively similar effects on the microstructure, which are expressed in an elongation of the grains along the specimen radius. The difference lies in the extent of the elongation. The aspect ratio of the hydraulically deformed specimen remains constant along the radius. This fact indicates a homogeneous strain. The electromagnetically deformed specimen shows an increased elongation along the radius, which means that in this case the strain varies.

2.2 Grain size and grain stretching

The quantitative evaluation of the ASTM G (G: grain size) by the use of metallographic micrographs is conducted in accordance with the standards ASTM E112 and DIN 50601, using an image processing software. For the analysis, the planimetric process was used. This calculating algorithm is based on a reconstruction of the grain boundaries and is insensitive where bothersome artifacts, such as inclusions and etch effects, are concerned.

Figure 5 shows the results of the grain size and grain elongation evaluation. The grain size is relatively homogenous, its mean value in the initial state is G = 8.4 and for the shaped specimens G = 8.5 ± 0.1. The grain elongation is then calculated as quotient of the vertical and horizontal grain size and is non-dimensional just like the grain size. The elongation of the grains in the initial state is 1.01. For the electro-magnetically shaped workpiece it increases continuously from 0.94 in the flange area (r4) up to 0.85 in the center of the specimen (r0). For the hydraulically shaped specimen the value 0.92 applies for the flange area (r4) and 0.89 in the areas r3 to r0.

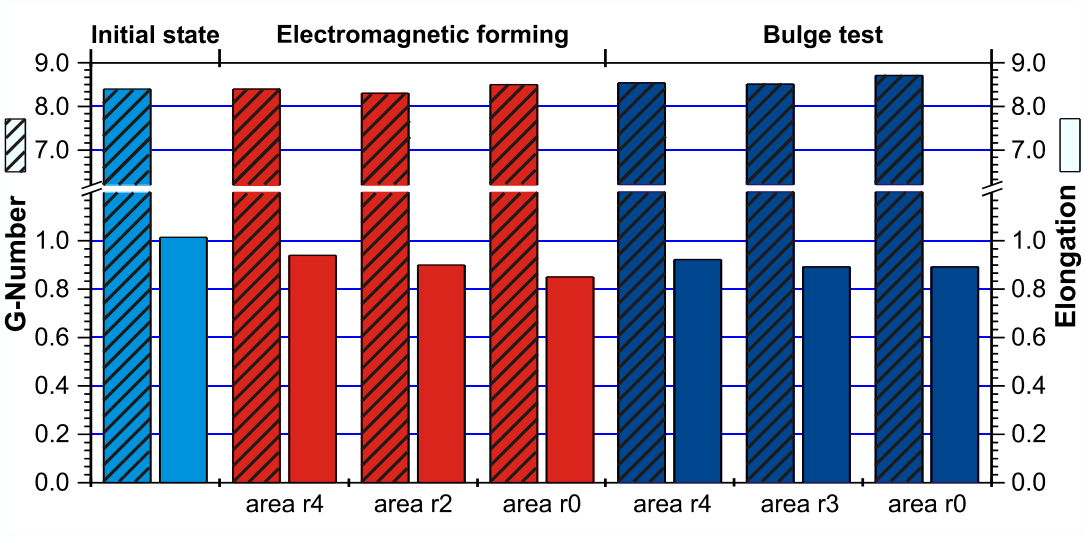

Figure 5: *Grain size and grain stretching of the initial state and both formed workpieces*

The evolution of grain morphology of electro-magnetically and hydraulically shaped specimens has been studied quantitatively. The investigations of the microstructure confirm the results of the analysis of the micrographs concerning the material behaviour.

2.3 Sheet metal thickness distribution

The wall thickness was measured along the radius of the specimens using a stereomicroscope and an image analysis program. For the tested workpieces no obvious difference in the comparison of the specimens taken in and transverse to the rolling direction could be determined (Figure 6). But for both shaping processes a reduction of the wall thickness along the radius in the direction towards the center of the specimen was found. For the hydraulically shaped specimen, the wall thickness decreases more continuously than for the electro-magnetically shaped one. The values of the wall thicknesses in the center of the specimen are identical at 660 ± 10 µm.

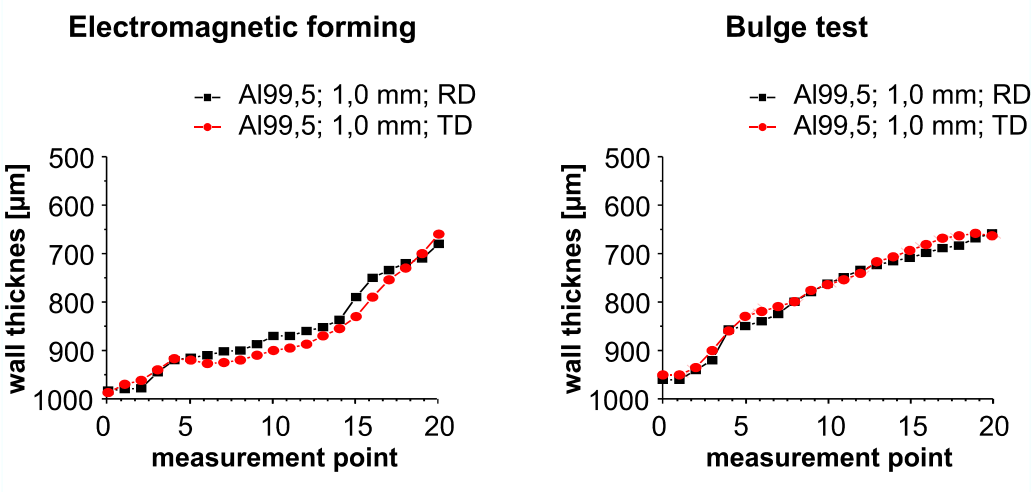

Figure 6: *Sheet metal thickness of the electromagnetically and hydraulically formed workpieces*

2.4 Micro hardness distribution

In the initial state the progression of the hardening depth along the thickness of the metal sheets was measured in order to detect existing differences between edge and center, and to compare these to the values of the shaped specimens (Figure 7, Figure 8 right). The hardness values determined in transversal direction did not show any obvious differences between the outer and the inner surface and the center of the specimen. The mean micro hardness is 29 ± 2 HV 0.5/10.

The electro-magnetically shaped workpiece shows a significant tendency for increased micro-hardness towards the direction of the center of the specimen. The results are shown in Figure 7. In the flange area (r4) it is 54 +/- 4 HV 0.5/10 and in the area r0 71 +/- 2 HV 0.5/10. The values along the thickness of the metal sheets differ and they are higher for the center of the sheet metal than for the outer and inner surface (Figure 7 top).

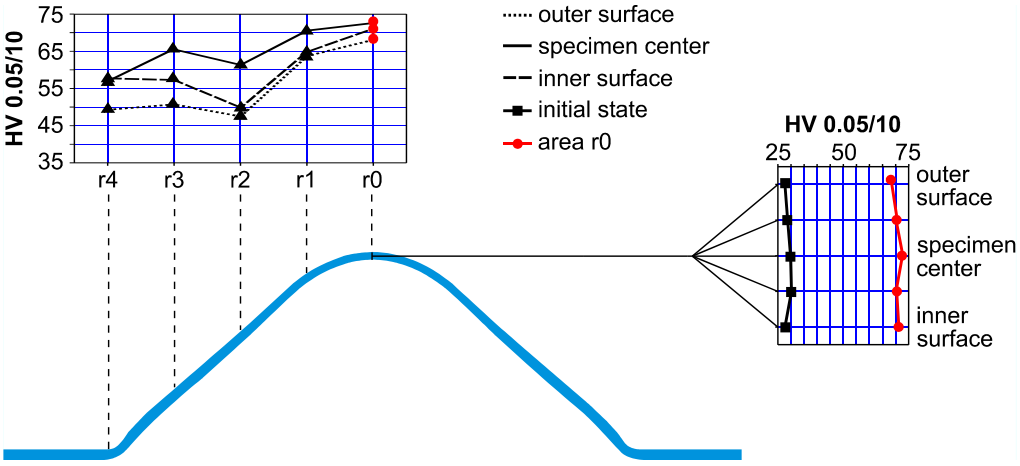

Figure 7: *Micro hardness of the initial state and the electromagnetically formed workpieces in TD*

The progression of the micro-hardening depth of the hydraulically shaped specimen is depicted in Figure 8. Here, an increase in hardness can be observed in comparison to the initial state. This does turn out to be lower than for the electro-magnetically shaped workpiece. The values in the examined areas r4 to r0 are relatively similar and their mean value is in the flange area (r4) 43 HV 0.5/10 and in the area r0 48 HV 0.5/10, there is minor increase in the direction towards the center of the specimen. No differences between the outer and the inner surface become evident in relation to the thickness of the metal sheets.

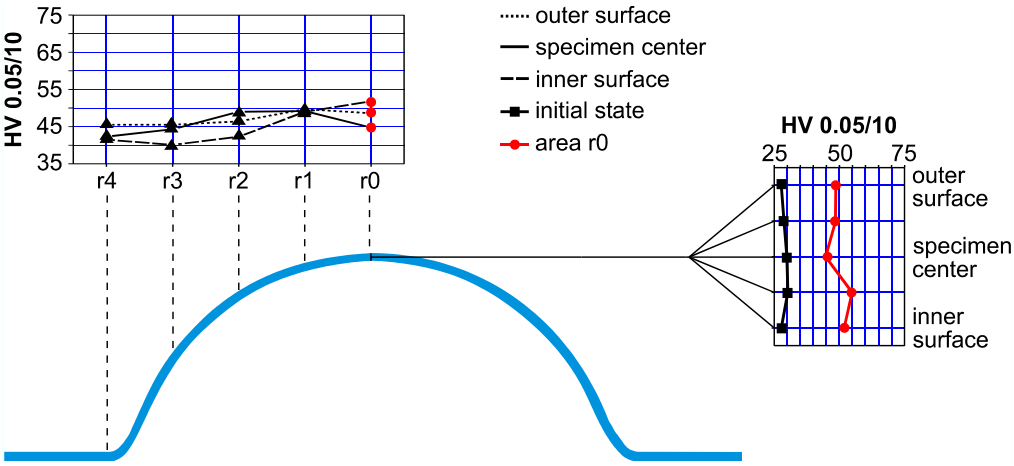

Figure 8: *Micro hardness of the initial state and the hydraulically formed workpieces in TD*

The results of the microhardness investigations indicate (assuming a similar wall thickness of the specimens) that the microhardness values rise as a function of the grain elongation and the strain.

3 TEM investigations

In order to gather a general understanding of the strain mechanisms and to enable a micro-structural modeling of the two strain processes, analyses under the transmission electron microscope (TEM) are necessary. For the individual sampling locations, which are shown in Figure 2, general micrographs with 20.000 and 40.000-fold magnification, respectively, were made. For especially interesting areas detailed micrographs with a magnification of 80.000 to 200.000 were made. Aluminum has a face-centered cubic lattice with 12 slip systems at room temperature. In the poly-crystalline material there are sufficient degrees of freedom to enable an arbitrary plastic deformation.

Figure 9 shows two areas that represent the initial state of the material. In the left part of the figure grain boundaries of a total of five grains can be seen. The TEM cannot produce images of the whole grain, due to the grain size. Because of the different orientations of the crystals, during the preparation of the specimen preparation artifacts occur, and as a result geometrically arranged patterns of the microstructure appear. In the picture, a number of precipitations as well as a few dislocations are visible. In the right part of the Figure 9, next to some dislocations, a sub grain boundary as dislocation orientation is visible. All in all, the dislocation density is very low, which can be explained by a heat treatment in the course of the sheet manufacture.

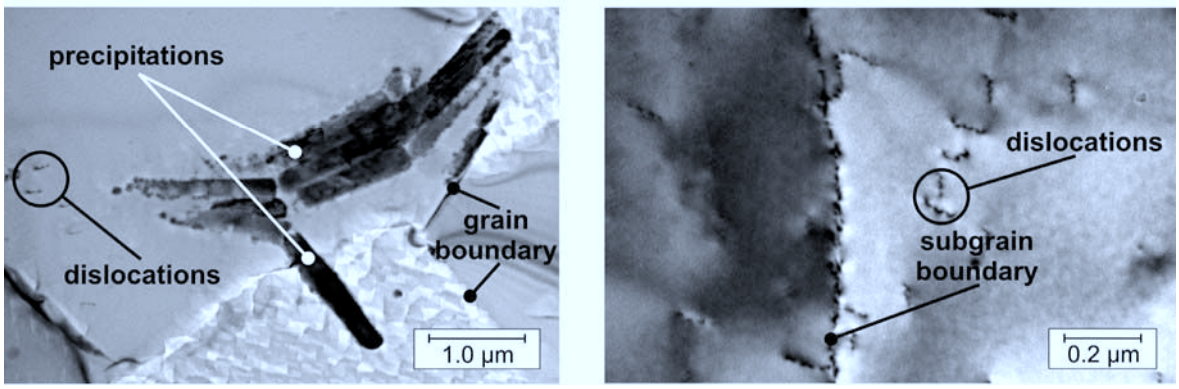

Figure 9: *Microstructure of the initial state*

Figure 10 shows the microstructure pictures of the electro-magnetically shaped work-piece. The specimens were taken from the flange area (r3). The microstructure can be characterised by two representative areas. For one: areas that show a number of single dislocations in comparison with the initial state. But the dislocation density overall is still not very high (Figure 10 top). For two: in parts, dislocation tangles and arrangements of a number of dislocations are visible. These arrangements, however, do not constitute sub-grain boundaries, but coupled dislocation groups.

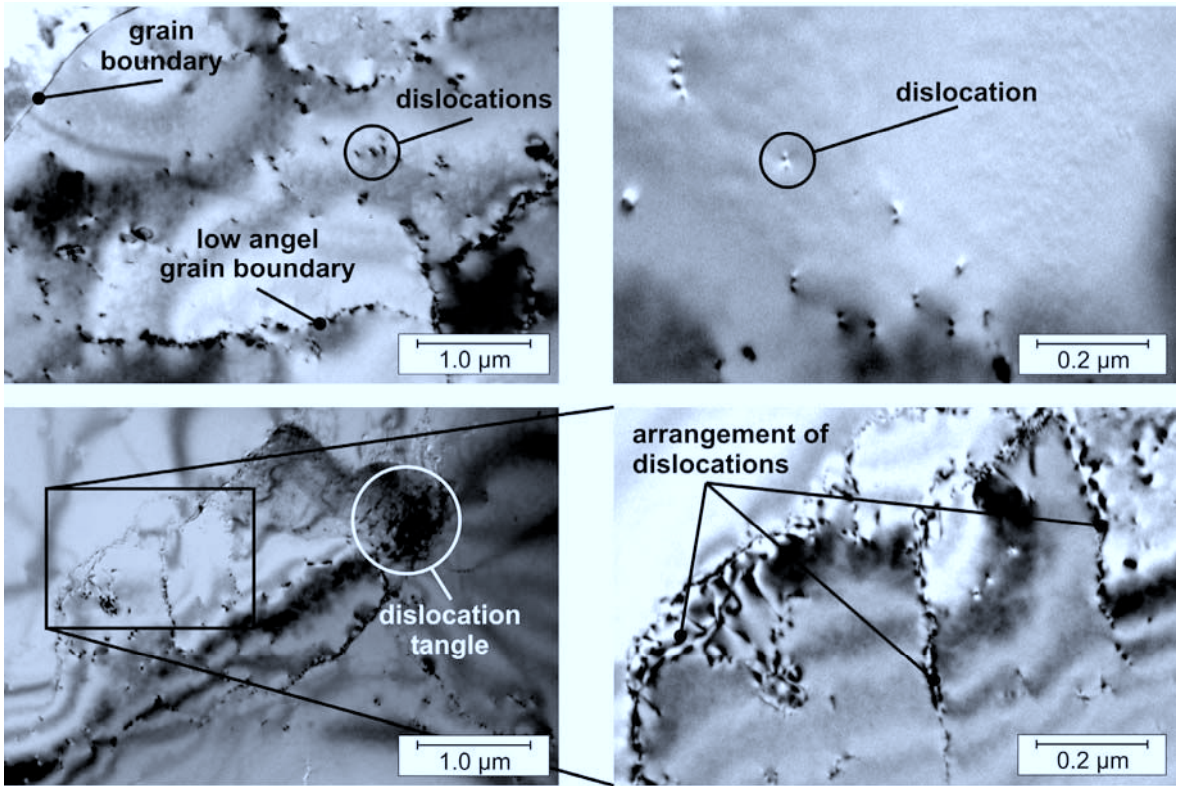

Figure 10: *Microstructure of the electromagnetically formed workpiece near to the flange region (area r3)*

The pictures from the center of the specimen (area r0) of the electro-magnetically shaped specimen are shown in Figure 11. Here, a distinctive cell structure is visible, which is characterised by a low cell wall thickness (Figure 11 top). The differences in contrast that can be seen in Figure 11, top left, indicate orientation differences between the differently defined areas. This means these are subgrains or areas separated by low angle grain boundaries. A number of the areas on the specimen show loosely coupled dislocation groups (Figure 11 bottom left). In many cases dislocation networks are visible (Figure 11 bottom), the cell walls, however, do show in part already subgrain boundary characteristics.

The corresponding areas were also examined on the hydraulically shaped workpiece. Significant differences appeared for the first specimen, which was taken in the vicinity of the blankholder (area r3), are shown in Figure 12. The specimen is characterised by areas with a very high dislocation density (Figure 12 top). A representative picture that shows all dislocations present in a certain area is impossible due to the different orientations of the dislocations. This is also the reason why there are areas in the pictures that seem free of dislocations. For a different tilt angle those areas also show a high dislocation density. There are a number of places with dislocation tangles (Figure 12 bottom left). Rarely, there are areas with a low dislocation density, such as in Figure 12 bottom right.

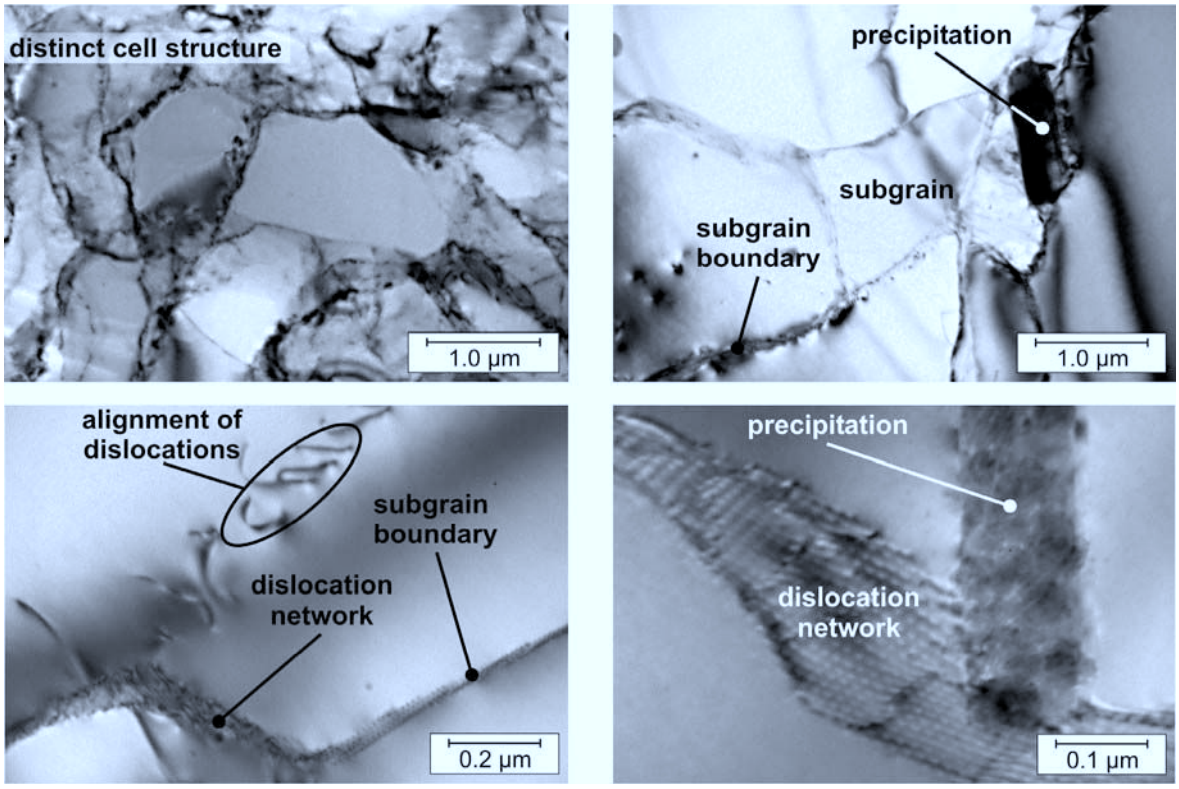

Figure 11: *Microstructure of the electromagnetically formed workpiece - r0 area*

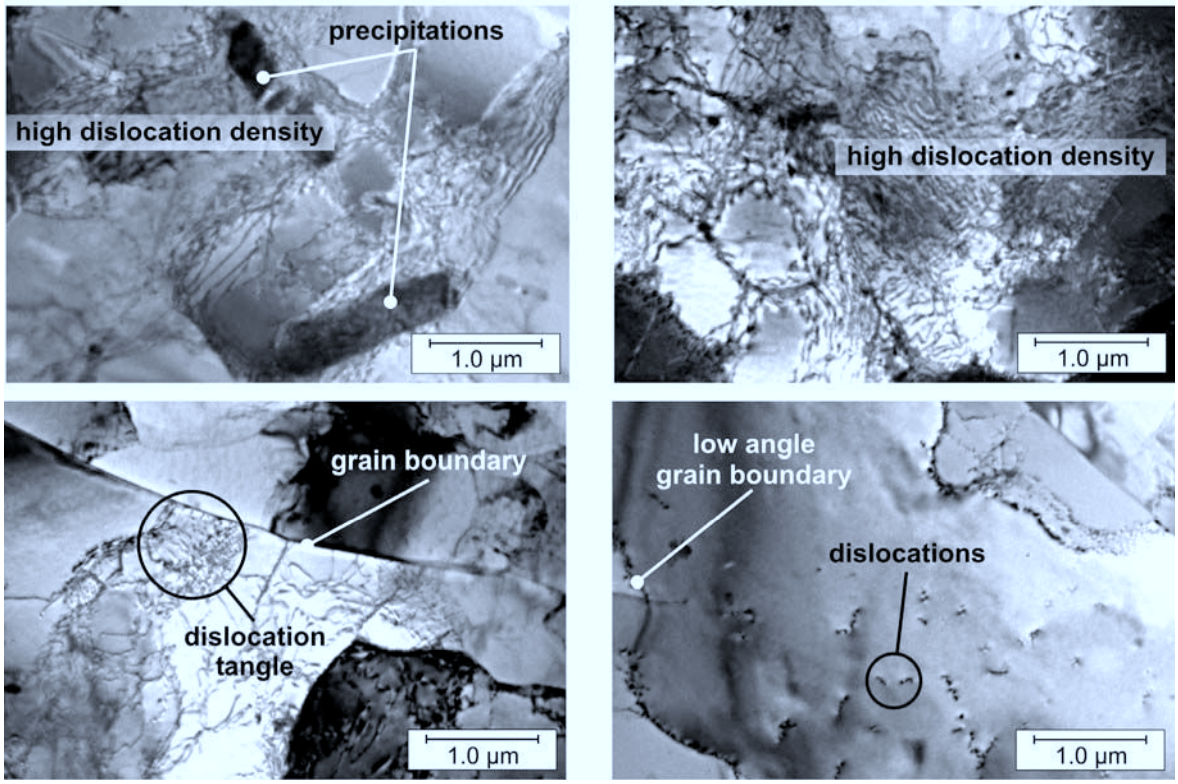

Figure 12: *Microstructure of the hydraulically formed workpiece near to the Blankholder (r3 area)*

The center of the specimen (area r0) of the hydraulically shaped workpiece is depicted in Figure 13. There are significant differences in the comparison of the specimens taken from the flange area. Similarly to the specimens shaped electro-magnetically, the dislocations in these cases establish cell structures. The cells do have thicker walls, though (Figure 13 top right); the interior of the cells again is relatively void of dislocations. These new structures created by the strain in part do not show a difference in contrast, and thus they have only few orientation differences. The two lower pictures show a grain photographed at different tilt angles. In the lower left picture the grain is apparently homogenous; in the right picture it becomes obvious that it is criss-crossed by low angle grain boundaries.

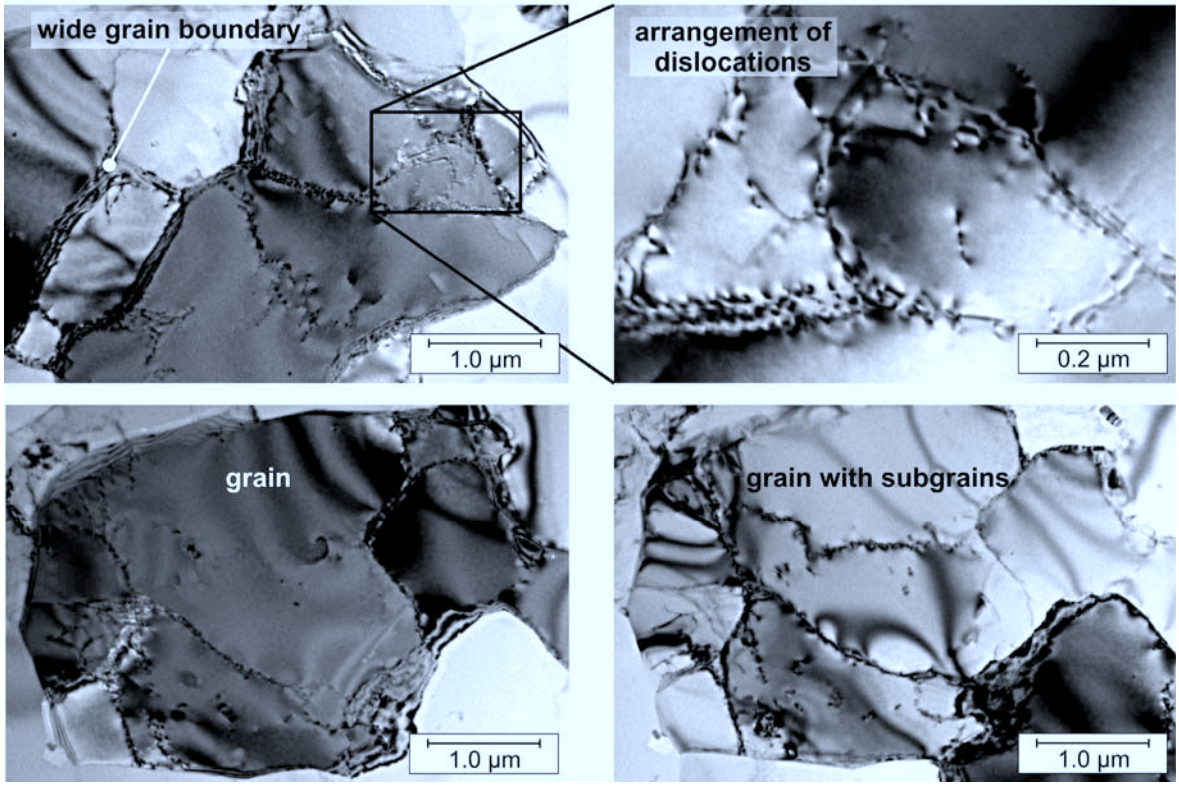

Figure 13: *Microstructure of the hydraulically formed workpiece in the middle of the specimen (r0 area)*

According to the crystal plasticity theory, macroscopic plastic deformation is mainly caused by the creation and the movement of dislocations. In the course of a plastic deformation the dislocation populations undergo several stages of development depending on the degree of straining. According to Honeycombe, these are divided into five areas depending on the strain [4]:

- area I – here mainly primary slip planes become active. Dislocations creep long distances, there is a low dislocation density.
- area II – here also secondary slip planes, active sources, and Lomer-Cottrell-dislocations are activated. There is a high dislocation density. In case of further strain, the dislocations localise and form dislocation tangles, which turn into cell structures.
- area III – here, in addition to the other activating processes, cross-slipping also starts. The three-dimensional structure of the cells turns into a two-dimensional dislocation net. This is the formation mechanism of a subgrain. If the deformation continues the subgrains are elongated and called micro-bands. In case of further deformation, so-called shear bands appear.
- For extreme strains, the areas IV and V can be observed, which are characterised by very distinct recovery mechanisms and a reduction of the established structures.

The transmission electron microscopy analyses of the examined strain processes show typical attributes of a deformation at low temperatures, this means temperatures lower as 0.4 T_s (T_s: melting point). Furthermore, divergent elongations were observed for the two processes. According to the classification by Honeycombe, the electro-magnetically shaped specimen has to be assigned the areas I to III depending on the stress, whereas the hydraulically shaped specimen belongs exclusively to area II.

4 Summary

The aim of the presented analyses is a comparison between two strain processes – the electro-magnetic and the hydraulic straining. The main difference between these processes lies in the type of material treatment. The electro-magnetic straining is a dynamic straining having strain rates of up to 10,000 s^{-1}, whereas the hydraulic straining constitutes a quasi steady-state straining process with strain rates lesser than 0.1 s^{-1}. The examined material was a sheet metal of technically pure 99.5 Aluminum with a thickness of 1 mm. The examined workpieces were strained to the identical draw depth of 23 mm. The analyses were conducted on different areas of the specimen, in order to accomplish a comprehensive characterisation of the strain processes. Next, the results are summarised.

The qualitative and quantitative metallographic analyses show a microstructure with constant grain size. The differences for the shaped specimens become evident mainly in the elongation of the grains. For the electro-magnetically shaped specimen the grain elongation along the radius of the workpiece increases, whereas it remains constant for the hydraulic straining.

The progression of the wall thickness along the radius of the specimen shows a constant decrease towards the center of the workpiece. In case of the hydraulic straining it runs more continuously than for the electro-magnetical one. The center of the specimen shows the least thickness of the metal sheets, it is identical for both types of straining.

The micro hardness increases significantly for the shaped specimens. For the hydraulic strain, the increase in micro hardness is distributed relative continuously over the whole radius of the specimen. In case of the electro-magnetically shaped workpiece, the micro hardness increases along the radius of the specimen towards the center of the specimen. Overall, the micro hardness values for the electro-magnetically shaped workpiece exceed those of the hydraulically shaped ones.

The TEM-analyses show a divergent behavior of the two straining types. Previous publications have shown that the straining of a workpiece occurs according to the crystal plasticity theory through the creation and movement of dislocations. In the course of a strain, at first the dislocation density increases, then the dislocations localise and make up dislocation tangles. Finally, a cell structure is established [5]. In the course of further deformation of the material, the cell size decreases and the interior of the cell becomes increasingly devoid of dislocations. For the hydraulically shaped specimen, interactions of this kind occur. In the flange area the dislocation density is high, towards the center of the specimen a transition into a cell structure occurs. In case the strain increases still, the cell wall thickness is reduced, owing to energetic reasons, and is converted from a three-dimensional to a two-dimensional structure. A dislocation network develops, which constitutes the grain boundary of a subgrain. The dislocation recovery in the interior of the subgrain occurs through the annihilation of dislocation pairs or by absorption at the subgrain

or grain boundaries. The resulting microstructure can be observed in the center of the specimen of the electro-magnetically shaped workpiece. The flange area, on the other hand, shows a comparatively low dislocation density which indicates a low strain. The different strain processes of the workpiece at the edge and in the center also explain the differences in grain elongation and micro hardness. Finally, it can be stated that the microstructural differences between both strain processes result only from the strain rate and the degree of strain. The TEM-analyses clearly show that both these processes are cold-working processes and, furthermore, that the electro-magnetically shaped workpieces signify different strain rates over the radius of the specimen.

References

[1] *Lange, K.* (Hrsg.): Umformtechnik, Vol. 1, Springer-Verlag, Berlin/Heidelberg, 1993.

[2] *Beerwald, C.; Brosius, A.; Homberg, W.; Kleiner, M.; Wellendorf, A.:* New Aspects of Electromagnetic Forming. Proceedings of the 6th International Conference on technology of Placticity, 19.-24. Sept. 1999, Nürnberg, vol. 3, p. 2471-2476.

[3] *Bach, Fr.-W.; Rodman, M.; Rossberg, A.; Weber, J.; Walden, L.:* Verhalten von Aluminiumwerkstoffen bei der elektromagnetischen Blechumformung; 2. Kolloquium elektromagnetische Umformung, 28. Mai 2003 Dortmund, 2003.

[4] *Honeycombe, R.:* The plastic deformation of metals, Edward Arnold Ltd. London, 2. ed., 1984.

[5] *Lan, Y.:* Verfestigungsverhalten und Versetzungsstruktur von Eisen und Aluminium bei niedriger Temperatur. Fortschritts-Berichte VDI, vol. 5, Nr. 249, 1992.

Recent Enhancements to Determine Flow Stress Data in High Speed Compression Tests*

T. Rehrmann, R. Kopp

Institute of Metal Forming (IBF), RWTH Aachen University, Germany

Abstract

The accuracy in numerical simulation and physical models is increasing continually. For this reason, the attention to the measurement of flow stress fields at hot forming conditions rises presently. The determination of flow curves at small and middle strain rates up to 100 /s has become a standard procedure. In the wide range between strain rates of 100 /s up to 500 /s no accurate experimental data of compression tests by the use of servo-hydraulic testing systems exists to date. In this context, the IBF investigated how compression tests especially on servo hydraulic testing-machines can be developed in order to expand the range of flow-curve fields clearly above 100 /s with strains up to $\varphi = 0.7$. The maximum tool speed of the IBF testing machine is 3000 mm/s.

This presentation shows the advances realised in this field. During the research activities, the existing servo-hydraulic high-speed testing machine has been optimised and new post processing techniques have been developed. Hence, valid flow stress values can now be determined up to strain rates of 300 /s in compression tests on the utilised servo hydraulic testing system. Present investigations have the aim to determine absolutely reliably flow stress data even for strain rates up to 500 /s.

Keywords:

Forming, Metal, Flow Stress, Measuring Instrument

1 Introduction

In this research project the fundamentals of the performance, evaluation, and analysis of compression tests on servo-hydraulic systems with completely new test parameters are developed. This was done especially for experiments in the range of high strain rates at

This work is based on the results of the DFG research project DFG Ko 579/54; the authors would like to thank the DFG for the financial support

large strain values in axisymmetric compression tests. Primarily, hot dynamic compression-tests are carried out at temperatures up to 1250 °C. These kinds of tests are important for the determination of flow-stress curves at high temperatures to obtain a basis for the FEM simulation of hot forming processes. Thereby, the progress in the experimental set-up and further possibilities with regard to the realisation of higher strain rates are most important. Tests with strain rates of up to 100 /s are performed on the installed servo hydraulic testing machine SERVOTEST by default. The usability of data determined on standard path controlled test methods in the range of strain rates higher than 50 /s was not assured at the beginning of this research project.

The above mentioned values in strain rates, or even higher strain rates can be found "locally" in modern industrial forming processes, like rod rolling or profile rolling, hammer forging, die forging, as well as extrusion. The goal of this project is to explore how to reach higher strain rates of about 200 /s to 500 /s or even up to 1000 /s. Then, modern industrial forming processes such as tandem mills can be very reliably simulated. Meanwhile, the set-up of the servo-hydraulic testing-machine is optimised to perform compression tests in the range of 100 /s to 300 /s at room temperature. Therefore, the new developed optimised testing methods close the gap in determination of flow curves between tests at low and medium strain rates on servo-hydraulic respectively mechanical machines and experiments at highest strain rates on Split-Hopkinson Pressure Bars (SHPB) [9] or on dynamic expansion test-systems. A further aim is to standardise the measurement of flow curves by compression tests at room temperature and at high temperatures in the range of high strain rates.

2 Used Testing Equipment

2.1 Hydraulic Testing Machine

The used SERVOTEST testing-system was installed at the IBF in 1995, see [6,8]. The servo hydraulic testing machine has a maximum force of 1200 kN and a maximum tool-velocity of 3000 mm/s. A miniaturisation of the specimen geometry down to h_0 = 6 mm and d_0 = 4 mm enables even tests with maximal nominal strain rates of 500 /s. Further, it was verified to what extend a variation of the specimen geometry influences the determination of flow stress data, e.g. [6,12,13].

2.2 Data Acquisition

The data logging is automatically carried out with separate A/D converters each one for the load, velocity, displacement, and temperature channel. Sample frequencies up to 20.48 kHz can be realised for each of the four channels above mentioned which is sufficient for the regarded high speed compression tests. Furthermore, the recently upgraded system enables the measurement with three additional thermocouples. In general, a standard load cell measures the forces on the basis of resistive wire strains in a shear-web-design. The sensors for velocity and displacement are the so-called Linear Variable Differential Transformer (LVDT) and the Linear Velocity Transducer (LVT). Both sensors operate inductively. The temperature is optionally measured with thermocouples.

3 Problem Description

Using the standard test set-up for cold compression tests at high strain rates, the measured load signal (Figure 1a) oscillates with a frequency about 1715 Hz due to the sudden impact [6,7,11,10]. The particular frequencies depend on the specific set-up of the testing system, [6]. No ringing in the load signal (Figure 1b) is recorded for “low” strain rates up to 50 /s, [6].

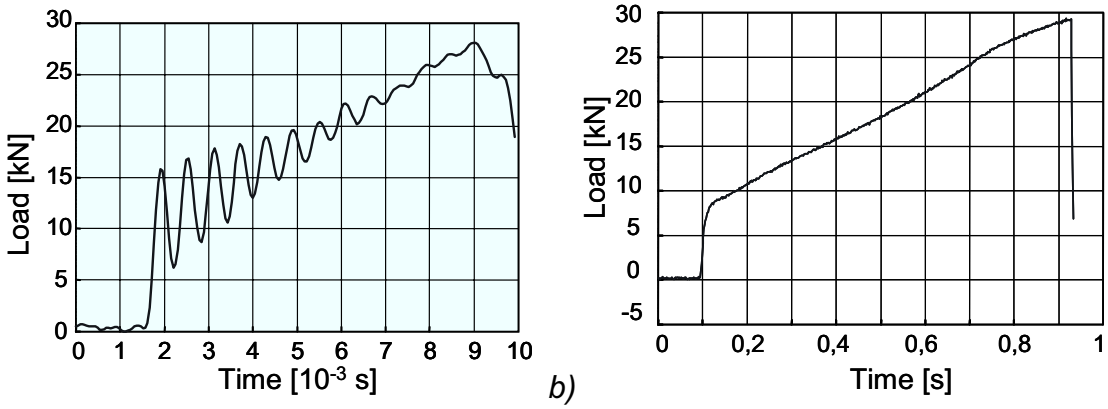

a) *b)*

Figure 1: *Load signal of an axisymmetric (uniaxial) compression test, 100Cr6, 25°C, h_0 = 10 mm, d_0 = 7 mm at a strain rate a) 300 /s and b) 1 /s*

First of all, the reason for the ringing was investigated. Thence, there could not be the possibility to determine accurate flow curve data from measured signal recorded during compression tests at high tool velocities. Insofar, the source of ringing was necessarily spied out. Furthermore, it was verified, in how far the load ringing can influence the actual forming process. The goal was either to suppress the ringing as good as possible or to develop an adequate post processing method in order to filter the ringing. The use of a signal filter is only feasible if the described oscillating phenomena can be separated from the actual forming process.

4 Troubleshooting

Due to the above described problem two tasks were carried out. On the one hand, the used testing set-up actually was analysed and modified. On the other hand, the existing post processing was replaced by a new and better suited method. In the following, the two traced scopes of duties will be described.

4.1 Data Post Processing

The vibration of the load signal is the main problem in determining flow curves by the use of (uniaxial) compression tests at elevated strain rates. Firstly, this problem has to be solved. Subsequently, other influences on the accuracy [4] of determining flow curves - like friction or dissipative heat generation - can be investigated. The use of attenuators in order to reduce the oscillations is not expedient. The reason being that any additional

dashpot will absorb a fraction of the force applied on the load cell. Measuring any instantaneous dynamic force value necessarily requires that the frequency response of the force measurement system must be sufficient in order to follow the rapidly changing force [3]. Any supplementary damping downgrades the inherent frequency response of each measurement system. For this reason, the ringing of the load signal has to be filtered out in detail. Standard algorithms used up to now are inapplicable because they falsify the original signal so much that an inference to the underlying excitation caused by the impact and the subsequent deformation of the sample is impossible [1,6].

If standard filtering techniques are used on the ringing load signal, the important information about the rise in the load at the beginning of the test is lost. General filtering techniques, like the use of low pass filters, are not applicable because the frequency response of the measurement system is close to the time scale of the initial load rise. In general, each filtering of signals implicates a delay and a phase shift, whereby in most of the cases the corrected signals are distorted. Hence, investigations to develop new methods of correcting measured data were required (by any means).

Another strategy of filtering the data is based on an idea by SERVOTEST [2]: To simplify the problem, a single undamped harmonic oscillation is assumed. This supposition corresponds to the above-mentioned model of a non-damped harmonic oscillation. Then the answer of the load sensor is

$$F_a(t) = F_e(t) + F_0 \cdot sin(\omega_0 t) \tag{1}$$

Hence, F_a is the answer signal detected by the load cell, F_e is the excitation force belonging to the underlying compression of the specimen, F_0 is the initial ringing amplitude, and ω_0 is the specified harmonic frequency.

Using the second derivate of (1) and combining the result with the original equation (1) an algebraic transposition results in

$$\frac{1}{\omega_0^2} \cdot \left(\frac{d^2}{dt^2} F_a(t) - \frac{d^2}{dt^2} F_e(t) \right) = F_e(t) - F_a(t) \tag{2}$$

Regarding now the direct neighbourhood of a single data point in the digitally recorded load signal. It can be assumed that the second derivative of the real excitation force source is negligible, so that the excitation force can be calculated from the recorded signal of the load sensor F_a and the determined excited natural frequency ω_0, according to

$$F_e(t) = F_a(t) + \frac{1}{\omega_0^2} \cdot \left(\frac{d^2}{dt^2} F_a(t) \right) \tag{3}$$

The thus corrected answer signal of the sensor F_a is the first approximation of the real force F_e which is necessary to compress the specimen with high impact tool velocities. The problem of an unknown amount of masses added to the sensor system is successfully avoided with this method (3).

The described calculation considers neither damping effects nor multiple frequencies in the oscillating signal. Consequently, the described method was optimised.

The results of the system analysis show that the oscillations in the load signal of high speed compression tests contain only the excited natural frequencies of the whole experimental set-up [6,7,10]. The number and amplitudes of registered frequencies de-

pend mainly on the initial impact forces and the different set-up principles. The recorded signal is a superposition of damped harmonic oscillations with linear independently excited natural frequencies $\omega_{0,i}$.

$$F_a(t) = F_a(t) + \sum_i F_{0,i} \cdot e^{\delta_i \cdot t} \cdot sin(\omega_{0,i} \cdot t) \tag{4}$$

The above described correction (3) can easily be applied to signals with more than one excited natural frequency separately for each estimated natural frequency in different steps. Further investigations also indicated that a multiple exertion of this correction calculation can sufficiently reconstruct the exciting force out of damped oscillations in the answer load signal as well.

Even the new extension of the frequency correction method does not consider the load cell's inertia correctly, i.e. the delayed answer of the sensor due to the sudden impact. The answer time of the load cell limits the detection of the generally steep ascending slope of the (deforming) load during a high speed compression test. In comparison to the determined stress-strain curves at low strain rates, the stress curves at high strain rates show a gradient slope that is too low if they are smoothed. Because the most important aspect of the analysis is a precise definition of the yield point, the correction of the signal must maintain the information of the initial load gradient. Therefore, the correction algorithm was again optimised. Because of the delayed answer of each used sensor, the real excitation force will be only followed by the recorded signal due to the physical limits of the used sensors. The quality of this effect depends mainly on the reaction time of the used sensor-system. Therefore, no sensor will be able to exactly reproduce the original unknown excitation source.

Regarding a thought experiment where the excitation force applied on the sensor is a rectangle signal, each sensor containing masses would also respond oscillating to this theoretical excitation by delay [6]. In order to have a reproducible correction, the first turning point after the initial load rise is chosen where the correction of the answer signal should start. With reference to a plain sine curve, this position is a neutral point, i.e. the first overshoot is kept out of the maintained uncorrected signal for all times. Applying this method, much better results in determining high speed flow curves were achieved [6]. Up to the present, the above discussed correction methods are the best technique to extract the "real" compression force for this special problem. Therefore, this algorithm has been implemented in the standard post processing software *FlowStressUtilities* which is currently being developed. High speed compression test data is now handled using this method by default.

4.2 Testing Set-Up

The unavoidable ringing in the load signal was analysed for the standard experimental set-up in order to develop an optimised measurement. Neither velocity nor displacement signals show a ringing behaviour during high speed compression tests [6,7,10]. Both the high speed compression test as well as a stroke with a copper-hammer result in a frequency of 1715 Hz in the load signal [6,10]. Therefore, it is safe to say that the oscillation is pure load cell ringing. Furthermore, measurements with strain gauges affixed directly to a specimen proved this assumption to be true [6].

A recorded load signal (Figure 1a) of a high strain rate compression test can be described as a combination of the following two effects. On the one hand, the forming force as a result of the proper compression of the sample acts on the load sensor. Secondly, the load cell ringing due to the impact of the specimen onto the upper die overlays the above described signal component. In a first approximation the oscillation in the load signal can be described as a rigid body movement considered as free vibrations around the changing equilibrium position corresponding to the forming force of the sample [6].

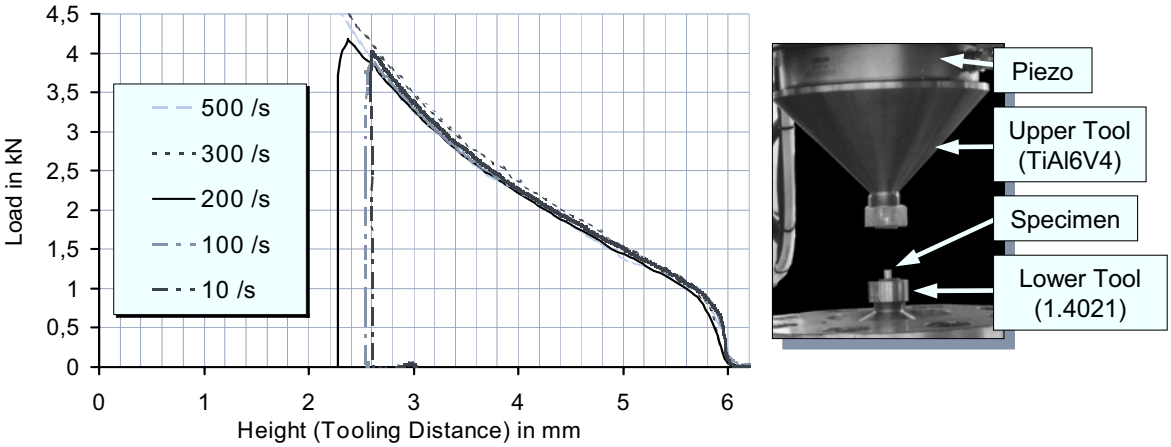

Figure 2: *Load signals and testing set-up of uniaxial compression tests on aluminium; 25°C; initial height h_0 = 6 mm, initial diameter d_0 = 4 mm; nominal strain rates 10/s to 500 /s*

The answer of each oscillating system to the excitation source depends on the natural frequencies . The higher the frequencies, the faster the reaction of the system will be [6].
If the masses (tools, cooling devices etc.) which are connected with the load cell can be reduced, the natural frequencies will be shifted to higher values [6,11]. In the first instance, the measuring system for room temperatures was reconstructed. The motive for optimising tests firstly at room temperature is mainly the easier examination of the modifications and their effects. Additionally, in this set-up high speed videotaping is possible. In order to reduce the masses as much as possible, an upper die was constructed using TiAl6V4 as tool material. The geometry of this die was adapted to the handling of reduced sample sizes (initial height h_0 = 6 mm, initial diameter d_0=4 mm). Furthermore, a stiffer and faster piezo force sensor [6] was installed (Figure 2).

Tests and the recorded video sequences using the described set-up show no oscillations for all velocities (Figure 2) in the case of nominal strain rates from 100 /s to 500 /s. The actual input is not sufficient to excite the first natural frequency of 5000 Hz determined by a FEM calculation. The necessary forming forces for the small specimen with maximum values of 4 kN as well as the decreased necessary testing speeds reduce the input to the sensor. These two facts are desired and positive secondary effects of the modification task. The optimised tests at room temperature can be used to determine flow stress data up to high strain rates.

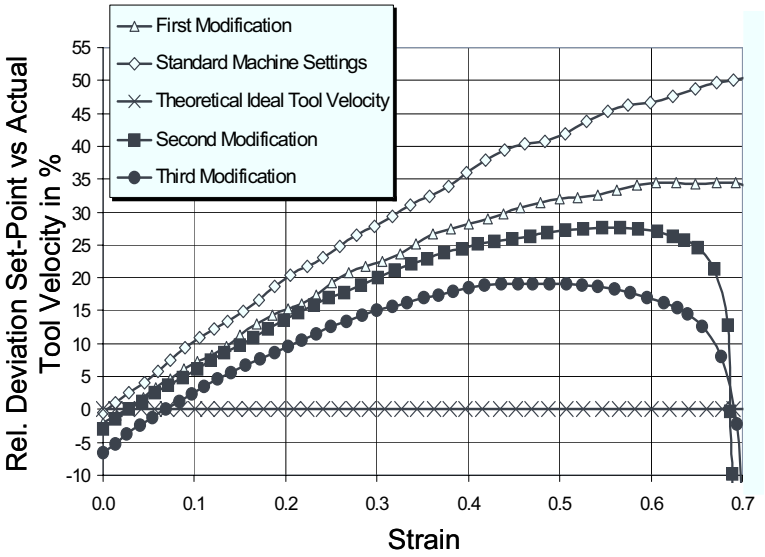

Figure 3: *Summary of velocity deviations for strain rate 300 /s tests. Variations of machine control parameters and the effect on the valve closing*

Comparing the required and the recorded strain rates leads to the next step of the optimisation task. In order to assure a constant strain rate during the whole test duration, a tool velocity profile according to

$$v_w(t) = h_0 \cdot |\dot{\varphi}| \cdot e^{-|\dot{\varphi}| \cdot t}, \quad \dot{\varphi} = \text{constant} \tag{5}$$

is necessaryly demanded. Because the testing machine is designed for loads of up to 1200 kN, sufficiently large, and thus not satisfactorily fast valves are installed. Ignoring the effects of oil compressibility for the moment, for a strain of 1 at 300 /s the velocity - and hence the valve opening – needs to be reduced to about 30% of the initial value in 3 ms. The maximum rate of change of each main valve spool position is about 10% per millisecond. In order to maximise the deceleration, all 4 main valves of the actuator must be used, so that the initial opening of each valve is as small as possible. Therefore, special machine parameters have been changed to allow the best closing procedure of all valves with an optimised pre-closing at the beginning of the compression. So, the maximum and the average relative deviation in tool velocity between the actual and set point values could be successfully reduced (Figure 3).

If experiments with the new construction for hot compression tests (Figure 4) are performed the recorded load signals still show ringing for strain rates above 100 /s (Figure 5). The used materials and the necessary installation of a cooling system as well as heat insulation put on more weight compared to the new set-up for room temperature. Anyway, with the new optimised construction, the natural frequency of the force measurement chain could be raised to a value of 2500 Hz. Combining the new construction with the new post processing correct data interpretation for flow stress values up to strain rates of 300 /s is possible.

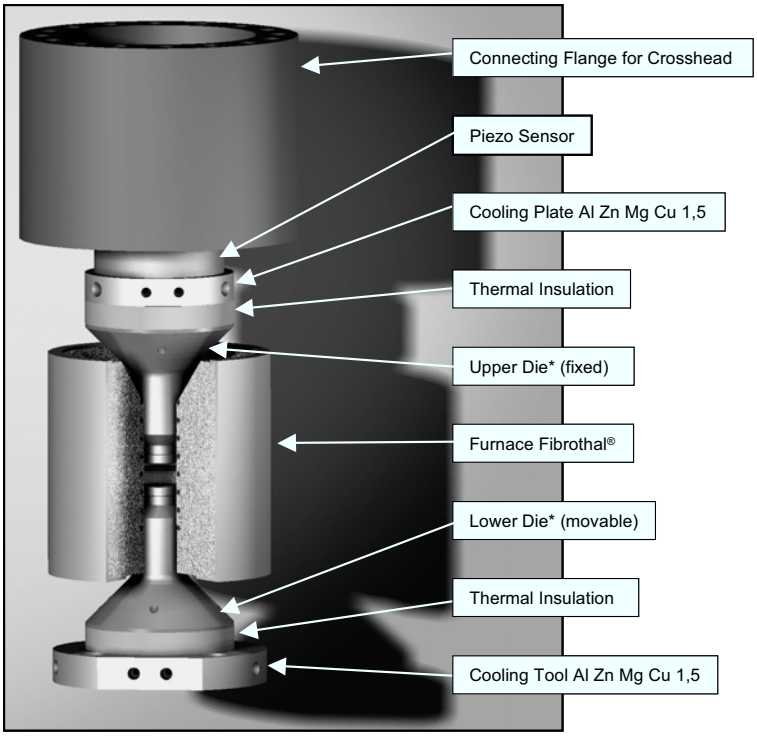

*ODS Superalloy PM 2000: 1.4768 dispersion strengthened, Plansee AG

Figure 4: *Optimised new set-up for hot uniaxial compression tests and high strain rates*

4.3 Discussion of the results

The modifications carried out for the testing set-up for experiments at room temperature and high temperature range show that the main influencing variables are the stiffness and the masses connected to the sensor.

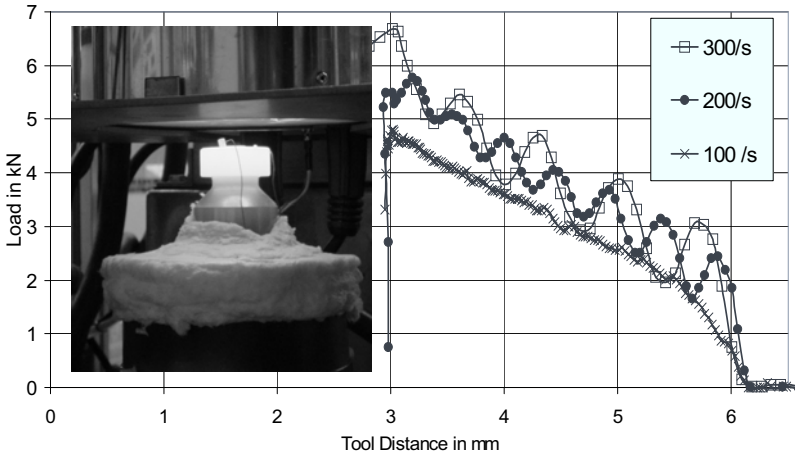

Figure 5: *Load signals of uniaxial compression tests on 16MnCr55; 1000 °C; h_0=6 mm; d_0=4 mm; nominal strain rates 100 /s to 300 /s*

Moreover, the input of kinetic energy exerts an important influence on the excited frequency response (magnitude of the ringing amplitude). The frequency is independent of the used specimen material and tool velocity [6,10]. Temperature effects are minimal due to the fact that the stiffness does not change much with the temperature. Even if the strain rate cannot be held strictly constant during the whole testing procedure, the variations of the real strain rates could be successfully minimised. Further optimisations may lead to a better dynamic behaviour of the well investigated versatile servo hydraulic testing machine. Furthermore, it is now possible to start the examination of the dynamic material behaviour by the use of common metallographic methods.

5 Summary

In the research project presented here, the strain rate (range) spectrum of path controlled axisymmetric compression tests was successfully expanded to 300 /s. By now, an adapted algorithm has been developed. With this new calculation rule, ringing measured load data can be used to determine ringing free flow curves. Further on, the measurement set-up was optimised by the use of a broad system analysis. Therefore, measurement readings are allocated which are not any more, or at least only insignificantly affected by ringing. These results allow a broader applicability in the strain rate range of industrial forming processes.

References

[1] *Bernrath, G.:* Weiterentwickelte Meßmethoden zur Erfassung von Werkstoffdaten für die Warmumformung, Shaker (Aachen), 2000, Bd. 92, Diss.ISBN 3-8265-7320-X.

[2] *Blows, F., Servotest Ltd, UK*: personal communication, Germany, 2002.

[3] *Hunt, A., et. al.:* Guide to the Measurement of Force. Institute of Measurement and Control, London, 1998, ISBN 0 904457 28 1.

[4] Kopp, R., Heußen, J.M.M, Philipp, F.-D., Karhausen, K.*:* Improvement of accuracy in determining flow stress in hot upset-ting tests. Steel Research 64 (1993) No. 8/9, p. 377-384.

[5] *Kopp, R., Rehrmann, T.:* „Determination of accurate flow-stress data in compression tests at intermediate strain rates“, CIRP-Workshop Simulation of Metal Cutting and Forging Processes, January 23. 2002.

[6] *Kopp, R., Rehrmann, T.:* „Enhancements in Determining High Speed Flow-Stress Data by the Use of Compression Tests“, WGP Production Engineering (Volume X/2), 2003; p. 19-24.

[7] *Kopp, R., Wolske, M., Rehrmann, T., Shimahara, H.:* „Determination of Forming Limits by Use of Process-Adapted Sample Geometries and Optimised High Speed Compression Tests“, Advanced Technology of Plasticity (2002), Vol. 2, Proceedings of the 7th ICTP, Oct. 28-31, 2002, Yokohama, Japan.

[8] *Kopp,. R.; Luce, R.; Leisten, B.; Wolske, M.; Tschirnich, M.; Rehrmann, T.; Volles, R.:* “Flow stress measuring by use of cylindrical compression test and spezial application to metal forming processes”. Steel Research 72 (2001) 10, p. 394-401.

[9] *Lindolm, U.S.:* “Some Experiments with the Split Hopkinson Pressure Bar”. J. Mech. Phys. Solids 12 (1964), p. 317-335.

[10] *Rehrmann, T., Kopp, R., Volles, R., Blows, F.*: „Load Cell Ringing and Optimised High Speed Compression Tests“, NPL Workshop Hot Deformation at High Rates, May 21, 2003, NPL London.

[11] *Rehrmann, T., Kopp, R.*: „Fortschritte bei der Ermittlung von Fließkurven im Zylinderstauchversuch für hohe Umformgeschwindigkeiten“, Tagung Werkstoffprüfung 2003 (Stahlinstitut VDEh), Bad Neuenahr, 4./ 5.12.2003.

[12] *Roebuck, B., et. al.*: Measuring Flow Stress in Hot Axisymmetric Compression Tests. Measurement Good Practice Guide No. 3, National Physical Laboratory, London, 2002, ISSN 1368-6550.

[13] *Wiegels, H.; Herbertz, R.:* Der Zylinderstauchversuch – ein geeignetes Verfahren zur Fließkurvenermittlung? Stahl und Eisen 101 (1981), 24/81, p. 1487-1492.

SESSION 2

MODELLING & SIMULATION

Numerical Simulation of Pulsed Electromagnetic Stamping Processes.

N. Bessonov[1], S. Golovashchenko[2]

[1] Institute of the Problems of Mechanical Engineering, Russian Academy of Sciences, St. Petersburg, Russia

[2] Manufacturing & Processes Department, Ford Research & Advanced Engineering, Dearborn, USA

Abstract

In earlier published papers simulation of electromagnetic forming (EMF) was often conducted assuming that pulsed electromagnetic load can be replaced by the pulse of mechanical force calculating its parameters similar to R-L-C electric circuit. However, in many practical cases, parameters of this circuit are variable during the process because of the displacement of the blank and from one operation to another due to the accumulation of heat in the coil. The distribution of electromagnetic forces is also non-uniform and may affect the quality of the part being stamped. In our opinion, the accuracy of the simulation of EMF can be significantly improved if the formulation of the problem includes Maxwell equations of the electromagnetic field propagation, equations of dynamic elastic-plastic deformation, and heat transfer equations all coupled together. In addition, this approach may provide knowledge of electromagnetic coil deformation, which was investigated earlier with significant simplifications. The complexity of the problem is defined by mutual dependence of all three physical processes (electromagnetic field propagation, dynamic elastic-plastic deformation, and heat transfer) and variable boundary conditions.

The propagation of the electromagnetic field is defined by quasi-stationary Maxwell equations transformed in Lagrangian form. The dynamics of elastic-plastic deformation is modeled using the solid mechanics equation of motion, the modified theory of elastic plastic flow, and the Von Mises yield criterion. The energy conservation law is employed for the simulation of heat transfer, which is important to define the appropriate stamping rate without overheating the coil.

The developed methodology is illustrated by 2D examples of cone formation from sheet using a flat coil and the conical die and 2D plane strain sheet formation by direct propagation of the electric current through the metal bar, serving as a coil, and through the deformed sheet.

Keywords:

Forming, Sheet, High Strain-Rate

1 Introduction

In earlier published papers simulation of electromagnetic forming (EMF) was often conducted assuming that pulsed electromagnetic load can be replaced by the pulse of mechanical force [1]. Parameters of this pulse were calculated similar to R-L-C electric circuit [2]. However, in many practical cases, parameters of this circuit are variable through the process because of the displacement of the blank and from one operation to another due to the accumulation of heat in the coil. The distribution of electromagnetic forces is also non-uniform and may affect the quality of the part being stamped. In our opinion, the accuracy of the simulation of EMF can be significantly improved if the formulation of the problem includes Maxwell equations of the electromagnetic field propagation, equations of dynamic elastic-plastic deformation, and heat transfer equations all coupled together. In addition, this approach may provide knowledge of the deformation of the electromagnetic coil, which was investigated earlier with significant simplifications [3].
The complexity of the problem is defined by mutual dependence of all three physical processes (electromagnetic field propagation, dynamic elastic-plastic deformation, and heat transfer) and variable boundary conditions.

2 Theoretical approach

The propagation of the electromagnetic field is defined by quasi-stationary Maxwell equations:

$$\nabla \times H = j \tag{1}$$

$$\mu_a \frac{\partial H}{\partial t} = -\nabla \times E \tag{2}$$

$$j = \sigma \cdot (E + \mu_a v \times H) \tag{3}$$

where H is the magnetic field intensity; j is the current density; E is the electric field intensity; σ is the electric conductivity; v is the velocity; μ_a is the magnetic permeability of medium under consideration. For short duration processes we assume $\mu_a = 4\pi 10^{-7}$ H/m.

Taking into account specifics of the electromagnetic forming processes, including an almost stationary coil, a die and a quickly accelerated blank, the equation for the magnetic field intensity H can be transformed in Lagrangian form. Based upon equations (1)-(3), the equation relating to the vector H can be written as:

$$\mu_a \frac{\partial H}{\partial t} = -\nabla \times \left(\frac{1}{\sigma} \nabla \times H - \mu_a v \times H \right) \tag{4}$$

or transformed in integral form

$$\mu_a \frac{d}{dt} \int_V H dV - \mu_a \oint_S v H ds = \oint_S \frac{1}{\sigma} ds \times (\nabla \times H) \tag{5}$$

Where V is the volume restricted by the surface s; $ds = ndS$; n is external normal to S; $d/dt = \partial/\partial t + v \cdot \nabla$.
Dynamic elastic-plastic deformation of solids can be defined by the following equations:

$$\rho \frac{d}{dt} \int_V v dV = \int_S \sigma \cdot ds + \int_V f dV \tag{6}$$

where

$$f = j \times B = -\mu_a H \times j = -\mu_a H \times (\nabla \times H) \tag{7}$$

$\sigma = pI + S$ is the stress tensor; ρ is the density; p is the pressure; S is the deviator part of the stress tensor,

$$p = K\left(\frac{V}{V_0} - 1\right), \; S = GB_D \tag{8}$$

V and V_0 are actual and original volumes respectively; B_D is the deviator part of the left Cauchy-Green tensor B; $B = F \cdot F^T$; $F = dx/dX$ is the deformation gradient tensor; x is the vector of actual location; X is the vector of original location; K and G are bulk and shear modulus respectively.
The Von Mises yield criterion is used to describe the elastic limit:

$$-J_2(S) \le \frac{\sigma_y^2}{3} \tag{9}$$

where σ_y is the current plastic flow stress (depends upon strain and strain rate).
The energy conservation law is employed in the following form:

$$\frac{d}{dt} \int_V c_V T dV = \int_V P dV \tag{10}$$

where T is the temperature; $P = j^2/\sigma$ is the power generated in the form of heat while the electric current is running through the coil and blank because of the active resistance of their materials.

The system of equations (5)-(10) represents the full formulation of the problem. This system is solved numerically using the finite volume method. Initially, the nonorthogonal Lagrangian mesh is introduced; a fragment of the 2D mesh (for simplicity) is shown in Figure 1(a). The computational domain is divided into cells. Each cell consists of two triangles in 2D case called elements (or six tetrahedrons in 3D case) as illustrated in Figure 1(b) and (c) respectively.

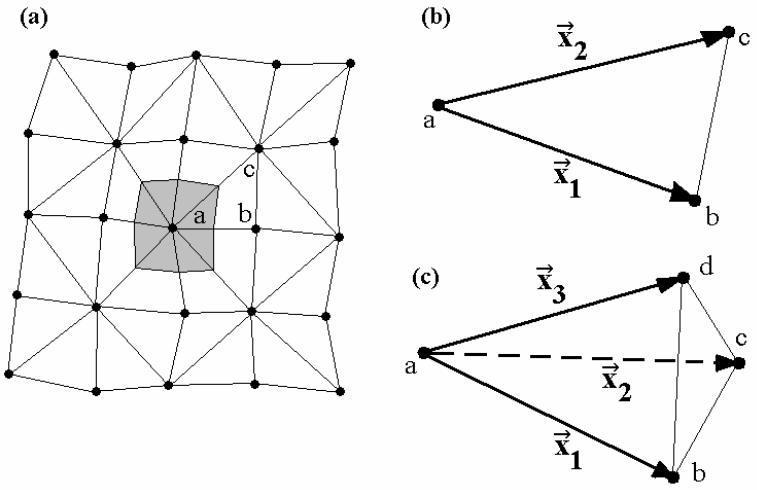

Figure 1: *(a) Fragment of 2D Lagrangian mesh (• are the nodes); (b) 2D element; (c) 3D element*

A control volume V (grey in Figure 1(a)) is corresponded to every node of the mesh. The explicit approximation is used for the calculation of new values of velocity in every node. Equations (5), (6) and (10) are solved using the technique described in [4].

For the solution of the elastic-plastic part of the problem (6)-(9) the new return-map algorithm was applied. Taking into account the equations (8), we can transform the condition (9) in the form

$$-J_2(B_D) \le \frac{\sigma_y^2}{3G^2} \equiv k^2 \tag{11}$$

where k^2 is a material characteristic. The condition (11) determines the restrictions on the deformation field. We will illustrate all the specifics of the new return-map algorithm considering only one tetrahedral element of the mesh *abcd* (Figure 1(c)). We denote the initial position of the tetrahedron vertices at the initial time by position-vectors X_a, X_b, X_c and X_d. Due to the deformation process, the vertices shift from their initial positions. We denote the actual position of the vertices of the tetrahedral element at time t by x_a, x_b, x_c and x_d. Let x_i and X_i (i = 1,2,3) be the right-hand set of vectors directed along any three different ribs of the tetrahedron (Figure 1(c)). Let us introduce the linear transformation of the element from its initial to its actual position (see more details in [4]):

$$x = A \cdot X + b \tag{12}$$

Using the transformation (12) we can find the deformation gradient tensor F in the element

$$F = \frac{dx}{dX} = \frac{\partial(A_{ik}X_k + b_i)}{\partial X_m} e_i e_m = A_{ik}\delta_{km} e_i e_m = A \tag{13}$$

We define A from the following system

$$\begin{aligned} x_1 &= A \cdot X_1 \\ x_2 &= A \cdot X_2 \\ x_3 &= A \cdot X_3 \end{aligned} \tag{14}$$

Then we obtain

$$A = x_i e_i \cdot (X_m e_i) \tag{15}$$

Finally, combining (13) and (15) we can define the finite difference approximation of B for the element:

$$B = R^T \cdot G \cdot R \tag{16}$$

where $G = e_k\, X^k \cdot X^m\, e_m$; $R = e_k\, x_k$; x^i and X^i are the sets of vectors reciprocal with x_i and X_i respectively (see for example [4]).

It is important to stress that all information about the initial configuration of the element is concentrated in tensor G and its initial volume V_0. We can assert that G and V_0 play the role of the memory of the element and keep the information about its initial configuration. Among two G and V_0, the condition (11) contains G only. We named it the tensor of initial configuration. If the deformation of the element exceeds the critical value, then condition (11) is not satisfied any more and the internal structure of the solid body is irreversibly changed. In other words, the initial configuration of the element and, consequently, the tensor G should be changed in such a way that the equation

$$-J_2(B_D) = k^2 \tag{17}$$

is satisfied.

We proceed step by step in time. At the initial time step in addition to all other values, we have to calculate G for every element of the mesh. Assuming that we had already found the new positions of the element vertices and then calculated the set of vectors $x_s{}^{n+1}$ at n + 1 time step, we carry out the predictor step and put

$$B' = \left(R^T\right)^{n+1} \cdot G^n \cdot R^{n+1} \tag{18}$$

If the condition

$$-J_2(B'_D) \le k^2 \tag{19}$$

is satisfied, then the tensor G^n does not change (i.e. $G^{n+1} = G^n$). Suppose that condition (19) does not hold. Then we should find the new tensor G^{n+1} for the element which satisfies the following equation for $B^{n+1} = (R^T)^{n+1} \cdot G^{n+1} R^{n+1}$:

$$-J_2\left(B_D^{n+1}\right) = k^2 \tag{20}$$

The value of G^{n+1} satisfying this condition may be defined in the form

$$G^{n+1} = aG^n + (1-a) \cdot G'^{n+1} \tag{21}$$

where $G' = e_k\, x^k \cdot x^m\, e_m$ and

$$a = \frac{k}{\sqrt{-J_2(B'_D)}} \tag{22}$$

Now equation (20) is satisfied exactly.

The “difference” (difference - not in a sense of withholding, but in a sense of shape difference) between G^{n+1} and G' is a critical elastic deformation of the element permissible by

the condition (19). The difference between G^{n+1} and G^{n} configurations is the plastic (irreversible) deformation.

3 Numerical examples

The described algorithm was employed for simulation of pulsed electromagnetic forming of aluminium sheet into a conical die cavity. The five-turn flat electromagnetic coil was used as a tool generating the electromagnetic pressure, as shown in Figure 3. The distribution of the electromagnetic field was defined in a 2D formulation assuming that the coil is axisymmetrical and includes five circular turns.

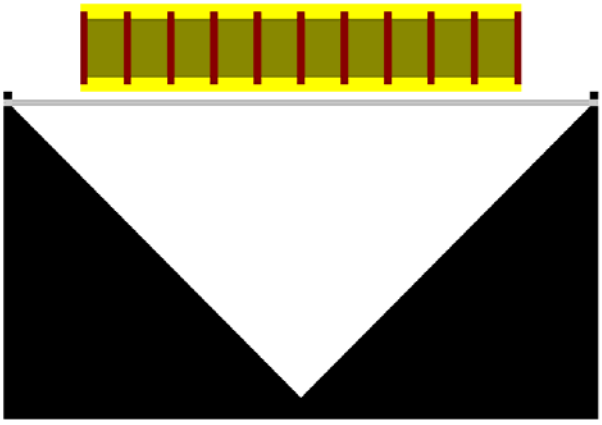

Figure 3: *Assumed 2D schematic of the process*

The electromagnetic forming machine serving as a generator of pulsed currents can be represented as a R-L-C circuit, as it is indicated in Figure 4. The electric current running into a coil-blank system as a boundary condition can be defined using an explicit integration procedure.

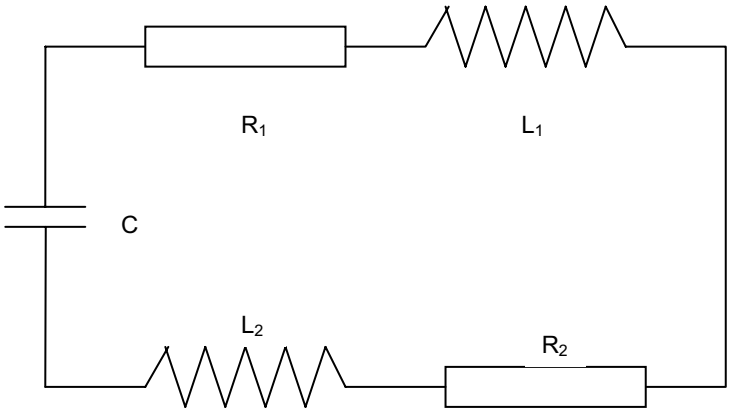

Figure 4: *R-L-C contour: R_1, L_1 and C are the characteristics of the electromagnetic forming machine; R_2 and L_2 are the characteristics of the coil*

The full electric current in this circuit can be defined from the following system:

$$\frac{d(LI)}{dt} + RI = U \tag{23}$$

$$C\frac{dU}{dt} = -I \tag{24}$$

where $L = L_1 + L_2$ and $R = R_1 + R_2$.
At every time step we solved equations (23) and (24) and, based upon the defined value of the current I, calculated the density of the electric current in the coil $j = I/S$, where S is the square of the cross-section of the coil.

Characteristics of the electromagnetic forming machine, serving as an external circuit to the coil-blank system, were the following: $R_1 = 0.01…0.001\ \Omega$; $L_1 = 10^{-9}$ H; $C = 2\cdot10^{-4}$ F; The charging voltage of the capacitor bank was $U_0 = 5$ kV. The values of R_2 and L_2 were defined at every time integration step.

The contact interaction between the blank and the die was modeled employing the mild contact algorithm. The whole problem was solved numerically using a Lagrangian mesh which was periodically re-meshed in the areas between the coil and the blank and between the blank and the die. The results of the simulation of a 1 mm aluminum sheet formation into a conical die cavity is shown in Figures 5 and 6. It can be indicated that the central part of the sheet is delayed relatively to the area adjacent to it. The transverse wave of plastic deformation propagates in radial direction from the periphery of the blank towards its center, as it was previously observed in experimental studies [6].

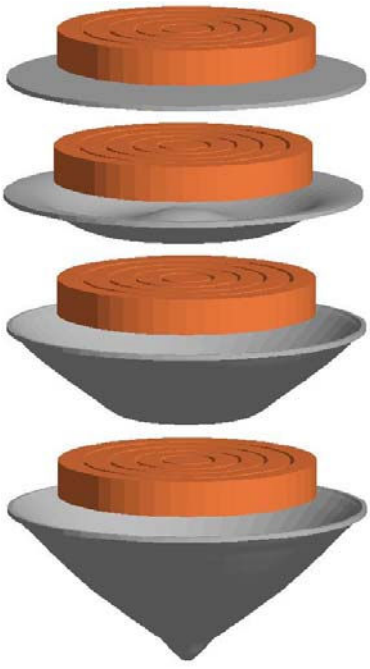

Figure 5: *Dynamics of forming of an aluminium sheet into a conical die*

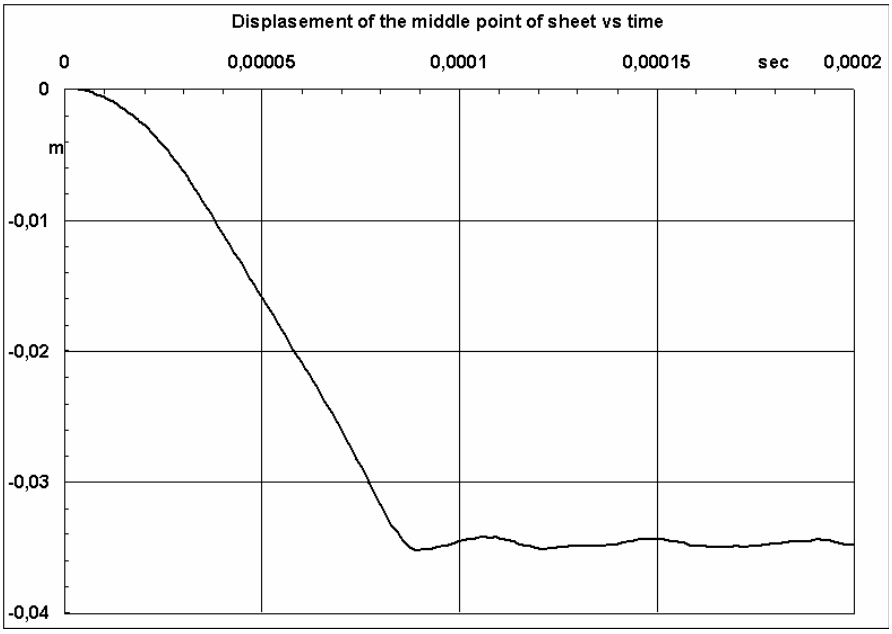

Figure 6: *Displacement of the middle point of the sheet vs time*

The distribution of the electromagnetic field intensity in transverse pulsed forming of sheets by direct propagation of the electric current through the metal bar, serving as a coil, and in opposite direction through the deformed aluminium sheet is shown in Figure 7. This test shows the important benefit of providing an almost uniform distribution of electromagnetic pulsed pressure on the sample. The corresponding formation of the 100 mm long and 1 mm thick aluminium strip is illustrated in Figure 8.

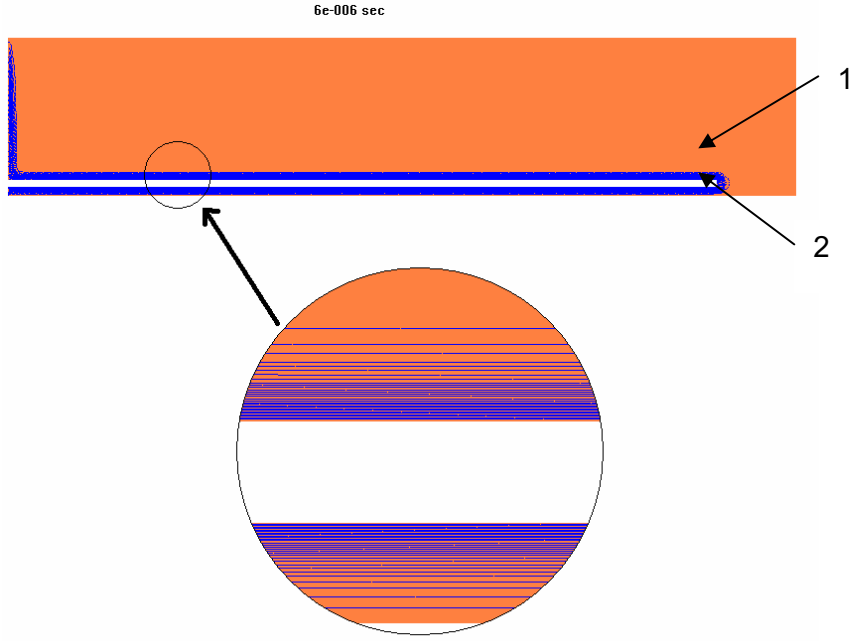

Figure 7: *Distribution of the electromagnetic field intensity for the 2D plane strain sheet formation by direct propagation of the electric current through the metal bar 1, serving as a coil, and through the deformed aluminium sheet 2*

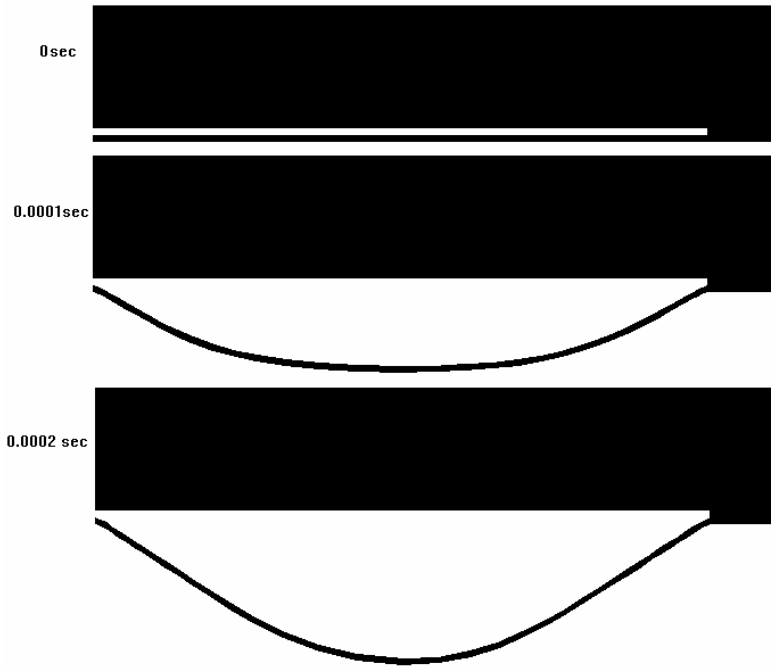

Figure 8: *Deformation process for the strip subjected to pulsed electromagnetic load by direct current propagation*

4 Conclusions

A fully coupled numerical procedure incorporating an electromagnetic field propagation, a dynamic elastic-plastic deformation, and a heat transfer has been developed based on the Finite Volume Method of integration. Provided examples validate the developed model for plane strain and axisymmetrical deformation.

References

[1] *Golovashchenko, S.; Bessonov, N.:* Numerical Simulation of High-Rate Stamping of Tubes and Sheets, CRM Proceedings and Lecture Notes. American Mathematical Society, Volume 21, 1999, p.199-207.

[2] *Beliy, I.; Fertik, S.; Chimenko, L.:* Reference book on magnetic-pulsed stamping, Charkov, USSR, 1976, 167p.

[3] *Golovashchenko, S.; Shutov, R.:* Numerical modeling of dynamics of deformation of multi-turn cylindrical coil for electromagnetic forming. Proceedings of High Educational Institutions. Ser. Mechanical Engineering, N 10, 1994, p.123-128 (in Russian).

[4] *Bessonov, N.; Song, D.:* Application of vector calculus to numerical simulation of continuum mechanics problems. Journal of Computational Physics. 167/1,1999, p.22-38.

[5] *Bessonov, N.; Golovashchenko S.:* New algorithm of simulation of elastic-plastic deformation based on updated initial configuration of solid body (In print).

[6] *Legchilin, A.:* Study of the stamping process using pulsed electromagnetic field. PhD Dissertation, Bauman Moscow High Technical School, Russia, 1969, 282p.

Development of Multi Field Software Solutions and their Application for the Optimization of Electromagnetic High Speed Forming processes*

M. Stiemer[1], B. Svendsen[2], J. Unger[2], F. T. Suttmeier[1], H. Blum[1]

[1]Chair of Scientific Computing, University of Dortmund
[2]Chair of Mechanics, University of Dortmund

Abstract

The simulation of complex processes in engineering solids involving coupled mechanical and non-mechanical fields represents a challenge to physicists, mathematicians, and engineers. Both, the formulation of such models and their numerical implementation involve a great number of difficulties. Electromagnetic forming is one example of such a process, whose modelling and simulation requires a coupled electromagnetic-thermomechanical model. The purpose of this contribution is to discuss some key issues associated with the modelling and simulation of electromagnetic metal forming (EF) and the corresponding development of a finite-element-based simulation tool for EF. In particular, the modelling is based on a thermodynamically-consistent electromagnetic-thermoelastoviscoplastic material and field model in which the energy and momentum balance are coupled to the quasi-static form of Maxwell's equations via the electromotive intensity and Lorentz force, respectively. On the algorithmic side, questions like the choice of meshes, the element formulation, the numerical treatment of nonlinearities, possible model simplifications, different discretisation strategies, realisation of the non-linear coupling etc. are discussed for the presented software solution. Such issues are investigated with the help of benchmark simulations that have been developed for this purpose. Finally, as an example of an application of the developed software tool, a computer–aided–manufacturing (CAM) problem is considered. Here, the size of the tool coil and the peak value of the current in the tool coil circuit are optimised in order to achieve the prescribed work-piece form within the given tolerance.

Keywords:

Modelling, Viscoplasticity, Electromagnetic metal forming

*This work is based on the results of the research group FOR 443. The authors wish to thank the Deutsche Forschungsgemeinschaft – DFG for its financial support.

1 Introduction

Electromagnetic metal forming (EF) is a high-speed forming process achieving strain rates of $\varphi_v \geq 10^3$ 1/s. In this method, a strong pulsed magnetic field is generated in the tool coil adjacent to an electrically-conducting work-piece to be formed. The interaction of the induced eddy currents in the work-piece with the magnetic field generates a Lorentz (body) force in the work-piece resulting in its deformation. The entire resulting highly dynamical forming process lasts on the order of 100-300 μs. EF represents an effective forming method for metals with good electrical conductivity like aluminum or copper. Compared to other forming methods, it offers advantages such as an increase in formability for certain kinds of materials, reduction in wrinkling, the ability to combine forming and assembly operations, reduced tool-making costs, *etc.*. Nevertheless, EF, is not yet sufficiently well understood to be routinely used as industrial forming process. In particular, further investigation of the strong dependence of the forming process on the details of the interaction between the transient magnetic field and evolving shape of the work-piece is needed, representing one purpose of the current work.

Beyond physically-reasonable models, such investigations require the availability and use of a reliable simulation tool for coupled multifield problems. The introduction of high-speed computers in the late 80's enabled the first numerical simulation of EF including the deformation of the work-piece. In contrast to Goudin [1, 2], the interaction between the magnetic field and the shape of the work-piece is considered in Takata [3]. In his approach, the influence of the change of shape of the work-piece during the electromagnetic forming process on the magnetic field, and the force it exerts on the work-piece are therefore modelled correctly. Fenton and Daehn [4] used the computer-code CALE [5] to simulate electromagnetic forming with complete magnetomechanical coupling numerically. Further, Beerwald *et al.* [6, 7] have used the commercial program MARC [8] to simulate electromagnetic forming processes. Recently, electromagnetic sheet metal forming has been investigated by Badelt *et al.* [9] and Beerwald *et al.* [10], respectively. In Beerwald *et al.* [10], both, a time harmonic simulation of the electromagnetic field using the finite-element programme FEMM [11] and a transient simulation using the finite-element programme EMAS [12] were combined with the simulation of the sheet metal deformation using the finte-element programme MARC [8]. Although viable, the black-box nature of these programmes as well as the required interfacing of these "by hand" to carry out the complete simulation is not terribly efficient nor sufficiently flexible to be able to incorporate new models and numerical methods needed to improve the realism, efficiency, and robustness of the numerical simulation. To this end, as well as in order to combine all aspects of the modelling and simulation of EF into one integrated, unified software environment, the finite element code SOFAR (**S**mall **O**bject orientated **F**inite-element-library for **A**pplication and **R**esearch) (SOFAR: [13]) has been applied and developed by a research group (FOR 443) in Dortmund, funded by the German Research Foundation (DFG). The underlying thermodynamically-consistent electromagnetic thermoinelastic multifield model has been developed in [14, 15]. The corresponding algorithmic formulation and efficient numerical implementation has been carried out and discussed in [16]. In work in progress, a number of benchmark simulations, such as those reported on in [17], are being systematically carried out in order to test the efficiency and numerical robustness of the new SOFAR-based simulation tools.

The purpose of the current work is to outline and discuss various issues involved in the

development and use of SOFAR as a tool for the simulation of EF. From the modelling point of view, SOFAR is used in particular for model identification and validation in the context of comparison with experimental results [9, 10]. On the algorithmic side, several different approaches have been tested and validated (see section 3). Moreover, the applicability of SOFAR to the simulation of optimisation and design problems is currently being investigated. As an example of this, the peak value of the current in the tool coil circuit is optimised in such a way that electromagnetically-formed sheet metal achieves a prescribed form within a given tolerance. The corresponding optimisation is based on a numerical method from [18] which converges for a wide class of objective functions. Moreover, no derivatives have to be computed. Such possibilities represent first steps in the development of computer-aided-manufacturing (CAM) methods based on SOFAR.

2 Coupled Model for Conducting, Thermoelastoviscoplastic Metals

The multifield material model used in the current work is derived from a general continuum thermodynamic approach [15] to the formulation of models for electromagnetic thermoinelastic solids. In particular, this model applies to the case in which a strong magnetic field induces electric currents in thermoelastoviscoplastic electric conductors and so a Lorentz force resulting in their deformation. This is the basic idea underlying the method of electromagnetic metal forming. Now, for all structural problems of interest, the frequencies of relevance (*i.e.*, less than 10 MHz) correspond to electromagnetic wavelengths which are much larger than the structures of interest. As such, the wave character of the electromagnetic fields is insignificant and can be neglected for such structural problems. This represents the so-called quasistatic approximation [19, §2.2 and §8.2]. In this case, it is shown in [15] that Maxwell's relations together with Ohm's law and the Coulomb gauge condition (*e.g.*, [20], §6.5) result in the weak forms*

$$\begin{aligned} \int_R \overset{*}{\boldsymbol{a}} \cdot \boldsymbol{a}_* + (\chi - \boldsymbol{a} \cdot \boldsymbol{v})\ \mathrm{div}\, \boldsymbol{a}_* + \kappa_{\mathrm{EM}}\ \mathrm{curl}\, \boldsymbol{a} \cdot \mathrm{curl}\, \boldsymbol{a}_* &= 0\ , \\ \int_R \chi\ \mathrm{div}(\nabla \chi_*) &= 0\ , \end{aligned} \tag{1}$$

for the usual vector $\boldsymbol{a}$ and the scalar χ potentials with respect to a spatial region R containing the work-piece and tool coil for the special case that $\boldsymbol{a}$ and χ are specified everywhere on ∂R. Here, $\boldsymbol{a}_*$ and χ_* represent test fields vanishing on those parts of the boundary ∂R of R where $\boldsymbol{a}$ and χ are specified.

Moreover, $\kappa_{\mathrm{EM}} := \sigma_{\mathrm{EM}}^{-1} \mu_{\mathrm{EM}}^{-1}$ represents the magnetic diffusivity, σ_{EM} the electrical conductivity, and μ_{EM} the magnetic permeability. In addition, $\boldsymbol{v}$ represents the spatial velocity of the work-piece or tool coil, $\dot{f} := \partial f + \nabla f \cdot \boldsymbol{v}$ the material time derivative, $\boldsymbol{D} := \mathrm{sym}(\boldsymbol{L})$ the deformation rate, and $\boldsymbol{L} := \nabla \boldsymbol{v}$ the velocity gradient. Further, $\overset{*}{\boldsymbol{a}} := \dot{\boldsymbol{a}} + \boldsymbol{L}^{\mathsf{T}} \boldsymbol{a} = \partial \boldsymbol{a} + (\nabla \boldsymbol{a}) \boldsymbol{v} + \boldsymbol{L}^{\mathsf{T}} \boldsymbol{a}$ represents the objective time-derivative of $\boldsymbol{a}$. On the timescale $\tau_{\mathrm{Exp}} \sim 10^{-4}$ s relevant to processes such as electromagnetic metal forming, the typical order of magnitude $\kappa_{\mathrm{EM}} \sim 10^{-1}$ m^2 s^{-1} for the magnetic diffusivity of metals implies that "significant" magnetic diffusion takes

*The volume dv and surface da elements are dispensed with in the corresponding integrands in this work for notational simplicity.

place over lengthscales of $\sqrt{\kappa_{\mathrm{EM}}\,\tau_{\mathrm{Exp}}} \sim 10$ cm. Since this is significantly larger than the smallest dimension of the engineering structures of interest (*e.g.*, sheet metal thickness ~ 1 mm), magnetic diffusion will be important in the applications to be discussed below.

Restricting attention to the case of axisymmetry, note that the above field equation for the vector potential $\boldsymbol{a}$ reduces to a scalar equation for the azimutal component a_φ of $\boldsymbol{a}$ and a Laplace equation $\Delta\chi = 0$ for the scalar potential χ. Indeed, since the flux density is constant in azimuthal direction, the vector potential is always perpendicular to the rz–plane, where r denotes the radial component and z the axial. In particular, this implies that the Coulomb gauge condition $\operatorname{div}\boldsymbol{a} = 0$ is always fulfilled, and thus the equations for $\boldsymbol{a}$ and χ decouple. In this case, standard nodal finite elements can be utilised. For three-dimensional problems, however, special elements are required which can deal with jump discontinuities in the vector potential field $\boldsymbol{a}$ (*e.g.*, [27, 28, 29]).

As discussed in [15], to a good first approximation, adiabatic conditions pertain during electromagnetic forming. In this case, the energy balance reduces to the evolution relation

$$\dot{\theta} = \varrho^{-1} c^{-1} (\omega + \sigma_{\mathrm{EM}} \boldsymbol{\epsilon} \cdot \boldsymbol{\epsilon}) \tag{2}$$

for the temperature, where ϱ represents the mass density, c the specific heat, ω the mechanical rate of heating, and $\boldsymbol{\epsilon}$ the electromotive intensity. In the adiabatic approximation, then, the temperature becomes homogeneous and can be treated formally as an internal variable (see below). As such, the deformation $\boldsymbol{\xi}$ is the only thermomechanical field. The weak balance relation for momentum is given by

$$\int_{B_{\mathrm{r}}} \{\varrho_r \ddot{\boldsymbol{\xi}} - \det(\boldsymbol{F})\, \sigma_{\mathrm{EM}}\, \boldsymbol{\epsilon} \times \operatorname{curl} \boldsymbol{a}\} \cdot \boldsymbol{\xi}_* + \boldsymbol{K} \cdot \nabla \boldsymbol{\xi}_* = \int_{\partial B_{\mathrm{c}}} \boldsymbol{t}_c \cdot \boldsymbol{\xi}_* \tag{3}$$

with respect to the reference $B_{\mathrm{r}} \subset R$ configuration of the work-piece or tool coil for all corresponding test fields $\boldsymbol{\xi}_*$ vanishing on those parts of the boundary ∂B_{c} of the current configuration $\partial B_{\mathrm{c}} \subset R$ where $\boldsymbol{\xi}$ is specified. Here, ϱ_r represents the referential mass density, $\boldsymbol{F} := \nabla\boldsymbol{\xi}$ the deformation gradient, $\boldsymbol{K}$ the Kirchhoff stress, and $\boldsymbol{t}_c$ the current traction vector. Note that the second term in (3) represents the Lorentz force.

Lastly, the model relations are completed by the material model. Perhaps the simplest model relevant to the case of electromagnetic forming in this regard is thermoelastoviscoplasticity with isotropic hardening. The relevant internal variables are then the elastic left Cauchy-Green deformation $\boldsymbol{B}_{\mathrm{E}}$ and the accumulated inelastic strain ϵ_{P}. On this basis, the thermodynamic formulation being pursued here ([15]) is based on specific model relations for the referential free energy density ψ as well as on the evolution relations for the internal variables. In particular, assuming for simplicity that the elastic behaviour is not affected by inelastic processes such as damage (*e.g.*, [24]), the split*

$$\psi(\theta, \boldsymbol{B}_{\mathrm{E}}, \epsilon_{\mathrm{P}}) = \psi_{\mathrm{E}}(\theta, \boldsymbol{B}_{\mathrm{E}}) + \psi_{\mathrm{P}}(\theta, \epsilon_{\mathrm{P}}) \tag{4}$$

of the free energy into thermoelastic and inelastic parts is justified. Assuming further for simplicity that the specific heat capacity c is constant, (*e.g.*, [22]), the form

$$\psi_{\mathrm{P}}(\theta, \epsilon_{\mathrm{P}}) = \varepsilon_{\mathrm{P}}(\epsilon_{\mathrm{P}}) - \theta\, \eta_{\mathrm{P}}(\epsilon_{\mathrm{P}}) \tag{5}$$

*In the current activation/transition-state context, the temperature dependence of the dynamic flow stress is contained in the inelastic potential; see (9) below.

for the inelastic part ψ_{P} of ψ is obtained. Here, ε_{P} represents the stored energy and η_{P} the entropy of cold work (see also [21]). In addition, the thermoelastic neo-Hooke form

$$\begin{aligned}\psi_{\mathsf{E}}(\theta, \boldsymbol{B}_{\mathsf{E}}) &= \tfrac{1}{8}\,\lambda_r\,(\ln J_{\boldsymbol{B}_{\mathsf{E}}})^2 - \tfrac{1}{2}\,(3\lambda_r + 2\mu_r)\,\alpha_r(\theta-\theta_r)\,\ln J_{\boldsymbol{B}_{\mathsf{E}}} + \tfrac{1}{2}\,\mu_r(I_{\boldsymbol{B}_{\mathsf{E}}} - 3 - \ln J_{\boldsymbol{B}_{\mathsf{E}}}) \\ &+ \varrho_r c_r\,[\theta - \theta_r - \theta\ln(\theta/\theta_r)]\end{aligned} \tag{6}$$

for the referential free energy density pertains, where λ_r and μ_r represent Lamé's constants, and θ_r a reference temperature. As for the inelastic part ψ_{P}, this is determined empirically with the help of experimental data, as discussed in the next section (see also [22]). Consider next the evolution of the internal variables and the inelastic behaviour. In the metallic polycrystalline materials of interest at low-to-moderate homologous temperature, inelastic deformation processes are controlled predominantly by the activation of dislocation glide on glide systems (*e.g.*, [23]), even at higher strain-rates. As such, higher homologous temperatures are required for other mechanisms such as dislocation climb or even dynamic recrystallisation to activate. Resistance to dislocation glide arises due to extended obstacles generating longer-range stress fields related in the phenomenological context to hardening behaviour. In addition, such resistance is caused by short-range local obstacles which can be overcome by thermal fluctuation under the action of the local effective stress, represented in the current phenomenological context by $|\mathrm{dev}(\boldsymbol{K})| + \varsigma_{\mathsf{P}}$, where

$$-\varsigma_{\mathsf{P}} := \psi_{,\,\epsilon_{\mathsf{P}}} = -\theta\,\varrho_r\eta_{\mathsf{P},\,\epsilon_{\mathsf{P}}} \tag{7}$$

represents the static contribution to the flow stress (in shear). On this basis,

$$f_{\mathsf{P}}(\theta, \epsilon_{\mathsf{P}}, \boldsymbol{D}, \boldsymbol{K}, \varsigma_{\mathsf{P}}) := \frac{|\mathrm{dev}(\boldsymbol{K})| + \varsigma_{\mathsf{P}}}{\sigma_{\mathsf{P}}(\theta, \epsilon_{\mathsf{P}}, \boldsymbol{D})} \tag{8}$$

represents an activation function or non-dimensional overstress in the current rate-dependent context. Here, σ_{P} represents the dynamic drag contribution to the effective flow stress in the system. On this basis, a power-law approximation of the more exact transition-state-based micromechanical relations for the kinetics of dislocation glide (*e.g.*, [23]) leads to the power-law form

$$\phi(\theta, \epsilon_{\mathsf{P}}, \boldsymbol{D}, \boldsymbol{K}, \varsigma_{\mathsf{P}}) = \frac{\gamma_{\mathsf{P}}(\theta, \epsilon_{\mathsf{P}}, \boldsymbol{D})\,\sigma_{\mathsf{P}}(\theta, \epsilon_{\mathsf{P}}, \boldsymbol{D})}{m_{\mathsf{P}}(\theta, \epsilon_{\mathsf{P}}, \boldsymbol{D}) + 1}\,\langle f_{\mathsf{P}}(\theta, \epsilon_{\mathsf{P}}, \boldsymbol{D}, \boldsymbol{K}, \varsigma_{\mathsf{P}})\rangle^{m_{\mathsf{P}}(\theta, \epsilon_{\mathsf{P}}, \boldsymbol{D})+1} \tag{9}$$

upon which the evolution of the internal variables is based. Here, γ_{P} represents a characteristic strain-rate, $\langle x\rangle := \frac{1}{2}\,(x + |x|)$ the MaCauley bracket, and m_{P} the strain-rate exponent. Since $|x|$ is a convex function of x, note that $\langle x\rangle$ is as well. In contrast to the general form, (9) has been assumed explicitly independent of $\boldsymbol{B}_{\mathsf{E}}$ in this simple case. More generally, *e.g.*for the case of deformation-induced anisotropic flow behaviour, this is no longer so (*e.g.*[24, 25, 26]). From (9), we have the specific forms

$$\begin{aligned}\overset{*}{\boldsymbol{B}}_{\mathsf{E}} &= -2\,\mathrm{sym}(\phi_{,\,\boldsymbol{K}}\,\boldsymbol{B}_{\mathsf{E}}) &&= -2\,\mathrm{sgn}(\mathrm{dev}(\boldsymbol{K}))\,\boldsymbol{B}_{\mathsf{E}}\,\varpi_{\mathsf{P}} \quad (\boldsymbol{K} \neq \boldsymbol{0})\,, \\ \dot{\epsilon}_{\mathsf{P}} &= \phi_{,\,\varsigma_{\mathsf{P}}} &&= \gamma_{\mathsf{P}}\,\langle f_{\mathsf{P}}\rangle^{m_{\mathsf{P}}} \quad (f_{\mathsf{P}} > 0)\,,\end{aligned} \tag{10}$$

for the evolution of the internal variables. In the current adiabatic context, the temperature θ is also treated formally as such a variable with evolution relation (2). Now, for the case of incompressible material behaviour, we assume that the isotropic forms of the viscoplastic

parameters γ_{P}, σ_{P} and m_{P} are independent of the trace $\boldsymbol{I} \cdot \boldsymbol{D}$ of the rate of deformation. In this case, the thermoelastic form

$$\boldsymbol{K} = 2\,\psi_{,\boldsymbol{B}_{\mathsf{E}}}\boldsymbol{B}_{\mathsf{E}} \tag{11}$$

for the Kirchhoff stress holds. In addition,

$$\omega_r = \gamma_{\mathsf{P}}\,(\sigma_{\mathsf{P}} f_{\mathsf{P}} - \theta\,\varrho_r \eta_{\mathsf{P},\,\epsilon_{\mathsf{P}}})\langle f_{\mathsf{P}}\rangle^{m_{\mathsf{P}}} - (3\lambda_r + 2\mu_r)\,\alpha_r\,\theta\,\dot{\overline{\ln\det(\boldsymbol{F})}} \tag{12}$$

then follows for the referential form of the mechanical heating rate. As indicated, ϕ is differentiable in ς_{P} everywhere except at $f_{\mathsf{P}} = 0$, and in $\boldsymbol{K}$ everywhere except at $f_{\mathsf{P}} = 0$ and at $\boldsymbol{K} = \boldsymbol{0}$. The corresponding subdifferentials exist everywhere. In the context of these forms for the evolution of the internal variables, the constraint $\gamma_{\mathsf{P}}(\theta, \epsilon_{\mathsf{P}}, \boldsymbol{0}) = 0$ on the constitutive form of γ_{P} follows in thermodynamic equilibrium.

This completes the basic model formulation. Its reduction to the case of small elastic strain, algorithmic formulation and numerical implementation in SOFAR have been carried out in [16]. Aspects of this are discussed in the next section.

3 Algorithmic Implementation of the Coupled Simulations in SOFAR

The idea behind the software environment SOFAR is to reduce the development time for finite-element-based algorithms and simulation by object orientation. Hence, the interface to the developer is implemented in JAVA. On the other hand, time critical jobs like basic linear algebra (BLAS-) operations are implemented in fast native C and FORTRAN code, respectively, that can be called from JAVA routines. The programing concept of SOFAR allows easy handeling of unstructured meshes. Such meshes are typical for adaptive refinement and remeshing strategies. In particular, SOFAR administrates geometric singularities as hanging nodes. The assembly of the corresponding stiffness matrices is done automatically. Moreover, SOFAR allows access to any geometric substructure of a particular element. This means edges or faces can be addressed at any time. The latter makes it easy to implement edge elements for instance which avoid the typical problems nodal elements exhibit in 3D electromagnetic field computation [27, 28]. Moreover, effective algorithms like multigrid solver or error estimators are available. SOFAR can easily be extended by external routines (written in C or FORTRAN) due to a user interface. This user interface was applied for the implementation of the above described coupled model. Its availability in SOFAR enables the implementation and use of various custom-tailored element formulations based on modern numerical methods.

Due to the vastly different timescales associated with changes in the electromagnetic and thermomechanical fields, the corresponding field relations are solved on separate finite-element meshes via a staggered solution algorithm. In particular, the electromagnetic field relations are solved on a fixed Eulerian mesh discretising the region of space containing the work-piece and tool coil. On the other hand, the momentum and energy balances for the work-piece are solved on a Lagrangian mesh using an implicit element formulation for the thermomechanical model discussed in the last section which is embedded into SOFAR via a user-element interface. Information concerning the evolving Lorentz force, electromotive power, and changing work-piece geometry are mapped back and forth between the two meshes during the solution procedure with the help of transfer operators. SOFAR provides an object oriented concept for

the necessary bookkeeping of element data and provides the input data to the user element. Moreover, the assembly of the stiffness matrix for the Newton iteration on structural level is performed by SOFAR. Use of this staggered scheme increases the stability of the simulation and reduces numerical efforts, as global remeshing is not necessary. However, adaptive local refinement in any time step seems reasonable to attain a maximal precision by a given numerical effort. In particular, the boundaries between different eddy current regions should be finely resolved, since $|\nabla \boldsymbol{a}|$ takes on large values there. A disadvantage of the fixed mesh for the electromagnetic fields is the necessity to consider the convective term $v \times \operatorname{curl} \boldsymbol{a}$ explicitly in the weak form of the field equations, where v denotes the velocity field of the structure. In case of a moving mesh, this term can be implicitely considered by replacing the time derivative of $\boldsymbol{a}$ by its complete differential [29]. But this drawback is compensated by the aforementioned advantages, particularly since the corresponding Péclet-number is small such that the influence of the convective term does not affect the stability of the method.

The time integration of the electromagnetic field relations was carried out using the generalized trapezoidal rule, and that of the momentum balance using Newmark's method. Using these methods, choice of the optimal parameter values provided an accuracy of $O(\Delta t^2)$, where Δt denotes the size of the time step. At the beginning of, as well as at several instances during the numerical solution, the parameter values of the trapezoidal rule are modified in order to avoid unphysical oscillations of the time derivative of the vector potential $\boldsymbol{a}$. In particular, such oscillations occur at the beginning of the simulation due to the switching on of the input current.

Consider next the staggered solution scheme. At the start, the magnetic field distribution is calculated with respect to the position and velocity of the structure in the nth time step. Then, the new position of the structure is determined such that a balance between inner and outer forces arises. Benchmark simulations have shown that this algorithm can be improved by adding an additional iteration loop. To ensure that the computed momentum balance of the structure in the $(n+1)$st time step represents a balance between the Lorentz forces in the $(n+1)$st time step and the inner forces of the structure at this instant, the following scheme is applied. Let all values having index n be variables of the nth time step. Then, the update for the $(n+1)$st time step takes the following form:

1. A predictor value $\boldsymbol{a}_1^{(n+1)}$ for the vector potential and for its time derivative in the $(n+1)$st step is computed according to the measured amperage in the tool coil at time $t^{(n+1)}$ and the kinematic state of the work-piece that it attained when the momentum balance was reached in the nth time step. For this, the assembly routine of the magnetic mesh checks wether a certain point lies in the work-piece or not. The values for conductivity and for the velocity of the structur (for the convective term $v \times \operatorname{curl} \boldsymbol{a}$) are chosen respectively.

2. The stiffness matrix and load vector in the work-piece mesh are assembled. For this, the nodal values for the current Lorentz force density

$$f_{\mathrm{L1}}^{(n+1)} = \boldsymbol{j}_1^{(n+1)} \times \boldsymbol{b}_1^{(n+1)} = \sigma_{\mathrm{EM}} \partial \boldsymbol{a}_1^{(n+1)} \times \operatorname{curl} \boldsymbol{a}_1^{(n+1)}$$

   are computed.

3. The assembled equation in the work-piece mesh is solved. The computed deformations are added to the vertex positions of the work-piece mesh. It is checked whether the

residual force associated with the resulting state of deformation is zero in the scope of the desired accuracy. If the latter is false another step of the Newton-Raphson iteration has to be performed with the altered position of the work-piece. Otherwise, the vector potential $\boldsymbol{a}_2^{(n+1)}$ is computed according to the new kinematic state of the structure. If it does not deviate from $\boldsymbol{a}_1^{(n+1)}$ within the scope of accuracy the next time step is started. Otherwise, the equilibrium position of the structure with respect to outer forces resulting from $\boldsymbol{a}_2^{(n+1)}$ and its time derivative is determined.

4. A series of vector potentials $\boldsymbol{a}_k^{(n+1)}$ and corresponding equilibrium positions of the mechanical structure is computed, until $\boldsymbol{a}_{k+1}^{(n+1)} = \boldsymbol{a}_k^{(n+1)}$ within the scope of accuracy. Then, a new time step is started.

4 Applications

In this section, the model implementation into SOFAR as discussed in the last two sections is applied to the case of sheet metal forming. Here, the work-piece consists of the aluminum alloy AC120. For this material, the semi-empirical form

$$-\eta_{\mathrm{P}}(\epsilon_{\mathrm{P}}) = \sigma_{\mathrm{F0}}\,\epsilon_{\mathrm{P}} + c_1\,(\epsilon_{\mathrm{P}} + c_2)^{c_3} + c_4\,\ln(1 + c_5\,\epsilon_{\mathrm{P}}) \tag{13}$$

was assumed for the inelastic specific entropy $\psi_{\mathrm{P}}(\epsilon_{\mathrm{P}})$ due to energy storage in the material resulting from quasi-static isotropic hardening. In particular, the room-temperature data of [7] for AC120 yielded σ_{F0} = 116.0 MPa, c_1 = −12.39 MPa, c_2 = 0.001, c_3 = 0.0697, c_4 = 80.31 MPa and c_5 = 36.59. Since experimental identification of the remaining dynamic viscoplastic parameters σ_{P}, γ_{P} and m_{P} represents work in progress, the values $\sigma_{\mathrm{P}r}$ = 90 MPa, $\gamma_{\mathrm{P}r}$ = 200000 s^{-1} and $m_{\mathrm{P}r}$ = 5 have been estimated for aluminum from the literature (*e.g.*[30]) in the high strain-rate regime (*i.e.*$|\boldsymbol{D}| > 10^3\ \mathrm{s}^{-1}$). As indicated by the results of the last section, generally speaking, these are all a function of temperature, accumulated inelastic strain, and strain rate. Indeed, in the conventional forming regime (*i.e.*, $10^{-1}\ \mathrm{s}^{-1} < |\boldsymbol{D}| < 10^3\ \mathrm{s}^{-1}$), one may estimate σ_{P} = 100 MPa, $\gamma_{\mathrm{P}r}$ = 6500 s^{-1} and $m_{\mathrm{P}r}$ = 4 in a similar fashion. Remaining parameter values assumed at θ_r = 298 K include λ_r = 39404 MPa, μ_r = 26269 MPa, α_r = 2.2 × 10^{-5} K^{-1}, ϱ_r = 2700 kg m^{-3}, and c_r = 903 J kg^{-1} K^{-1}.

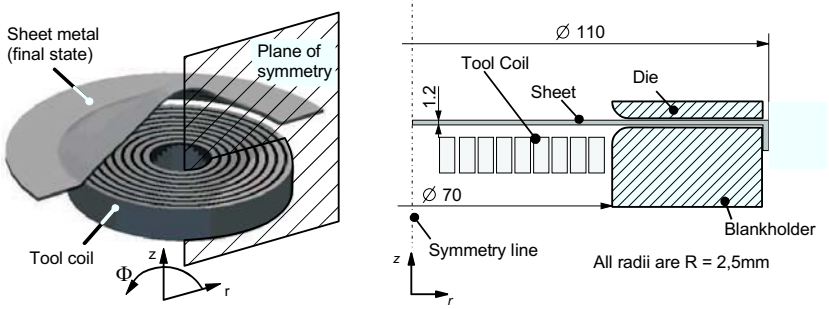

***Figure* 1:** *Geometry of work-piece, die and tool coil for the sheet metal case.*

The simulated magnetic field development resulting in a Lorentz force in the sheet metal plate driving the forming process is shown in Figure 2. In particular, the distribution of the radial

component of the magnetic flux at 20 (above) and 80 μs (below) during forming is shown. As can be seen, after 80 μs the intensity of the magnetic flux, and so the Lorentz force has decayed significantly such that further plate deformation is driven by inertial forces alone. The forming stages corresponding to the magnetic field development in Figure 2 are displayed in Figure 3 along with the development of the accumulated inelastic deformation. At the beginning of the process, the center of the plate remains at rest. On the other hand, at r = 21 mm the plate experiences high Lorentz forces and begins to accelerate. In later stages, the center of the plate is then pulled along by the rest of the plate and accelerated via predominantly inertial forces, resulting in the cap-shaped structure at the end of the process. This is mirrored by the evolution of the accumulated inelastic strain ϵ_P which is maximal at the top of the cap.

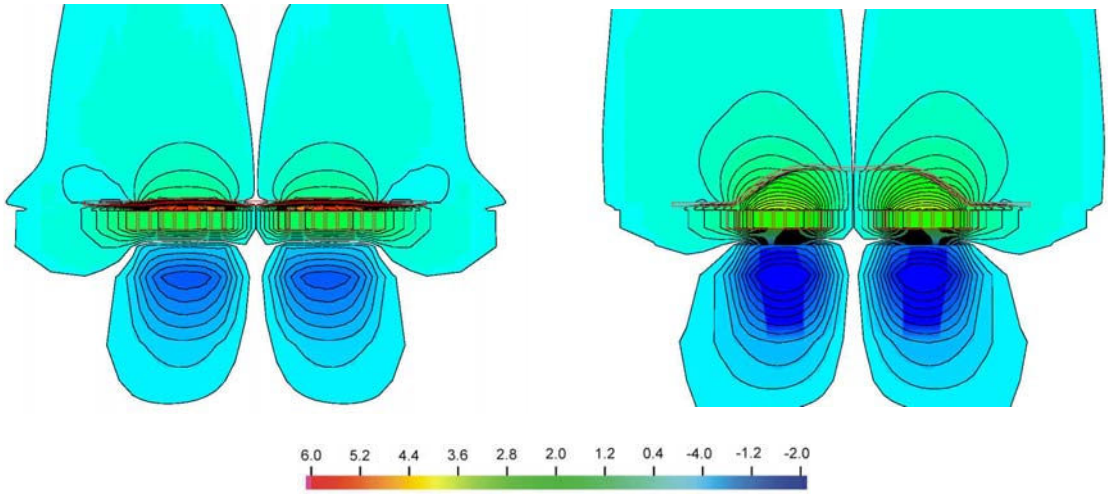

***Figure* 2:** *Radial (i.e.horizontal) component of the magnetic flux $\mathbf{b}$ at 20 μs (left) and 80 μs (right). Values shown are given in Tesla. Sheet metal plate and magnetic tool coil are also shown (in red).*

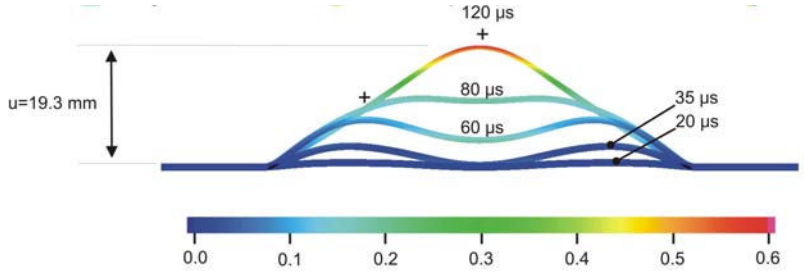

***Figure* 3:** *Sheet metal profile and accumulated inelastic strain ϵ_P at various stages during the forming process. For comparison, corresponding experimentally-determined sheet metal heights for the final profile are shown (+).*

Comparison of the simulated and experimentally-determined sheet metal profiles in Figure 3 imply that the current simulation underestimates the amount of forming slightly. Since the corresponding elastoplastic simulation from [17] agrees exactly with the experimental heights, this discrepancy would seem to be due more to the simulation of the Lorentz force than that due to the inaccuracy of the dynamic viscoplastic parameters σ_P, γ_P and, m_P. As mentioned above, their determination represents work in progress.

5 Use of SOFAR in Computer-Aided Design Problems

A major application of the above described simulation tool is the solution of different types of optimisation problems. On one hand, the identification of material parameters requires the solution of such problems, where the objective function to be minimised measures the deviation of the simulation result to experimental data. The problem consists of finding those parameter values that minimise the objective function. On the other hand, process parameters are to be identified. Here, the objective function represents the deviation of the simulation result from a desired output of the process. Thus, the method is applied to design an optimised process. Such problems are called computer aided manufacturing problems (CAM).

For a reliable and effective performance of these optimisation problems an efficient mathematical method is necessary. An adequate choice depends on details of the regarded problem. Recently, Becker and Vexler developed a mathematical theory for the error estimation for parameter identification processes that are based on Newton's method [31].

Although the free forming of aluminum offers only limited freedom to produce a desired shape, we will regard the following *academic* problem as a test for the implemented algorithm. The forming process described in the preceding section is regarded (see Figure 1). It is parametrised by two quantities. The first of these is the radius R of the tool coil, and the second is the maximum value I of the current in the circuit of the tool coil. We assume that the shape of the current curve can be held constant by the power supply, indepent of its peak value and of the size of the tool coil (which is of course another academic assumption). Next, a finite number n of radii $0 \leq r_1 < \ldots < r_n$ is chosen and n values $y_1, \ldots, y_n$ representing the height of the deformed work-piece at these radii are prescribed. We are now interested in finding those parameter values that minimise

$$f(R, I) = \sum_{i=1}^{n} (h(r_i) - y_i)^2 \tag{14}$$

where $h(r)$ describes the height of the deformed work piece at the radius r. As optimisation algorithm the Nelder-Mead simplex search is taken [18]. It is a direct search method that does not require gradients or other derivative information. At each step of the search a new point in or near the current simplex is generated according to a simple algorithm. The function value at the new point is compared with the function's values at the vertices of the simplex and, usually, one of the vertices is replaced by the new point, giving a new simplex. If a certain point x has been maintained as simplex vertex during a specified number of steps, the simplex is shrinked by a certain scaling factor such that x remains a vertex of the smaller simplex. These steps are repeated until the diameter of the simplex is less than the specified tolerance.

6 Conclusions

A multifield model for coupled electromagnetic thermomechanical composite systems has been implemented in the object oriented finite-element software environment SOFAR. The corresponding simulation tool has been applied to the case of electromagnetic sheet metal forming and used for parameter identification as well as process optimisation. The particular algorithmic implementation utilised in SOFAR has been developed with the help of a set of benchmark

tests applied to different cases of EF. The unification of coupled multifield simulation problems such as EF in a single software environment like SOFAR makes it possible to achieve more reliable, numerically-efficient and robust simulations which take advantage of the most recent advances in element technology and numerical methods, something of crucial importance to further development and improvement of such simulations.

References

[1] *W. H. Gourdin.* Analysis and assessment of electromagnetic ring expansion as a high-strain rate test. *J. Appl. Phys.*, 65:411, 1989.

[2] *W. H. Gourdin, S. L. Weinland, and R. M. Boling.* Development of the electromagnetically-launched expanding ring as a high strain-rate test. *Rev. Sci. Instrum.*, 60:427, 1989.

[3] *N. Takata, M. Kato, K. Sato, and T. Tobe.* High-speed forming of metal sheets by electromagnetic forces. *Japan Soc. Mech. Eng. Int. J.*, 31:142, 1988.

[4] *G. Fenton and G. S. Daehn.* Modeling of electromagnetically formed sheet metal. *J. Mat. Process. Tech.*, 75:6–16, 1998.

[5] *R. Tipton. CALE User's Manual*. Lawrence Livermore National Laboratory, 1992.

[6] *C. Beerwald, A. Brosius, W. Homberg, M. Kleiner, and A. Wellendorf.* New aspects of electromagnetic forming. In *Proceedings of the 6th International Conference on the Technology of Plasticity*, volume III, pages 2471–2476, 1999.

[7] *C. Beerwald, A. Brosius, and M. Kleiner.* Determination of flow stress at very high strain-rates by a combination of magnetic forming and fem calculation. In *Proceedings of the International Workshop on Friction and Flow Stress in Cutting and Forming (CIRP)*. ENSAM - Paris, 2000.

[8] *MSC.Software.Cooperation.* Marc, version 2001, 2001.

[9] *M. Badelt, C. Beerwald, A Brosius, and M. Kleiner.* Process analysis of electromagnetic sheet metal forming by online-measurement and finite element simulation. In *Proceedings of the 6th International ESAFORM Conference on Material Forming, 28.-30. April 2003, Italy*, pages 123–126. ESAFORM 2003, 2002.

[10] *C. Beerwald, A. Brosius, W. Homberg, M. Kleiner, M. Klocke, and S. Kulig.* Extended finite element modelling of electromagnetic forming. In *Proceedings of the 10th International Conference, 14.-16. April 2003, United Kingdom*, pages 559–566. SheetMetal 2003, 2003.

[11] *D. Meeker.* Femm, version 3.2, 2002.

[12] *Ansoft Corporation.* Emas, version 4.0, 1999.

[13] *H. Blum, H. Kleemann, A. Rademacher, T. Rauscher, A. Schroeder, and M. Stiemer.* SOFAR. www.mathematik.uni-dortmund.de/lsx/sofar, 2003.

[14] *B. Svendsen and T. Chanda.* Continuum thermodynamic modeling and simulation of electromagnetic metal forming. *Technische Mechanik*, 23:103–112, 2003.

[15] *B. Svendsen and T. Chanda.* Continuum thermodynamic formulation of models for electromagnetic thermoinelastic materials with application to electromagnetic metal forming. *Cont. Mech. Thermodyn.*, 2004. submitted.

[16] *M. Stiemer, J. Unger, H. Blum, B. Svendsen.* Algorithmic formulation and numerical implementation of coupled multifield models for electromagnetic metal forming simulations. in preparation, 2004.

[17] *M. Kleiner, A. Brosius, H. Blum, F. T. Suttmeier, M. Stiemer, B. Svendsen, J. Unger, S. Reese.* Benchmark simulation for coupled electromagnetic-mechanical metal forming processes. Annals of the German Society for Production Technology, in press, 2004.

[18] *J. A. Nelder and R. Mead.* A simplex method for function minimization. *Computer J.*, 7:308–313.

[19] *F. Moon. Magnetic interactions in solids*. Springer-Verlag, 1980.

[20] *J. D. Jackson. Classical Electrodynamics*. John Wiley and Sons, 1975.

[21] *J. Lubliner.* On the thermodynamic foundation of solid mechanics. *J. Nonlinear Mech.*, 7:237–250, 1972.

[22] *P. Rosakis, A. J. Rosakis, G. Ravichandran, and J. Hodowany.* A thermodynamic internal variable model for the partition of plastic work into heat and stored energy in metals. *J. Mech. Phys. Solids*, 48:581–607, 2000.

[23] *C. Teodosiu.* Dislocation modeling of crystalline plasticity, in *Large plastic deformation of crystalline aggregates*, C. Teodosiu, ed., CISM V. 376, pp. 21–80, Springer, 1997.

[24] *B. Svendsen.* On the modeling of anisotropic elastic and inelastic material behaviour at large deformation. *Int. J. Solids Structures*, 38:9579–9599, 2001.

[25] *S. Reese and B. Svendsen.* On the modeling of internal variables as structure tensors in anisotropic, finite-deformation inelasticity. *J. de Physique IV*, 14, 2003.

[26] *B. Svendsen and S. Reese.* On the modeling of internal variables as structure tensors in anisotropic, finite-deformation inelasticity. *Int. J. Plasticity*, 2004. accepted.

[27] *J. C. Nédélec.* Mixed finite elements in $\mathbb{R}^3$. *Numerische Mathematik*, 35:315–341, 1980.

[28] *J. C. Nédélec.* A new family of mixed finite elements in $\mathbb{R}^3$. *Numerische Mathematik*, 50:57–81, 1986.

[29] *M. Schinnerl, J. Schöberl, M. Kaltenbacher, and R. Lerch.* Multigrid methods for the 3d simulation of nonlinear magneto-mechanical systems. *IEEE transactions magnetics*, 38:1497–1511, 2002.

[30] *N. Jones. Structural Impact*. Cambridge University Press, 1989.

[31] *R. Becker and B. Vexler.* Adaptive finite element methods for parameter identification problems. Preprint, University of Heidelberg.

Validation of Different Approaches to Coupled Electrodynamic – Structural Mechanical Simulation of Electromagnetic Forming*

M. Stiemer[1], M. Klocke[2], F. T. Suttmeier[1], H. Blum[1], A. Joswig[2], S. Kulig[2]

[1]Chair of Scientific Computing, University of Dortmund
[2]Institute of Electrical Machines, Drivers and Power Electronics, University of Dortmund

Abstract

Electromagnetic forming (EF) is a high speed forming process in which strain rates of over 10^3 s^{-1} *are achieved. The workpiece is deformed by the Lorentz force resulting from the interaction of a fast varying electro magnetic field with the eddy currents induced by the field in the workpiece. Within a research group (FOR 443) funded by the German Research Foundation (DFG) an object oriented simulation tool for this multi physical process has been developed (SOFAR), that can handle the fully coupled simulation in a single software environment. In this contribution, details of the algorithmic implementation of the electromagnetic side of the coupled model are discussed and validated. Basis of this validation are benchmark simulations developed for this purpose. In particular, the implementation of transient field computation for coupled problems within SOFAR is compared with an experienced FD-code (FELMEC) developed at the Institute of Electrical Machines, Drives and Power Electronics.*

Keywords:

Modeling, Simulation, Electromagnetic Forming

1 Introduction

Electromagnetic forming (EF) is a dynamical forming process that is driven by the interaction of a pulsed magnetic field with eddy currents induced by the exciting field. The workpiece to be formed consists of good conducting material like copper or aluminum. A tool coil adjacent to the workpiece is excited by a fast time varying current. The resulting pulsed magnetic field diffuses into the work piece and induces eddy currents there. These eddy currents again in-

*This work is based on the results of the research group FOR 443. The authors wish to thank the Deutsche Forschungsgemeinschaft – DFG for its financial support.

teract with the exciting magnetic field which results in a material body force, e.g. the Lorentz force representing an additional supply of momentum that results in deformation. EF offers advantages over other forming methods such as increase in formability for certain kinds of materials, reduction in wrinkling, the ability to combine forming and assembly operations, reduced tool making costs etc.. Despite these advantages, its industrial application is concentrated on joining tubular semifinished material (see [1, 2]), whereas electromagnetic sheet metal forming (ESF) has not been developed to a point where it may be routinely used for industrial purposes yet. The determination of the optimal progression of the magnetic field strength including the design of tool coils and power supply devices requires still scientific research. Nevertheless, recent research activities [3, 4] have led to a precise description and process analysis of the free forming of aluminum sheet metal.

The above mentioned difficulties demonstrate the significance of reliable simulation tools for EF. However, these require a non linear coupling of a mechanical simulation considering the material's dependence on the strain rate with an electromagnetical one. Since the introduction of high speed computers in the late 80's, several different approaches to EF have been carried out (see [5, 6, 7, 8, 1, 2, 3, 9]). The simulation developed within the DFG research group FOR 443 is based on a general approach to the formulation of continuum thermodynamic models for a class of rate-dependent metallic engineering materials dynamically formed via strong magnetic fields due to Svendsen and Chanda [10, 11]. The validity of (a specialised form of) these models has been verified experimentally in Brosius et al. [12, 13]. The algorithmic formulation of the coupled model and its efficient numerical implementation has been carried out and discussed in [14]. As software environment the object oriented code SOFAR (**S**mall **O**bject orientated **F**inite-element-library for **A**pplication and **R**esearch) has been chosen [15]. Moreover, the mechanical side of the simulation has been validated by benchmark simulations in [16].

In the present contribution we discuss different algorithmic approaches to the modeling of the electromagnetic subsystem of the coupled process and report on its validation by a benchmark procedure. It is analysed which numerical techniques are best suited to solve certain problems arising in the simulation. In particular, the algorithmic implementation within SOFAR is compared to a well experienced FD-code (FELMEC) developed and maintained at the Institute of Electrical Machines, Drivers and Power Electronics. In addition, results from experiments carried out at the chair of forming at the university of Dortmund by Badelt et al. [3] and Beerwald et al. [4] serve as references.

2 Model Formulation of the Electromagnetic Subsystem

2.1 Derivation of Basic Equations

The state of an electrodynamic system is characterized by for vector fields $\vec{E}$, $\vec{D}$, $\vec{B}$, $\vec{H}$, fulfilling Maxwell's equations

$$\begin{aligned} \text{div}\,\vec{D} &= \rho & \text{div}\,\vec{B} &= 0 \\ \text{curl}\,\vec{H} &= \vec{J} + \dot{\vec{D}} & \text{curl}\,\vec{E} &= -\dot{\vec{B}}\,. \end{aligned} \tag{1}$$

Here $\vec{J}$ denotes the conducting current and ρ the density of electric charges, which is zero in the given situation. Dots indicate total derivatives. In the realm of the quasistatic hypothesis, which applies to EF since the characteristic wave length of the electromagnetic field are much longer than the structure of interest, displacement currents $\dot{\vec{D}}$ are negligible (see e.g. [17] or [18]). The region Ω in which the forming process takes place consists of three parts, the workpiece $\mathcal{W}$, the tool coil $\mathcal{S}$ and the space around workpiece and tool-coil. We assume that the respective materials possess linear isotropic polarization and magnetization with permittivity ε and permeability $\mu = \mu_0$ such that $\vec{B} = \mu\vec{H}$ and $\vec{D} = \varepsilon\vec{E}$ may be assumed throughout Ω within the scope of accuracy, where μ_0 denotes the permeability of the vacuum. We further assume that the tool coil remains stationary during the process such that $\dot{\vec{B}}$ equals the time derivative $\dot{\vec{B}} = \partial_t \vec{B}$ outside $\mathcal{W}$. If the workpiece moves at a velocity $\vec{v}$, we obtain $\dot{\vec{B}} = \partial_t \vec{B} + \operatorname{curl}(\vec{v} \times \vec{B})$ inside $\mathcal{W}$. Finally, $\vec{J}$ is related to the other fields by the constitutive equation

$$\vec{J} = \gamma\vec{E}\,. \tag{2}$$

Here, $\gamma = \gamma(\vec{x}, t)$ denotes the conductivity of the material at a point $\vec{x}$ at time t. To solve Maxwell's equations, a vector potential $\vec{A}$ and a scalar potential Φ are introduced. If $\vec{A}$ and Φ fulfill the coupled equations

$$\begin{aligned} \operatorname{curl}\frac{1}{\mu}\operatorname{curl}\vec{A} + \gamma\,\partial_t\vec{A} - \gamma\left(\vec{v}\times\operatorname{curl}\vec{A}\right) &= -\gamma\operatorname{grad}\Phi \\ \Delta\Phi = \operatorname{div}\partial_t\vec{A} - \operatorname{div}\left(\vec{v}\times\vec{B}\right)&\,, \end{aligned} \tag{3}$$

then $\vec{B} = \operatorname{curl}\vec{A}$, $\vec{E} = \gamma\left(-\operatorname{grad}\Phi - \partial_t\vec{A} + \vec{v}\times\vec{B}\right)$, $\vec{D} = \varepsilon\vec{E}$, $\vec{H} = 1/\mu\vec{B}$ fulfill the quasistatic version of Maxwell's equation for linear isotropic materials in each part of the region Ω. Solutions to (3) need not to be continuous at interfaces between two materials. However, the components of $\vec{B}$ and $\vec{J}$ normal to the interface are continuous as well as the tangential components of $\vec{E}$. In the following, we assume that a Coulomb gauge condition $\operatorname{div}\vec{A} = 0$ holds. If additionally $\operatorname{div}\left(\vec{v}\times\vec{B}\right) = 0$ holds, equations (3) decouple. Both the Coulomb gauging and the latter condition are generally fulfilled for 2D problems or in the axisymmetric situation. Consequently, the second equation can be solved independent of $\vec{A}$ and $\operatorname{grad}\Phi$ can be inserted in the first one. In addition to equation (3), boundary conditions are necessary to determine $\vec{A}$ and Φ: As before, Ω denotes the domain, in which a magnetic field distribution is to be computed and $\mathcal{S}$ is the domain of a coil with (congruent) front surfaces $\mathcal{F}_1$ and $\mathcal{F}_2$ and a spiral lateral surface $\mathcal{L}$. Further, let the potential U_1 and U_2 be given on $\mathcal{F}_1$ and $\mathcal{F}_2$ respectively. As the area adjacent to $\mathcal{S}$ possesses conductivity $\gamma = 0$, Φ solves on a stationary tool coil $\mathcal{S}$ the equation

$$\begin{aligned} \Delta\Phi = 0 \quad &\text{in } \mathcal{S} & \Phi = U_1 \quad &\text{on } \mathcal{F}_1 \\ \Phi = U_2 \quad &\text{on } \mathcal{F}_2 & \partial_n\Phi = 0 \quad &\text{on } \mathcal{L}\,, \end{aligned} \tag{4}$$

where ∂_n denotes the derivative in direction of the outer normal. Outside $\mathcal{S}$ we may assume $\Phi = 0$. Although there exists no boundary for $\vec{A}$, it is justified to restrict it to a bounded domain Ω and to assume that $\vec{A}$ vanishes on its boundary, since $\vec{A}(\vec{x}) = O(1/|\vec{x}|^2)$ for $|\vec{x}| \to \infty$. If instead of the potential U on the front sides of the coil the total current $I = I(t)$ in the tool coil is known,

then the two equations (3) have to be tackled simultanously, i.e. the system

$$\operatorname{curl} \frac{1}{\mu} \operatorname{curl} \vec{A} = -\gamma \left(\partial_t \vec{A} + \operatorname{grad} \Phi - \vec{v} \times \operatorname{curl} \vec{A} \right) \quad \text{in } \Omega$$
$$\Delta \Phi = 0 \quad \text{in } \mathcal{S} \qquad\qquad \Phi = 0 \quad \text{in } \Omega \setminus \mathcal{S} \tag{5}$$

has to be considered together with the afore mentioned boundary conditions for $\vec{A}$ and Φ and with

$$-\gamma \int_{\mathcal{C}} \left(\partial_t \vec{A} + \operatorname{grad} \Phi \right) \, d\vec{a} = I \tag{6}$$

for any cross section $\mathcal{C}$ parallel to $\mathcal{F}_1$ and $\mathcal{F}_2$ ($d\vec{a}$ = surface element).

2.2 The Axisymmetric Situation

Spiral coils as used for EF are not axisymmetric, but can be approximated in good accuracy by the following idealization: If $\mathcal{S}$ consists of n windings, each winding is replaced by a torus of the same cross section $\mathcal{C}$. The resulting n tori are cut at an azimuthal angle of $\varphi = 0$. These cuts are considered as perfectly isolating. Next, the cross section at $\varphi = 0$ of each torus (except of the first one) is set on the same potential level as the cross section of the preceding torus at $\varphi = 2\pi$. If $\mathcal{T}_k$ denotes the kth torus resulting from this process and U_k the potential of $\mathcal{T}_k$ at $\varphi = 0$, then $\Phi = \Phi(r, \varphi, z)$ satisfies for $k = 1 \ldots n$

$$\Delta \Phi = 0 \quad \text{in } \mathcal{T}_k \qquad\qquad \Phi = U_k \quad \text{for } \varphi = 0 \quad (\text{in } \mathcal{T}_k)$$
$$\Phi = U_{k+1} \quad \text{for } \varphi = 2\pi \quad (\text{in } \mathcal{T}_k) \qquad\qquad \partial_n \Phi = 0 \quad \text{on } \partial\mathcal{T}_k \, . \tag{7}$$

Consequently, Φ possesses the form

$$\Phi(r, \varphi, z) = U_k + \delta U_k \frac{\varphi}{2\pi} \tag{8}$$

with $\delta U_k = U_{k+1} - U_k$. For the determination of

$$\nabla \Phi = \frac{\delta U_k}{2\pi r} \vec{e}_\varphi \, , \tag{9}$$

where $\vec{e}_\varphi$ denotes a unit vector in azimuthal dircection, only the potential differences δU_k need to be considered. They can be obtained from the measured total current $I = I(t)$ in the coil as follows: The average over all currents flowing through an arbitrary cross section $\mathcal{C}_k$ through the kth torus amounts to

$$I = -\gamma \int_{\mathcal{C}_k} \left(\partial_t \vec{A} + \operatorname{grad} \Phi \right) \, d\vec{a} = -\gamma \int_{\mathcal{C}_k} \left(\partial_t \vec{A} + \frac{\delta U_k}{2\pi r} \vec{e}_\varphi \right) \, d\vec{a} \, . \tag{10}$$

From relation (10), δU_k can be determined:

$$\delta U_k \cdot \int_{\mathcal{C}_k} \frac{1}{2\pi r} \vec{e}_\varphi \, d\vec{a} = -\frac{I}{\gamma} - \int_{\mathcal{C}_k} \partial_t \vec{A} \, d\vec{a} \tag{11}$$

implying

$$\delta U_k = -2\pi \left(h \ln \frac{b_k}{a_k} \right)^{-1} \cdot \left(\frac{I}{\gamma} + \int_{\mathcal{C}_k} \partial_t \vec{A} \, d\vec{a} \right) \tag{12}$$

for a coil with rectangular cross section, where h is the height (= size in z-direction), a_k the inner and b_k the outer radius of the kth winding. Thus, we obtain

$$\nabla \times \frac{1}{\mu} \operatorname{curl} \vec{A} + \gamma \, \partial_t \vec{A} = \begin{cases} \left(r \cdot h \ln \dfrac{b_k}{a_k} \right)^{-1} \cdot \left(I + \gamma \displaystyle\int_{\mathcal{C}_k} \partial_t \vec{A} \, da \right) & \text{in } \mathcal{S} \\ \vec{v} \times \operatorname{curl} \vec{A} & \text{in } \mathcal{W} \\ 0 & \text{in } \Omega \setminus (\mathcal{S} \cup \mathcal{W}) \, . \end{cases} \tag{13}$$

The coefficients a_k and b_k in this equation depend on the spatial variable $\vec{x}$ in so far as they assume a certain value depending on the coil winding in which $\vec{x}$ is located.

3 Discussion of different Algorithmic Implementations

There exist several possibilities to model the electromagnetic subsystem. The finite element (FE) method offers a flexible method that can easily be adapted to changing demands and that offers various numerical algorithms that allow an optimized performance for a large scale of different problems. In particular, both the electromagnetic and the mechanical subsystem can be implemented in a single software environment which results in an enormous gain of performance. The latter is much more difficult with the FD method or the boundary element method due to their inherent restrictions. In addition, the FE method allows the use of unstructured meshes and adaptive refinement such that it can cope with singularities, problems having solutions with restricted regularity or other numerical difficulties. Thus the software environment SOFAR had been chosen for the development of a simulation tool for EF. On the other hand, complex computer code is susceptible for errors and thus a well experienced, clearly written code that serves as reference is desirable. For this purpose, the above mentioned FD code is applied.

3.1 Program Structure

Essential for an FE tool to be applied in research is its clear structure such that extensions and new algorithms can quickly be implemented. Such a structure can be reached by an object oriented design as done in SOFAR: The interface to the developer is implemented in JAVA. On the other hand, time critical jobs like basic linear algebra (BLAS-) operations are implemented in fast native C and FORTRAN Code. Unstructured meshes which are typical for adaptive refinement and remeshing strategies can easily be handled. In particular, SOFAR administrates geometric singularities as e.g. hanging nodes. The assembly of the corresponding stiffness matrices is done automatically. Moreover, SOFAR allows access to any geometric substructure of a particular finite element like edges or faces. The latter enables easy implementation of edge elements which are used for 3D electrodynamical problems [19, 20]. Moreover, effective algorithms like multigrid solver or error estimators are available. SOFAR can be extended by external routines (written in C or FORTRAN) due to a user interface. This user interface was e.g. applied for the implementation of structural mechanic finite elements developed at the chair of Mechanics at the University of Dortmund.

3.2 Design of suitable Meshes

One has to decide wether the whole coupled problem is treated in one mesh or if each subsystem is simulated in a mesh of its own. The first approach offers the advantage that a consistent linearization of the coupled non linear equation can easier be implemented. On the other hand coefficients of largely differing magnitude within the common stiffness matrix lead to largely differing eigenvalues and thus probably disturb the stability of the method. Moreover, the numerically sensitive parts of the electrodynamical and the mechanical subsystem are localized in different spatial areas. A treatment in different meshes allows to adapt the particular mesh by local refinement. Consequently, electromagnetic and mechanical subsystem are simulated in different meshes in case of the SOFAR simulation.

It is *natural* that the mechanical mesh moves with the structure. Whether the electromagnetic mesh should rest or move is a difficult question: A moving electromagnetic mesh, representing the Lagrangian point of view offers two advantages: First, data exchange between the structure mesh and the electromagnetic mesh is easier, because node-oriented data can be transferred without rearrangement. Second, the convective term $\vec{v} \times \operatorname{curl} \vec{A}$ need not to be considered explicitely if the time derivative $\partial_t \vec{A}$ is replaced by the total derivative $\dot{\vec{A}}$ in (13) (see [18]), since

$$\dot{\vec{A}} = \partial_t \vec{A} + \operatorname{grad}_{\vec{A}} \left(\vec{v} \cdot \vec{A} \right) - \vec{v} \times \operatorname{curl} \vec{A} \,. \tag{14}$$

The term $\operatorname{grad}_{\vec{A}} \left(\vec{v} \cdot \vec{A} \right)$ disappears if $\vec{v}$ and $\vec{A}$ are perpendicular which is the case for all 2D or axisymmetric problems. In a moving mesh, $\dot{\vec{A}}$ is simply obtained by considering corresponding nodal values of two subsequent meshes. On the other hand, a fixed mesh, representing an Eulerian approach, avoids global remeshing in every time step. Then $\vec{v} \times \operatorname{curl} \vec{A}$ has to be considered in the weak form of (13). As the Péclet-number

$$P_e = \frac{\mu \gamma |\vec{v}| h}{2} \approx 0.5 \tag{15}$$

is small in the given situation, the stability of the numerical solution process is not affected. The circumstance that the resulting stiffness matrices are no longer symmetric such that (preconditioned) conjugate gradient solvers cannot be applied is of minor importance, as SOFAR is equipped with a BICGSTAB solver that can treat the corresponding linear equations effectively. Moreover a fixed mesh reduces the expenses for the accumulation of the stiffness matrix because only part of it needs to be reassembled. While the electromagnetic field calculation in SOFAR works on a fixed mesh, the FD method uses a moving one. A detailed comparison of the performance and accuracy of these two approaches represents work in progress.

3.3 Finite Element Formulation

While a standard finite element approach with so called nodal elements is applicable for 2D problems or problems with certain symmetries, numerical field computation in 3D requires a more sophisticated approach. Therefore, Nédélec introduced edge elements in 1980 and 1986 [19, 20]. Here the degrees of freedom that have to be determined are not nodal values of $\vec{A}$ but integrals over $\vec{A}$ along the edges of the discretizing mesh. These elements simulate the typical jumps, solutions to Maxwell's equations exhibit at interfaces between different materials

and, hence, avoid locking and spurious modes. As the benchmark problem considered below is formulated for an axisymmetric situation, nodal elements with four nodes are applied.

We derive now the weak form of equation (13) and its discretization in the axisymmetric situation, which is the basis of the FE simulation. If A_φ denotes the azimuthal component of $\vec{A}$ and r the radial component of a point and z its axial component then (13) is equivalent to

$$\frac{1}{\mu}\int_\Omega \left(r\left(\partial_r A_\varphi \partial_r A^* + \partial_z A_\varphi \partial_z A^*\right) + \frac{A_\varphi A^*}{r}\right) - \gamma \int_{\mathcal{W}} \left(v_r \partial_r A_\varphi + v_z \partial_z A_\varphi + \frac{v_r A_\varphi}{r}\right) A^*$$
$$+ \gamma \int_\Omega \partial_t A_\varphi A^* \qquad = \begin{cases} \displaystyle\int_{\mathcal{S}} r \left(h \ln \frac{b_k}{a_k}\right)^{-1} \cdot \left(I + \gamma \int_{\mathcal{C}_k} \partial_t A_\varphi \right) \cdot A^* & \text{in } \mathcal{S} \\ 0 & \text{in } \Omega \setminus \mathcal{S} \end{cases}$$

for all test functions $A^* \in H^1$ that decay sufficiently fast for $r \to 0$. In all integrals, the integration has to be carried out with respect to $drdz$. Inserting the FE basis representation of A_φ and A^* we obtain a linear system of equations. The first integral leads to the permeability matrix K, the third to the conductivity matrix B and the second to an unsymmetric matrix C representing the convective part. Since the source vector $\vec{f} = \vec{f}(\dot{\vec{a}})$ is a function of $\dot{\vec{a}}$ the resulting equation

$$K\vec{a} + C\vec{a} + B\dot{\vec{a}} = \vec{f}(\dot{\vec{a}}) \tag{16}$$

has to be solved iteratively. This can be avoided by discretization of $\int_{\mathcal{C}_k} \partial_t A_\varphi$ and adding the resulting linear equations to the stiffness matrix. But the management of the additional coupling of degrees of freedom, that are not linked to each other by a neighbor relation, is more expensive than the implementation of the iterative scheme. Moreover, in each iteration step only $f(\dot{\vec{a}})$ has to be reassembled such that numerical costs remain small. Benchmark tests have shown that this methods exhibits satisfactory performance.

3.4 Finite-Difference Approach

The Finite-Difference method is usually restricted to structured orthogonal grids. However, a generalization to nonstructured meshes including triangular and nonrectangular quadrangular cells is possible. The arising methods, one of which is applied in the inhouse FD-code FELMEC, are e.g. referred to as Box-Techniques, the resulting difference schemes of which are closely related to schemes based on Finite Elements [21].

The method used here is based on a modified vector potential $\Psi' = r \cdot A_\varphi$ for axisymmetric arrangements and described in [22, 23]. The values of Ψ' on the nodes are the primary unknowns of interest. In order to compute them, for each time step a system of linear equations is set up by evaluating Ampere's law for each node on a path through the grid cells adjacent to the node under consideration.

It should be mentioned that the values of the nodal amperage I_0 are not prescribed as external quantities, but are themselves unknown in workpiece and tool coil. For nodes in free space they are zero anyway, whereas for the tool coil cross-section I_0 is replaced by an expression including the time derivative of Ψ'_0 and the external driving voltage u_{ex} along the winding turn under consideration. All winding turns are also regarded as branch elements of a network, for which Kirchhoff's laws are applied. The prescribed current i of the tool coil is given by a current source. The necessary voltage-current relations of the windung turns are set up

as a summation of the nodal amperages I_0 on the winding cross-section. The resulting overall system of equations is solved directly for each time step.

In contrast to [23], where the coupling of the moving structure to the orthogonal base grid is carried out by an interpolation strategy leaving the original base grid unaltered, here a remeshing procedure is applied. First, all grid cells of the base grid, which are totally or partially covered by the workpiece, as well as cells with nodes lying to close to the workpiece mesh are deactivated. Hence, an interior boundary in the base grid occurs. Then, the exterior workpiece contour and the resulting interior base grid contour are linked by triangular cells forming a coherent mesh. Here, additional triangular cells occur, whenever nodes of the interior base grid contour are connected diagonally. In order to ensure that all nodes of the original workpiece mesh are adjacent to four quadrangular grid cells, an extended workpiece mesh with an additional layer of nonconductive grid cells is used for the procedure described above. The topology regularized by this mesh extension is considered advantageous for the computation of nodal forces by evaluating Maxwell's stress tensor. Figure 1 shows a detail of a mesh generated for a workpiece geometry at 63 μs, which resulted from the staggered EMAS-MARC coupling presented in [9]. As pointed out before, the coefficients for the generalized FD-scheme or Box-

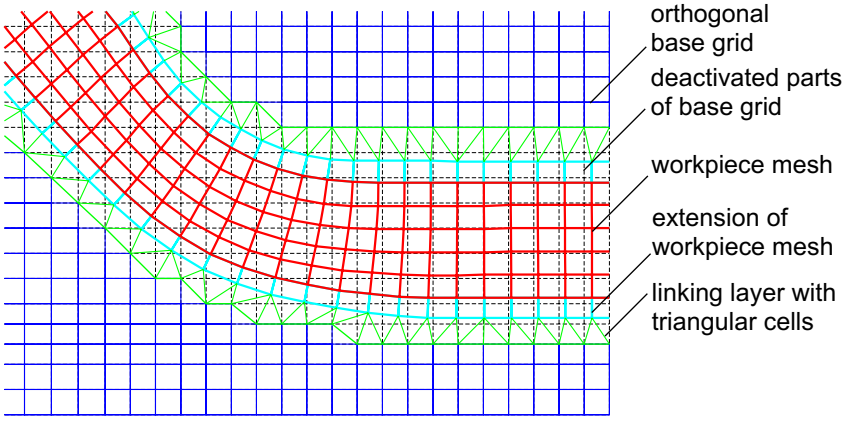

***Figure* 1:** *Detail from remeshed Finite-Difference grid showing the workpiece mesh, its nonconductive extension and the linking layer to the remaining active base grid.*

scheme can be derived in quite the same way as in the basic orthogonal grid by evaluating Ampere's law. In order to obtain expressions for the magnetic field strength in a triangular cell depending on the nodal values of Ψ', a linear approximation for Ψ' in z and r^2 in the triangle is chosen:

$$\Psi'(r,z) = c_0 + c_r r^2 + c_z z\,. \tag{17}$$

The constants c_0, c_r and c_z are computable in dependence on the three nodal values Ψ'_{I}, Ψ'_{II} and Ψ'_{III} by solving a linear system of equations. The coefficients c_r and c_z are related to the flux density components in the triangular cell as a result of $\vec{B} = \mathrm{curl}\,\vec{A}$:

$$B_z = 2c_r \;\;,\quad B_r(r) = -\frac{c_z}{r}\,. \tag{18}$$

The contribution to the circulation of the magnetic field around a node under consideration, which results from the part of the integrational path through the triangle from one edge to

another according to Fig. 2, can be calculated as follows:

$$\int_{M_{\mathrm{I,II}}}^{M_{\mathrm{I,III}}} \vec{H}\, d\vec{l} = \frac{1}{\mu} \int_{M_{\mathrm{I,II}}}^{M_{\mathrm{I,III}}} \left(-c_z \frac{dr}{r} + 2c_r\, dz \right) . \tag{19}$$

Since it does not depend on the path itself due to curl $\vec{B}$ = 0 for the field in (18) and $\mu = const.$

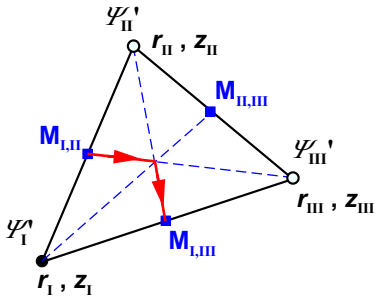

Figure 2: *Triangular cell with nodes I, II and III, edge median points $M_{\mathrm{I,II}}$, $M_{\mathrm{II,III}}$ and $M_{\mathrm{I,III}}$ and part of integrational path (arrows) surrounding node under consideration, here No. I, along median lines.*

inside the cell, simply a parametrized straight line can be assumed for evaluating (19). The constants c_r and c_z are replaced by the nodal values of Ψ'. Finally, a linear combination of these modified nodal vector potentials is obtained:

$$\int_{M_{\mathrm{I,II}}}^{M_{\mathrm{I;III}}} \vec{H} d\vec{l} = \alpha_{\mathrm{I,II}} \Psi'_{\mathrm{II}} + \alpha_{\mathrm{I,III}} \Psi'_{\mathrm{III}} - \left(\alpha_{\mathrm{I,II}} + \alpha_{\mathrm{I,III}} \right) \Psi'_{\mathrm{I}} . \tag{20}$$

Here, e.g. the coefficient $\alpha_{\mathrm{I,II}}$ is given by

$$\alpha_{\mathrm{I,II}} = \frac{1}{\mu \Delta} \left((z_{\mathrm{III}} - z_{\mathrm{I}})(z_{\mathrm{III}} - z_{\mathrm{II}}) + \left(r_{\mathrm{III}}^2 - r_{\mathrm{I}}^2 \right) \ln \frac{r_{\mathrm{III}} + r_{\mathrm{I}}}{r_{\mathrm{II}} + r_{\mathrm{I}}} \right) \tag{21}$$

and Δ stands for

$$\Delta = \left(r_{\mathrm{II}}^2 - r_{\mathrm{I}}^2 \right) (z_{\mathrm{III}} - z_{\mathrm{I}}) - \left(r_{\mathrm{III}}^2 - r_{\mathrm{I}}^2 \right) (z_{\mathrm{II}} - z_{\mathrm{I}}) . \tag{22}$$

The logarithmic expression in $\alpha_{\mathrm{I,II}}$ results from integrating the $1/r$-dependence. However, it can be shown that for large radii and comparably low radial distances of the nodes the coefficients α become approximately those expressions, which are obtained in rectangular coordinates (2D problems) for first order finite elements.

The quadrangular grid cells in the workpiece are treated in a similar way based on a subdivision of such a cell into four underlying triangles. The modified vector potential Ψ'_{c} of the center point as the point in common for the four triangles is assumed to be a linear combination of the values $\Psi'_{1\ldots4}$ of the quadrangle's vertices with weighting coefficients $\kappa_{1\ldots4}$ depending on geometry and their sum equaling one. The paths of integration are led from the edge median points to the center point right through the adjacent triangle. The according contribution to the magnetic circulation under consideration depends on Ψ'_{c} as well as on two vertex potentials. After replacing Ψ'_{c} by the aforementioned linear combination only the vertex potentials occur and the resulting coefficients for matrix assembly are obtained.

In contrast to the base grid, where matrix assembly is carried out row by row, i.e. nodal

equation by nodal equation, for the nonorthogonal parts of the mesh the matrix is assembled by adding the contributions e.g. arsing from (21) to the coefficient matrix grid cell by grid cell, similar to matrix assembly in the Finite Element Method.

3.5 Timestepping

As time stepping for the electromagnetic subsystem the generalized trapezoidal rule has been chosen. Only the conductivity matrix B and the convective matrix C have to be reassembled in every time step, while the permeability matrix K does not change due to the choice of a fixed mesh. At the beginning of the process vibration due to the switching on of power have to be filtered out. Consequently the parameter of the generalized trapezoidal rule has to be chosen close to the backward Euler situation. Later, the optimal parameter yielding an acurracy of $O(\delta_t^2)$ can be chosen, where δ_t is the size of the time step.

In the FD-code the same method also known as θ-method is applied. According to the following approximation of integrals of a quantity $q(t)$ over one time step

$$\int_t^{t+\delta_t} q(\tau)\, d\tau = (1-\theta)\delta_t q_{t+\delta t} + \theta \delta_t q_t \,, \tag{23}$$

θ = 0 results in the backward Euler formula, whereas θ = 0.5 is the mere trapezoidal rule. For the computations carried out here for θ a value of about a third has been chosen sometimes referred to as Galerkin approach. A moving mesh is used, so that the convective term does not occur explicitly. All contributions to electromagnetic induction, motion conditioned as well as arising from field variation, are included by evaluating the total derivative of the nodal modified vector potentials Ψ'. However, the reluctance matrix has to be regenerated in every time step.

3.6 Coupling Strategies

The coupling between the two subsystems is carried out in a staggered way. This means that the magnetic field distribution is calculated with respect to the position and velocity of the structure in the nth time step. After that the new position of the structure is determined such that a balance between inner and outer forces arises. However, benchmark simulation have shown that this algorithm can be improved by adding an additional iteration loop: To ensure that the computed momentum balance of the structure in the $(n+1)$st time step represents a balance between the Lorentz forces in the $(n+1)$st time step and the inner forces of the structure at this instant, the following scheme is applied: Let all values having index n be variables of the nth time step. Then the update for the $(n+1)$st time step looks like this:

1. A predictor value $\vec{A}_1^{(n+1)}$ for the vector potential and for its time derivative in the $(n+1)$st step is computed according to the measured amperage in the tool coil at time $t^{(n+1)}$ and the kinematic state of the workpiece. For this, the assembly routine of the magnetic mesh checks wether a certain point lies in the workpiece or not. The values for conductivity and for the velocity of the structure are chosen respectively.

2. The stiffness matrix and load vector in the workpiece mesh are assembled. For this, the nodal values of the current Lorentz force density are computed according to

$$f_{\mathrm{L}}^{(n+1)} = \vec{J}_1^{(n+1)} \times \vec{B}_1^{(n+1)} = \gamma\, \partial_{\mathrm{t}}\, \vec{A}_1^{(n+1)} \times \mathrm{curl}\, \vec{A}_1^{(n+1)} \,. \tag{24}$$

3. The assembled equation in the workpiece mesh is solved. The computed deformations are added to the vertex positions of the workpiece mesh. It is checked, whether the residual force associated with the resulting state of deformation is zero in the scope of desired accuracy. If the latter is false, another step of the Newton-Raphson iteration has to be performed with the altered position of the workpiece. Otherwise, the vector potential $\vec{A}_2^{(n+1)}$ according to the new kinematic state of the structure is computed. If it does not deviate from $\vec{A}_1^{(n+1)}$ within the scope of accuracy, the next time step is started. Otherwise, the equilibrium position of the structure with respect to outer forces resulting from $\vec{A}_2^{(n+1)}$ and its time derivative is determined.

4. A series of vector potentials $\vec{A}_k^{(n+1)}$ and corresponding equilibrium positions of the mechanical structure is computed, until $\vec{A}_{k+1}^{(n+1)} = \vec{A}_k^{(n+1)}$ within the scope of accuracy. Then a new time step is started.

Using the Finite-Difference code FELMEC for the electromagnetic subsystem one can set up an explicit coupling scheme, the accuracy of which is considered sufficient, if a small time step of e.g. 0.1 ... 0.2 μs is chosen. Having calculated the nodal forces in the workpiece the electromagnetic simulation has to be interrupted after each time step. The calculation of nodal forces is carried out by a local evaluation of Maxwell's stress tensor on a surface around a node under consideration. The list of nodal forces is written out and passed to the structural mechanical part of SOFAR as a prescribed load, which calculates an update of the workpiece shape and mesh. With this updated mesh the electromagnetic computation is continued. Control and synchronization of the two processes are carried out by a shell script and JAVA-routines in SOFAR.

4 Validation by Benchmark Problems

Details of the implementation of the coupled electromagnetic field computation described above have been validated by several benchmark simulations involving comparisons with the programs EMAS, FEMM and ANSYS. The mechanical side has been tested in [16]. Here we present a benchmark test that allows to validate the fully coupled simulation, where the above described FD-code serves as reference. Although many questions have already been clarified, the benchmark process and the optimization of SOFAR are still work in progress.

To validate whether SOFAR computes a correct force distribution, first a fully coupled simulation is carried out with SOFAR. Thereby the same geometry and input currency are regarded as described in [16]. In particular, the mechanical side is simulated by an elastoplastic element. Although this modeling fails to account for the rate dependency of the mechanical structure it suffices for a validation of the electromagnetic field computation as it leads to approximatively correct results (see [16] or [1, 2, 3, 9]). Next, the FD-code is coupled with SOFAR such that the computation of the electromagnetic field is carried out by the FD-Software, while SOFAR simulates the mechanical subsystem. The results of these simulations are compared to each other and to experimental results. Both simulations mirror the forming process qualitatively correctly: Figure 3 shows the shape of the work piece after 35 μs. The form of the work piece stays extremly similar during the whole forming process in both simulations. This

shows that both approaches, although completely different, are basically numerically equivalent for this example. Moreover, comparison to experimental data from [3, 4] shows that the

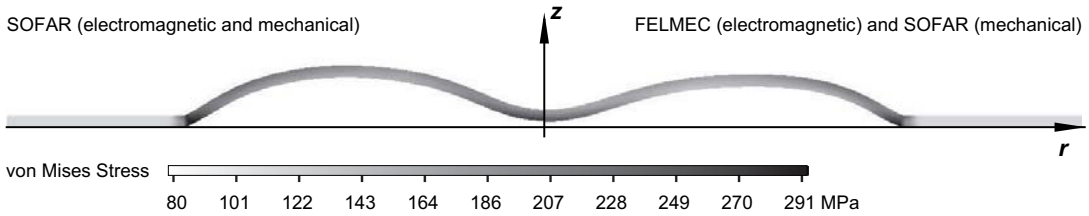

***Figure* 3:** *Workpiece contour and von Mises stress at instant of time* t = 35 μs

coupling of SOFAR with the FD-code leads to a satisfactory result*: Figure 4 shows the vertical displacement of the structure on the axis and at a radius of 21 mm for both simulations in comparison with experimental data. However, with the current parameters, SOFAR computes

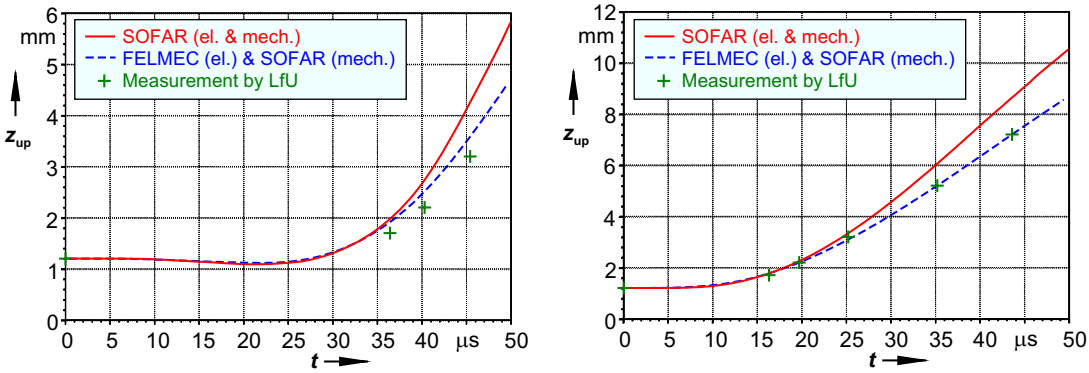

***Figure* 4:** *Position of upper workpiece surface on axis* r = 0 mm*, graph on left hand side, and at* r = 21 mm*, graph on right hand side.*

a slightly larger distribution of forces than the FD-simulation leading to more deformation of the work piece. In the beginning, both simulations yield nearly the same displacement but after 35 and 20 μs respectively the deviation becomes obvious achieving a value of about 2 mm after 60 μs. This deviation is mainly caused by the different spatial discretizations used for electromagnetic field computation (up to 47000 unknowns in the case of the FD-SOFAR simulation and 1126 unknowns for the SOFAR computation). The results of the simulation show that the discretization within SOFAR has been chosen much too coarse. To increase the accuracy of SOFAR without reducing its efficiency, adaptive meshing algorithms based on local error estimation will be implemented soon. Moreover, the choice of optimal numerical parameters is still work in progress and will be carried out with the help of further benchmark tests.

5 Conclusions

The algorithmic implementation of the electromagnetic subsystem of a fully coupled simulation tool for electromagnetic forming has been presented. Details of the realization of the underlying physical model are discussed. In particular, the tool coil is correctly modeled as massive

*Note that an elastoplastic model slightly overestimates the deformation of the workpiece (see e.g. [16]).

conductor with the help of an iterative scheme. Convective terms are accounted within the weak form of the field equations. The non linear coupling between the magnetical and mechanical subsystem is performed in a staggered but implicit way, allowing for larger time steps. The applied algorithms have been tested and optimized with the help of suitable benchmark tests. Although SOFAR can in principle cope with the computation of the Lorentz force distribution coupling the electromagnetic system and the mechanical structure, further improvements concerning the accuracy of the field computation are necessary to obtain full accordance to experimental data. In particular, numerical algorithms for error control and adaptive refinement have to be implemented and validated by further benchmark simulations. This will improve SOFAR to a convenient and reliable tool for the simulation of EF forming processes.

References

[1] *C. Beerwald, A. Brosius, W. Homberg, M. Kleiner, and A. Wellendorf.* New aspects of electromagnetic forming. In *Proceedings of the 6th International Conference on the Technology of Plasticity*, volume III, pages 2471–2476, 1999.

[2] *C. Beerwald, A. Brosius, and M. Kleiner.* Determination of flow stress at very high strain-rates by a combination of magnetic forming and fem calculation. In *Proceedings of the International Workshop on Friction and Flow Stress in Cutting and Forming (CIRP)*. ENSAM - Paris, 2000.

[3] *M Badelt, C. Beerwald, A Brosius, and M. Kleiner.* Process analysis of electromagnetic sheet metal forming by online-measurement and finite element simulation. In *Proceedings of the 6th International ESAFORM Conference on Material Forming, 28.-30. April 2003, Italy*, pages 123–126. ESAFORM 2003, 2003.

[4] *C. Beerwald, A. Brosius, M. Kleiner, and V. Psyk.* Einfluss des magnetischen Druckes bei der elektromagnetischen Blechumformung. In *2. Kolloquium Elektromagnetische Umformung*. Forschergruppe “Untersuchung der Wirkmechanismen der elektromagnetischen Blechumformung”, 2003.

[5] *W. H. Gourdin.* Analysis and assessment of electromagnetic ring expansion as a high-strain rate test. *J. Appl. Phys.*, 65:411, 1989.

[6] *W. H. Gourdin, S. L. Weinland, and R. M. Boling.* Development of the electromagnetically-launched expanding ring as a high strain-rate test. *Rev. Sci. Instrum.*, 60:427, 1989.

[7] *N. Takata, M. Kato, K. Sato, and T. Tobe.* High-speed forming of metal sheets by electromagnetic forces. *Japan Soc. Mech. Eng. Int. J.*, 31:142, 1988.

[8] *G. Fenton and G. S. Daehn.* Modeling of electromagnetically formed sheet metal. *J. Mat. Process. Tech.*, 75:6–16, 1998.

[9] *C. Beerwald, A. Brosius, W. Homberg, M. Kleiner, M. Klocke, and S. Kulig.* Extended finite element modelling of electromagnetic forming. In *Proceedings of the 10th International Conference, 14.-16. April 2003, United Kingdom*, pages 559–566. SheetMetal 2003, 2003.

[10] *B. Svendsen and T. Chanda.* Continuum thermodynamic modeling and simulation of electromagnetic forming. *Technische Mechanik*, 23:103–112, 2003.

[11] *B. Svendsen and T. Chanda.* Continuum thermodynamic formulation of models for electromagnetic thermoinlastic materials with application to electromagnetic metal forming. *Cont. Mech. Thermodyn.*, 2004. submitted.

[12] *A. Brosius, M. Kleiner, and B. Svendsen.* Finite-element modeling and simulation of the material behaviour and structural behaviour during electromagnetic metal forming of metal tubes and sheet metal. 2003. in preparation.

[13] *A. Brosius, T. Chanda, M. Kleiner, and T. Svendsen.* Finite-element modeling and simulation of material behavior during electromagnetic metal forming. In *Proceedings of the 6th International ESAFORM Conference on Material Forming 28.-30. April 2003, Italy*, pages 971–974. ESAFORM 2003, 2003.

[14] *M. Stiemer, J. Unger, H. Blum, and B. Svendsen.* Algorithmic formulation and numerical implementation of coupled multifield models for electromagnetic metal forming simulations. 2004. in preparation.

[15] *H. Blum, H. Kleemann, A. Rademacher, T. Rauscher, A. Schroeder, and M. Stiemer.* SOFAR. www.mathematik.uni-dortmund.de/lsx/sofar, 2003.

[16] *M. Kleiner, A. Brosius, H. Blum, F. T. Suttmeier, M. Stiemer, B. Svendsen, J. Unger, and S. Reese.* Benchmark problems for coupled electromagnetic-mechanical metal forming processes. *Annalen der wissenschaftlichen Gesellschaft für Produktionstechnik*, 2004. in press.

[17] *F. Moon. Magnetic interactions in solids*. Springer-Verlag, 1980.

[18] *M. Schinnerl, J. Schöberl, M. Kaltenbacher, and R. Lerch.* Multigrid methods for the 3d simulation of nonlinear magneto-mechanical systems. *IEEE transactions magnetics*, 38:1497–1511, 2002.

[19] *J. C. Nédélec.* Mixed finite elements in $\mathbb{R}^3$. *Numerische Mathematik*, 35:315–341, 1980.

[20] *J. C. Nédélec.* A new family of mixed finite elements in $\mathbb{R}^3$. *Numerische Mathematik*, 50:57–81, 1986.

[21] *Ch. Großmann and H.-G. Roos. Numerik partieller Differentialgleichungen*. Teubner Studienbücher-Mathematik, Stuttgart, 1994.

[22] *S. Kulig, M. Klocke, A. Joswig, D. Peier, and M. Hinck.* Modellierung und Simulation der nichtlinearen elektromagnetischen kopplung zwischen Werkstück und Umformspule. In *Kolloquium elektromagnetische Umformung 2003*, 2003.

[23] *M. Klocke.* Computation of axisymmetric transient electromagnetic fields by finite-difference schemes including prescribed motion. In *6. International Symposium on Electric and Magnetic Fields (EMF) 2003*, 2003.

A new Finite Element Technology for the Numerical Simulation of High Speed Forming Processes

S. Reese[1], C. Leppin[2]

[1]Institute of Mechanics, Ruhr University Bochum, Germany;
[2]Alcan Technology & Management Ltd, Neuhausen, Switzerland

Abstract

In this contribution we propose a new solid-shell element formulation based on the concept of reduced integration with hourglass stabilization. Due to the absence of shear locking thin structures can be computed with only one element layer over the thickness. This enhances the computational efficiency in two ways. First of all the number of elements is reduced. Secondly, working with an explicit scheme, a larger critical time step is obtained. The damping and the mass matrix are not affected by the element technological treatment. The formulation is validated at first by typical element examples as well as two forming simulations.

1 Introduction

The numerical simulation of high speed forming processes demands high standards of finite element technology because the workpieces undergo extreme bending whereas the material is plastically incompressible. Especially in these situations standard low order finite element formulations exhibit the undesirable effect of locking. Consequences of this problem are too high stress values and an underestimation of the deformation. Obviously, if the finite element analysis is expected to support the production process by means of quantitatively reliable results the locking must be eliminated. One possibility is to work with higher order elements. However, such formulations require complicated meshing procedures and the coupling with contact algorithms is difficult. Another idea is to enrich the standard displacement-based low order formulation with additional modes in such a way that non-physical constraints (which are the basis for the locking) no longer appear. This so-called method of incompatible modes (or enhanced strain method in more modern terms) is based on a mixed variational principle, i.e. the so-called incompatible strain and the stress act as additional independent variables [1-4]. Formulations of this kind have the disadvantage that internal element variables have to be additionally determined. So their use leads to higher computational cost. In addition, numerical instabilities are frequently encountered in compressive deformation states.

Recently, several authors [5-12] have worked on the problem to transfer the enhanced strain method into finite element formulations based on reduced integration with hourglass

stabilization. It is well-known that such elements, see e. g. the Flanagan-Belytschko approach implemented into ABAQUS, show the important advantages of low numerical cost (in particular in explicit simulations) and robust deformation behaviour. Earlier approaches of this kind, as for instance the just mentioned one, have, however, suffered from the problematic facts that (I) the solution depends on a user-defined parameter and (II) the performance in bending is not satisfactory.

These difficulties are now overcome in the here proposed solid-shell approach (see also [12]) where additionally the "dynamic contributions", i. e. mass and damping terms, have been incorporated. In the suggested new formation the computation of these matrices can be performed in the same way as in the standard displacement approach. The dynamic simulation therefore poses hardly any additional coding effort. The keypoint of the new formulation is the Taylor expansion of the relevant stress quantity (usually the first Piola-Kirchhoff stress tensor) with respect to the normal through the centre of the element. In this way the original nine internal element variables can be reduced to three. Further the integration over the element volume reduces to an integration in thickness direction. Therefore only two Gauss points are needed in total which makes the element very efficient from the computational point of view. Certainly for certain applications it is recommended to work with several Gauss points over the thickness. Important is also the fact that the element, although it is able to exhibit the typical shell-like behaviour, has still eight nodes which are associated solely to *displacement* degrees-of-freedom. For this reason it is very suitable to be used in contact problems and can be easily coupled to classical solid elements. In contrast to many other shell formulations, no assumptions about the kinematics or the stress state are needed. So we are able to model a full three-dimensional stress state. Consequently, continuum mechanical material laws can be implemented without modification. It should also be emphasized that in explicit simulations the computational effort is proportional to the number of Gauss points. If we need only two Gauss points instead of eight in one element, the numerical cost is reduced by 75 $\%$.

In the present contribution we investigate the high speed forming of an axisymmetric workpiece by means of an implicit simulation where also the contact with the blankholder is taken into account. A similar computation has been carried out in [13], however with a different element technology. Questions such as convergence behaviour, robustness, computational efficiency, time stepping are discussed. The results show that the new element formulation has the potential to develop into an excellent tool for practical high speed forming simulations.

2 Variational functional

The present stabilization technique is strongly related to the enhanced strain method (EAS method) of Simo & Armero [1] whose formulation is based on the Hu-Washizu variational functional. To extend their approach to dynamics, we state the three equations

$$\begin{array}{lllll} \text{(I)} & \text{balance of linear momentum} & : & \operatorname{Div}\mathbf{P} + \rho_0\left(\mathbf{b}_v - \ddot{\mathbf{u}}\right) & = \mathbf{0} \\ \text{(II)} & \text{constitutive equation} & : & \mathbf{P} - \dfrac{\partial W}{\partial \mathbf{H}} - \mathcal{A}_d : \dot{\mathbf{H}} & = \mathbf{0} \\ \text{(III)} & \text{kinematical relation} & : & \mathbf{H} - \operatorname{Grad}\mathbf{u} & = \mathbf{0} \end{array} \tag{2.1}$$

where the strain energy function $W = W\left(\mathbf{H}, (\mathbf{X}_i, i = 1, ..., n)\right)$ is a function of the strain tensor $\mathbf{H}$ and n internal variables $\mathbf{X}_i$ $(i = 1, ..., n)$ to model inelasticity. The vector $\mathbf{u}$ is the displacement vector. The tensor $\mathbf{P}$ represents the first Piola-Kirchhoff stress tensor and $\mathcal{A}_d$ a constant fourth order tensor to model the damping properties of the material. The quantity $\rho_0\,\mathbf{b}_v$ denotes a volume force (e. g. gravity), ρ_0 is the mass density in the undeformed configuration. The dot characterizes a derivative with respect to time. In a linear elasticity framework ($\boldsymbol{\sigma}$ stress tensor, $\mathcal{C}$ elasticity tensor, $\mathcal{D}$ tensor to model damping properties), above equations would take the form (I) $\operatorname{div}\boldsymbol{\sigma} + \rho_0\left(\mathbf{b}_v - \ddot{\mathbf{u}}\right) = \mathbf{0}$, (II) $\boldsymbol{\sigma} - \mathcal{C} : \boldsymbol{\varepsilon} - \mathcal{D} : \dot{\boldsymbol{\varepsilon}} = \mathbf{0}$, (III) $\boldsymbol{\varepsilon} - \operatorname{sym}\left(\operatorname{grad}\mathbf{u}\right) = \mathbf{0}$. The present element technology is based on the idea to fulfill these three equations only in weak form, i. e. not pointwise. In this way so-called incompatible modes, expressed by the so-called "enhanced" strain $\mathbf{H}_{\mathrm{enh}} = \mathbf{H} - \operatorname{Grad}\mathbf{u}$, can be introduced. They are constructed in such a way that the undesirable defect of low order finite elements ("locking") is avoided. In the following sections of the paper the compatible strain $\operatorname{Grad}\mathbf{u}$ is alternatively denoted as $\boldsymbol{H}_{\mathrm{comp}}$.

The equations 2.1 are multiplied with test functions $\delta\mathbf{u}$, $\delta\mathbf{H}$ and $\delta\mathbf{P}$, respectively, followed by an integration over the domain under investigation (B_0). Assuming further that $\mathbf{P}$ is constant within the element, we can finally eliminate the independent stress field and arrive at two equations of weak form:

$$g_1\left(\mathbf{u}, \mathbf{H}_{\mathrm{enh}}\right) = \int_{B_0} \left(\frac{\partial W}{\partial \mathbf{H}} + \mathcal{A}_d : \dot{\mathbf{H}}\right) : \operatorname{Grad}\delta\mathbf{u}\; dV + \int_{B_0} \rho_0\,\ddot{\mathbf{u}} \cdot \delta\mathbf{u}\; dV - g_{\mathrm{ext}} \tag{2.2}$$

$$g_2\left(\mathbf{u}, \mathbf{H}_{\mathrm{enh}}\right) = \int_{B_0} \left(\frac{\partial W}{\partial \mathbf{H}} + \mathcal{A}_d : \dot{\mathbf{H}}\right) : \delta\mathbf{H}_{\mathrm{enh}}\; dV = 0 \tag{2.3}$$

where g_{ext} is a short hand notation for the virtual work of the external loading. Obviously, the stress-like strain-dependent quantity

$$\bar{\mathbf{P}} = \frac{\partial W}{\partial \mathbf{H}} + \mathcal{A}_d : \dot{\mathbf{H}} \tag{2.4}$$

takes over the role of the originally introduced stress $\mathbf{P}$. Due to the fact that $\mathbf{P}$ has been eliminated, we can simplify notation by omitting the bar in what follows: $\mathbf{P} = \bar{\mathbf{P}}$.

3 Interpolation

The present paper is restricted to 2D problems (assumption of plane strain or axisymmetry). It is then suitable to work with the vector notation

$$\boldsymbol{H}^T = \{H_{11}, H_{22}, H_{12}, H_{21}, H_{33}\} \tag{3.1}$$

where H_{ij} $(i, j = 1, 2, 3)$ are the coefficients of $\boldsymbol{H} = \sum_{i=1}^{3}\sum_{j=1}^{3} H_{ij}\,\mathbf{e}_i \otimes \mathbf{e}_j$ with $\mathbf{e}_i$ $(i = 1, 2, 3)$ denoting a cartesian basis. In order to distinguish between the plane strain and the axisymmetric case, we further introduce with $\boldsymbol{H}_{\mathrm{PS}}$ the part of $\boldsymbol{H}^T = \{\boldsymbol{H}_{\mathrm{PS}}^T, H_{33}\}$ which is needed to model plane strain. The vector notation of the other second order tensors is constructed analogously, whereas the fourth order tensors are accordingly reduced to 5x5 matrices.

We now work with the interpolation (indicated by the index h)

$$\boldsymbol{H}_{\mathrm{PS}}^h = \underbrace{\left(\boldsymbol{B}_0 + \boldsymbol{j}_0\,\boldsymbol{L}_{\mathrm{hg}}\,\boldsymbol{M}_{\mathrm{hg}}\right)\boldsymbol{U}_e}_{= (\boldsymbol{H}_{\mathrm{PS}}^h)_{\mathrm{comp}} = \boldsymbol{B}\,\boldsymbol{U}_e} + \underbrace{\boldsymbol{j}_0\,\boldsymbol{L}_{\mathrm{enh}}\,\boldsymbol{W}_e}_{= (\boldsymbol{H}_{\mathrm{PS}}^h)_{\mathrm{enh}}}. \tag{3.2}$$

Here $\boldsymbol{B}_0$ denotes the constant part of the classical "$\boldsymbol{B}$"-matrix. The latter is used to compute the "compatible" part of $\boldsymbol{H}^h_{\rm PS}$ ($\boldsymbol{U}_e$ element vector of nodal displacements). The matrix $\boldsymbol{j}$ is given by

$$\boldsymbol{j} = \begin{bmatrix} \dfrac{\partial\xi}{\partial X} & \dfrac{\partial\eta}{\partial X} & 0 & 0 \\ 0 & 0 & \dfrac{\partial\xi}{\partial Y} & \dfrac{\partial\eta}{\partial Y} \\ \dfrac{\partial\xi}{\partial Y} & \dfrac{\partial\eta}{\partial Y} & 0 & 0 \\ 0 & 0 & \dfrac{\partial\xi}{\partial X} & \dfrac{\partial\eta}{\partial X} \end{bmatrix}. \tag{3.3}$$

The quantities ξ and η are local coordinates defined on the reference domain $\Omega_e = [-1,1] \times [-1,1]$, the cartesian coordinates X and Y refer to the undeformed configuration. A quantity evaluated at the centre of the element ($\boldsymbol{\xi} = \{\xi,\eta\}^T = \boldsymbol{0}$) is indicated by the index 0. The vector $\boldsymbol{W}_e$ contains the additional (internal) element degrees-of-freedom. The matrices $\boldsymbol{L}_{\rm hg}$, $\boldsymbol{M}_{\rm hg}$, $\boldsymbol{L}_{\rm enh}$ read

$$\boldsymbol{L}_{\rm hg} = \begin{bmatrix} \eta & 0 \\ \xi & 0 \\ 0 & \eta \\ 0 & \xi \end{bmatrix}, \quad \boldsymbol{M}_{\rm hg} = \begin{bmatrix} \boldsymbol{\gamma}^T & \boldsymbol{0} \\ \boldsymbol{0} & \boldsymbol{\gamma}^T \end{bmatrix}, \quad \boldsymbol{L}_{\rm enh} = \begin{bmatrix} \xi & 0 & 0 & 0 \\ 0 & \eta & 0 & 0 \\ 0 & 0 & \xi & 0 \\ 0 & 0 & 0 & \eta \end{bmatrix}. \tag{3.4}$$

The vector $\boldsymbol{\gamma}$ represents the so-called stabilization vector originally introduced in [14].

In contrast to the plane strain case ($H_{33} = 0$), we need to find a suitable interpolation for H_{33} for the axisymmetric deformation case. It is well-known that H_{33} can be computed with $H_{33} = \frac{u_1}{R}$ where u_1 is the displacement in X-direction and R the X-coordinate of the point where we wish to calculate H_{33}. Using the standard isoparametric bilinear shape functions for the interpolation of u_1, H_{33} becomes a linear function of ξ and η. So it is not necessary to consider here the incompatible modes which would yield an additional quadratic contribution. We arrive with $N_I = (1+\xi\,\xi_I)\,(1+\eta\,\eta_I)/4$ at

$$H^h_{33} = \frac{u^h_1}{\bar{R}} = \sum_{I=1}^{4} N_I\, U_{e\,2\,I-1}/(4\,\bar{R}). \tag{3.5}$$

The latter equation can be rewritten as $H^h_{33} = (\boldsymbol{B}_{3\,0} + \boldsymbol{B}_{3\,\xi}\,\xi + \boldsymbol{B}_{3\,\eta}\,\eta + \boldsymbol{B}_{3\,\xi\eta}\,\xi\,\eta)\,\boldsymbol{U}_e$ with the matrices $\boldsymbol{B}_{3\,0}$, $\boldsymbol{B}_{3\,\xi}$, $\boldsymbol{B}_{3\,\eta}$ and $\boldsymbol{B}_{3\,\xi\eta}$ being defined as

$$\begin{array}{lllllll} \boldsymbol{B}_{3\,0} & = & \{1,0,1,0,1,0,1,0\}/(4\,\bar{R}), & & \boldsymbol{B}_{3\,\xi} & = & \{-1,0,1,0,1,0,-1,0\}/(4\,\bar{R}) \\ \boldsymbol{B}_{3\,\eta} & = & \{-1,0,-1,0,1,0,1,0\}/(4\,\bar{R}), & & \boldsymbol{B}_{3\,\xi\eta} & = & \{1,0,-1,0,1,0,-1,0\}/(4\,\bar{R}) \end{array} \tag{3.6}$$

Although R certainly varies in the element, it is set equal to the constant

$$\bar{R} = \frac{1}{4}\,(X_1 + X_2 + X_3 + X_4), \tag{3.7}$$

where X_I ($I = 1,...,4$) are the X-coordinates of the four nodes.

4 Constitutive equations

One central idea of the present formulation is to replace the stress vector $\boldsymbol{P}$ by its Taylor expansion around a point on the line $\boldsymbol{\xi}_\star = \{0, \eta\}^T$ (see Figure 1).

$$\begin{aligned} \boldsymbol{P} &\approx \boldsymbol{P}_\star + \left.\frac{\partial \boldsymbol{P}}{\partial \xi}\right|_{\boldsymbol{\xi}=\boldsymbol{\xi}^\star} (\xi - 0) \\ &= \boldsymbol{P}_\star + \left.\frac{\partial \boldsymbol{P}}{\partial \boldsymbol{H}^h_{\mathrm{PS}}}\right|_{\boldsymbol{\xi}=\boldsymbol{\xi}^\star} ((\boldsymbol{j}_0\, \boldsymbol{L}'_{\mathrm{hg}}\, \boldsymbol{M}_{\mathrm{hg}})\, \boldsymbol{U}_e + \boldsymbol{j}_0\, \boldsymbol{L}'_{\mathrm{enh}}\, \boldsymbol{W}_e) \\ &\quad + \left.\frac{\partial \boldsymbol{P}}{\partial H^h_{33}}\right|_{\boldsymbol{\xi}=\boldsymbol{\xi}^\star} (\boldsymbol{B}_{3\,\xi}\, \xi + \boldsymbol{B}_{3\,\xi\eta}\, \xi\, \eta)\, \boldsymbol{U}_e \end{aligned} \tag{4.1}$$

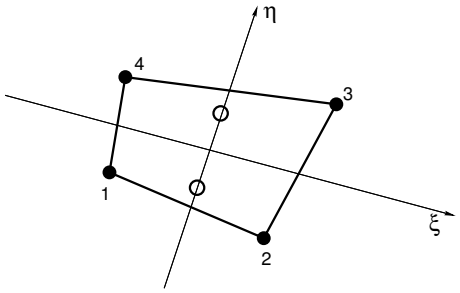

Figure 1: *Four-node element with coordinate system*

The expressions $\boldsymbol{L}'_{\mathrm{hg}}$ and $\boldsymbol{L}'_{\mathrm{enh}}$ are short notations for the partial derivatives $\partial \boldsymbol{L}_{\mathrm{hg}}/\partial\xi|_{\boldsymbol{\xi}=\boldsymbol{\xi}^\star}\ \xi$ and $\partial \boldsymbol{L}_{\mathrm{enh}}/\partial\xi|_{\boldsymbol{\xi}=\boldsymbol{\xi}^\star}\ \xi$, respectively. The relation 4.1 shows that $\boldsymbol{P}$ is now represented by a function which is linear in ξ. However, all three summands of $\boldsymbol{P}$ certainly still depend strongly non-linearly on the deformation. At this point one should be aware of the fact that a consistent linearization of these modified constitutive equations becomes highly complex. The computation of a so-called consistent tangent operator is necessary if the resulting finite element equation system is treated with an implicit solution scheme in combination with Newton's method. In the latter case, it is suitable to further simplify Equation 4.1 by replacing the partial derivatives of $\boldsymbol{P}$ with respect to $\boldsymbol{H}^h_{\mathrm{PS}}$ and H^h_{33} by constant matrices. Using additionally the assumption that $\boldsymbol{P}_{\mathrm{PS}}$ only depends on $\boldsymbol{H}^h_{\mathrm{PS}}$ whereas P_{33} is considered to depend on only H^h_{33} we finally obtain the constitutive equation

$$\boldsymbol{P} = \begin{Bmatrix} \boldsymbol{P}^\star_{\mathrm{PS}} \\ P^\star_{33} \end{Bmatrix} + \begin{bmatrix} \boldsymbol{A}^\star_{\mathrm{PS}} & \boldsymbol{0} \\ \boldsymbol{0}^T & A^\star_{33} \end{bmatrix} \begin{Bmatrix} \boldsymbol{j}_0\, \boldsymbol{L}'_{\mathrm{hg}}\, \boldsymbol{M}_{\mathrm{hg}}\, \boldsymbol{U}_e + \boldsymbol{j}_0\, \boldsymbol{L}'_{\mathrm{enh}}\, \boldsymbol{W}_e \\ (\boldsymbol{B}_{3\,\xi}\, \xi + \boldsymbol{B}_{3\,\xi\eta}\, \xi\, \eta)\, \boldsymbol{U}_e \end{Bmatrix} \tag{4.2}$$

The structure of the matrix $\boldsymbol{A}^\star_{\mathrm{PS}}$ is similar to the one of the elasticity matrix (with the Lamé constant Λ set equal to zero):

$$\boldsymbol{A}^\star_{\mathrm{PS}} = \begin{bmatrix} 2\,\mu^\star & 0 & 0 & 0 \\ 0 & 2\,\mu^\star & 0 & 0 \\ 0 & 0 & b\,\mu^\star & b\,\mu^\star \\ 0 & 0 & b\,\mu^\star & b\,\mu^\star \end{bmatrix}, \quad A^\star_{33} = 2\,\mu^\star \tag{4.3}$$

The factor b is equal to the ratio of the shorter with respect to the longer side length in one element. The parameter $\mu^\star$ equals the shear modulus if elastic material behaviour is considered. In plasticity we define the modulus $\mu^\star = \mu\, \widetilde{H}/(\widetilde{H} + E)$ where $\widetilde{H}$ represents the hardening

modulus at the onset of plastification (accumulated strain zero). For more details about the derivation of $\mu^\star$ and b see the discussion in [11], [15] and [12].

To conclude it should be mentioned that the influence of the second summand in Equation 4.2 vanishes with increasing number of elements. The material behaviour is dominated by the part $\boldsymbol{P}^\star$ which is left unchanged if one compares with the standard formulation. The second term yields the so-called "hourglass cernel" the choice of which is relatively arbitrary. Note that we provide here a physically-based form such that the "hourglass parameter" $\mu^\star$ does not have to be chosen manually.

5 Derivation of element matrices and vectors

The modified constitutive equations 4.2 are now inserted into the weak forms 2.3. Additionally, it is important to mention that the determinant J of the Jacobi matrix $\boldsymbol{J} = \partial \boldsymbol{X}/\partial \boldsymbol{\xi}$ (with $\boldsymbol{X} = \{X, Y\}^T$) is always evaluated in the centre of the element. The error introduced by this approximation vanishes with increasing number of elements. On the other hand we gain the important advantage that many terms drop out of the formulation.

5.1 Computation of internal element variables

From the second part of the weak form which has to be fulfilled elementwise one obtains

$$\boldsymbol{R}_w\,(\boldsymbol{U}_e, \boldsymbol{W}_{e\,\eta}) = \int_{\eta=-1}^{\eta=1} (\boldsymbol{L}_{\mathrm{enh}}^{\bullet\star})^T\, \boldsymbol{j}_0^T\, \boldsymbol{P}_{\mathrm{PS}}^\star\; J_0\, 2\, t\, d\eta = \boldsymbol{0} \tag{5.1}$$

where the matrix $\boldsymbol{L}_{\mathrm{enh}}^{\bullet\star}$ is computed with

$$(\boldsymbol{L}_{\mathrm{enh}}^{\bullet\star})^T = \begin{bmatrix} 0 & \eta & 0 & 0 \\ 0 & 0 & 0 & \eta \end{bmatrix}. \tag{5.2}$$

The letter t indicates the thickness of the element if we deal with the plane strain case. For axisymmetry t reads $t = 2\,\pi\,\bar{R}$. The vector of the internal element variables $\boldsymbol{W}_e^T = \{W_{e\,1}, W_{e\,2}, W_{e\,3}, W_{e\,4}\}^T$ can be split into two parts. Two of the four internal element variables ($W_{e\,1}$ and $W_{e\,3}$, included in $\boldsymbol{W}_{e\,\xi} = \{W_{e\,1},\, W_{e\,3}\}^T$) are never explicitly determined because the vector $\boldsymbol{W}_{e\,\xi}$ can be expressed in terms of the nodal degrees-of-freedom:

$$\boldsymbol{W}_{e\,\xi} = -\boldsymbol{K}_{ww}^{-1}\, \boldsymbol{K}_{wu}\, \boldsymbol{U}_e \tag{5.3}$$

The matrices $\boldsymbol{K}_{ww}$ and $\boldsymbol{K}_{wu}$ read

$$\begin{aligned} \boldsymbol{K}_{ww} &= \int_{\xi=-1}^{\xi=1} (\boldsymbol{L}_{\mathrm{enh}}^{\prime\star})^T\, \boldsymbol{j}_0^T\, \boldsymbol{A}_{\mathrm{PS}}^\star\, \boldsymbol{j}_0\, \boldsymbol{L}_{\mathrm{enh}}^{\prime\star}\; J_0\, 2\, t\, d\xi \\ \boldsymbol{K}_{wu} &= \int_{\xi=-1}^{\xi=1} (\boldsymbol{L}_{\mathrm{enh}}^{\prime\star})^T\, \boldsymbol{j}_0^T\, \boldsymbol{A}_{\mathrm{PS}}^\star\, \boldsymbol{j}_0\, \boldsymbol{L}_{\mathrm{hg}}^{\prime}\, \boldsymbol{M}_{\mathrm{hg}}\; J_0\, 2\, t\, d\xi := \boldsymbol{K}_{uw}^T \end{aligned} \tag{5.4}$$

with $(\boldsymbol{L}_{\mathrm{enh}}^{\prime\star})^T$ being defined as

$$(\boldsymbol{L}_{\mathrm{enh}}^{\prime\star})^T = \begin{bmatrix} \xi & 0 & 0 & 0 \\ 0 & 0 & \xi & 0 \end{bmatrix}. \tag{5.5}$$

In summary, the relation 5.1 represents a non-linear equation to determine the internal variables $\boldsymbol{W}_{e\,\eta} = \{W_{e\,2}, W_{e\,4}\}^T$ at the element level. The integration over η has to be performed numerically, i.e. the integrand has to be evaluated at (at least) two Gauss points located on the line $\boldsymbol{\xi}^\star = \{0, \eta\}^T$ (see the circled positions in Figure 1). Since $\boldsymbol{R}_w$ depends on $\boldsymbol{U}_e$ the solution of Equation 5.1 has to be embedded in the solution of the "global" finite element equations to be derived in what follows.

5.2 Derivation of the global equation system

The first part of the weak form yields after several calculation steps the relation

$$\begin{aligned} \tilde{g}_{1\,e} &= \delta\boldsymbol{U}_e^T\,(\boldsymbol{R}^0_{u\,\mathrm{PS}} + \boldsymbol{R}^0_{u\,33} + \boldsymbol{R}^{\mathrm{hg}}_{u\,\mathrm{PS}} + \boldsymbol{R}^{\mathrm{hg}}_{u\,33} + \boldsymbol{D}_e\,\dot{\boldsymbol{U}}_e + \boldsymbol{M}_e\,\ddot{\boldsymbol{U}}_e \\ &\quad + (\boldsymbol{K}^{\mathrm{hg}}_{uu\,\mathrm{PS}} + \boldsymbol{K}^{\mathrm{hg}}_{uu\,33})\,\boldsymbol{U}_e + \boldsymbol{K}_{uw}\,\boldsymbol{W}_{e\,\xi}) \end{aligned} \tag{5.6}$$

The first two summands are the parts of the classical residual force vector computed by means of the constant $\boldsymbol{B}$-matrices $\boldsymbol{B}_0$ and $\boldsymbol{B}_{3\,0}$, respectively:

$$\boldsymbol{R}^0_{u\,\mathrm{PS}} = \int_{\eta=-1}^{\eta=1} \boldsymbol{B}_0^T\,\boldsymbol{P}^\star_{\mathrm{PS}}\,J_0\,2\,t\,d\eta, \quad \boldsymbol{R}^0_{u\,33} = \int_{\eta=-1}^{\eta=1} \boldsymbol{B}_{3\,0}^T\,P^\star_{33}\,J_0\,2\,t\,d\eta \tag{5.7}$$

The parts $\boldsymbol{R}^{\mathrm{hg}}_{u\,\mathrm{PS}}$ and $\boldsymbol{R}^{\mathrm{hg}}_{u\,33}$ would also appear in a fully integrated element. They take here the forms

$$\boldsymbol{R}^{\mathrm{hg}}_{u\,\mathrm{PS}} = \int_{\eta=-1}^{\eta=1} \boldsymbol{M}^T_{\mathrm{hg}}\,(\boldsymbol{L}^{\bullet\star}_{\mathrm{hg}})^T\,\boldsymbol{j}_0^T\,\boldsymbol{P}^\star_{\mathrm{PS}}\,J_0\,2\,t\,d\eta, \quad \boldsymbol{R}^{\mathrm{hg}}_{u\,33} = \int_{\eta=-1}^{\eta=1} \eta\,\boldsymbol{B}_{3\,\eta}^T\,P^\star_{33}\,J_0\,2\,t\,d\eta \tag{5.8}$$

The computation of the element damping matrix $\boldsymbol{D}_e$ and the element mass matrix $\boldsymbol{M}_e$ is carried out as in classical displacement-based formulations, see the common text books [16] or [17]. If finally remains to determine the matrices $\boldsymbol{K}^{\mathrm{hg}}_{uu\,\mathrm{PS}}$ and $\boldsymbol{K}^{\mathrm{hg}}_{uu\,33}$:

$$\begin{aligned} \boldsymbol{K}^{\mathrm{hg}}_{uu\,\mathrm{PS}} &= \int_{\xi=-1}^{\xi=1} \boldsymbol{M}^T_{\mathrm{hg}}\,(\boldsymbol{L}'_{\mathrm{hg}})^T\,\boldsymbol{j}_0^T\,\boldsymbol{A}^\star_{\mathrm{PS}}\,\boldsymbol{j}_0\,\boldsymbol{L}'_{\mathrm{hg}}\,\boldsymbol{M}_{\mathrm{hg}}\,J_0\,2\,t\,d\xi \\ \boldsymbol{K}^{\mathrm{hg}}_{uu\,33} &= \frac{4}{3}\,\boldsymbol{B}^T_{3\,\xi} A^\star_{33}\,\boldsymbol{B}_{3\,\xi}\,J_0\,t + \frac{4}{3}\,\boldsymbol{B}^T_{3\,\eta} A^\star_{33}\,\boldsymbol{B}_{3\,\eta}\,J_0\,t + \frac{4}{9}\,\boldsymbol{B}^T_{3\,\xi\eta} A^\star_{33}\,\boldsymbol{B}_{3\,\xi\eta}\,J_0\,t \end{aligned} \tag{5.9}$$

Using Equation 5.3, the second line of Equation 5.6 reduces to $(\boldsymbol{K}^{\mathrm{hg}}_{uu\,\mathrm{PS}} + \boldsymbol{K}^{\mathrm{hg}}_{uu\,33} - \boldsymbol{K}_{uw}\,\boldsymbol{K}^{-1}_{ww}\,\boldsymbol{K}_{wu})\,\boldsymbol{U}_e := \boldsymbol{K}_{\mathrm{stab}}\,\boldsymbol{U}_e$. Due to the fact that the integrands included in the matrices $\boldsymbol{K}^{\mathrm{hg}}_{uu\,\mathrm{PS}}$, $\boldsymbol{K}^{\mathrm{hg}}_{uu\,33}$, $\boldsymbol{K}_{ww}$ and $\boldsymbol{K}_{uw}$ are polynomials in ξ, the corresponding integrations can be performed analytically. Therefore we do not need any numerical integration procedure to determine the "hourglass stabilization matrix" $\boldsymbol{K}_{\mathrm{stab}}$. One finally arrives at the relation

$$\tilde{g}_{1\,e} = \delta\boldsymbol{U}_e^T\,(\boldsymbol{R}_u\,(\boldsymbol{U}_e, \boldsymbol{W}_{e\,\eta}) + \boldsymbol{D}_e\,\dot{\boldsymbol{U}}_e + \boldsymbol{M}_e\,\ddot{\boldsymbol{U}}_e + \boldsymbol{K}_{\mathrm{stab}}\,\boldsymbol{U}_e), \tag{5.10}$$

where the abbreviation

$$\boldsymbol{R}_u := \boldsymbol{R}^0_{u\,\mathrm{PS}} + \boldsymbol{R}^0_{u\,33} + \boldsymbol{R}^{\mathrm{hg}}_{u\,\mathrm{PS}} + \boldsymbol{R}^{\mathrm{hg}}_{u\,33} \tag{5.11}$$

has been introduced.

The element quantities are assembled to yield the global time-continuous differential equation system

$$\boldsymbol{R}_{u\,G}\left(\boldsymbol{U}\right) + \boldsymbol{K}_{\mathrm{stab}\,G}\,\boldsymbol{U} + \boldsymbol{D}_G\,\dot{\boldsymbol{U}} + \boldsymbol{M}_G\,\ddot{\boldsymbol{U}} - \boldsymbol{F}_{\mathrm{ext}} = \boldsymbol{0} \tag{5.12}$$

where the index G refers to the global level and $\boldsymbol{U}$ denotes the *global* vector of nodal displacements. $\boldsymbol{F}_{\mathrm{ext}}$ is the global external load vector. It is assumed that the internal element variables $\boldsymbol{W}_{e\,\eta}$ are determined at the element level such that they do not enter the global equation system.

The time discretization can be carried out with any implicit or explicit integration scheme, such as e.g. the Newmark method, the generalized α-method (implicit schemes) or the method of finite differences (explicit scheme). Note that only the former procedure requires the solution of a non-linear equation system.

5.3 Summary

To conclude we summarize the differences of the present stabilized reduced integration technique with respect to standard displacement-based approaches as well as alternative locking-free element formulations.

Implementation:

- Instead of a full (2x2) integration the present formulation requires only two Gauss points (located on the line $\boldsymbol{\xi}^{\star} = \{0, \eta\}$).
- We have to solve the non-linear equation $\boldsymbol{R}_w = \boldsymbol{0}$ at the element level. These are two scalar equations. Obviously the computational effort caused by this additional step is very small.
- The hourglass stabilization matrix which is given by an analytical expression has to be computed once per time step in an extra subroutine.
- The use of the modified constitutive equations means to work with an “anisotropic” ansatz. For this reason in each element a coordinate transformation has to be carried out which clearly identifies the thickness direction.
- The formulation can be easily implemented into a commercial finite element code. In contrast to the standard displacement approach the storage of the internal element variables has to be performed. This is, however, also necessary for the enhanced strain method which is already commonly offered in commercial finite element tools. The additional element variables are not needed for thin shell geometries.

User:

- Neither the input nor the computation requires special care. For certain applications a manual choice of the hourglass parameter $\mu^{\star}$ and the shear reduction factor b would be useful.

Advantages:

- The element is free of volumetric, shear and membrane locking. This property is usually only achieved in the framework of highly sophisticated shell formulations.
- Due to the absence of shear locking, thin shell computations can be carried out with only one element over the thickness. First of all this reduces the computational effort enormously. Secondly, the ratio of the element side lengths is less extreme such that the critical time step for the explicit time integration is significantly increased.

  Thus both, the number of elements and the number of time steps can be reduced!
- The element possesses four nodes. The extension of the structure in thickness direction is correctly displayed. This property proves to be in particular advantageous for the contact modelling.
- It is trivial to take several elements over the thickness. Usually this is necessary for the modelling of thick structures.
- The elements can be easily coupled to classical 2D elements.

6 Examples

6.1 Cylindrical shell under line load

Geometry and boundary conditions for this example are plotted in Figure 2a. All quantities are given in N and mm. The material is elastic (with the parameters given in Section 5.4.1 [18]). We investigate first a cylindre with a rather small length/thickness ratio ($L/t = 10$). The discretization is chosen in such a way that the element side length ratio is equal to one. The load is applied in 100 equal steps (inertia effects neglected). For such a so-called thick shell it cannot be expected that one element over the thickness is sufficient. The results of the present element formulation (Q1SPs) are compared to the ones obtained with the reduced integration technique Q1SPe [15] where the special shell-like deformation behaviour is not taken into account. The study of convergence (Figure 2b) shows that the use of Q1SPs yields much better convergence behaviour. A discretization with 4x40 elements is already sufficient to obtain an accurate result. It becomes also evident that the choice of $\mu^\star$ influences the convergence behaviour but not the final result ("mopt"$= \mu$). It is recommended to choose $\mu^\star$ ("m") as small as possible. However, too small values make the element rather sensitive to severe mesh distortion. If the internal element variables are set equal to zero we obtain the result described by "oenh". Practically then we work with a thin shell element technology which is (as expected) not suitable for thick shell applications.

For a very thin shell geometry with $R/t = 1000$ the element shows an outstanding convergence behaviour. The load is applied in the following way: 10 x 0.001, 19 x 0.01, 20 x 0.04. We

obtain for the maximum displacement in horizontal direction the results: 10x1 el.: 2.96, 20x1 el.: 3.00, 40x1 el.: 3.02, 80x1 el.: 3.03 ($\mu^\star = 4\,\mu$). These results do not vary if the discretization in thickness direction is refined. Further the enhanced degrees-of-freedom are not needed here, i.e. they do not influence the results. It can be concluded that we obtain a very strong *thin* shell element if the additional element degrees-of-freedom are set equal to zero. Interestingly also the factor b has a very small influence on the result. In contrast, Q1SPe reacts very sensitively, it is clearly not suitable for such thin structures.

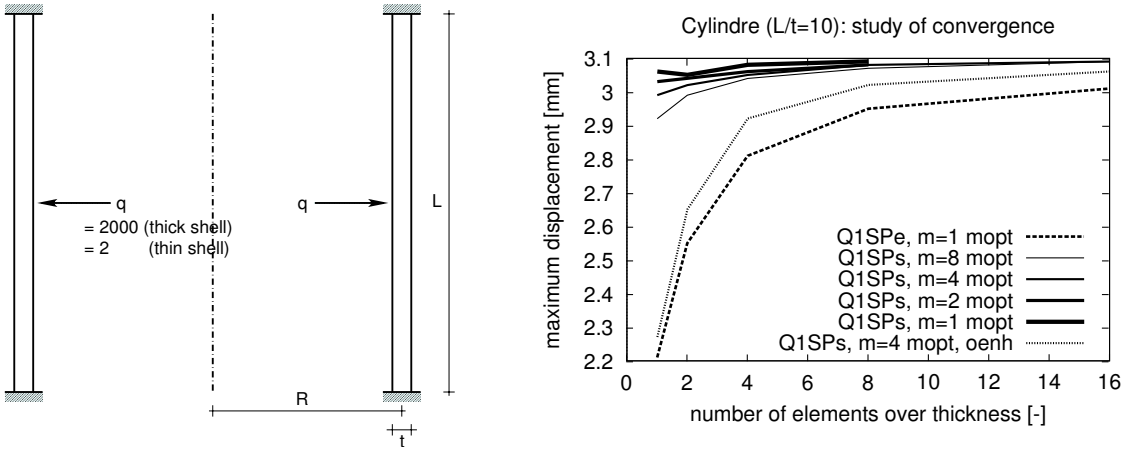

Figure 2: *(a) Geometry and boundary conditions of a cylindrical shell*
(b) Study of convergence (shell with $R/t = 10$)

6.2 Pinched cylinder with end diaphragms

Another challenging example to test the bending behaviour is the so-called “cola can”. We work here with a general shell geometry, i.e. the eight-noded Q1SPs. For symmetry reasons, only one eighth of the structure has to be discretized (see Figure 3a). The displacement w_A at node A ($X_1 = X_3 = 0\,\mathrm{mm}$, $X_2 = 301.5\,\mathrm{mm}$) is controlled in such a way that it moves downwards (w_A). Besides the symmetry conditions applied on the planes $X_1 = 0\,\mathrm{mm}$, $X_2 = 0\,\mathrm{mm}$ and $X_3 = 0\,\mathrm{mm}$ we have constraints in X_1- and X_2-direction (diaphragm) on the plane $X_3 = 300\,\mathrm{mm}$. The material is assumed to be elasto-plastic, see [11] for more details.

In Figure 4a, the contours of the yield criterion Φ are plotted on a deformed configuration of the structure ($w_A = 200\,\mathrm{mm}$). Figure 4b shows the plastic zone. A study of convergence is plotted in Figure 3b. The comparison with QM1/E12 (see Wriggers et al. [19]) and the 6-parameter shell formulation of Eberlein & Wriggers [20] shows that the convergence behaviour is very satisfactory. Concerning the choice of the load steps it should be mentioned that with increasing number of elements also the problem of wrinkling, i. e. structural instability, arises. So for the discretization 64x2x32 the load step had to be partially reduced to $\Delta w_A = 0.5\,\mathrm{mm}$. In comparison, for the mesh 32x2x16, the computation could be performed with $\Delta w_A = 2\,\mathrm{mm}$.

6.3 Electromagnetic forming

The following example serves to validate Q1SPs in the context of high speed forming. For this purpose we carry out the finite element simulation of an electromagnetic forming process.

The tool coil creates a magnetic field which introduces an electric current in the sheet metal. Due to the interaction with the magenetic field Lorentz forces are generated and the workpiece deforms. The experimental procedure yields the distribution of the Lorentz forces in normal and tangential direction at discrete points in space (radius r, thickness coordinate y) and time.

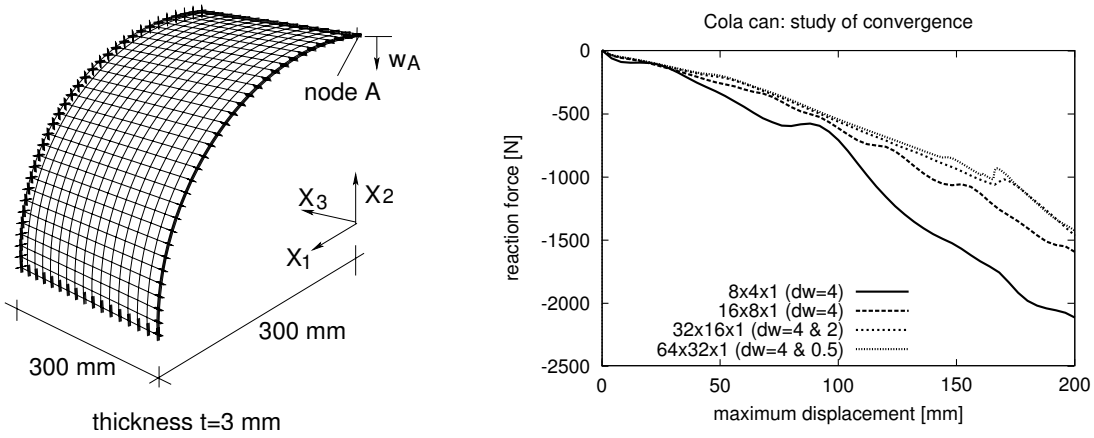

Figure 3: *Pinched cylinder (a) Geometry, discretization, boundary conditions (b) Study of convergence*

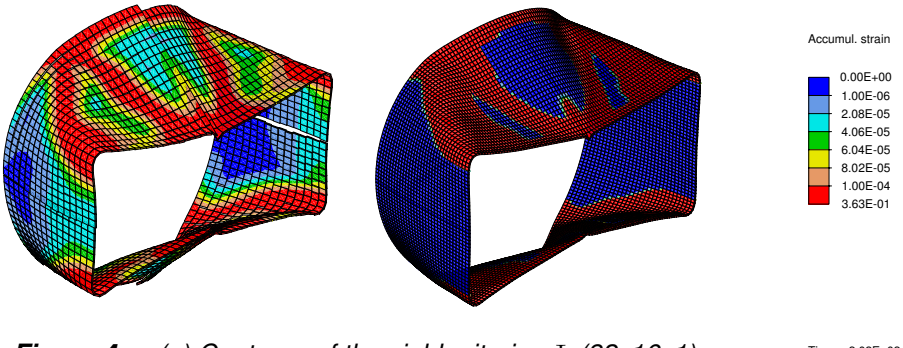

Figure 4: *(a) Contours of the yield criterion Φ (32x16x1) (b) Plastic zone (64x32x1)*

To prepare the data for the input into the finite element program system, each point $P = (r, y)$ has to be associated with the closest Gauss point in the structure discretized with finite elements. This is suitably done by means of a search procedure to find the element which includes the point P followed by a computation of the distances to the Gauss points of the corresponding element. In the FE computation, the element routine reads at each time the Lorentz force components for this Gauss point. The present time is compared to the discrete times where the function is prescribed. In between a linear dependence on time is assumed. The Lorentz force acts together with the mass inertia as volume force on the finite element system.

Interestingly, in comparison to the previous examples, the shear locking plays here only a subordinate role. This might be attributed to the fact that the structural behaviour is membrane-like, i.e. bending plays only a subordinate role. Nevertheless we have still the important advantage that the computation can be performed with only one element over the thickness, something not possible with Q1SPe [13]. In Figure 5, the computed deformed configurations

with the present code (FEAP, Finite Element Analysis Program) are compared to the results achieved with MARC [13], however using a slightly different hardening rule in the elastoplastic material law. Obviously a highly satisfactory agreement is obtained.

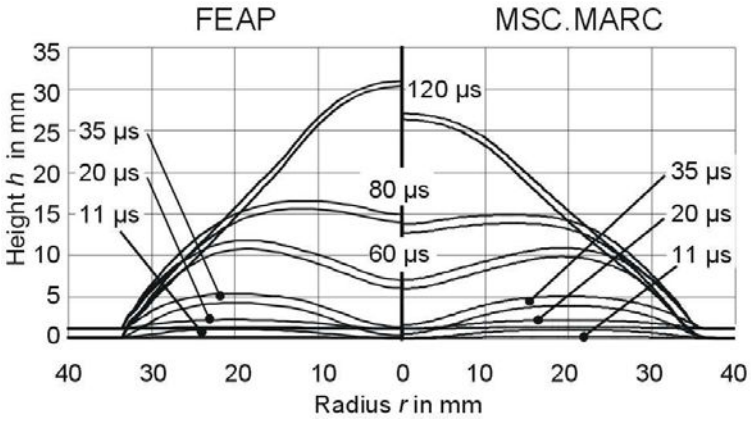

Figure 5: *Intermediate stages of the simulation*

6.4 Deep drawing

We finally investigate the deep drawing of a sheet metal of the radius a and the thickness $3.7714 \cdot 10^{-3}\, a$. More details about the geometry and the boundary conditions cannot be documented due to secrecy agreements. The structure is discretized with 60 elements in radial direction and only one element over the thickness. The frictional contact between the punch and the workpiece is taken into account by means of a penalty formulation. The intermediate stages of the deep drawing process are shown in Figure 6. The contours refer to the accumulated plastic strain.

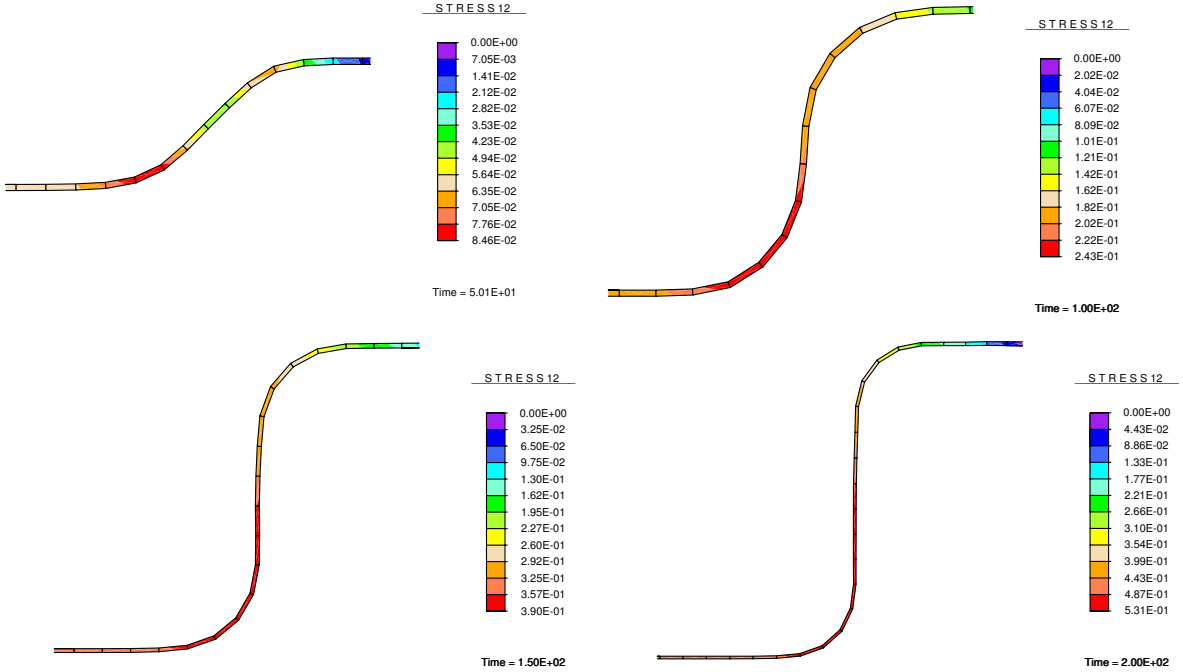

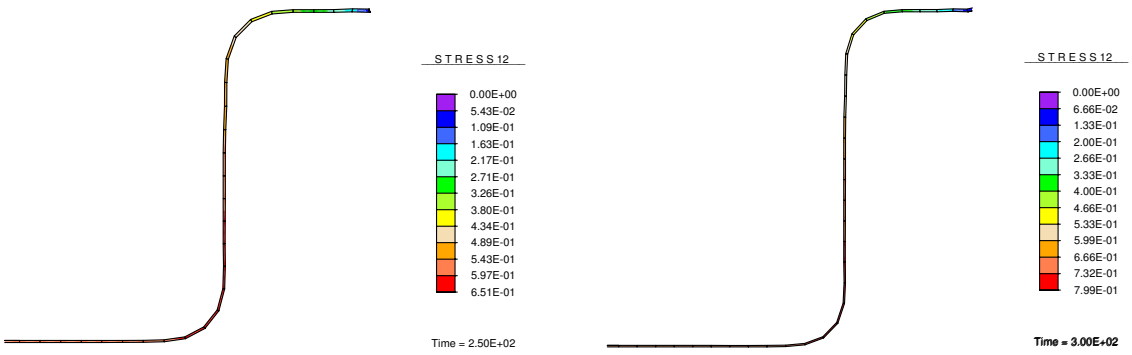

Figure 6: *Intermediate stages in deep drawing simulation*

The simulation can be performed with 3000 implicit steps and takes about 10 min on a modern personal computer. Interestingly the thick shell formulation behaves in this application rather sensitively. The computation can be performed robustly only with the thin shell formulation (without the internal element degrees-of-freedom). However, the radius/thickness ratio of the sheet metal is such that the thin shell assumption is easily justified, especially if one takes the extreme thinning of the structure in the last stages into account.

Future work should be directed to more complex forming applications and a comparison with experimental data.

References

[1] *Simo, J.C., F. Armero*, Geometrically nonlinear enhanced strain mixed methods and the method of incompatible modes. *International Journal for Numerical Methods in Engineering* **33**, 1413–1449, 1992.

[2] *Simo, J.C., F. Armero, R.L. Taylor*, Improved versions of assumed enhanced strain tri-linear elements for 3D finite deformation problems. *Computer Methods in Applied Mechanics and Engineering* **110**, 359–386, 1993.

[3] *Cao, Y.P., N. Hu, J. Lu, H. Fukunaga, Z.H. Yao*, A 3D brick element based on Hu-Washizu variational principle for mesh distortion. *International Journal for Numerical Methods in Engineering* **53**, 2529–2548, 2002.

[4] *Areias, P.M.A., J.M.A. César de Sá, C.A. Conceicao António, A.A. Fernandes*, Analysis of 3D problems using a new enhanced strain hexahedral element. *International Journal for Numerical Methods in Engineering* **58**, 1637–1682, 2003.

[5] *Belytschko, T., L.P. Bindeman*, Assumed strain stabilization of the eight node hexahedral element, *Computer Methods in Applied Mechanics and Engineering* **105**, 225–260, 1993.

[6] *Liu, W.K., Y. Guo, S. Tang, T. Belytschko*, A multiple-quadrature eight-node hexahedral finite element for large deformation elastoplastic analysis, *Computer Methods in Applied Mechanics and Engineering* **154**, 69–132, 1998.

[7] *Puso, M.A.*, A highly efficient enhanced assumed strain physically stabilized hexahedral element, *International Journal for Numerical Methods in Engineering* **49**, 1029–1064, 2000.

[8] *Reese, S., B.D. Reddy, P. Wriggers*, A new locking-free brick element technique for large deformation problems in elasticity, *Computer and Structures* **75**, 291–304, 2000.

[9] *Cardoso, R.P.R., J.-W. Yoon, J.J. Grácio, F. Barlat, J.M.A. César de Sá*, Development of a one point quadrature shell element for nonlinear applications with contact and anisotropy, *Computer Methods in Applied Mechanics and Engineering* **191**, 5177–5206, 2002.

[10] *Legay, A., A. Combescure*, Elastoplastic stability analysis of shells using the physically stabilized finite element SHB8PS, *International Journal for Numerical Methods in Engineering* **57**, 1299–1322, 2003.

[11] *Reese, S.*, On a physically stabilized one point finite element formulation for three-dimensional finite elasto-plasticity, submitted to *Computer Methods in Applied Mechanics and Engineering*, 2004.

[12] *Reese, S.*, On a new large deformation solid-shell concept based on reduced integration, submitted to *International Journal for Numerical Methods in Engineering*, 2004.

[13] *Kleiner, M., A. Brosius, H. Blum, F.-T. Suttmeier, M. Stiemer, B. Svendsen, J. Unger, S. Reese*, Benchmark simulation for coupled electromagnetic-mechanical metal forming processes, to be published in WGP.Annalen, 2004.

[14] *Belytschko, T., J.S.-J. Ong, W.K. Liu, J.M. Kennedy*, Hourglass control in linear and nonlinear problems, *Computer Methods in Applied Mechanics and Engineering* **43**, 251–276, 1984.

[15] *Reese, S.*, On a consistent hourglass stabilization technique to treat large inelastic deformations and thermo-mechanical coupling in plane strain problems, *International Journal for Numerical Methods in Engineering* **57**, 1095–1127, 2003.

[16] *Bathe, K.-J.*, *Finite-Elemente-Methoden*,Springer, Berlin, 1986.

[17] *Hughes, T.J.R.*, *The Finite Element Method*, Prentice-Hall, Englewood Cliffs, 1987.

[18] *Eberlein, R.*, Finite-Elemente-Konzepte für Schalen mit großen elastischen und plastischen Verzerrungen, Dissertation, Fachbereich Mechanik, Technische Universität Darmstadt, 1997.

[19] *Wriggers, P., R. Eberlein, S. Reese*, A comparison of three-dimensional and shell elements for finite plasticity, International Journal of Solids and Structures **33**, 3309–3326, 1996.

[20] *Eberlein, R., P. Wriggers*, Finite element concepts for finite elastoplastic strains and isotropic stress response in shells: theoretical and computational analysis, *Computer Methods in Applied Mechanics and Engineering* **171**, 243–279, 1999.

Influence of Different Material Models on the Result of Numerical High Speed Cutting Simulations*

Th. Halle[1], L. W. Meyer[2]

[1] Materials and Impact Engineering, Chemnitz University of Technology, Germany
[2] Chair Materials and Impact Engineering, Chemnitz Univ. of Technology,Germany

Abstract

Extreme conditions for the workpiece and the tool can occur in high speed cutting processes. Temperatures above 1000 °C at very high strains over 3 and strain rates near 105 1/s are not unusual. In the first part of this paper an overview about the well known and new developed testing methods for these extreme conditions is given. For numerical simulations it is necessary to formulate closed material models which include strain, strain rate, and the temperature.

In the second part some well known material models are presented and compared. Furthermore, advantages and disadvantages are named. The flow stress behaviour of two types of steel (1.1191, 1.2311) as a function of strain rate and temperature is presented. A Johnson-Cook and a Zerilli-Armstrong model is used for the comparative numerical simulations of an orthogonal cutting process. To indicate the process of chip segmentation, a damage model is often used. The influence of various damage models with different damage parameters and failure modes is shown. The calculated cutting forces and the shape of the chips are compared with results determined at a quickstop cutting device with integrated force measurement. Additionally, the calculated chip formation is compared with the measured shape by means of highspeed photography. The temperatures, forces, and chip shape for both used models are presented and the influence of different material models are evaluated and named.

Keywords:

Material, Modelling, Simulation

**This work is based on the results of DFG priority program "High Speed Cutting". The authors would like to thank the Deutsche Forschungsgemeinschaft (DFG) for their financial support.*

1 Introduction

For the simulation of High Speed Cutting processes, it is necessary to have reliable material data, friction data, and some other important variables. For highest accuracy of the FE-Simulation, these data measured should match the range of temperature, strain, and strain rate which occur in the machining processes. This paper gives a short overview of the devices to obtain this data and demonstrates the influence of material models on the simulation results. In order to describe the effect of different material data, all other variables, like friction, heat capacity, etc. are kept constant. Therefore, influence of friction and other parameters are not considered (see [1] for a description and reliable values of these parameters). In order to use constitutive equations of the Johnson/Cook- or Zerilli/Armstrong-type, the measured high rate adiabatic data have to be transferred into isothermal data.

2 Material and methods

In the case of High Speed Cutting (HSC) strain rates up to 2*105 do occur. To obtain the relevant material data, many researchers use the split Hopkinson pressure bar [2]. Depending on the specimen geometry, strain rates up to 20.000 1/s are possible. In the case of compression tests the maximum strain is about 0.5…0.6. The strain limit in tension testing is about 0,25, for high strength materials this value is reduced to 0,1 or less. Only with torsion tests it is possible to obtain flow stresses at very high strain rates and higher strains. In addition to the difficulty to measure flow stresses at high strain rates, it is essential to measure the flow behaviour at high temperatures up to 1000 °C. An overview of the possibilities to estimate material data at very high strain, temperatures, and strains is given in these proceedings by Meyer [3]. Therefore, in this paper only two devices developed for material testing at high strain rates and simultaneous high temperatures are named shortly.

2.1 Materials

Two steels C45E (1.1191) and 40CrMnMo7 (1.2311) were tested. The steel C45E is a quenched and tempered steel and is used in a wide range of technical

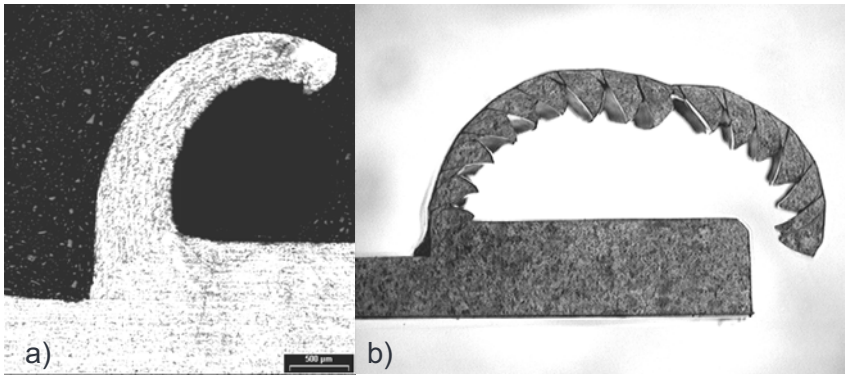

Figure 1: *a) continued chip C45 and b) segmented chip 40CrMnMo7 both obtained at a quick-stop device [4]*

applications. The steel 40CrMnMo7 is a tool steel and is often used for molds and dies. This material presents different chip shapes at HSC conditions. The C45E exhibits continuous chips up to high cutting speeds for cutting depths lower than 0.65 mm. In contrast to C45E the 40CrMnMo7 lead to chip segmentation (see Figure 1).

2.2 Testing Devices

In order to achieve highest strain rates, two testing devices were applied to measure the flow stress behaviour. For dynamic compression loading the split-Hopkinson-pressure-bar was used. High rate torsion loading was accomplished with a high speed torsion machine. Both test set-ups will be introduced briefly. For a closer look or other testing devices which can be used to determine high strain rate properties, the reader is reprehend to Meyer [3].

At the TUC the principle of SHPB is implemented in a rotating wheel which is described elsewhere [5]. The load is directly applied to the sample. A specification of the test set-up is presented in [6]. Tests up to strain rates of $10^4\,s^{-1}$ at temperatures above 1000°C are possible. However, flow curves up to relatively low strains of 0.05 to 0.15 can be obtained. For a simulation, flow stresses at higher strains are necessary. Therefore, a new type of torsion setup was developed in Chemnitz [3]. The principle is based on a direct loading of the torsion sample which is connected to a torsion Hopkinson bar. The machine is able to rotate up to 3000 rpm with no limitations regarding the rotating angle. This means, in dependence of the used specimen geometries, strain rates up to 10^4 1/s are possible.

2.3 Material Models

For the examination of the influence of various constitutive equations on the quality of the simulation, the models proposed by Johnson-Cook and Zerilli-Armstrong are used. Both models have a wide distribution to describe the flow stress behaviour of metallic materials. Especially the Johnson-Cook (JC) [7] model is often used for numerical simulations and is implemented in many implicit or explicit simulation tools. The Zerilli-Armstrong (ZA) [8] model is based on semi-empiric equations with respect to the mechanism of thermal activation [9].
The following equations represent the models of JC (Equation 1) and ZA (Equation 2, 3):

$$\sigma = \left(A + B\varepsilon^{n}\right)\cdot\left(1 + C\,ln\,\dot{\varepsilon}\right)\cdot\left[1 - \left(\frac{T - T_{room}}{T_{melt} - T_{room}}\right)^{m}\right] \tag{1}$$

$$\overset{krz}{\sigma} = \Delta\sigma_G + B_0\cdot exp\left[\left(-\beta_0 + \beta_1\,ln\,\dot{\varepsilon}\right)T\right] + k_0\varepsilon^{n} + k_{\varepsilon}\lambda^{-\frac{1}{2}} \tag{2}$$

$$\overset{kfz}{\sigma} = \Delta\sigma_G + B_0\cdot exp\left[\left(-\beta_0 + \beta_1\,ln\,\dot{\varepsilon}\right)T\right] + k_{\varepsilon}\lambda^{-\frac{1}{2}} \tag{3}$$

Both models have advantages and disadvantages to represent the “real” material. JC and also ZA are not able to describe the strain induced ageing. Both models can only describe a monotone decreasing flow stress with increasing temperatures. ZA and JC use an exponential approach. For JC (see Equation 1), only the “m” parameter describes the thermal softening behaviour of the modelled material. In the ZA model, three constants B_0, β_0

and β_1 have influence on the material softening. For this model, the softening behaviour is also dependent on the strain rate. As example for the C45E material in Figure 2, the influence of the used data pool on the fitting of the material parameters is explained. The used data pool of experimental tests is given by the following limits: strain rate between 0,0001 and 200.000 1/s, strain up to 4, and temperatures up to 1000°C. In the first case (see Figure 3a) only temperatures lower than 600°C were implemented in the data collection used to calculate the material parameters. A very good approximation, especially for the ZA model, with the measured data up to temperatures of 600°C is found. An extrapolation above temperatures of 200°C revealed a different performance of the ZA model and the JC model. The ZA model runs into saturation against the value of $\sigma_{sat} = \Delta\sigma_G + k_0\varepsilon^n$. On the other hand, if the JC Model is extrapolated beyond the fitting range the flow stresses decrease continuously. As a consequence, flow stresses lower than zero would be computed at higher temperatures. However, the "real" data are in good agreement up to 1000°C. Flow stresses lower than zero can lead to numerical

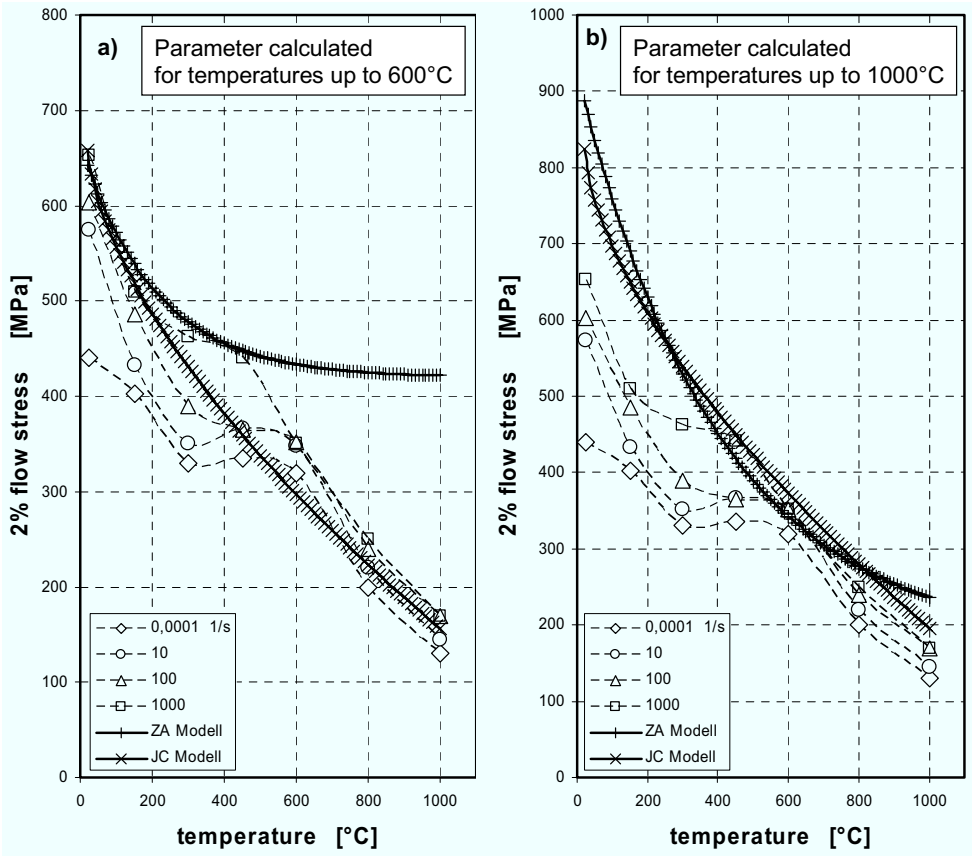

Figure 2: *Comparison of experimental data with ZA and JC models (both at a strain rate of 1000 1/s) by different data pools for fitting*

instabilities and incorrect results. On the other hand, the overestimated flow stresses by extrapolation of the ZA model lead to deviations by factors of about three at 1000°C. When the data pool for fitting the material parameters include tests at temperatures up to 1000°C, the progression presented in Figure 2b for ZA and JC is given. Both models overestimate the "real" material behaviour. Another important difference between the JC and the ZA model is the treatment to regard the strain rate. JC represents the strain rate

in a logarithmic scale in contrast to ZA, where the strain rate is represented by a double logarithmic scale. A linear increase in a logarithmic scale often does not represent the real material behaviour vs. the strain rate. Figure 3 illustrates this model behaviour in a dashed line for the steel C45E. Only the ZA model is able to calculate the progress of flow stresses vs. strain rate in a wide range of testing velocities. At very high strain rates the differences between the ZA and the JC model grow exponential. Therefore, it is concluded that an extrapolation above the given limits, especially to higher temperatures, is problematic. Numerical instabilities or flow stress values above factor 2 or higher compared with the "real" material behaviour are possible. Both models show in some areas relatively great differences to the experimental values. The question is: How important is the used material model for the quality of a numerical simulation of an orthogonal high speed cutting process?

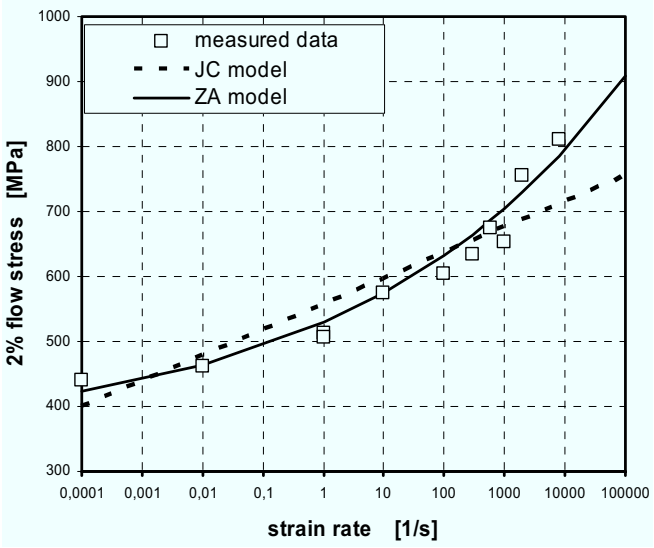

Figure 3: *Experimental data and fitting by the ZA and the JC model versus the strain rate under tensile loading of steel C45*

3 Results

3.1 Numerical Simulations

All following presented numerical simulations accord to a quick-stop device with integrated force measurement and high speed photography. This device was described in [4]. For all simulations, the FE-Program DEFORM® in 2D was used. In 3D some imported program features like self contact are not implemented yet. To obtain the influence of different material or failure models, the following approached boundary conditions are used: an orthogonal cutting process with a cutting speed of 600 m/min, a chip angle of 0°, and a free angle of 6°. In all cases the friction was assumed as shear type with a constant value of 0.3. Three possibilities to incorporate the flow stress data were used. Firstly, the measured data were transferred carefully into piecewise (PW) isothermal curves. In both other cases the experimental data were transferred into a Johnson-Cook (JC) and a Zerilli-Armstrong (ZA) model. The parameter calculation for both models was made without any constrains for the parameters to receive a high coefficient of determination r^2.

Both models are not available in the 2D Version of the used FE-Code. Therefore, it was necessary to implement both models as flow stress routines into the code. This was realised by writing two FORTRAN subroutines. For these routines, the equation 1 and also the both derivations w.r.t. strain (equation 4) and strain rate (equation 5) were used to formulate the Johnson-Cook model. In the same way the Zerilli-Armstrong model was implemented by using the equations 2, 6 and 7.

$$\frac{d\sigma}{d\varepsilon} = \left(1 + C\,ln\,\dot{\varepsilon}\right)\cdot\left[1-\left(\frac{T-T_{room}}{T_{melt}-T_{room}}\right)^{m}\right]\cdot\frac{Bn}{\varepsilon}\varepsilon^{n} \tag{4}$$

$$\frac{d\sigma}{d\dot{\varepsilon}} = \left(A + B\varepsilon^{n}\right)\cdot\left[1-\left(\frac{T-T_{room}}{T_{melt}-T_{room}}\right)^{m}\right]\cdot C\frac{1}{\dot{\varepsilon}} \tag{5}$$

$$\frac{d\sigma}{d\varepsilon} = \frac{nk_0\varepsilon^{n}}{\varepsilon} \qquad \text{when n<1} \tag{6}$$

$$\frac{d\sigma}{d\dot{\varepsilon}} = \frac{B_0\beta_1 T}{\dot{\varepsilon}\cdot exp\left(\beta_0 T\right)}exp\left(\beta_1 T\,ln\,\dot{\varepsilon}\right) \tag{7}$$

For the failure model evaluation, eleven different failure models are used.

3.2 Comparison of different material models for steel 1.1191

To evaluate the influence of a material model, calculations in a wide range of cutting speeds and cutting depths were performed. The ascertained deviations between the three used data pools are generally not large. Representative for all calculations a simulation of 600 m/min with a cutting depth of 0.5 mm is shown.

In Figure 4 the differences between the models for the maximum of temperature, strain, strain rate, and the cutting force are presented. The shown values are determined at a path along the calculated chip surface. The deviations for all values are relatively small. The values for the calculated temperatures and cutting forces vary at about 5% and decrease a little bit with increasing cutting depth and increase with decreasing cutting speed. For the maximum equivalent strain and the strain rate, the results vary about 10-20%. These results demonstrate that both models can be used instead of piecewise data in numerical simulations of high speed cutting processes without generating large errors. Especially for cutting force calculations the error generated by using a material model is smaller than 5%.

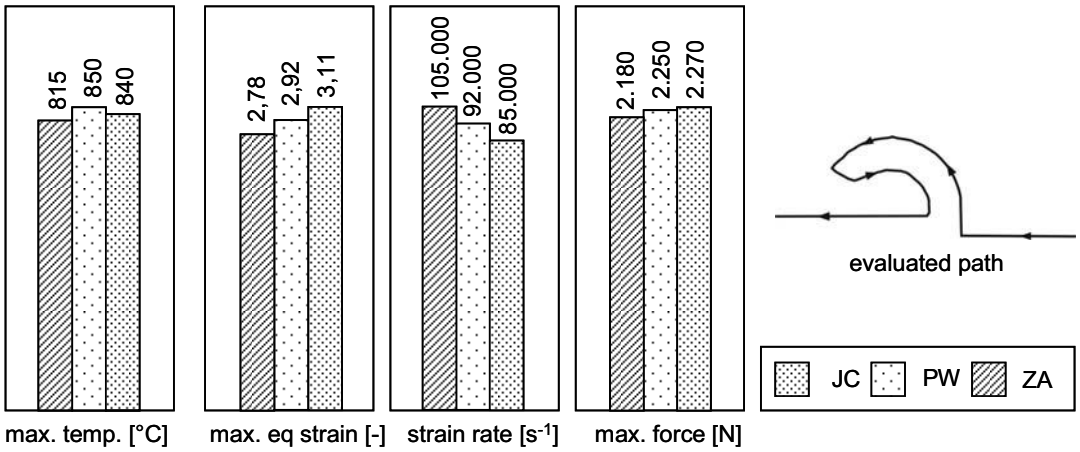

Figure 4: *Influence of different material models on simulation results*

The effects of different models on the computed chip shape are presented in Figure 5. Simulated was a quick-stop test with a cutting path of 7 mm. After a cutting distance of 2 mm all three simulations reveal nearly the same chip geometry. With increasing cutting distance the influence of the used models grows. This leads to a self contact at 6.5 mm distance of cutting for the ZA model. The PW simulation gives the best match with the experimental results (see chapter 3.4). Nevertheless, the other material models are very close to these results.

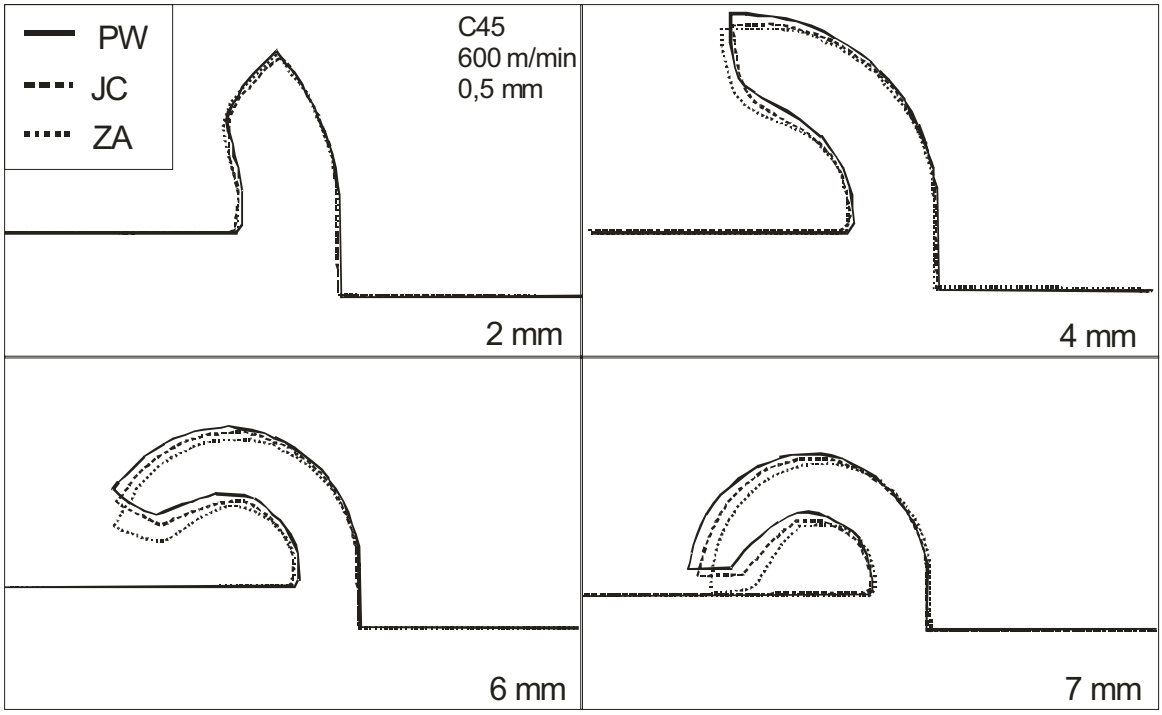

Figure 5: *Chip shape simulation results for PW, JC and ZA input data with increasing path of cutting.*

3.3 Comparison of different failure models for steel 1.2311

In addition to the simulations with different flow stress models, some calculations with varied failure models were executed with the tool steel 1.2311. The material data for 1.2311 are used by PW data. In a first step, calculations with failure parameters according to literature data or estimated parameter without element deletion are computed. These simulations are performed to estimate the critical values for each of the eleven tested models. In a second step, an element deletion for these calculations is used and the calculations were started again. All simulations stop due to numerical instabilities and the last simulation step of this procedure is presented in Figure 6.

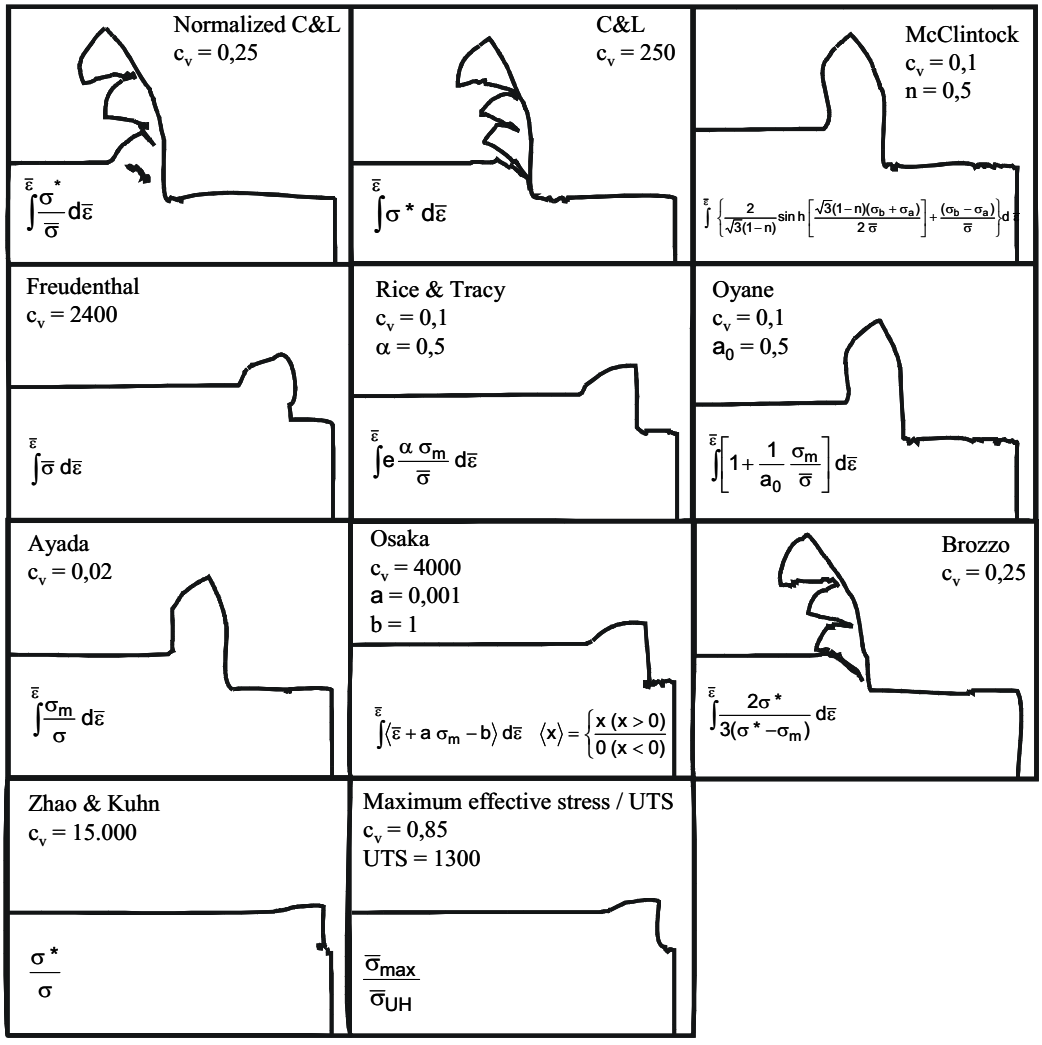

Figure 6: *Chip shape simulation results different failure models at 1.2311*

For the used simple approach only three models are able to reach a macroscopic match with the experimental cutting results (see Figure 1). The adiabatic shear instability, which occurs in reality, can not be obtained with the used simulation configuration.

3.4 Comparison of experimental and simulation results

To demonstrate the good geometry match between numerical simulations and experimental results, a comparison of an obtained chip formation process is shown in Figure 7. A picture series was taken during a quick-stop-test at the C45E material with a cutting depth of 0.76 mm. A Imacon® highspeed CCD Camera with a macro lens was used. These pictures have a time resolution between each picture of 0.08 ms. Over these pictures the calculated chip shape at the same time step is laid. For further analyses with the concept of visioplasticity, a grid is upset on the material surface. Up to 5 mm distance of cutting a good match between calculated and the real experiment is visible. The simulation calculates cutting forces in the range (± 10%) of the measured forces obtained at the quick-stop-device. In addition, the calculated temperatures are slightly overestimated compared with the high rate experimental data [10]. Temperatures of approximately 800°C were measured. The compression of the chip is overestimated. This means that the real chip is thinner and slightly longer. Also the shear angle is not exact the same value like in the numerical simulation.

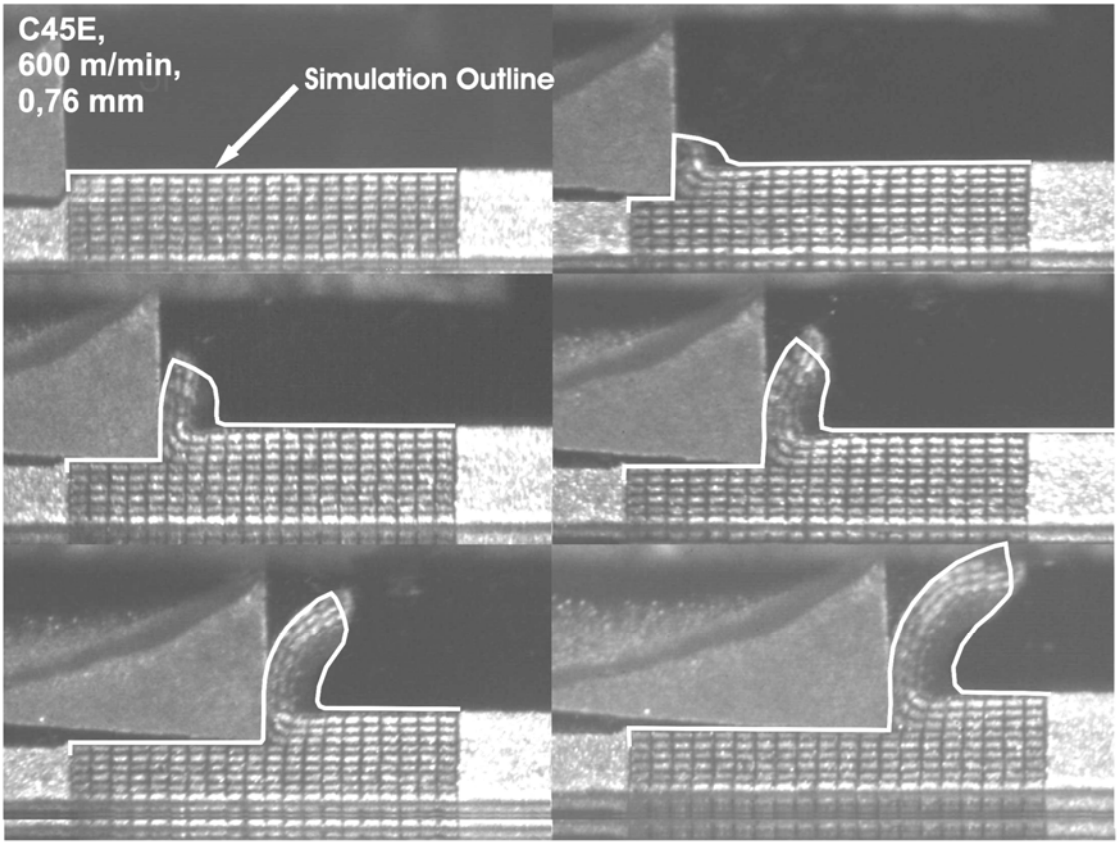

Figure 7: *Comparison of computed chip shape contours with pictures obtained with high speed photography at a quick-stop test*

4 Conclusions

The influence of material models on the results of high speed cutting simulations is evaluated and leads to deviations between 5 and 20%. Especially for determining the cutting forces for a tool analysis it is regardless which kind of material model is used. The ZA and the JC model can deliver good results in relation to the quality of the measured material data. It seems that only three of the used failure models are able to represent the macroscopic segmentation behaviour for the chip formation of the 1.2311 tool steel.

References

[1] *Boisse, P.; Altan, T.; Luttervelt, K. van.:* Friction and flow stress in forming and cutting, Kogan Page Science, 2003, ISBN 1-9039-9641-4.

[2] *(Rusty) Gray III, G.T.:* Classic Split-Hopkinson Pressure Bar Testing. Mechanical Testing and Evaluation. ASM International, Materials Park, Ohio, 2000, p.462-476., 10th ed. Handbook No.8.

[3] *Meyer, L.W.:* Material Behaviour at High Strain Rates. Proceedings of "1st International Conference on High Speed Forming", Dortmund, 2004.

[4] *Meyer, L.W.; Hahn, F.; Halle, T.:* Gestoppte Span- und Zugversuche - Schädigungsentwicklung und –fortschritt. Proceedings of "Werkstoffprüfung 2000", Bad Nauheim, 2000, p.323-333. DVM.

[5] *Meyer, L.W.; Halle, T.; Abdel-Malek, S.:* Tensile Testing, ASM International, Materials Park, Ohio, 2000, p.452-454. 10th ed. Handbook No.8.

[6] *Meyer, L.W.; Halle, T.:* Schlagdynamisches Werkstoffverhalten der Stähle C45E und 40CrMnMo7 bei erhöhten Temperaturen und hohen Dehngeschwindigkeiten unter Zugbeanspruchung. Proceedings of "Werkstoffprüfung 2000", Bad Nauheim, 2000, p.349-358.

[7] *Johnson, G.R.; Cook, W.H.:* A Constitutive Model and Data for Metals Subjected to Large Strains, High Strain Rates and High Temperatures. Proceedings of "7th Symposium on Ballistics", 1983, p.541-547.

[8] *Zerilli, F.J.; Armstrong, R.W.:* Constitutive Relations for the Plastic Deformation of Metals. American Institute of Physics, 1994, p.989-992.

[9] *Vöhringer, O.:* Effect of Temperature and Strain Rate on the Deformation Behaviour at Uniaxial Loading of Metallic Materials. Microstructure and Mechanical Properties of Materials, DGM Informationsgesellschaft mbH, Oberursel, 1991, p.41-50.

[10] *Frohmüller, R.:* Entwicklung, Aufbau und Funktionserprobung von Strahlmesstechnik zur Messung der Temperaturen in der Wirkzone bei hochdynamischen Zerspanvorgängen, Otto-von-Guericke-Universität Magdeburg, thesis, 2002.

Electro-magnetic Tooling for Metal Forming and Powder Compaction: Numerical Simulation

A.G. Mamalis[1], D.E. Manolakos[1], A.G. Kladas[2], A.K. Koumoutsos[1]

[1] Manufacturing Technology Division National Technical University of Athens, Greece
[2] Electric Power Division National Technical University of Athens, Greece

Abstract

The multipurpose FE Code ANSYS is employed to simulate an electro-magnetic forming process. A complicated compression coil with a ferromagnetic outer screen and a stepped field shaper is considered. Details on FE model building are thoroughly discussed. The calculated parameters are the magnetic flux density around the conductors as well as the Lorentz forces developed in both the field shaper and the workpiece. A simplified analysis of the workpiece deformation characteristics is also provided. An equivalent circuit method is employed in order to validate the results from the electro-magnetic FE model. Results from both analyses are in good agreement, denoting that the FE results are valid from an engineering point of view.

Keywords:

Electro-magnetic forming, Tool analysis, Tube compression

1 Introduction

In industrial practice, the tools of electro-magnetic forming and dynamic compaction processes are more complicated than a single-layer solenoid winding [1,2]. For this reason, the analytical calculation of the magnetic pressure acting on the workpiece is very difficult. However, electro-magnetic forming has been widely applied in aerospace and automotive industry since its economic restriction to relatively small parts has allowed trial - and - error development to overcome the handicap of the existing lack of knowledge. In literature, there are only a few papers on the analytical calculation of the magnetic field when a field shaper is employed in an electro-magnetic forming process [3-6]. The most effective approach, from an engineering point of view, is the equivalent circuit method proposed by Göbl [7]. Furthermore, useful engineering calculations regarding the thermal as well as the mechanical aspects of field shapers design are found in references [8,9]. In the present paper, a finite element analysis of an industrial compression coil contributes to the more systematic analysis of the process, offering valuable information for tooling design.

2 Model Description

2.1 The Electro-Magnetic Model

The Multiphysics High Option, Release 6 version of ANSYS is employed for the modelling of the forming coil. The drawing of the forming coil is presented in Figure 1a/b. It is a single-layer, four-turn solenoid coil with a ferromagnetic outer screen and a stepped field shaper. Due to the slit existence, the problem cannot be treated as axisymmetric. So, a 3D modelling is applied and since the tool possesses both a transverse and a longitudinal plane of symmetry, the simulation may be conducted considering the geometry shown in Figure 1c.

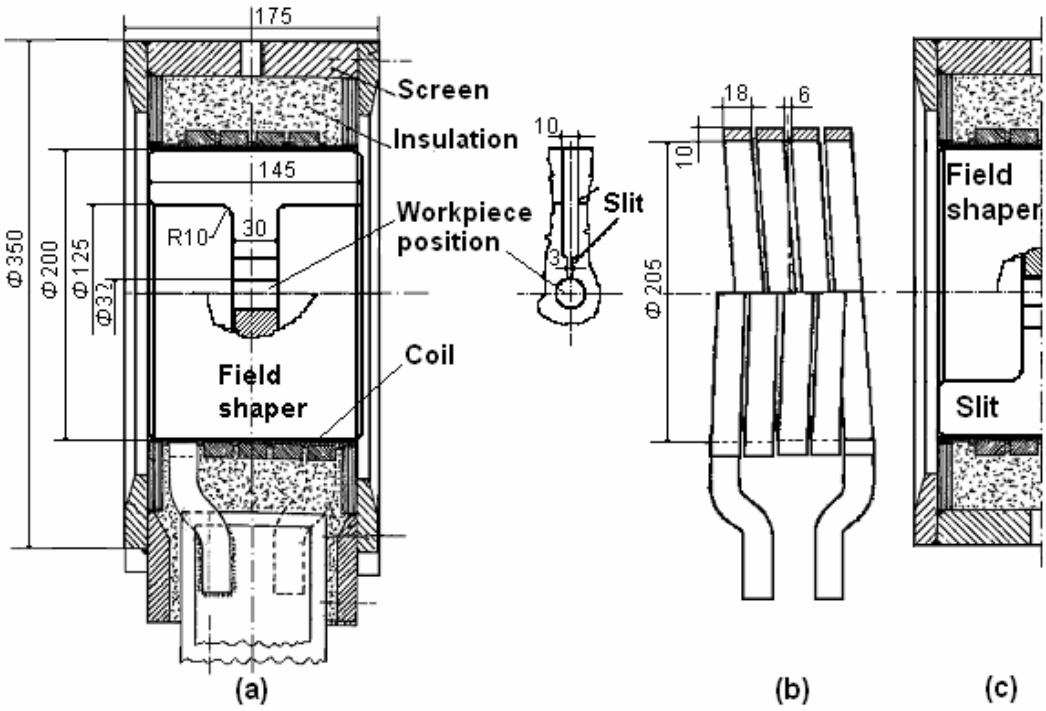

Figure 1: *The electro-magnetic forming tool for tube compression and powder compaction (a) the tool assembly, (b) the coil winding, and (c) the simulated region of the tool*

The above-mentioned code has a limitation of 32000 elements or nodes. A mapped-meshing type is selected, enabling the exact determination of the number of nodes and elements. So, the model applied is practically a plain lattice swept around its axis in order to create the corresponding volume, see Figure 2. The first block (0°- 171°) is the main block, the second block (171°- 175°) represents the region near the slit, and the third block (175°- 180°) corresponds to the slit region. The slit direction is assumed radial rather than transverse for modelling simplification. In electro-magnetic forming practice the width of the slit just above the workpiece is crucial, because the magnetic pressure is reduced in this area. In the drawing of the forming tool this gap is given 3 mm, while in the model this gap is actually a small arc, which length is given by the product of the angle of the third block times the radius of the hole of the field shaper, i.e. $[(5/180)\cdot\pi]\cdot 16 = 1.4 \approx 3/2 = 1.5$ mm, which is acceptable.

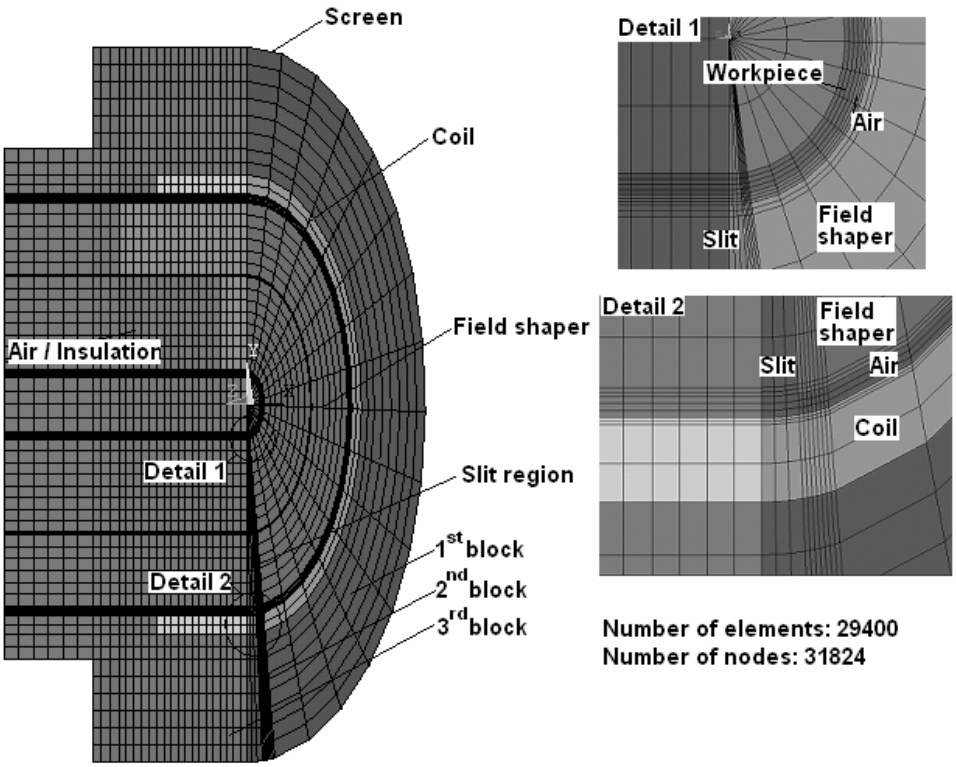

Figure 2: *The meshing of the electro-magnetic model*

The necessary material properties of each entity of the model and the chosen element type with their corresponding degrees of freedom are given in Table 1. The nodal and the element coordinate system are rotated to the local cylindrical coordinate system WX, WY, WZ, according to the orientation indicated in Table 2. The boundary conditions and loads are also referred to the local cylindrical coordinate system. However, in all figures the depicted coordinate system of the model as well as of the results is the global Cartesian one. The main load is the current flowing in the coil. In practice, it can be easily measured by means of a Rogowski coil connected to an oscilloscope. In the electro-magnetic forming process the current is approximately expressed by the following equation:

$$I(t) = I_o \cdot exp(-\gamma \cdot t) \cdot sin(\omega_d \cdot t) \tag{1}$$

where, I_0 = 124600A, γ = 4805.8 s^{-1}, ω_d = 43564 rad/s in the present analysis. This current is produced by a discharge of 6 kV stored in a capacitor bank of 480 μF. Due to the transient nature of the process, the current flows near the surface of the conductors. The penetration depth of each conductor can be calculated via the well-known equation

$$\delta = \sqrt{\frac{2 \cdot \rho_e}{\mu_r \cdot \mu_o \cdot \omega_d}} \tag{2}$$

where, μ_0 = 4 π 10^{-7} H/m. Finite element analysis requires at least one or two elements through the penetration depth.

S/N	Entity - Material	ρ_e $10^{-8}\cdot$ [Ω·m]	μ_r	Element	Degrees of freedom
1	Coil - Cu	1.79	1	SOLID97	A_x, A_y, A_z[(a)], Volt[(b)]
2	Workpiece - Al	3.33	1	SOLID97	A_x, A_y, A_z, Volt
3	Screen - Mild Steel		100	SOLID96	Mag[(c)]
4	Field shaper - Al	3.33	1	SOLID97	A_x, A_y, A_z, Volt
5	Surroundings - Air or Insulator		1	SOLID97	A_x, A_y, A_z
6	Interface (3) / (5)			INTER115	

[(a)] A: The magnetic vector potential and X, Y, Z, the radial, tangential and axial component, respectively
[(b)] Volt: The time-integrated potential
[(c)] Mag: The magnetic scalar potential

Table 1: *The data of the electro-magnetic model*

According to the above mentioned details and taking into account that the radius of the inner hole of the field shaper is 16 mm and that the angle of the block, which represents the region near the slit, is 4°, then it should be checked that the inner arc of the field shaper part, which belongs to this block, is bigger than its skin depth. Indeed, (4°/180°) π 16 = 1.12 mm > δ_{Al} = 1.11 mm, which is valid. Furthermore, the necessary number of elements in the tangential direction can be found if the outer arc of the same block of the field shaper is divided by the skin depth, i.e. (4°/180°)·π·100/1.11 = 6.28, so seven elements are enough. The mesh density in the rest of the model is selected according to the general rule that the mesh density should be proportional to the energy density, e.g. the energy density is high in the gaps between two adjacent current carrying conductors, see Figure 2. Load and boundary conditions are both applied to nodes. In the transverse and longitudinal plane of symmetry, flux normal and flux parallel boundary conditions are established respectively. An additional entity with air elements has been placed adjacent to the free bound of the modelled part of the tool in order to enhance the development of the magnetic field, since it is very difficult to establish the required far field boundary conditions there, see Figure 2. A more detailed presentation of the boundary conditions is given in Table 3.

Components of a common cylindrical coordinate system	Local cylindrical coordinate system	Global Cartesian coordinate system
Radial	WX	+Y
Tangential	WY	-Z
Axial	WZ	-X

Table 2: *Determination of the coordinate system used in the model*

The coil is considered to be a single-turn for modelling simplification, so the input current (I_{eq}) should be corrected with a factor in order to ensure that the induced magnetic field is approximately the same in both cases, according to the approximate relation:

$$\frac{N \cdot I(t)}{\ell_1} = \frac{1 \cdot I_{eq}(t)}{0.5 \cdot \ell_1} \Rightarrow I_{eq}(t) = 0.5 \cdot N \cdot I(t) \tag{3}$$

where, N = 4, the number of the coil turns and ℓ_1: the coil length. Equation (3) is valid for long coils. However, it is employed for the present coil, which is short (i.e. the diameter is comparable to the length), because the flux is entrapped in small gaps and its pattern consists of parallel straight lines.

S/N	WZ=0	WY=0	WY=180o	WX=150 [mm]	WX=125 [mm]	WZ=72.5 [mm]
1	A_z=0	Volt=0 (in skin depth), A_x=A_z=0	Couple volt in skin depth, A_x=A_z=0			
2	A_z=0	Volt=0, A_x=A_z=0	Volt=0, A_x=A_z=0			
3	Mag=0					
4	A_z=0	Volt=0 (in skin depth), A_x=A_z=0				
5	A_z=0	A_x=A_z=0	A_x=A_z=0			
6				A_x=0	A_x=0	A_z=0

Table 3: *The entities and their areas onto which boundary conditions are applied*

The current is applied in transient analysis in increments of 1 microsecond. Only the first half of the current period is considered, because it corresponds to the first peak of magnetic pressure, which is assumed to be responsible for the plastic work produced on the workpiece. Another assumption that has been considered is that the current is applied in the inner skin depth of the coil. In fact, the current flows all around the surface of the coil winding. But in the present model the inductive coupling between the outer surface of the coil and the screen is ignored, because the selected type of analysis (Magnetic Vector Potential - Nodal Based) cannot treat eddy currents in ferromagnetic materials. So, the outer screen serves only as a “ferromagnetic trap” for the flux outside the coil. The workpiece deformation and its influence on the magnetic field evolution and the resulting forces are disregarded from the present analysis. Moreover, some further assumptions and restrictions possessed by the present model are the following:

- The workpiece thickness (2 mm) is bigger than its skin depth (1.11 mm) and the length of both workpiece and field shaper is equal. These restrictions are possessed by the equivalent circuit method.
- The workpiece material is non-magnetic.
- The current frequency is lower than 30 kHz, thus no electro-magnetic wave effects are considered.
- All the contributing materials are isotropic.
- The temperature dependence of material properties is ignored.

2.2 The Structural Model

The loosely coupling approach is considered; i.e. calculating first the Lorentz forces, neglecting the influence of workpiece deformation on magnetic field evolution, and applying them as input load to the mechanical problem. In the electro-magnetic compression proc-

ess only moderate deformations are usually desirable due to the limitation imposed by the wrinkling defect. So, the abovementioned simplification may be acceptable in many cases; however, experimental validation is always required.

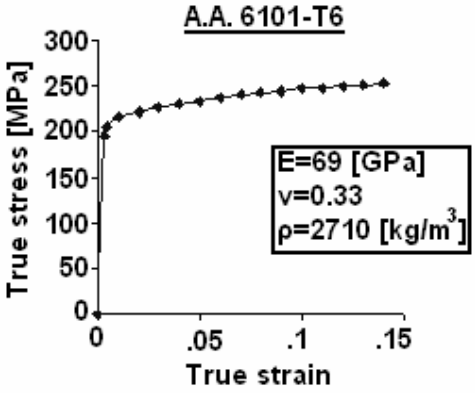

Figure 3: *The mechanical properties of the workpiece*

The structural model consists only of the workpiece. The applied load is the mean magnetic pressure acting on the part of the workpiece, which lies in the middle step of the field shaper (i.e. the sum of the radial component of Lorentz forces divided by the corresponding external area of the workpiece, see below). The tangential distribution of the magnetic pressure cannot be taken into account, because during the simulation the forces are unbalanced in radial direction and the solid-body motion is inevitable. The axial distribution of the magnetic pressure can be neglected. Regarding the abovementioned considerations the model can be 2D axisymmetric, which means more simplicity and less CPU time. The properties of the workpiece material are presented in Figure 3. The model is meshed in a mapped pattern via the four-node PLANE182 element, which is suitable for large deformations of elastoplastic materials. In the present model X, Y, Z axes represent the radial, axial, and tangential directions respectively. Finally, the axial displacement of the nodes, which lie in the transverse plane of symmetry, should be constrained.

3 Results and Discussion

By deriving Equation (1) it yields that the maximum of the input current occurs at 33.5 μs. According to Figure 4(a), the time variation of magnetic flux density follows the one of the input current, as it is expected.

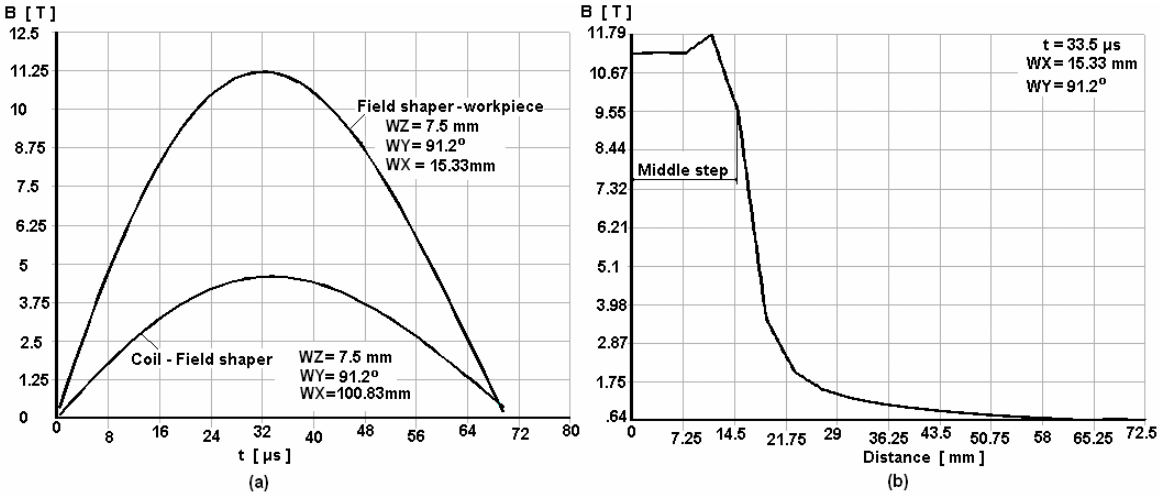

Figure 4: *(a) The magnetic flux density in the gap between the coil and the field shaper as well as between the field shaper and the workpiece vs. time. (b) The distribution of the maximum magnetic flux density along the gap between the field shaper and the workpiece*

The maximum magnetic flux density in the gap between the coil and the field shaper occurs at 33.5 μs, while in the gap between the field shaper and the workpiece the maximum occurs at 31.5 μs, but this difference is negligible. From Figure 4(b) it yields that only at the centre of the middle step of the field shaper the magnetic flux density is uniformly distributed in the axial direction. Outside the middle step the magnetic flux density is sharply reduced, as it is expected [4,5]. However, the distribution of magnetic flux density around the periphery of the gap between the field shaper and the workpiece is not uniform, as it can be seen from Figure 5a. With increasing distance to the slit, the magnetic flux density increases with a decrescent rate. A similar graph can also be obtained for the gap between the coil and the field shaper, see Figure 5b.

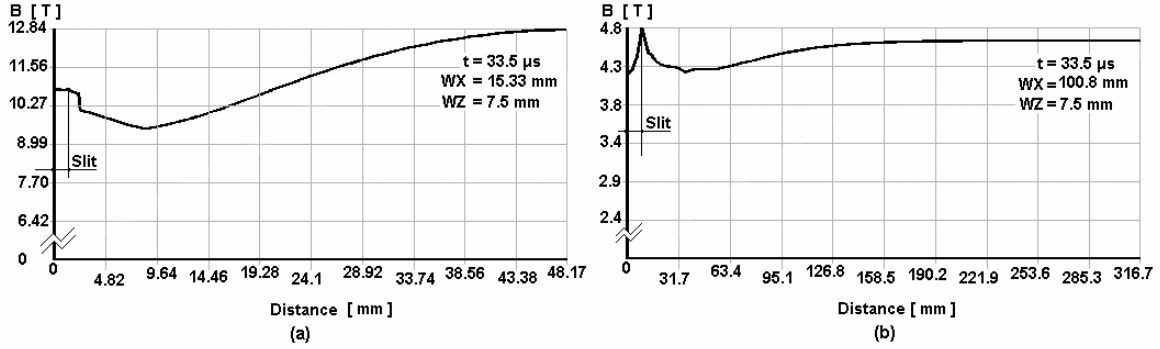

Figure 5: *The distribution of magnetic flux density around the periphery in the gap (a) between the field shaper and the workpiece, and (b) between the coil and the field shape*

The mean magnetic flux density can be calculated according to the following integrals:

$$B_{C-FS} = \frac{1}{307.8} \cdot \int_{8.8}^{316.6} B_{C-FS} \cdot ds \Rightarrow B_{C-FS} = 4.54T \tag{4}$$

and

$$B_{FS-W} = \frac{1}{46.8} \cdot \int_{1.34}^{48.14} B_{FS-W} \cdot ds \Rightarrow B_{FS-W} = 11.25T \tag{5}$$

for the gap between the coil and the field shaper and between the field shaper and the workpiece respectively, excluding the slit region. The corresponding results according to the equivalent circuit method (see Appendix) are $B_{C\text{-}FS}$ = 4.6 T and $B_{FS\text{-}W}$ = 11.3 T, respectively. The results from the two methods are in good agreement, so the FE model is valid from an engineering point of view. It is notable that the latter method meets some limitations (e.g. the case of a very short workpiece), in contrast to the FE analysis, whose capabilities are practically unlimited. Another way to validate the results is the experimental measurement by means of search coils placed in the relevant gaps and connected to a memory oscilloscope.

In fact, the real forces acting on the workpiece will be lower than those presented in Figure 6, because the gap between the field shaper and the workpiece will increase due to the latter's deformation. From Figure 6 it can also be seen that the Lorentz forces on the part of the workpiece under the slit region decrease, as it has been already discussed. The Lorentz force action on the field shaper tends to split it in the slit region (Figure 6). For this reason, a rubber bandage is often placed around the field shaper above the middle step region. This bandage fits tightly the field shaper to the inner insulation of the coil thus preventing the failure of the former.

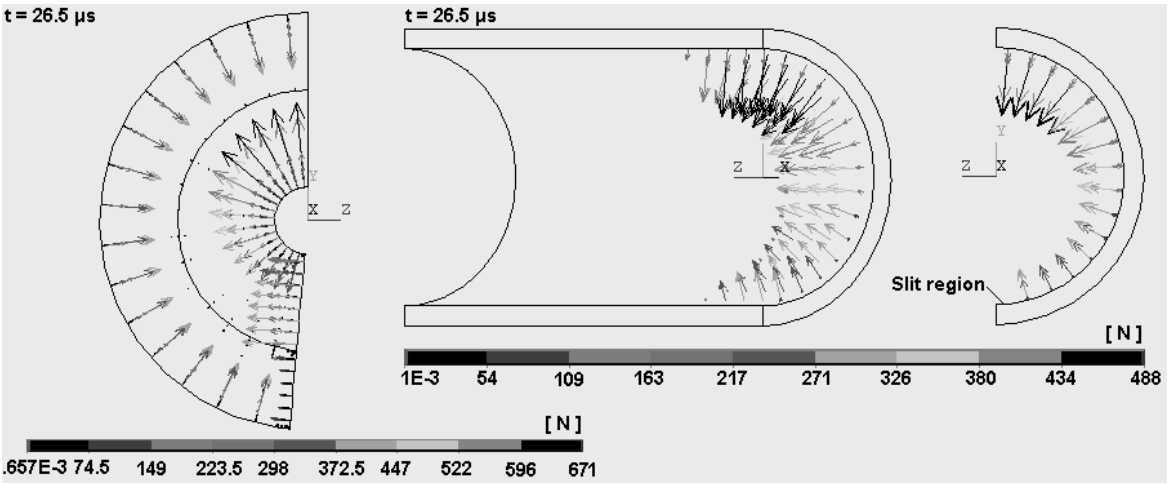

Figure 6: *A vectorial depiction of the Lorentz force distribution over the field shaper and the workpiece*

The final shape of the workpiece is shown in Figure 7a. The central part of the workpiece gains the maximum deformation velocity, which reaches the value of 53.5 m/s at 43 µs, resulting in an equivalent plastic strain rate of 3967 s^{-1}. The deformation process is practically fulfilled at 60 µs, see Figure 7b. The accuracy of the presented results should be

confirmed experimentally. However, they give a first sense regarding the order of magnitude of the corresponding parameters.

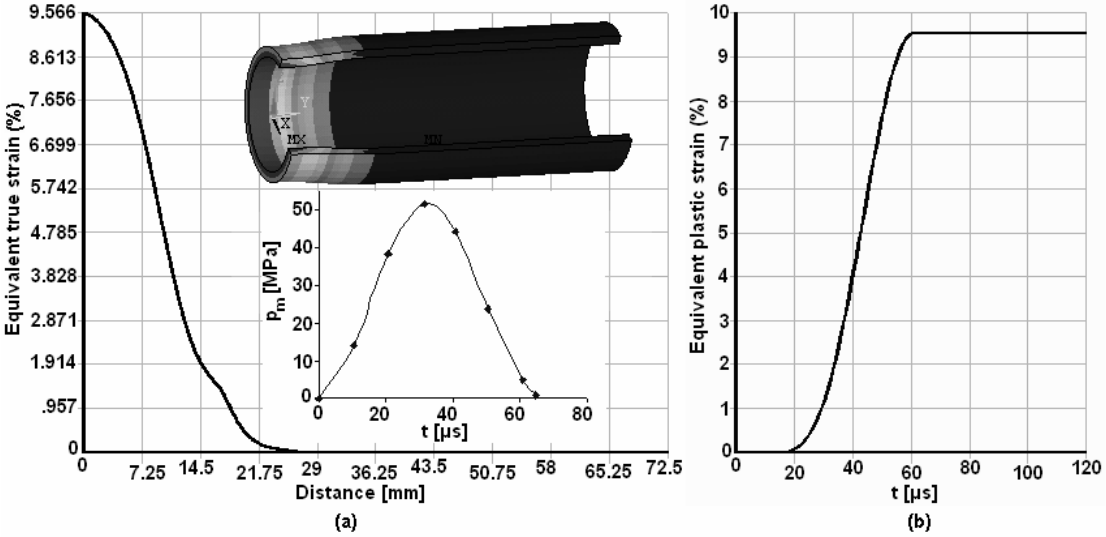

Figure 7: *(a) The final shape of the workpiece and the distribution of the equivalent plastic strain along the workpiece as well as the variation of the mean magnetic pressure vs. time. (b) The equivalent plastic strain in the middle of the workpiece vs time*

4 Conclusions

In the present paper, a methodology based on FE for calculating the operational parameters of the electro-magnetic forming process is presented. An industrial compression coil of complicated geometry is considered. The results of magnetic flux density are valid from an engineering point of view, since they are in close accordance with those obtained from the equivalent circuit method. A simplified analysis of the deformation characteristics of the workpiece is also attained. All the obtained results are consistent to the theory. However, the tenability of the various assumptions considered during the simulation process should be experimentally confirmed. The present analysis can be further developed if the coupling nature of each aspect of the process is taken into account.

References

[1] *Lange, K.:* Handbook of metal forming, McGraw-Hill, 1985, p.27.32-27.39.

[2] *Livshitz, Y.; Gafri, O.:* Technology and equipment for industrial use of pulse magnetic fields, IEEE International Pulsed Power Conference, vol.1, 1999, p.475-478.

[3] *Wilson, M.N.; Srivastava, K.D.:* Design of efficient flux concentrators for pulsed high magnetic fields, Rev. of Sci. Instr. 36 (8), 1965, p.1096-1100.

[4] *von Dietz, H; Lippmann, H.-J.; Schenk, H.:* Theorie des Magneform – Verfahrens: Erreichbarer Druck, ETZ-A ,88 (9), 1967, p. 217-222.

[5] *von Dietz, H; Lippmann, H.-J.; Schenk, H.:* Theorie des Magneform – Verfahrens: Abgestufter Feldkonzetrator, ETZ-A, 88(19), 1967, p.475-780.

[6] *Serbanescu, M.:* Calculation of the magnetic field intensity for slotted field concentrators, Rev. Roum. Sci. Tech.-Electrotechn. Et Energ., 21 (3), 1976, p.365-376.

[7] *Göbl, N.:* Unified calculating method of equivalent circuits of electro-magnetic forming tools, PhD Thesis, Tech. Univ. of Budapest, Fac. of Elec. Eng., 1978.

[8] *Batygin, Y.V.; Daehn, G.S.:* The pulse magnetic fields for progressive technologies, Monograph, Kharkov-Columbus, 1999, available at: http://www.er6.eng.ohio-state.edu/~DAEHN/hyperplasticity.html.

[9] *Altynova, M.M.:* Electro-magnetic metal forming handbook, Mat. Sci. and Eng. Dept, The Ohio State Univ., Transl. of the Russian book: SPRAVOCHNIK PO MAGNITNO-IMPUL' SNOY OBRABOTKE METALLOV by IV Belyy, SM Fertik and LT Khimenko, VISCHA SHKOLA available at: http://www.er6.eng.ohio-state.edu/~DAEHN/hyperplasticity.html.

Appendix

According to the equivalent circuit method [7], there is a transformer coupling between the coil and the rest parts of the forming tool. Thus, an equivalent circuit (Figure 8) can simulate the operation of the forming tool. The equivalent circuit consists of resistances and inductances connected in series and in parallel, which represent every detail of the forming tool. The current is considered AC. This assumption is valid only for the first half period of the current pulse, during which the effect of the damping factor on the amplitude is small and, moreover, this is the most important period of time for the electro-magnetic forming process. Undoubtedly, this is an approximate method, but the obtained results are found to be close to experimental measurements [7].

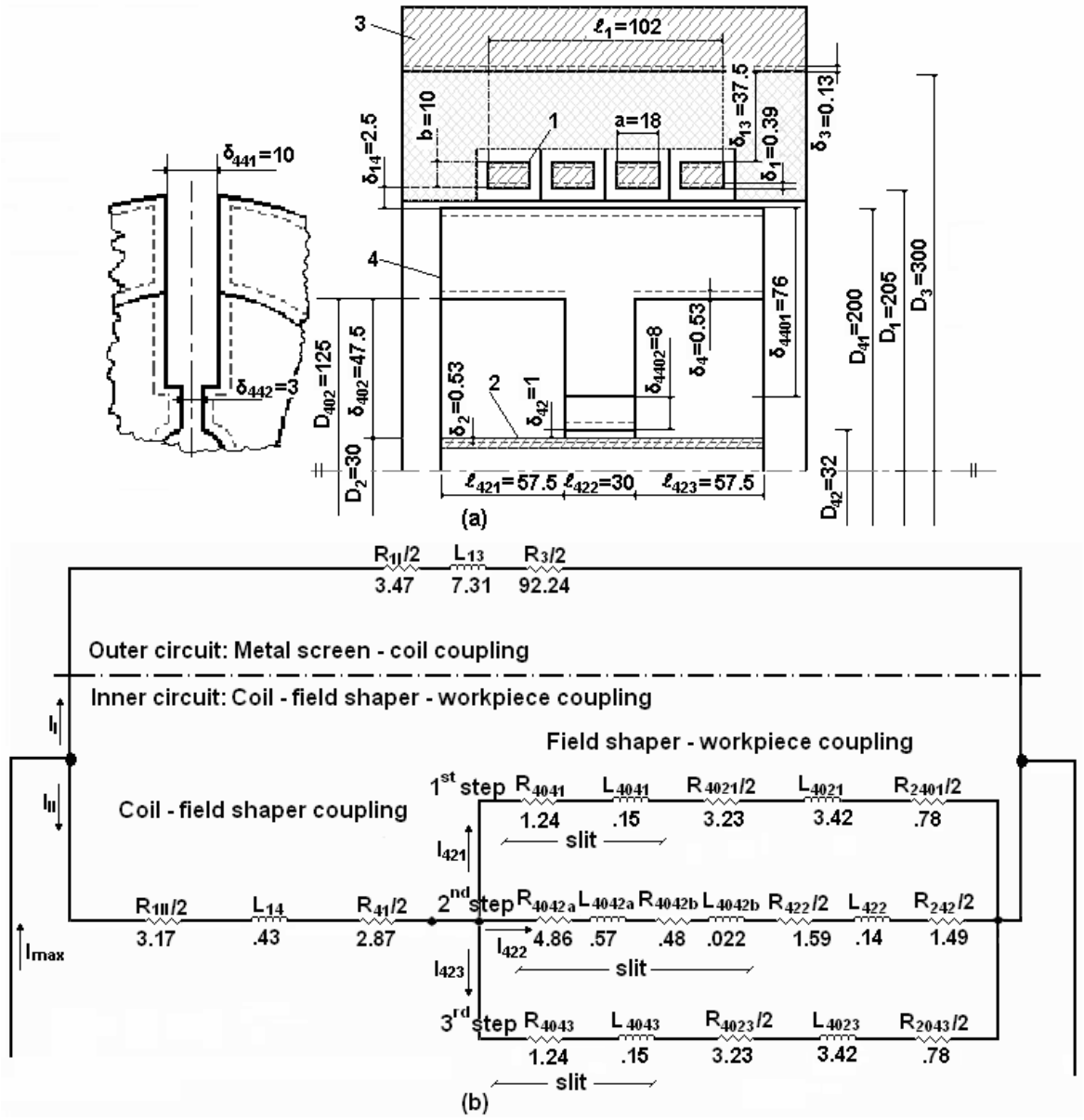

Figure 8: *(a) The equivalent scheme of the modelled forming tool and the relevant dimensions in mm and (b) The corresponding equivalent circuit with the relevant resistances and inductances in mΩ and μH respectively*

Taking into account that the inductances L_{14} and L_{422} correspond to the gap between the coil and the field shaper and between the middle step of the field shaper and the workpiece respectively, and applying the current and the voltage Kirchhoff's Laws in the equivalent circuit, then the currents I_{II} and I_{422} can be determined. So, the magnetic energy in the gaps between the coil and the field shaper and between the field shaper and the workpiece can be expressed by the following equations respectively:

$$E_{m14} = \frac{1}{2} \cdot L_{14} \cdot |I_{II}|^2 = \left(\frac{B_{14}^2}{2 \cdot \mu_o} \right) \cdot v_{14} \tag{6}$$

and

$$E_{m422} = \frac{1}{2} \cdot L_{422} \cdot \left| I_{422} \right|^2 = \left(\frac{B_{422}^2}{2 \cdot \mu_o} \right) \cdot v_{422} \tag{7}$$

where, v_{14} and v_{422} the volume of the corresponding gaps, given by the equations:

$$v_{14} = \left[1 - \frac{\delta_{441}}{\pi \cdot D_{41}} \right] \cdot \\ \cdot \left\{ 0.5 \cdot \pi \cdot \left[\left(D_1 + 2 \cdot \delta_1 \right) + \left(D_{41} - 2 \cdot \delta_4 \right) \right] \cdot \left(\delta_1 + \delta_4 + \delta_{14} \right) \cdot \left[\ell_1 + 0.5 \cdot \left(\delta_1 + \delta_4 + \delta_{14} \right) \right] \right\} \tag{8}$$

and

$$v_{422} = \left[1 - \frac{\delta_{442}}{\pi \cdot D_2} \right] \cdot \left\{ 0.5 \cdot \pi \cdot \left[\left(D_{42} + 2 \cdot \delta_4 \right) + \left(D_2 - 2 \cdot \delta_2 \right) \right] \cdot \left(\delta_4 + \delta_2 + \delta_{42} \right) \cdot \ell_{422} \right\} \tag{9}$$

excluding the slit region and taking into account the effective dimensions of the contributing conductors. Finally, the magnetic flux densities yield from Equations (6) and (7) and the corresponding calculated values are $B_{14} = B_{C\text{-}FS} = 4.6$ T and $B_{422} = B_{FS\text{-}W} = 11.3$ T respectively.

SESSION 3

PROCESS TECHNOLOGIES

Direction Change of the Force Action upon Conductor under Frequency Variation of the Acting Magnetic Field

Yu. Batygin, V. Lavinsky, L. Khimenko

National Technical University "Kharkov Polytechnic Institute", Ukraine

Abstract

The present work is dedicated to the description of the thin-walled conductor attraction effect by the pulse magnetic field. This phenomenon was displayed experimentally. The effect pointed out relates to the direction of the pulse magnetic fields energy practical usage for the different technologies in manufacture. In the scientific literature this direction is known as the magnetic pulse metal forming.

A hypothesis about the physical essence of the displayed phenomenon is suggested.

Keywords:

Magnetic fields, Thin-walled metals, Force action

The present work is dedicated to the description of the thin-walled conductor attraction effect by the pulse magnetic field. This phenomenon was displayed experimentally. The effect pointed out relates to the direction of the pulse magnetic fields energy practical usage for the different technologies in manufacture. In the scientific literature this direction is known as the magnetic pulse metal forming or working (MPMF) [1].

The most effective use of MPMF was fixed for the technological processes where the massive conducting objects were subjected to the force action in accordance with the ordered production operation. Their working out was fulfilled in the skin-effect regime which can be realized practically for high frequencies of the acting fields. The resulting forces act as a pressure between the workpiece to be formed and the field source – a coil inductor.

During experimental work with the force action of the pulsed magnetic fields upon thin-walled metals a drawing effect between workpiece and coil inductor could be achieved by decreasing the working frequency below some defined values in conjunction with the electrical, physical and geometrical properties of the workpieces.

Formally, the skin effect regime which is responsible for this drawing effect can be described by the inequality:

$$\omega \cdot \mu_0 \cdot \gamma \cdot d^2 << 1 \qquad (1)$$

where ω is the cyclic frequency of the acting magnetic field, μ_0 is the vacuum permeability, γ and d are the specific conductivity and thickness of the metal.
A scheme of the experiment is represented on Figure 1.

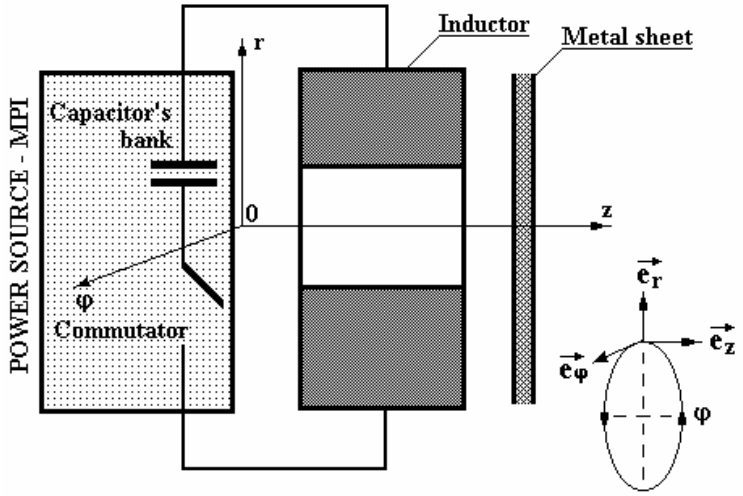

Figure 1: *A scheme of the experiment*

Some steel plates with a thickness of ~ *0.5 mm* were taken as experimental samples. The generators of the magnetic field were the single turn solenoid inductors which were connected to the source with a stored energy of ~ *10 kJ*.

Under frequency of ~ *2.2 kHz* the force action from the magnetic field led to an attraction of the steel sample part and to the creation of the dent according to the cross dimensions of the inductor working zone. An according experimental specimen is represented in Figure 2a.

Under increasing the working frequency up to ~ *7.5 kHz* the same part of the steel plate experienced repelling. A convexity creation takes place, that is an result of the known effect of the magnetic pressure upon the conductor. Figure 2b illustrates the result of this experiment.

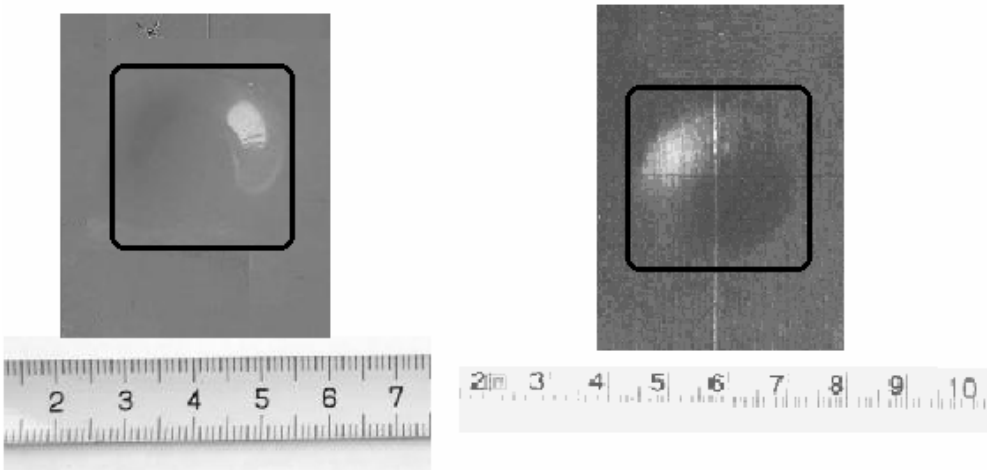

a) b)

Figure 2*: Experimental specimen*

A probable hypothesis about the nature of the displayed phenomenon can be based on the following statements.

In the skin-effect regime the pressure upon the plane conductor with the thickness *d* is caused exclusively by the difference of the squares of the tangential component of the magnetic field strength at the workpiece surface ($H_r(t,r,0)$ and $H_r(t,r,d)$, accordingly to the cylindrical coordinate system in Figure 1) [1]:

$$P_z(t,r) = \frac{\mu_0}{2} \cdot \left(H_r^2(t,r,0) - H_r^2(t,r,d)\right) \tag{2}$$

This formula is always reliable when the normal component of the magnetic field intensity vector is absent. Otherwise additional correspondent force vector components appear. Let us try to point out a possible reason for its appearance.

If the inductor system in Figure.1 has an axial symmetry, the induced azimuthal current density and the electrical field intensity (j_φ and E_φ) as well as the radial and normal components of the magnetic field intensity (H_r and H_z) will appear in the sheet metal.
The Maxwell equation for the current density are:

$$\frac{\partial H_r(t,r,z)}{\partial z} - \frac{\partial H_z(t,r,z)}{\partial r} = j_\varphi(t,r,z) \tag{3}$$

where $j_\varphi(t,r,z) = \gamma \cdot E_\varphi(t,r,z)$; ε_0 - is the vacuum permittivity.

As it can be seen in the equation (3) the induced current density is the difference of the particular derivatives that is two components with different signs. Physical contents may be given to these components: each of them represents a current density caused by the according component of the magnetic field vector. Connecting to the conductor surface these are the tangential and normal components of the field intensity.
The components of the integral induced current have opposite directions. Dependent on the level of each of them the integral current (induced into the sheet metal) can have one or the other direction. The direction change of the induced current means the change of sign of the vector product in the Lorenz force expression and finally the ponder-motor forces being excited direction change.

Thus, the magnetic pulse field action upon the conductor can lead to the known repulsive forces as well as to the magnetic attractive forces. Obviously for well conductor working in skin-effect regime the attractive force will be very small due to the very small normal component of the magnetic field intensity (on the surface of the ideal conductor it would be exactly zero). But in the case of very thin-walled workpieces this component of the field vector becomes very essential according to an intensive diffusion of the magnetic field through the workpiece wall. The first component of the induced current decreases, but the second one increases here. For the some conditions their difference in the Maxwell equation may change its sign and action of the attraction forces (as it was pointed out!) becomes excelling. The sheet metal will be attracted to the magnetic pulse field source. These statements may be illustrated by some formulas.

The normal component of the distributed ponder-motor force $-P_z(t,r)$ acting upon the conductor with the thickness d if to take in account the vector's product sign will be equaled in the received coordinate system:

$$P_z(t,r) = -\mu_0 \cdot \int_0^d \left[j_\varphi(t,r,z) \times H_r(t,r,z) \right] dz = -\mu_0 \cdot \gamma \cdot \int_0^d \left[E_\varphi(t,r,z) \times H_r(t,r,z) \right] dz \quad (4)$$

To pick out in (4) an addendum according to the magnetic pressure (2) let us substitute expression (3) for $j_\varphi(t,r,z)$ in (4).
We shall get after necessary identical transforming

$$P_z(t,r) = \frac{\mu_0}{2} \cdot \left(H_r^2(t,r,0) - H_r^2(t,r,d) \right) + \mu_0 \cdot \int_0^d \frac{\partial H_z(t,r,z)}{\partial r} \cdot H_r(t,r,z) \cdot d\,z \quad (5)$$

The comparison of (4) and (2) shows that in addition to the typical force action a second algebraic addendum is being defined in the formula (5). Obviously this component of the excited force defines the attraction of the thin-walled metal by the pulsed magnetic field.

The physical mechanism of the experimentally shown phenomenon should point out that the radial component of the magnetic field intensity does not depend on the longitudinal space coordinate z (the smooth distribution!) under quite low frequency because of the intensive field penetration. And this component derivative along z must be equated to zero. It means that the current density induced in the sheet metal (formula (3)) will be determined exclusively by the derivative of the normal component of the magnetic field intensity along the radius, that is

$$j_\varphi \approx -\frac{\partial H_z}{\partial r} \quad (6)$$

According to expression (5), the ponder-motor force component repelling the sheet metal will be absent. From the magnetic field hand it will experience the action of the attracting forces to the inductor only.
Regarding a finishing discussion of the probable reasons for this attraction effect it should be marked that the suggested physical hypothesis about the displayed phenomenon nature is not the only possible hypothesis. Other explanations are quite probable. For a final conclusion it is necessary to perform more strict theoretical and experimental work, but the known Ampere Low speaks in favor of the suggested hypothesis: As it is known opposite directed currents repel each other (the high frequencies under skin effect). But currents in the same direction attract each other (the low frequency under intensive diffusion of the acting fields). This means that the displayed phenomenon of attraction must be connected with the change of direction of the current induced in the metal which should be deformed.

References

[1] *Batygin Yu.V., Lavinsky V.I.*: The Pulse Magnetic Fields for Progressive Technologies. Kharkov: Publishing House NTU "KhPI". 2001. - 272p. (Russian).

Improved Crimp-Joining of Aluminum Tubes onto Mandrels with Undulating Surfaces

Inaki Eguia[1], Peihui Zhang[2], Glenn S. Daehn[3]

Department of Materials Science and Engineering, The Ohio State University Columbus, OH, U.S.A
[1] Visiting Scholar, Mechanical Engineer, LABEIN Centro Tecnologico (Vizcaya, Spain)
[2] Presently Staff Engineer, EWI, Columbus, OH
[3] Daehn.1@osu.edu

Abstract

Over its history electromagnetic forming (EMF) has probably seen far and away more application in assembling tubes or rings onto (or into) nominally axisymmetric mating elements. The vast majority of these assemblies does not require any significant structural integrity or strength. However, a small fraction of these are designed and fabricated for mechanically-demanding applications. There are two key factors (which seem to be largely independent) that are key in the design and performance of a crimped-electromagnetic tube joint. First is the state of residual stress that exists after the crimped joint is created. A natural interference fit seems to be a fairly general feature of EMF crimp joints. This interference gives a backlash-free joint that will not fret. The second key issue is the configuration of the joint. The fabrication of designed interlocking geometries is required to create a joint that maximizes mechanical strength while minimizing the electromagnetic energy and forces required to create it. Both of these issues will be considered here. Here we consider crimping onto 'textured' surfaces such as screw threads and knurls. We show experimentally that approaches of this type can give joints that exceed the strength of the tube both in torsion and axial loading. Analysis methods based on coupling impact-indentation and break-before-strip criteria can be used to compare joints made in this way with those based on the more traditional large scale deformation of the tube. One of the advantages of forming onto 'textured' surfaces is that a number of small pulses (possibly generated by small and inexpensive capacitor banks) can be used to create a joint that has the strength of the parent tube, without any heat affected zones or distortion. Again, the natural interference fit developed by impact eliminates the potential for fretting.

Keywords:

Joining, Strength, Aluminum, Electro-impulse

1 Introduction

Electromagnetic forming (EMF) is most commonly used to create assemblies by collapsing tubes or rings onto (or into) nominally axisymmetric mating elements. The majority of these assemblies does not require significant structural integrity or strength. However, a fraction of these are designed and fabricated for mechanically-demanding applications. One example of the use of electromagnetically crimped joints in a very demanding application are torque tubes that are used in the Boeing 777 and other recent Boeing aircraft models. Here, aluminum tubes are crimped onto steel yolks. The development of high performance crimp joints via electromagnetic forming has many very attractive advantages. Most important among these:

- The joints can match the strength of the parent tube. This is seen in many photographs in papers and websites [1,2], but has been otherwise poorly documented.
- The joints made are distortion-free and can be very dimensionally accurate because there is little heat input.
- Again, because there is minimal heat input there is no heat affected zone in the joint. Therefore it is possible to reach the strength of the parent tube. This is not typically possible with fusion joints.
- There has been significant interest in using electromagnetically driven high velocity impact to produce impact-welded structures. This is largely due to public statements and advertisements by companies such as Pulsar and Dana. However, high impact velocity is required for impact welding (>500 m/s is typical). This makes the fabrication of robust electromagnetic forming coils and capacitor bank systems difficult.

We believe high strength structural joints can be very cost effectively fabricated by electromagnetic crimping, without requiring the very high pressures normally required with electromagnetic pulse welding. The purpose of the present work is to demonstrate that one can rather easily develop fretting-free joints between cylindrical tubes and nominally cylindrical nodes that do not require excessive energy to form and have the same strength as the parent metal tube. Directions that may lead to comprehensive models of strength are also indicated.

2 Elements of Crimp-Joint Strength and Performance

Despite the fact that electromagnetic crimp tube joining has been extensively practiced, and there are some publications [3] that analyze the creation and strength of these, there is not nearly a sufficient published base of understanding that would allow an engineer to be able to design an EMF crimp joint, nor can its performance be reliably predicted.

There are three key factors that are divided because they require separate analytical approaches that dictate design and performance of a crimped-electromagnetic tube joint.

- There is a state of residual stress that exists after the crimped joint is created. A natural interference fit seems to be a fairly general feature of EMF crimp joints. This interference gives a backlash-free joint that will not fret.

- The second key issue is the bulk configuration of the joint. Recesses in the node to be joined require bulk deformation of the tube to separate the units.
- Lastly, indentation of the surface (with indentation depths on the order of the sheet thickness, or less) is also important. Such surface recesses are the mechanisms by which bolts carry axial loads.

Here we discuss some recent experiments and thinking on each of these three issues and we will suggest directions towards the development of quantitative design methods for crimp joints. The emphasis will be on the issues of the interference fit formed by high velocity forming and the use of surface indentation to create joint strength.

We have recently carried out experimental and analytical studies with the aim of understanding the residual stress state that exists in an axisymmetric crimped joint after formation. There are two important components. The impact creates a natural interference fit and gives a radial distribution to the stress state. Also cooling from the temperatures induced by EMF creates a strain that must be considered. Experiments give a clear trend of increasing interference with increasing impact energy, while modeling results are less clear.

The configuration of the mandrel upon which a tube is crimped is also a matter of concern. In past designs [3,5,7], depressions that were several times the tube thickness in width and depth were considered. This is the approach taken by Boeing and others. Here we consider crimping onto 'textured' surfaces such as screw threads and knurls. We show experimentally that approaches of this type can give joints that exceed the strength of the tube both in torsion and axial loading. Analysis methods based on coupling impact-indentation and break-before-strip criteria can be used to compare joints made in this way with those based on the more traditional large scale deformation of the tube. One of the advantages of forming onto 'textured' surfaces is that a number of small pulses can be used to create a joint that has the strength of the parent tube, without any heat affected zones or distortion. Again, the natural interference fit developed by impact eliminates the potential for fretting.

3 Interference Fits

Empirically, it is very clear that in high velocity crimp-joining an interference fit between a collapsed tube and mandrel is very common. It is also common if a tube is expanded into a cylindrical cavity. Ultimately, it would be quite useful to have analytical models to predict this level of interference. First, it is useful to have measured data for this. That is the goal here, to measure the level of interference developed in several simple tube-collapse experiments onto varied mandrels.

Fairly simple experiments involving crimping onto mandrels of three different materials were performed. The tube used for crimping is aluminum 6061-T6 with outer diameter of 28.5 mm and wall thickness of 1.67 mm. The crimped tubes had a height of 12.7 mm. These were collapsed onto mandrels with very different elastic stiffness. The stiffest mandrel used was mild steel, 6061-T6 aluminum had elastic properties matching those of the ring, and the reinforced phenolic composite known by the trade name G-10 was used as the last mandrel. A simple single turn coil was used for crimping. High conductivity copper was chosen for this coil design to provide both enough strength and conductivity. The coil

is 25.4 mm thick and has a 29.1 mm hole inside to provide concentrated current flow in the internal surface of the coil. The 29.1 mm hole was tapered down to 12.7 mm in height, which is the coil's working area during electromagnetic process. A standard 16 kJ (8.3 kV @16 kJ) Maxwell-Magneform capacitor bank was used as the energy source. Crimps were made at varied bank energies as indicated by fractional energy stored.
After crimping, each sample was strain gauged and the strain gauge was zeroed. Then the ring was cut with a band saw longitudinally at a location diametrically opposed to the strain gage location. See Figure 1 for the overall system used in crimping and strain gauging. The entire ring develops a measured compressive hoop strain at the surface that is measured by the strain gage after cutting. This measured strain as a function of crimping energy is shown in Figure 2. There are two separable components to this strain. First, the ring changes its radius of curvature from that of the mandrel (on the inside) to one that is always larger, as the ring opens up on cutting. Ring opening displacements were measured for each ring after cutting and this can be related to the tensile strain gradient across the ring as:

$$\Delta\varepsilon_{max} = \frac{t}{2}\cdot\left(\frac{1}{\rho_1}-\frac{1}{\rho_2}\right) \tag{1}$$

where t is the ring thickness and ρ represents radius of curvature. The strain change between the inner and outer surface is calculated and presented in Figure 1.

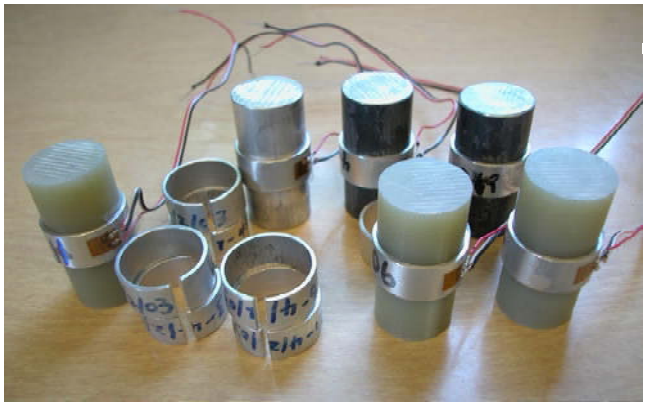

Figure 1: *Photograph of typical crimped rings, mandrels, and strain gauges*

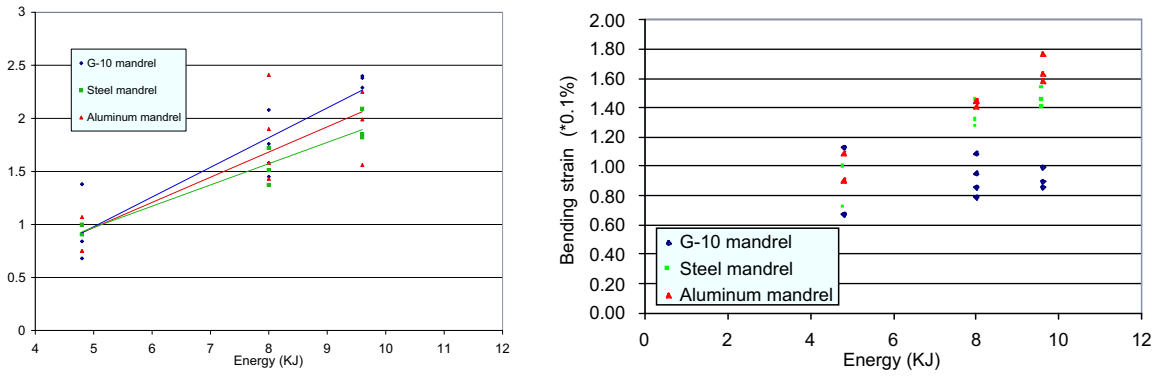

Figure 2: *Raw data showing: The strain measured by the strain gage (left) and the strain contributed by bending as measured by opening of the ring after cutting (right)*

By subtracting the bending strain from the strain measured at the surface gauge, we can estimate the pure extension strain that exists on the inside surface of the gauge prior to cutting. This is shown in Figure 3. This shows that there are significant interference strains for all three mandrels and the level of interference increases with increasing discharge energy and also increases as the stiffness of the mandrel decreases. These strains are also on the same order as one may expect based on thermal contraction. Ring heating is often on the order of 30°C. In the case of aluminum, cooling from this temperature can cause a contraction of about 0.07%. It seems that this is not a sufficient explanation for the interference fits observed, however because one can also develop interference by expanding rings into hollow cylinders.

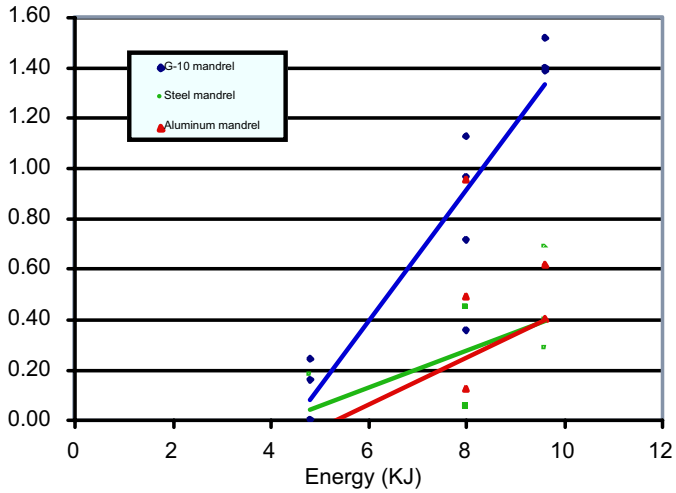

Figure 3: *Measurement of the overall interference strain developed on ring crimping for each mandrel as a function of discharge energy*

4 Surface Indentation

4.1 A Brief Theory of Indentation Joining Mechanics

As pointed out in the introduction there are two basic ways one can fabricate a tube joint based upon interlocking shapes. These two basic mechanisms are distinguished largely upon the way we analyze them. If one is to make the bulk of the tube interlock with features that are larger than the tube thickness one can use the approach published by Golovashenko [8]. Another approach is based upon forming into the tube sheet indentations that have a height less than that of the tube thickness. The examples we will study here are based on indentation onto a screw thread, knurled surface or axially-grooved screw thread.

The concept we will follow here is derivative of what has been used in the design of bolted joints. In the design of a bolted joint an axial force is carried by the bolt and produces a normal axial stress through most of the bolt. At the threaded end this axial stress becomes a shear stress through the threads. A bolt will have full structural efficiency if, when tested destructively, it fails by normal rupture of the bolt and opposed by stripping the threads. The length of bolt that must be engaged to ensure that the bolt will fail in tension can be easily estimated. First we assume that the area that must be sheared, A_s, is

equal to the length engaged by the nut $A_s=\pi DI$. Here, D is the nominal diameter of the bolt and I is the length of the nut. This assumes that the entire area engaged by the nut must be sheared at once. The shear force that the bolt can hold is related to the shear flow stress, τ_o, of the material as $F_s=\pi DI\tau_o$. The axial force $F_a=\sigma_o\ \pi(D/2)^2$, of course. We note that typically the shear stress of a material is about 1/2 the axial stress (Tresca criterion) and based on this we can find the nut length that ensures axial failure instead of shear as being about one-half the diameter of the bolt. Note that within the important assumption that the bolt is well-engaged by the nut; the pitch or depth of the thread is unimportant.

One of the things we would like to do presently is to 'optimize' the fabrication of a high velocity crimp created by the axial implosion of a tube onto a mandrel with a textured surface. Let us be a bit more specific as to what 'optimize' may mean. First, we would like to make a joint that has as much or more axial and/or torsional strength than the tube we will join to a mandrel. (Note: joint strength beyond the breaking point of the tube has no value). We would also like to make this joint using the minimum electromagnetic energy expenditure. Higher energy expenditure requires larger capacitor banks and more expensive/elaborate coils. Higher-level considerations (a bit beyond the scope of the present article) are that we may desire joints that remain tight after a given impact or joints that are fatigue resistant.

As impact velocity will scale with energy input, next we create a simple model for estimating the impact energy required to form a fully-engaged indentation joint. Let us assume a tube with thickness, t, made from a material with density ρ, and axial flow stress, σ_o, is imploded towards a mandrel. The mandrel can be taken as non-deformable and has a textured surface where the texture has an amplitude of depth d, and a wavelength λ. The kinetic energy per unit of area of the tube, $E_k=0.5\ t\ r\ v^2$, where v is the tube inward velocity. The tube will decelerate upon striking the textured surface and kinetic energy will be dissipated as plastic work in generating indentations in the metal surface. The plastic work done in creating the indented surface can be taken as the integral of the force acting on the deforming tube integrated over the depth of penetration of the mandrel pattern into the tube. An exact calculation of this integral is very difficult because of many real-world complications (chiefly, difficulties in knowing friction and the appropriate constitutive behavior of the materials). However, there are clear bounds on this integral. First, the total depth of possible indentation is d, and a plastically deforming surface will take the shape of a rigid, arbitrarily-shaped surface at a pressure of $3\sigma_o$. Thus, the maximum possible amount of energy that would be absorbed plastically while engaging the surfaces is $3\sigma_o d$. The actual value would be some fraction, F_1, of this value (which depends upon details such as coefficients of friction and the shape of the undulating surface that is to be joined. Based on equating kinetic energy and that absorbed on impact through an efficiency factor, E, one can estimate the impact velocity required to engage the tube and mandrel as:

$$V=\sqrt{\frac{6F_1\sigma_o d}{Et\rho}} \tag{2}$$

For typical values (a 2 mm thick aluminum tube engaged onto 1 mm deep grooves using F_1 = 0.5 and E = 0.5) we estimate impact velocities on the order of 150 m/s required for full engagement. Note that terms such as E and F_1 are very difficult to estimate accurately (but not too difficult to bound), the scaling relationship provided by Equation (1) is quite useful. It basically says that as the depth of the indentations decreases, the required im-

pact velocity for engagement decreases. Note that traditional screw theory states that the strength of the joint does not depend on depth of engagement. Thus, as long as the joint is robust, this analysis indicates that a rather shallow surface texture is desired to minimize the kinetic energy required to make the joint.

4.2 An Experimental Study of Indentation Joining

Experiments were performed to characterize the strength of the union developed with mandrels with different surface configurations. The tubes subjected to crimp were made of Aluminum 6061-T6 alloy and had a total length of 64 mm with an outer diameter of 28.5 mm and wall thickness of 1.47 mm. Two different types of mandrels were used in the experiments: with knurled and threaded surfaces. The threaded mandrels can only effectively resist axial forces, while the knurled geometry was chosen because it is a commonly-available surface configuration that may resist axial and shear loading. The screw threads have a much sharper apex angle than the knurled surfaces.

The knurled mandrels were made of 12L14 low carbon steel. Cylindrical mandrels of three diameters were machined and subsequently knurled to obtain the desired surface finish. Diameters 20.8, 21.59 and 22.6 mm and length of 38.1 mm were knurled obtaining two different surface finish sizes that we will refer to as coarse and fine knurls. From the 22.6 mm in diameter mandrels, coarse and fine knurls were obtained and only fine knurls were machined in the 21.59 and 20.8 mm cylinders. Threaded rods of two pitch sizes (standard coarse and fine one inch diameter screw threads) were used in the second set of experiments. Samples that were 50.8 mm long were cut in each case. Examples of the knurled and threaded mandrels along with treaded mandrels with axial grooves for shear resistance are shown in Figure 4. The same capacitor bank and coil that were used in the interference-fit part of this study were used for joining here. Figure 5 shows an example of a crimp joint made using the coarse screw thread that was subsequently tested in compression, causing the tube to fail. Also shown in that figure is a cross sectional image of that part showing how the tread indents into the tube. Lastly is an image of a joint made from a knurled surface.

Figure 4: *Example of some of the mandrel surfaces. Left to right: coarse knurl, fine knurl, fine screw thread with axial grooves, and coarse screw thread*

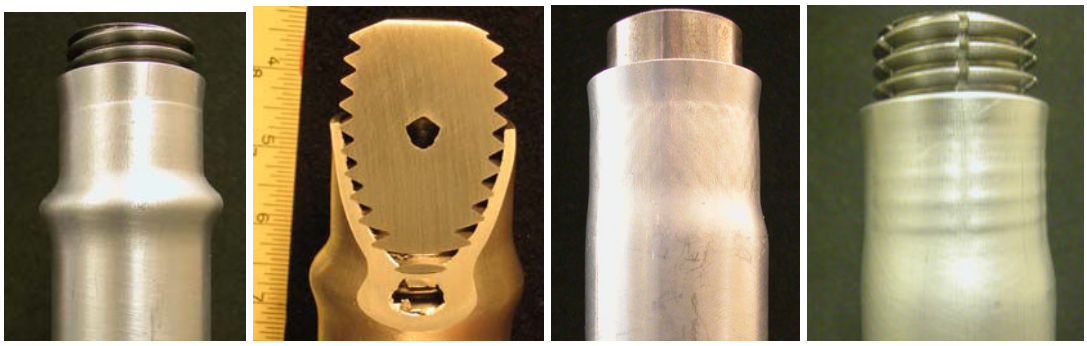

Figure 5: *Examples of crimp joints based on surface impression. From left: joint based on a 25.4 mm coarse screw thread tested in compression (14 kJ impulse onto a coarse thread screw); angled cross section of similar joint; a joint based on a knurled mandrel*

If one is to follow the approach described above to design a system to join tubes by crimping we would like to optimize impact velocity, and join a mandrel that has a fine pitch and has features that would fully engage the surface. Figure 6 shows predictions of the tube velocity-time profile expected in these experiments. Note that at discharge energies of more than about 10 kJ, the optimal standoff is predicted to be between about 1 and 1.5 mm. Also, we find that it is important to center the mandrel, tube, and coil about a single axis. If centering is poor one can develop a joint that has some slop. Further research is required to understand conditions that do and do not develop slop.

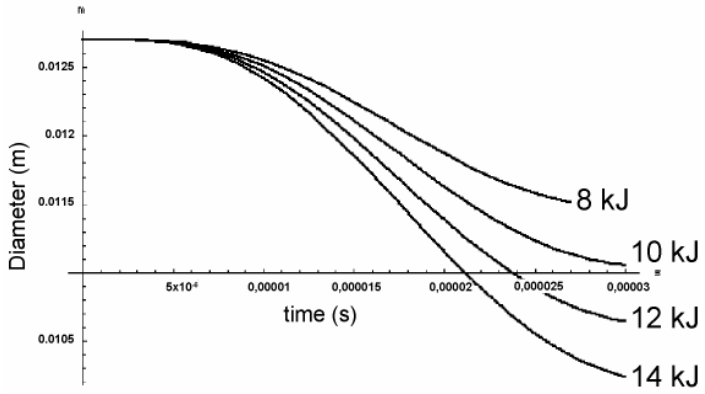

Figure 6: *Simulations of tube radius as a function of time using our capacitor bank system and launch energies of 8, 10, 12 and 14 kJ. Note that impact velocity would be relatively constant for a range of mandrel diameters and that the optimum standoff will increase with increasing launch energy*

Figures 7-9 show the results of axial strength testing of tubes that have been crimped as described. Figure 7 shows the effect of varied tube-mandrel gap and the same mandrel surface. The 1.5 mm gap is generally predicted to have the largest impact velocity (Figure 6) and it shows the highest axial strength. At other studied gap distances the tube is beginning to decelerate significantly. Figure 8 shows that, as predicted by Equation (2), the fine knurled surface generally creates the strongest joint when impacted at the same nominal velocity. The use of multiple impulses to improve joint strength was also studied. When multiple EM impulses were applied to the same section of tube, strength is not in-

creased significantly. However, if the crimp length is increased by moving down the tube, joint strength is increased as shown in Figure 9. However, the strength is not increased linearly with crimp length, as predicted by the simple theory.

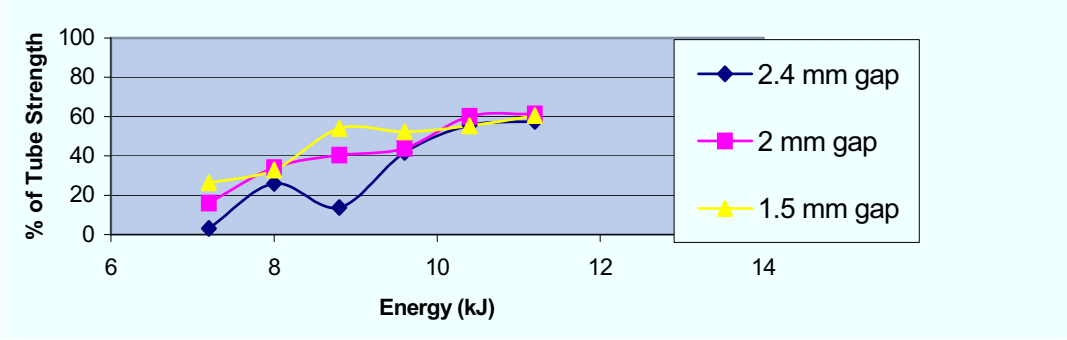

Figure 7: *Axial strength of high velocity crimp joints made onto fine knurled surfaces. Of the gaps studied the smallest is predicted to have the highest impact velocity and it also has the highest strength*

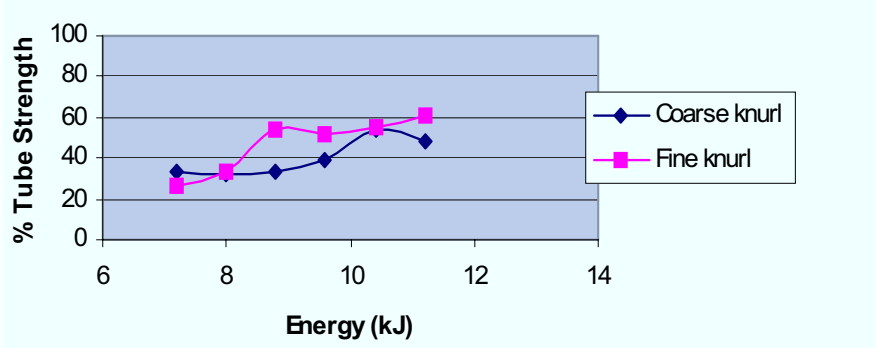

Figure 8: *Axial strength of joints made by collapse onto knurled surfaces with a fixed gap of 1.5 mm*

Often, torsional strength in tube-to-mandrel crimp joints. The threaded joints have very little intrinsic torsional strength. However, when crimping onto the fine knurled mandrel at 14 kJ with a 1.5 mm gap, we were able to produce a joint that had the full torsional strength of the tube. Also, by cutting grooves in threaded joints significant torsional strength can be attained, as shown in Figure 10.

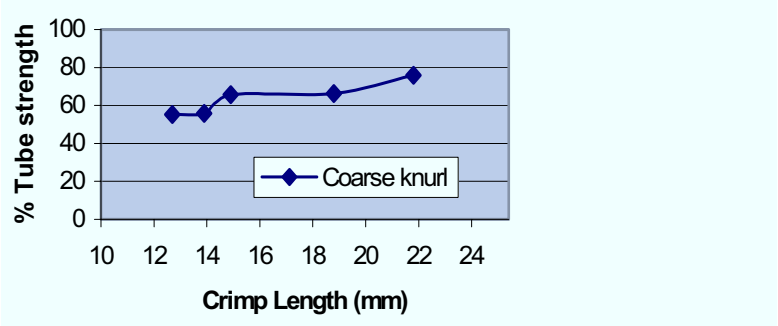

Figure 9: *Compressive axial tube strength on a coarse knurled surface using a 1.5 mm gap and 14 kJ discharge energy*

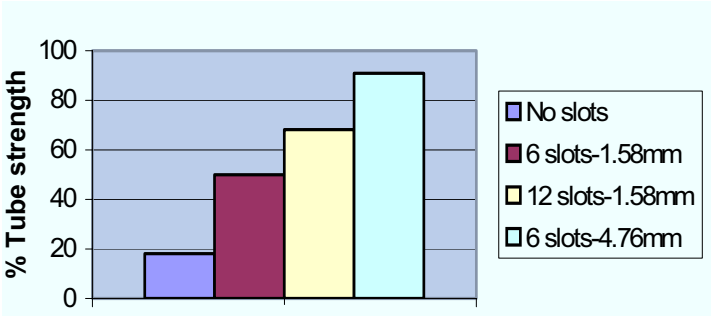

Figure 10: *Torsional strength developed by cutting grooves in threaded mandrels (see Figure 5)*

5 Conclusions

Crimp joining offers a particularly effective, low-cost, and efficient way of joining tubes to mandrels. Two aspects are especially appealing. First, high velocity forming typically develops a natural interference fit that resists motion. Second, by forming onto undulating surfaces (such as screw, threads, cut screw threads, and knurls) joints that have the strength of the parent tube in torsion and tension can be created at modest impact velocities and have been demonstrated. This combination of high strength and simplicity makes this kind of joining unique.

References

[1] See website of Maxwell-Magneform at www.magneform.com.

[2] *G. S. Daehn*: "High Velocity Metal Forming, Chapter in forthcoming ASM Handbook, Volume 14, Forming and Forging, (2004).

[3] *S. Golovashchenko*: "Methodology of Design of Pulsed Electromagnetic Joining of Tubes", in Innovations in Processing and Manufacturing of Sheet Materials, M Demeri, Ed., TMS 2001.

[4] *Peihui Zhang:* PhD Thesis, "Joining Enabled by High Velocity Deformation", The Ohio State University, 2003.

[5] *A. Arena, R. L. Benoit:* "Torsion Resistant Grooved Joint", U. S. Patent, 4,523.872

[6] *Bruno,E.J., ed.:* "High Velocity Forming of Metals", American Society of Tool and Manufacturing Engineers, Dearborne, MI, (1968).

[7] *G.S. Daehn:* "High Velocity Metal Forming", Chapter in forthcoming ASM Handbook, Volume 14, Forming and Forging, (2004).

[8] *S. F. Golovashchenko:* "Numerical and Experimental Results on Pulsed Tubes Calibration", Proceedings of a 1999 TMS Symposium "Sheet Metal Forming Technology", San Diego, 117-127, (1999).

[9] *S.B. Carl and C.M. Foster:* "Aerostar Aluminum Driveshaft", Technical Paper, Series 841697, Society of Automotive Engineers, (1984).

Electromagnetic Compression as Preforming Operation for Tubular Hydroforming Parts *

V. Psyk, C. Beerwald, W. Homberg, M. Kleiner

Chair of Forming Technology, University of Dortmund, Germany

Abstract

With the aim to extent the forming limits of tube hydroforming a concept of using a previous electromagnetic compression operation will be introduced. One important limit for the possibilities of tube hydroforming is set by the initial circumference and the maximum tangential strain of the used material, whereby the initial circumference is typically determined by the smallest local circumference of the workpiece. The application of an appropriate contoured preform makes it possible to use tubes with a larger initial circumference.

In the paper the investigation of the suitability of electromagnetic tube compression for the production of such a preform will be presented. The valuation is based on geometric criteria and material properties of the resulting preform which are strongly influenced by the process parameters. The discussed aspects are the roundness of the preform and the strain hardening of the material.

Keywords:

Electromagnetic forming, Tube compression, Hydroforming, Process combination

---

* *The present study has been performed by the authors within the European project "Electromagnetic forming of tube and sheet metal for automotive parts – EMF – G3RD-CT-2002-00798". The conclusions drawn and the views put forward here do only reflect the opinions of the authors and not necessarily those of the rest of the project consortium. The project has been funded by the European Commission and the consortium has the following partners: Volvo Cars Body Components, Centro Richerche Fiat SCpA, DaimlerChrysler AG, PSA Peugeot- Citroën Automobiles, Alcan Technology & Management Ltd, Beijing Research Institute of Mechanical and Electrical Technology, ESI SA, University of Dortmund and University of Trento.*

1 Introduction

The production of complex components from tubular semi-finished parts is often realised by hydroforming. Especially for the forming of lightweight construction components for the automotive industry the hydroforming process represents a new technique and offers a new production potential. [1, 2, 3, 4]

The achievable strain of hydroformed tubes is limited by the stress strain behaviour of the workpiece material as well as by the initial circumference of the tube. The smallest local circumference of the finished workpiece geometry typically determines the maximum possible initial tube circumference. This forming limit can be extended by applying an appropriate contoured preform which makes it possible to use tubes with a larger initial circumference for the hydroforming process. These tubes are locally compressed during the preforming operation.

Since the automotive industry uses more and more hydroforming parts from aluminium alloys the electromagnetic forming process (EMF) seems to open upnew possibilities for such preforming operations. For the EM- compression process the tube is arranged within a compression coil, and a pulsed magnetic field in the gap between tool coil and tube generates a strong pressure pulse in radial direction. This short pressure pulse causes a symmetric reduction of the tube diameter with typical strain rates of about 10^4 s^{-1}. In comparison to conventional quasistatic forming processes the EMF process offers several advantages, as for example

- **the possibility to compress rotationally symmetric geometries without a form defining tool (mandrel):**
  Due to the high forming velocities, localising effects are reduced and the compression process can be performed as a free forming operation. For example, a compression operation would be difficult by means of hydroforming and it is not practicable without a mandrel.
- **the possibility to perform a compression process in a process chain after a bending operation:**
  In contrast to incremental forming processes, like e.g. spinning, the EMF- compression is not limited to straight profiles, but it can be performed close to corners and radii.
- **the possibility to form geometries which are not rotationally symmetric:**
  If the EMF- process is performed with a form defining tool it is possible to use mandrels with cross sections which are not round. The potential geometries are limited by the possibilities to remove the mandrel from the tube. Therefore, it is not possible to realise indentations using this forming strategy.

In the following paper the investigation of the suitability of electromagnetic tube compression as a preforming operation in combination with the hydroforming process will be presented. The valuation is based on geometric criteria and material properties of the resulting preform which are strongly influenced by the process parameters. The most important aspects for the investigation are wrinkling effects, respectively the roundness of the preform, and the strain hardening of the material. In the present article some basic correlations concerning the effects of the electromagnetic forming on the workpiece will be presented and results of the free compression process as the most simple setup will be shown for one selected material (AA 5754).

2 Determination of Significant Process Parameters

An important precondition for the valuation and optimisation of the electromagnetic preforming operation is the knowledge of significant process parameters and their influence on the forming process as well as on the forming result.

The effective load acting on the workpiece is one important aspect affecting the process. It is influenced by properties of the tool coil, the forming machine, and the charging energy of the capacitor battery. For the definition and quantification of the effective load, the pressure distribution and the pressure course can be used. The pressure course is characterised by its maximum and duration, both influencing the achievable tangential strain in a free forming operation, as well as the pressure rise time which significantly influences the forming velocity.

Due to this perception, the description of the acting load becomes independent of the EMF- equipment. For the determination of the magnetic pressure p the measured coil current serves as an input. On this basis the course and the distribution of the magnetic field and the magnetic pressure can be calculated [5,6].

In addition to the load, the initial condition of the workpiece also has a great influence on the deformation process and the forming result. It can be described by geometric attributes including diameter, roundness, wall thickness, and its distribution as well as by material properties like strength, hardness, and maximum strain determined by the quasistatic tensile test and the quasistatic burst test.

The investigations presented in the following article have been performed using tubes made of AA 5754 with a nominal diameter of 40 mm and a nominal wall thickness of 2 mm. To classify the initial condition of the tube material, exact values of the inner and outer roundness as well as the wall thickness distribution along the circumference are shown in Figure 1.

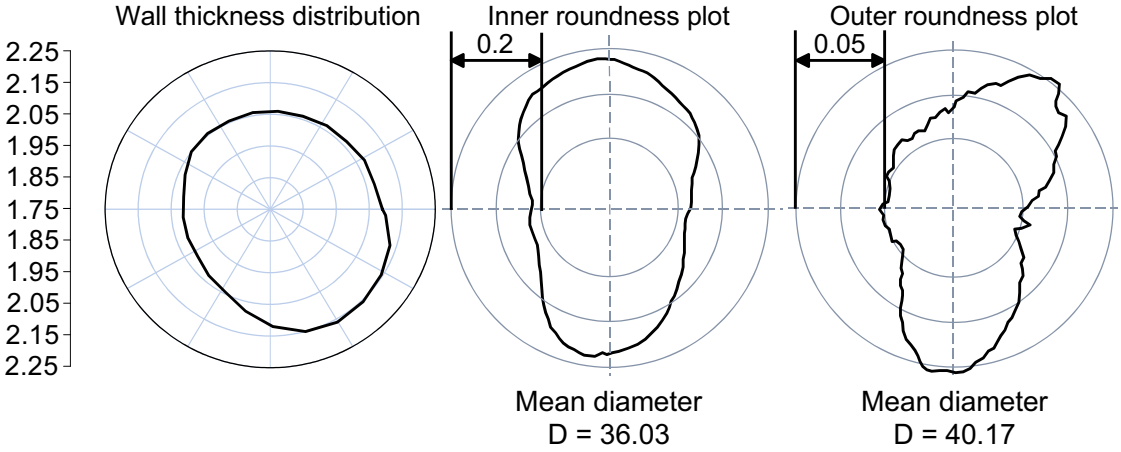

Figure 1: *Roundness and wall thickness distribution of the investigated material*

According to the requirements for extrusion profiles defined in DIN EN 12020-2, the tolerance for the diameter is ± 0.3 mm and the tolerance for the wall thickness is ± 0.25 mm. As it can be seen in Figure 1 the used material meets these demands. Furthermore, the investigated material has been produced without any extrusion seams, so that a good homogeneity of the material along the circumference is granted.

Additional material characteristics have been determined by means of Vickers hardness tests, tensile tests, and hydraulic burst tests. The determined data is summarised in Table 1.

Tensile strength R_m	approx. 250 N/mm²
Yield strength $R_{p0.2}$	approx. 125 N/mm²
Maximum axial strain (quasistatic tensile test) $A_{0,\ axial}$	approx. 23%
Maximum tangential strain (quasistatic burst test) $A_{0,\ tangential}$	approx. 8%
Vickers hardness *HV*	approx. 81 HV5

Table 1: *Material characteristics of the investigated material*

The effective load and the material properties of the workpiece represent the input parameters of the forming process, causing the deformation behaviour of the workpiece. This behaviour includes the radial deformation, the forming velocity, and the final geometry, characterised by roundness and contour, as well as the increase of strength and hardness of the material.

The online measurement of the radial deformation is performed by means of an optic method. The shadowing of a linear laser beam, which shines in axial direction through the workpiece, is measured by a Position Sensitive Device (PSD). The voltage signal of the PSD is proportional to the radial deformation of the tube's smallest cross section. On this basis the tangential strain and the strain rate can be calculated[5, 6].

3 Influence of the Tangential Strain

3.1 Correlation between Tangential Strain and Roundness

As already mentioned, the pressure course can be characterised by the pressure maximum and the pressure rise time. If the parameters of the forming machine, the tool coil, and the workpiece are equal an increase of the charging energy will lead to an increase of the pressure maximum, while the pressure rise time remains approximately the same.

The resulting geometry of tubular specimen compressed in free forming operations with different maximum pressures has been measured with a coordinate measurement system and exemplary results are presented in Figure 2.

As expected, an increase of the pressure maximum leads to a higher deformation of the workpiece. Furthermore, the increasing tangential strain is correlated to a worsening of roundness respectively to an increasing wrinkling effect. This wrinkling effect seems to be connected to the distribution of the tube's wall thickness. The reason might be that the stiffness of the tube, which is characterised by the ratio of wall thickness and radius, decreases with a decreasing wall thickness, and that a smaller stiffness is more susceptible to wrinkling. Another aspect influencing the roundness is the homogeneity of the material. As already mentioned, the investigated material is of good homogeneity. In other cases it can be expected that inhomogeneities, like e.g. extrusion seams, cause earlier and more extreme wrinkling.

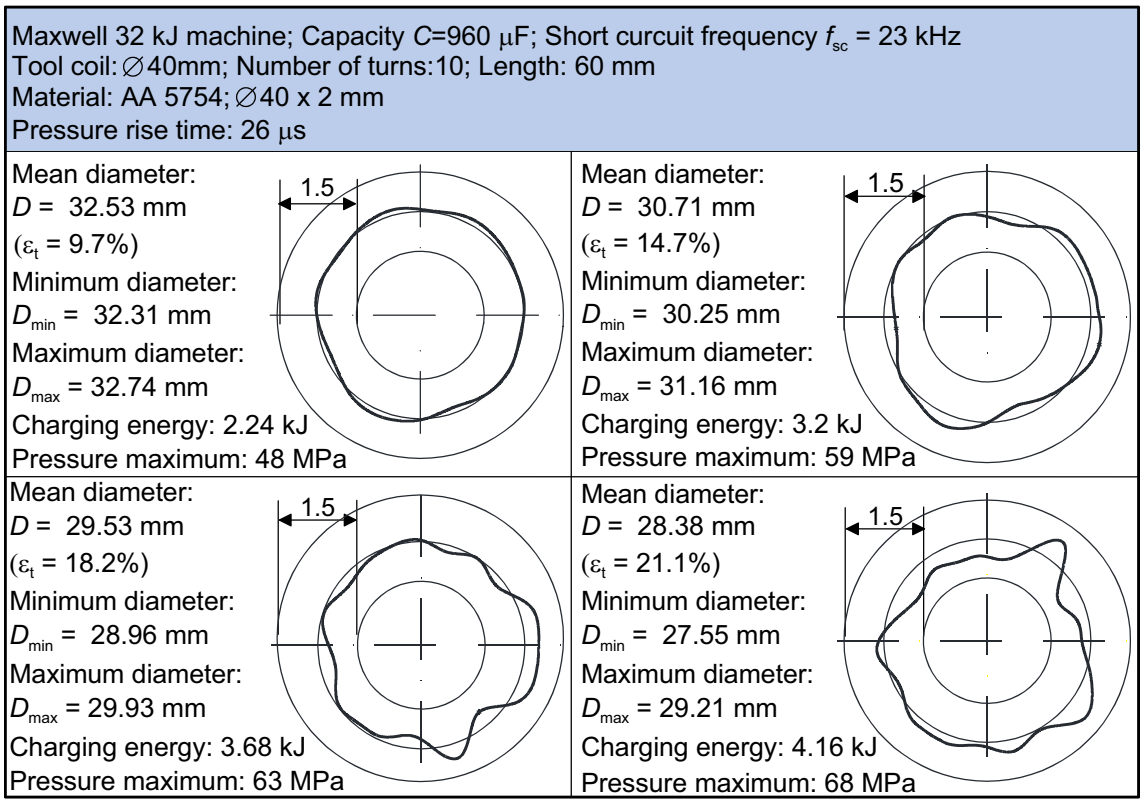

Figure 2: *Roundness plots of specimen of different tangential strain*

For the valuation of the achieved roundness it has to be taken into account that the compression process is a preforming operation and that the calibration shall be realised by the subsequent hydroforming step. It is not necessary to achieve the geometric tolerances requested for the final part, but up to a certain limit geometric deflections can be corrected and wrinkles are reversible.

3.2 Correlation between Tangential Strain and Strain Hardening Effect

In addition to the described influence on the roundness of the preform, the tangential strain also influences the material properties which can be characterised by the hardness. To analyse this influence, Vickers hardness tests have been performed on specimen with different tangential strain. Figure 3 shows the results of selected experiments.

As it is known from quasistatic forming operations, the hardness in this high speed compression process also increases with a rising tangential strain due to the strain hardening effect. Furthermore, the increase of hardness seems to be stronger for small deformations and to decline slightly for further strain.

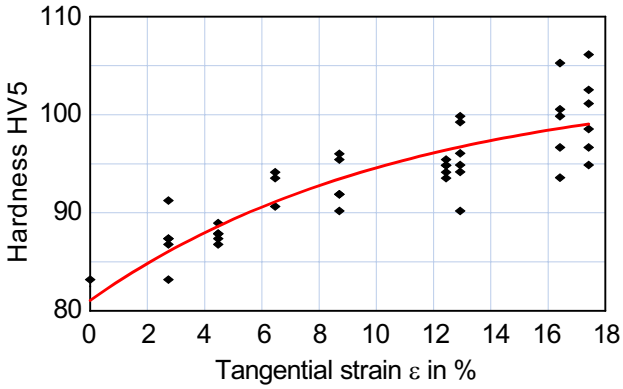

Maxwell 32 kJ machine
Tool coil: ∅80 mm; fieldshaper
Number of turns:8; Length: 90 mm
Workpiece AA5754 ∅40 x 2 mm

Figure 3: *Vickers hardness of tubular specimen with different tangential strain*

The strain hardening, resulting from the electromagnetic preforming operation, is of particular importance for the subsequent hydroforming step, because the remaining forming capability in the preformed workpiece areas will be reduced due to an increasing reduction of the tube diameter. Furthermore, the needed pressure during the hydraulic expansion is higher for harder materials.

To quantify these effects, hydraulic burst tests are necessary. Since there is no distinct correlation known between the maximum tangential strain and the maximum uniaxial strain determined in tensile tests, the burst test is essential to estimate the formability in case of tube hydroforming conditions. Although the forming capability of the material decreases according to the increasing hardness (compare Figure 3), it is not completely depleted after the electromagnetic compression up to a tangential strain of about 18%.

4 Influence of the Forming Velocity

4.1 Influence of the Pressure Rise Time on the Strain Rate

The frequency of the pressure course, and therefore also the pressure rise time, directly refers to the frequency of the coil current which is determined by the elements of the oscillating circuit, especially the inductance and the capacity. This means that the pressure course can be adjusted by the adaptation of tool coil and forming machine [7].

With the aim of analysing the influence of the pressure rise time on a tube deformation process, experiments have been performed with several tool coils and two different forming machines available at the Chair of Forming Technology of the University of Dortmund. Figure 4 presents two examples of different pressure over time curves leading to the same final workpiece deformation. The according compression of the tubes is quantified as the course of the radial displacement of the smallest cross section. For the comparison of these curves it is helpful to use the derivation which corresponds to the tangential strain rate. Therefore, the strain rate over strain functions, which are the referring values for velocity and displacement, can also be seen in Figure 4.

The comparison of the pressure course and the according displacement course shows that after the beginning of the pressure rise there is a short delay before the workpiece deformation starts. This retardation is caused by inertia effects which have to be exceeded by the applied pressure. Furthermore, it can be seen that the plastic deformation of the workpiece is completed during the first half wave of the magnetic pressure. This

behaviour has been observed in every compression process of aluminium tubes, because here, in contrast to the electromagnetic expansion and sheet metal forming, the stiffness of the workpiece increases due to the forming operation.

From the comparison of the two processes shown in the diagrams it can be concluded that in order to achieve a defined radial deformation with a shorter pressure rise time, the maximum pressure has to be higher. Additionally, it is obvious that a faster rise of the pressure also leads to a higher strain rate.

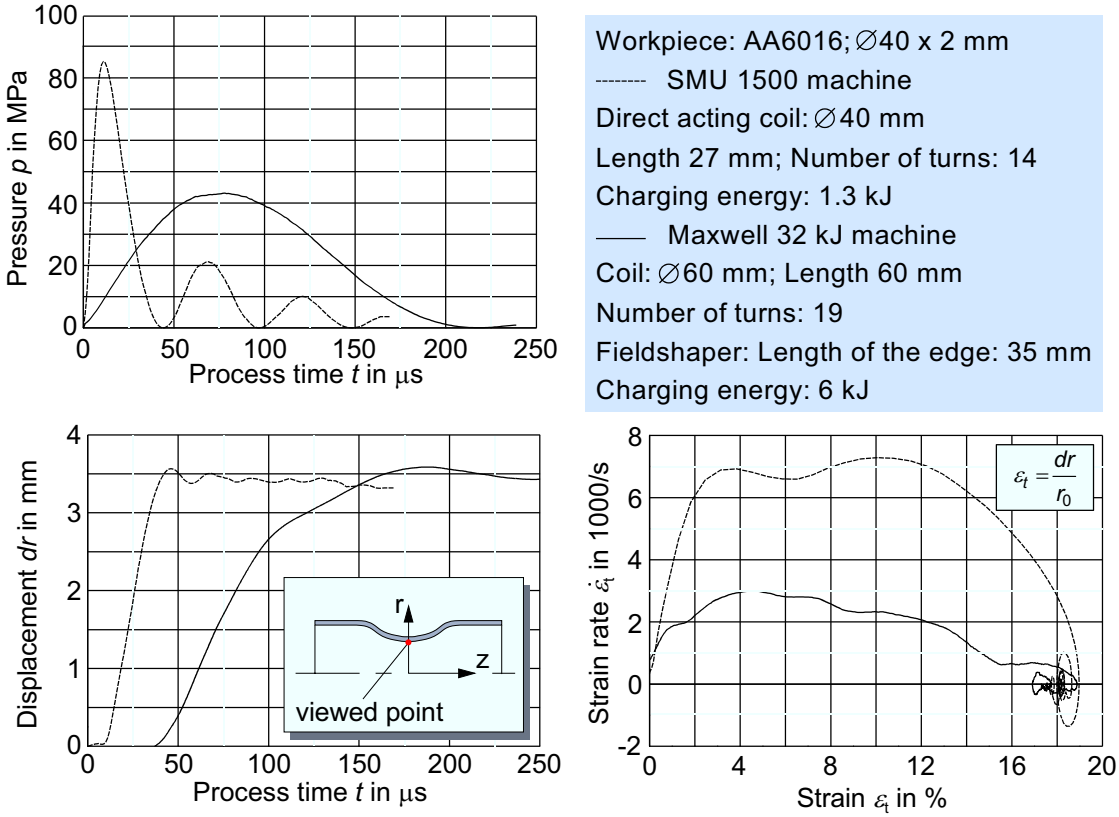

Figure 4: *Different pressure impulses and according workpiece deformations*

4.2 Influence of Pressure Rise Time on Roundness

For further investigations regardind the influence of the pressure rise time on the roundness of the resulting preform, additional experiments have been performed. To except the influence of the tool coil parameters, especially the length, several experiments have been performed using one and the same tool coil. The variation of the pressure course has been realised by using an EMF-machine, provided by the company Poynting GmbH, Dortmund. This machine offers a maximum charging energy of 60 kJ. Depending on the charging energy needed it is possible on this machine to use capacitor banks of different sizes separately or in any user-defined combination in order to optimise the pressure course for a special forming task. Different specimen with nearly the same tangential strain have been produced with this machine. Exemplary results are shown as roundness plots in Figure 5.

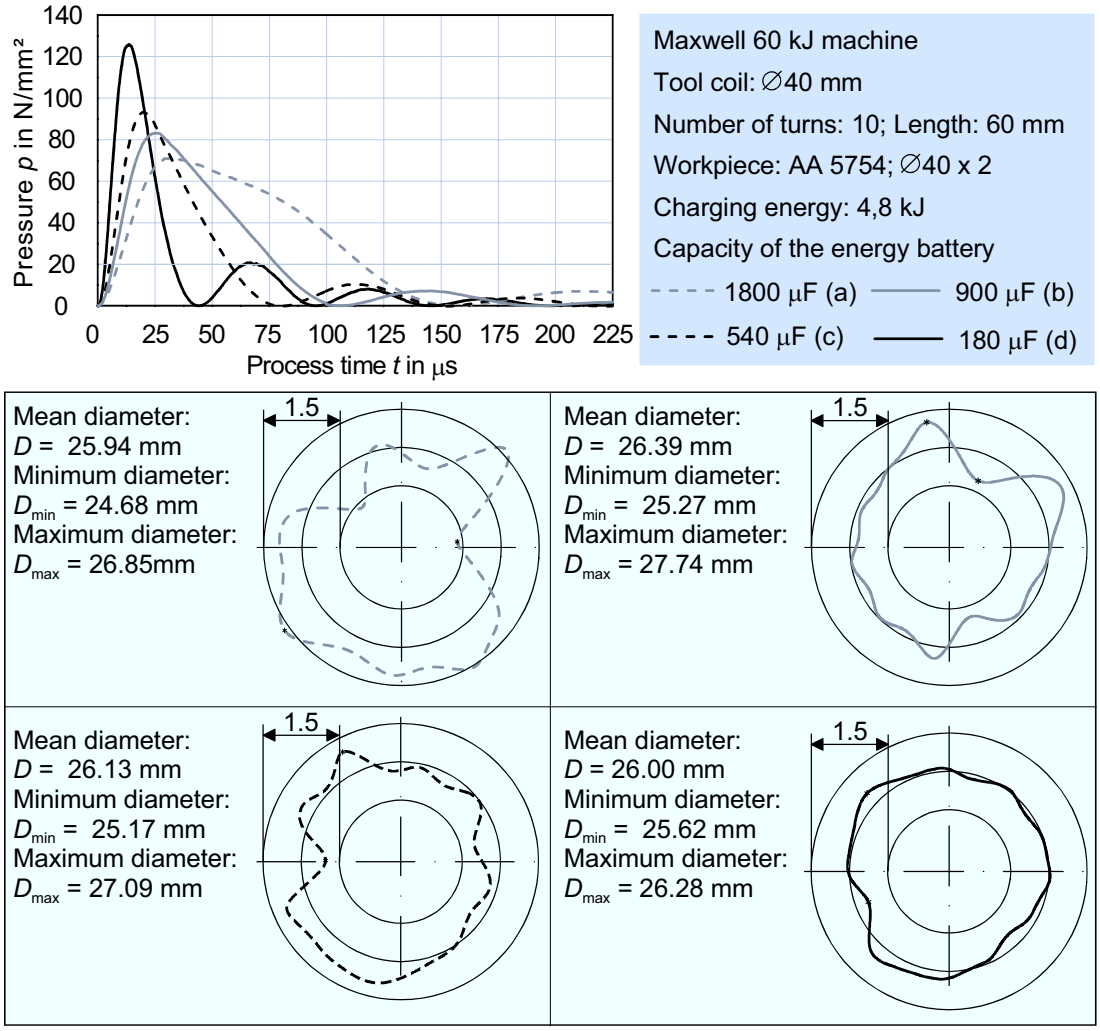

Figure 5: *Influence of the strain rate on the roundness*

As it can be seen from this Figure, the mean diameter of the compressed tubes is similar. It varies between 25,94 mm and 26,39 mm. The deformations have been achieved using nearly the same charging energy of the capacitors.

Furthermore, a trend of an improved roundness due to a shorter pressure rise time and the according higher strain rate can be seen. This shows that a faster process reacts less sensitive to inhomogeneities, like e.g. extrusion seams or differences in the wall thickness. Localising effects seem to be reduced for higher forming velocities. The comparison of quasistatic and highspeed tube compression processes is an extreme example confirming this result. As already mentioned, a free compression is, in general, not possible by means of hydroforming. In contrast to this, a free electromagnetic compression process shows in many cases good results.

4.3 Influence of Pressure Rise Time on Strain Hardening

In addition to the influence of the pressure rise time on the resulting roundness of the preform, a possible dependence of the strain hardening on the pressure rise time has been investigated as well. To clarify, whether the forming velocity has an influence, results of

Vickers hardness tests performed on tubes, compressed with different strain rates, have been compared. Figure 6 shows the resulting hardness of the specimen according to the roundness plots presented in Figure 5, whereby the different strain rates are labelled as a, b, c, and d (with a < b < c < d). The measured hardness here is very similar for all specimen and no clear trend due to an increasing strain rate can be recognised. Therefore, it can be concluded that within the range of the regarded velocities the strain hardening only depends on the tangential strain and not on the strain rate.

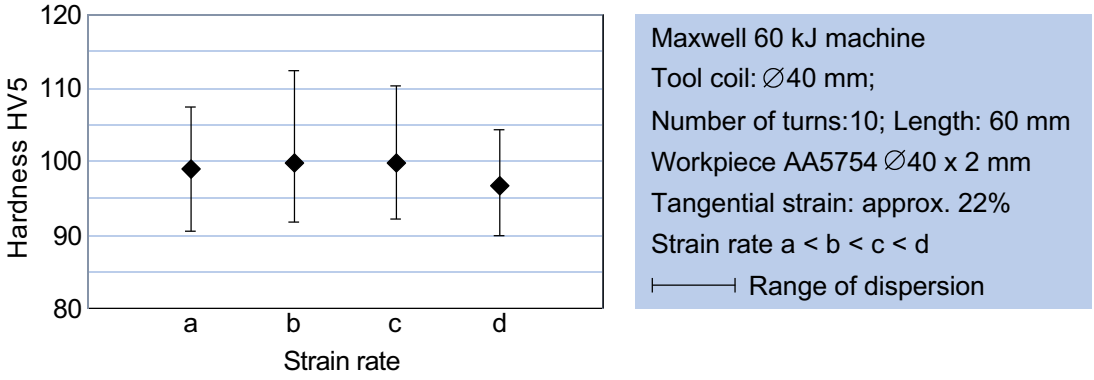

Figure 6: *Influence of the strain rate on the strain hardening*

This perception has been approved by the comparison of quasistatic and high speed forming processes. For this purpose Vickers hardness tests have been performed on electromagnetically and hydraulically expanded tubes. This approach assumes that the direction of the deformation does not influence the resulting hardness. This means that for the same tangential strain, compression and expansion will lead to the same hardness.

The tests have shown that, for example, a tangential strain of approx. 7.5% leads to a hardness of approx. HV5 = 92 in case of the hydraulically expanded tube, and to a hardness of approx. HV5 = 94 in case of the electromagnetically expanded tubes. A comparison with the results shown in Figure 3 approves the assumption that the hardness does not depend on the direction of the radial deformation.

5 Conclusions and Outlook

The investigations and results presented in this paper concentrate on the free electromagnetic compression process used as a preforming operation for hydroforming workpieces. An important precondition for this approach is that the remaining forming capability is high enough, so that occurring geometric deflections can be reversed and the final workpiece geometry can be realised by the subsequent hydroforming step.

It has been shown that a higher tangential strain, achieved by a higher pressure impulse, is correlated to an increasing wrinkling effect as well as to an increasing strain hardening effect. Furthermore, it has been found out that for a defined tangential strain a higher strain rate, caused by a shorter pressure rise time, leads to a better roundness, while the strain hardening remains unaffected. Comparing burst tests of tubes in the initial condition and on electromagnetically preformed tubes indicate that the forming capability is not depleted after the electromagnetic compression.

The consequent continuation of the presented research work is the investigation of the form defined electromagnetic compression. This allows an extension of the range of applications and makes it possible to produce geometries which typically occur in hydroforming parts for the automotive industry. Complicated forms including asymmetric cross section geometries as well as shifted ones [8] shall already be realised in the preforming step by means of electromagnetic forming. In this case, the preformed areas of the workpiece should have a shape which is as close as possible to the finished part geometry. The further investigation of this approach strongly depends on the desired workpiece geometry and will be performed within the above mentioned EU- project, exemplary by the production of a demonstrator.

References

[1] *Birkert, A.:* Herstellung von Strukturbauteilen durch Innenhochdruck-Umformen, Diss., Institute for Metal Forming Technology, University of Stuttgart, 2000.

[2] *Heizmann, J.:* Activator Assisted Forming Technologies – Status and Outlook, Proceedings of the International Conference on Hydroforming, Fellbach, 2003, p. 1- 6.

[3] *Dohmann, F.; Lange, K. (publisher):* Innenhochdruckumformen, Umformtechnik - Handbuch für Industrie und Wissenschaft, Volume 4, Springer-Verlag, Berlin/ Heidelberg, 1993.

[4] *Schroeder, M.:* Recent Developments in the Hydroforming of Tubular and Sheet Blanks – Semi Productive and Productive, Proceedings of the International Conference on Hydroforming, Volume 3, Fellbach, 2003, p. 165- 184.

[5] *Beerwald, C.; Brosius, A.; Homberg, W.; Kleiner, M.; Wellendorf, A.:* New aspects of electromagnetic forming, Proceedings of 6th International Conference on Technology of Plasticity, Nürnberg, 1999, p. 2471- 2476.

[6] *Beerwald, C.; Brosius, A.; Kleiner, M.:* Determination of flow stress at very high strain-rates by a combination of magnetic forming and FEM calculation, Proceedings of the International (CIRP) Workshop on Friction and Flow Stress in Cutting and Forming, Paris, 2000, p. 175- 182.

[7] *A. Henselek, M. Beerwald, C. Beerwald:* Design and Adaption of EMF Equipment - From Direct Acting Multi-turn Coils to Separable Tool Coils for Electromagntic Tube Compression, Proceedings of the International Conference on High Speed Forming, Dortmund, 2004.

[8] Verein Deutscher Ingenieure (publisher): VDI- Richtlinie 3146, Hydroforming – Basic knowledge, VDI- Verlag, Düsseldorf, 1999.

Non-thermal Laser Forming of Sheet Metal*

H. Schulze Niehoff, F. Vollertsen

Bremer Institut für angewandte Strahltechnik, Germany

Abstract

In this paper the results of some preliminary experiments are presented on non-thermal microforming of thin metal sheets with laser induced optical breakdown shock waves. Three sheet metal forming processes are realized with this method. The most deeply investigated process is laser stretch-forming, since the influence of parameters like defocussing, power density, pulse energy, number of pulses, and material could be worked out. The results show that uniform shaped domes with a dome height over 250 µm with diameters of 1.4 mm could be produced. Additionally, first investigations on laser stamping and laser embossing have been carried out, but are not presented in this paper.

Keywords:

Laser forming, Sheet metal forming, Stretch-forming

1 Introduction

Laser forming of sheet metal is well known as a process where different thermal mechanisms cause a bending of the sheet metal [1]. The most commonly known thermal mechanism is the temperature gradient, which causes inhomogeneous strains within the material, which results in an incremental forming process. In contrast to this process, non-thermal laser forming is a fairly new process, which does not use thermal mechanisms, but the optical low-threshold surface breakdown [2,3], which results in the creation of a shock wave. Its principle was first shown by O'Keefe [4]. He used a Q-switch Nd:YAG-Laser with a maximum power density of 1.7 GW/cm². The experiments showed thermal and mechanical damaging, but were not used for deeper investigations on sheet metal forming processes.

The shock wave is the responsible energy source for this forming process. This means that the forming velocity is mainly driven through the velocity of the shock wave.

*This work has been funded by the Leibniz-award Vo 530/7-1; the authors would like to thank the Deutsche Forschungsgemeinschaft for their financial support

The forming behaviour can hence be compared to the one of a high speed forming process like electromagnetic forming or explosive forming. The whole process duration cannot be assessed yet, but it is probably longer than the laser pulse duration of 20 ns, since the plasma formation, shock wave propagation, and bending processes occur successively.

The laser induced shock wave can in principle be used for all sheet metal forming processes, as long as the parts are in micro- or mesoscopic range. The following investigations are in non-thermal laser stretch-forming.

2 Method

Laser induced shock waves are well known and can be applied on metals by pulsed excimer laser beams through very high energy densities and are currently used for shock hardening. Figure 1 shows different laser surface treatments by excimer laser versus energy density, whereby the shock hardening requires the highest energy density, even higher than the energy density for ablation. This indicates that shock hardening is always accompanied by ablation. But ablation can be reduced by confined plasma through a transparent facing like transparent plastics or fluids like water. An interesting side effect of such facings is the increase of pressure of the shock wave on the target [5].

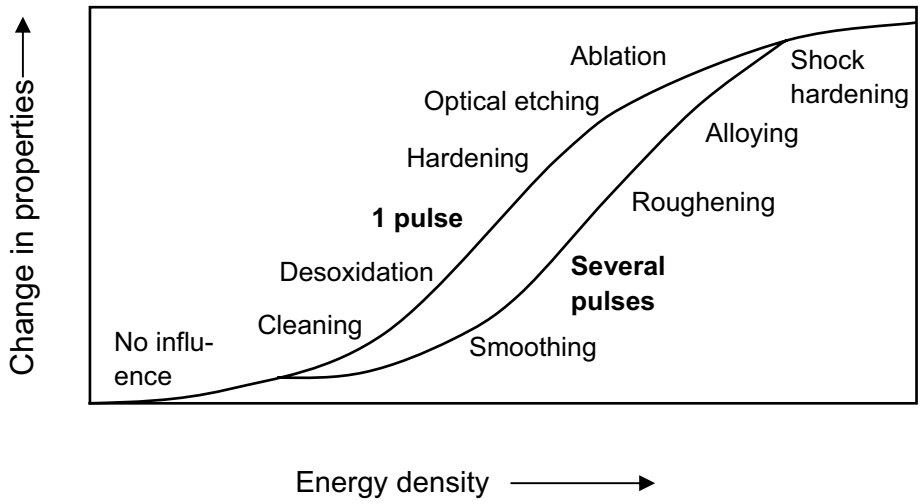

Figure 1: *Surface treatment of metals by excimer lasers [5]*

This preliminary knowledge about shock hardening was the basis for the test setup for non-thermal laser induced stretch-forming experiments, see Figure 2. The sheet metal is wet by a water film of several millimetres in height in order to generate a confined plasma and than placed on a circular die and clamped by a blank holder. In a next step one short laser pulse hits the sheet metal and causes ablation at the surface of the sheet, accompanied by a plasma pulse. As a counter-reaction of the plasma formation a shock wave occurs and causes the stretch-forming of the sheet.

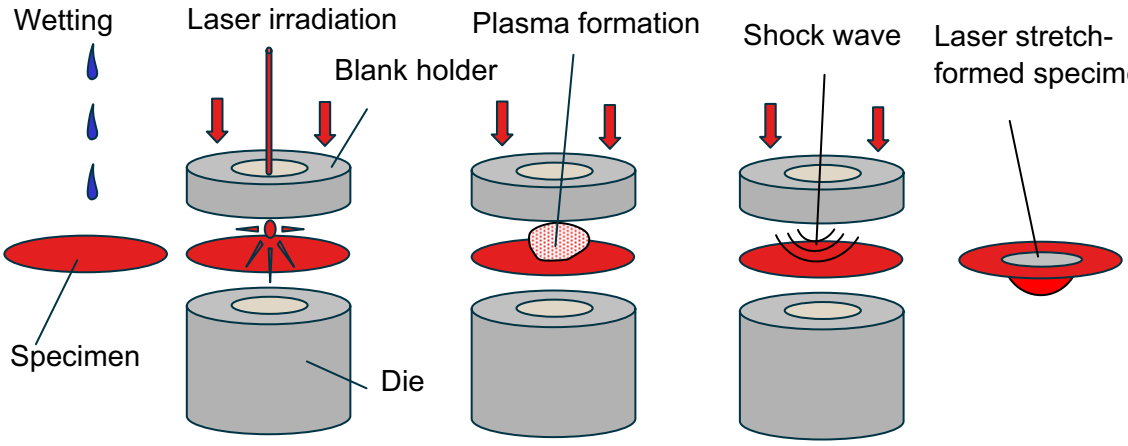

Figure 2: *Schematical process of non-thermal laser stretch-forming*

3 Experimental results

Several laser induced stretch-forming experiments were carried out, while changing parameters, such as defocussing, water height, number of pulses, pulse energy, material, and diameter of the die. The used excimer laser has a wave length of 248 nm and a pulse duration of 20 ns. The maximum pulse energy is 250 mJ and the maximum power density is 6.4 GW/cm², whereby a power density of 0.1 GW/cm² is sufficient to ignite a plasma [6].The dome height of the laser stretch-formed parts can be seen as a degree for the forming, as long as a uniform dome is formed.

3.1 Influence of defocussing and water film

The defocussing z_f is defined as distance between work piece and focus of the laser beam, whereby z_f is positive if the focus is above the work piece, and negative if the focus is within the work piece. The highest energy density is thus at a defocussing of zero. The maximum applied stress of the shock wave will then also be found at a defocussing of zero.
Single laser shots on an aluminium foil of 50 µm in thickness were carried out with different defocussings with and without a water film. Figure 3 shows the size of the spot while changing the defocussing from -1.5 mm to +2.0 mm. It can bee seen that significant ablation takes place in the focus. In comparison to this, the same experiments were carried out with a water film of 2 mm height, see Figure 4. The smallest spot area is at a defocussing of +1 mm, which means that the focus is shifted by 1 mm towards the work piece. This is due to the fact that the laser light is diffracted at the transition point from air to water, since the refraction index for water is higher than for air. The ablation is significantly less compared to the experiments without water film.

a) z_f = -1.5 mm b) z_f = -1.0 mm c) z_f = -0.5 mm d) z_f = 0.0 mm

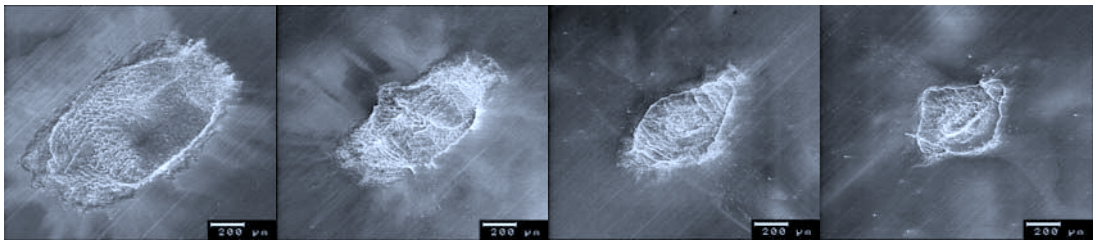

e) z_f = 0.5 mm f) z_f = 1.0 mm g) z_f = 1.5 mm h) z_f = 2.0 mm

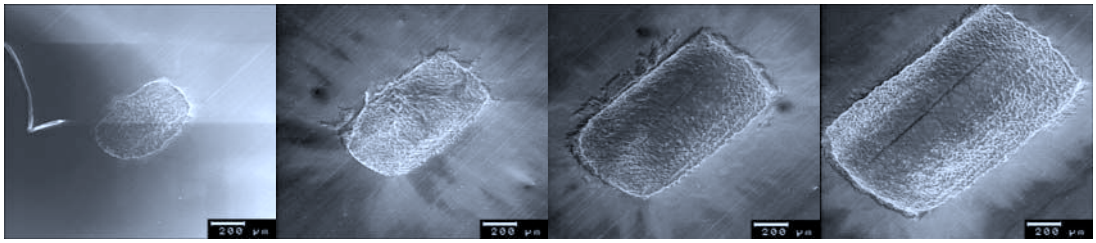

Figure 3: *Laser spot on 50 µm Aluminium foil, without water film, wave length 248 nm, puls duration 20 ns, puls energy 250 mJ, power density 6.4 GW/cm², variation of the defocussing z_f in steps of 0.5 mm from a) to h)*

The highest dome height of laser stretch-formed parts without the use of a water film can be reached in the focus where the average dome height is 225 µm, see Figure 5. The dome height of other experiments with a defocussing of +0.5 till +1.5 mm was significantly lower. It has to be said that the parts which were formed in the focus without a water film did not constitute a uniform shape, but a peak similar to the example in Figure 7b), so that these parts are scrap.

a) z_f = -1.5 mm b) z_f = -1.0 mm c) z_f = -0.5 mm d) z_f = 0.0 mm

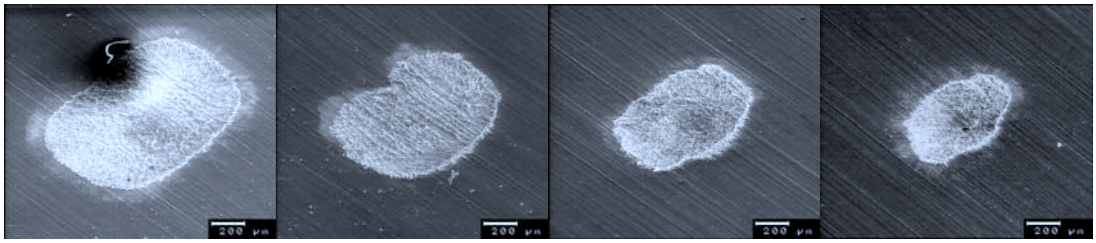

e) z_f = 0.5 mm f) z_f = 1.0 mm g) z_f = 1.5 mm h) z_f = 2.0 mm

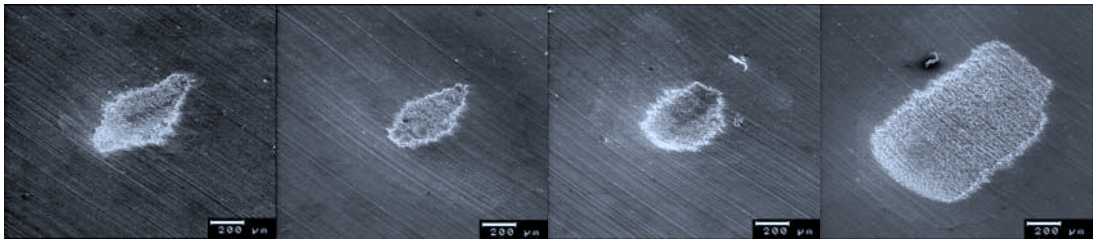

Figure 4: *Laser spot on 50 µm Aluminium foil, water film height 2 mm, wave length 248 nm, puls duration 20 ns, puls energy 250 mJ, power density 6.4 GW/cm², variation of the defocussing z_f in steps of 0.5 mm from a) to h)*

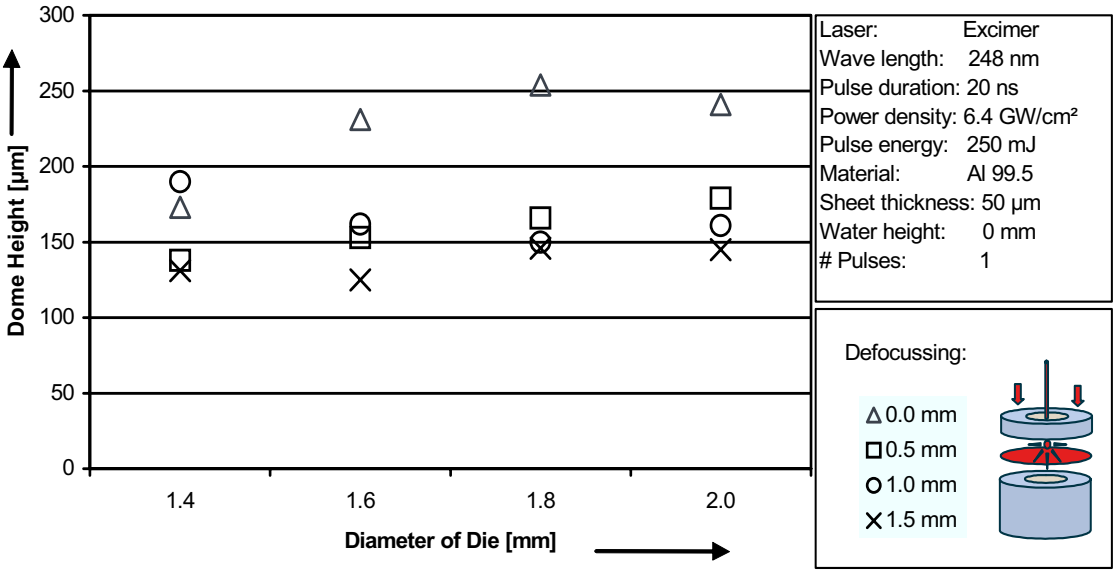

Figure 5: *Dome height of laser stretch-formed parts depending on the defocussing (no water film)*

The same experiments under the use of a 2 mm water film procued not only consistently uniform shaped parts, but also an average dome height of 256 µm at a defocussing of +0.5 mm, see Figure 6. Experiments with other defocussings resulted in lower dome heights, which means that the best working point under the use of a water film has been shifted from the focus to a defocussing of +0.5 mm (not taking into account the diffraction through the water).

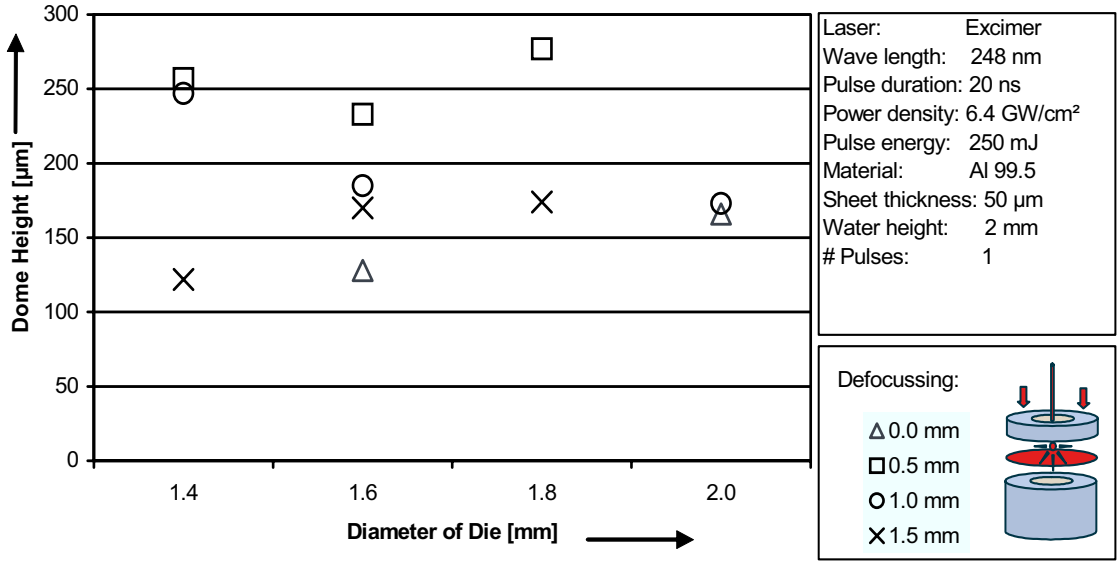

Figure 6*: Dome height of laser stretch-formed parts depending on the defocussing (with use of a water film)*

3.2 Influence of the number of pulses

The use of one laser pulse for stretch-forming usually leads to a uniform dome shape of the part if a water film is used, see Figure 7a). All experiments where a second or more laser pulses were used lead to a second local forming, so that a peak in the dome can be seen, see Figure 7b). Eight pulses in this experiment lead to perforation of the sheet. The local forming in parts with more than one laser pulse could be explained by the fact that the surface of the parts is preliminary damaged at a local area through the first laser pulse. Ablation took place and the surface properties were changed at this point, resulting in a higher local absorptivity. The second laser pulse hence causes significantly higher ablation than the first laser pulse, so that the local thinning is much higher. The ignition of the plasma takes place after the thinning and then causes higher deformation at thinner points. The increased ablation might also be the reason for the non uniform forming of laser stretch-formed parts without a water film – as described in the previous chapter – since the water reduces ablation.

a) b)

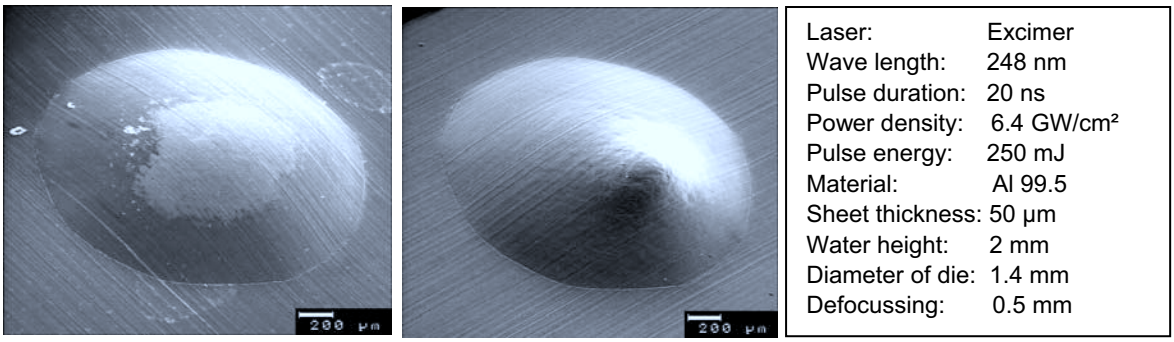

Figure 7: *Shape of laser stretch-formed parts with a) one and b) two pulses*

3.3 Influence of the power density

The power density is proportional to the pulse energy and decisive for the forming result. The pulse energy of 250 mJ and thus the power density was reduced from 100% to 5% in the following experiments. It can be seen that the dome height tends to result in decrease with decreasing pulse energy. Unfortunately, the experiments show a certain scatter, since these are preliminary investigations. The forming still takes place at 5% of the power density, since 5% are three times the minimum power density for plasma ignition, see Figure 8. The decrease of the power density decreases the velocity of the shock wave, and thus the available forming energy.

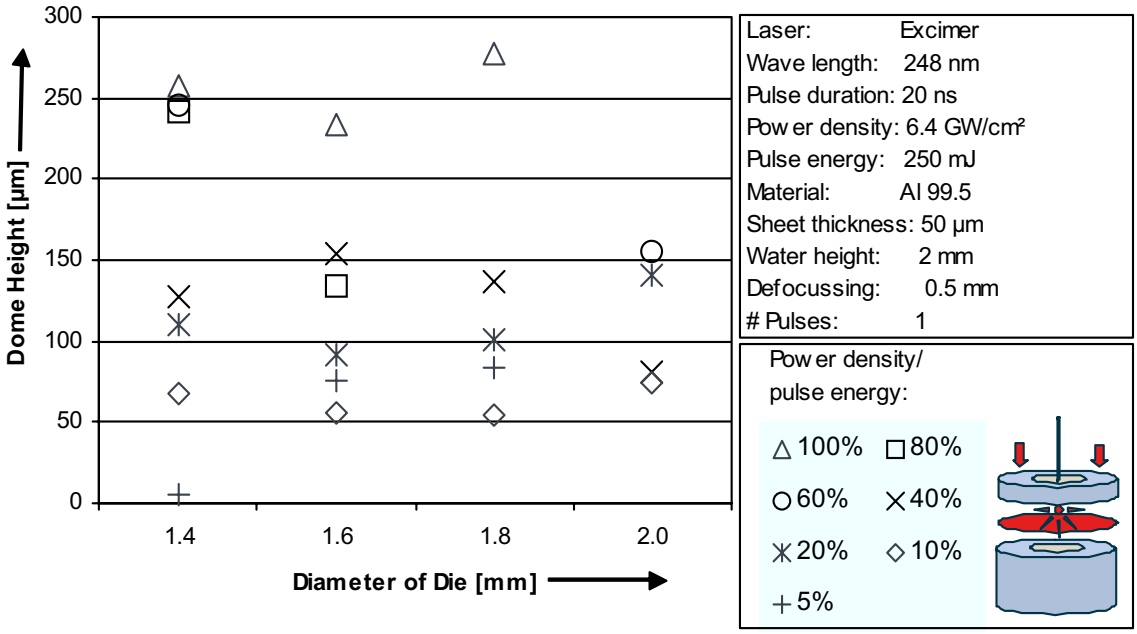

Figure 8: *Dome height of laser stretch-formed parts depending on the pulse energy*

3.4 Influence of the diameter of the die

An appropriate statement about the influence of the diameter of the die on the forming result for single test series cannot be made, since the number of experiments is too small. But a review of all experiments provides better statistical reliability. Figure 9 shows that the average dome height over all experiments, which resulted in a uniform dome shape, is almost the same for diameters of the die of 1.4, 1.6, 1.8 and 2.0 mm. The dome height can also be set in a relation to the diameter of the die, and the aspect ratio can be calculated. The aspect ratio is highest for parts with 1.4 mm in diameter and decreases with increasing diameter. This means that the highest forming degree could be reached with the smallest diameter of the die, which might be due to the fact that the shock wave is applied on a smaller surface, since the hole in the blank holder is smaller. Thus, more forming energy per area is available.

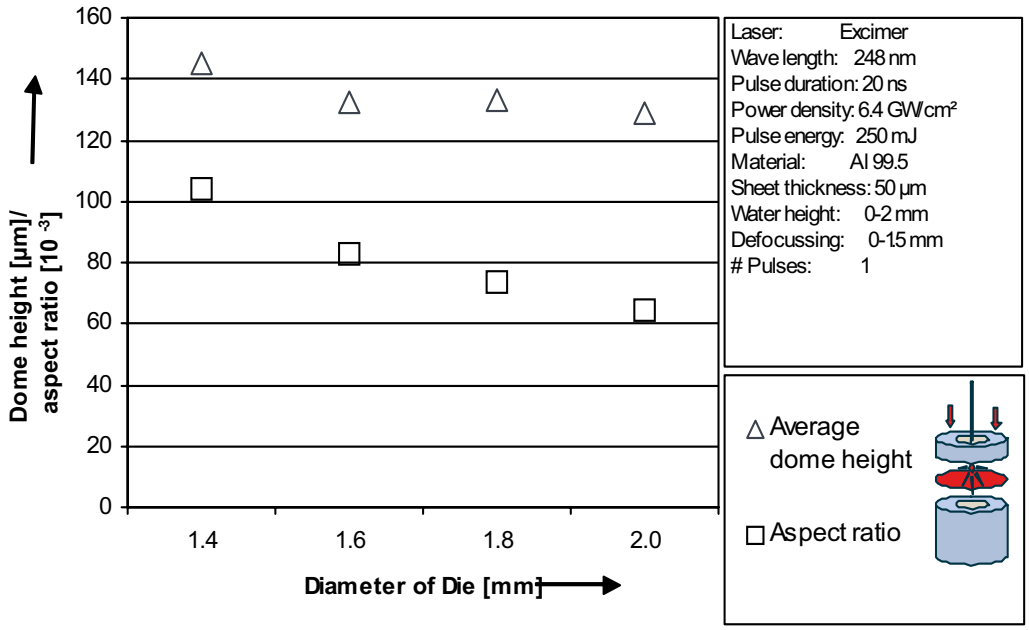

Figure 9: *Dome height of laser stretch-formed parts depending on the diameter of the die*

3.5 Influence of the material

In addition to the experiments with Al99.5 some experiments with stainless steel have been carried out. Figure 10 shows that the dome height of stretch-formed parts out of stainless steel remain under 25 µm, whereby parts out of Al99.5 reached a dome height of more than 250 µm. This is comprehensible, since the yield strength of the stainless steel is twice the yield strength of Al99.5, but the reduction of the sheet thickness of the stainless steel by 50% did not lead to better results. Another reason could be that the oxide film of the aluminium sheet allows a quicker ignition of the plasma and hence causes a more powerful shock wave.

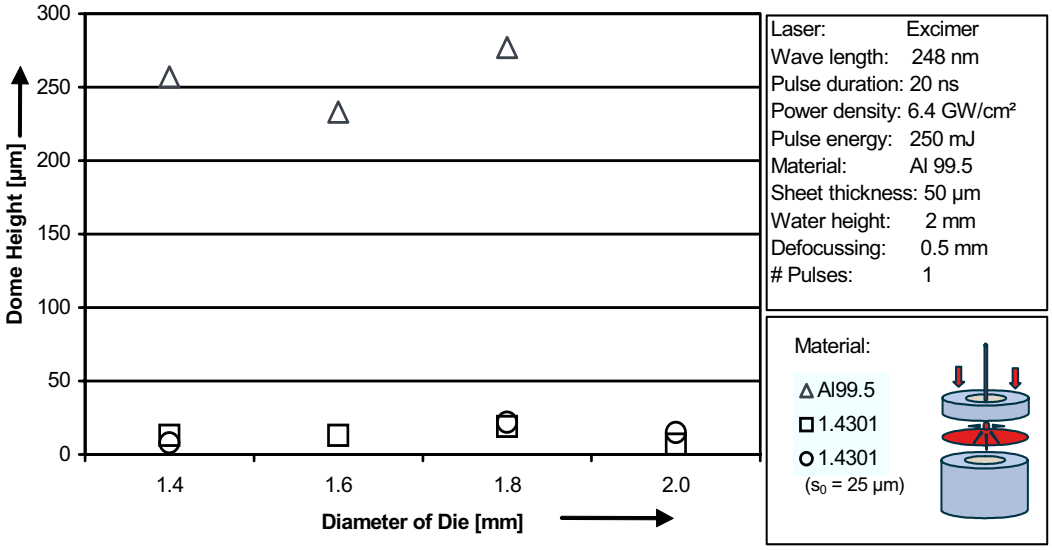

Figure 10: *Dome height of laser stretch-formed parts depending on the material*

4 Conclusions

1. Laser induced shock waves can be used for sheet metal forming as a high speed forming process in micro- and mesoscope.
2. Laser stretch-forming allows to form uniform shaped domes with heights over 250 µm and diameters of 1.4 mm of Al99.5 foils with 50 µm in thickness.
3. The use of a water film increases the forming degree, decreases the amount of ablation and therefore increases the quality of the formed shape.
4. The power density of laser radiation is directly related to the forming degree: A decrease in power density leads to a decrease in dome height in laser stretch-forming experiments.
5. The use of several laser pulses causes undefined, non-uniform shapes in laser stretch-forming, since the thinning through ablation is to high.

5 Outlook

The experiments show encouraging results, which can be used for further investigation in laser stretch forming. Influences like the inertia of the air in forming direction, geometry, and surface quality of the die as well as the reproducibility of the geometry of the work piece have to be investigated. Other sheet metal forming processes like bending and embossing provide a broad research field, and deep drawing with laser induced shock waves is imaginable. The processes have a high potential for bulk production, since today's excimer lasers have pulse frequencies up to 2 kHz. Lasers, which provide higher power densities, will probably allow even higher forming degrees than shown in this paper.

References

[1] *Vollertsen, F.:* Laserstrahlumformen – Lasergestützte Formgebung: Verfahren Mechanismen, Modellierung. Meisenbach Verlag, 1996.

[2] *Pirii, A. N.; Schlier, R.; Northam, D.:* Momentum transfer and plasma formation above a surface with a high-power CO_2 laser, Applied Physics Letters, 1972, 21(3), p. 79-81.

[3] *Ageev, V.; Barchukov, A.; Bunkin, F.; Konov,V.; Metev, S.; Silenok, A.; Chapliev, N.:* Breakdown of gases near solid targets by pulsed CO_2 laser radiation, Soviet Physics Journal, 1977, 11, p. 35-60.

[4] *O'Keefe, J.; Skeen, C.:* Laser-induced deformation modes in thin metal targets. Journal of Applied Physics, Vol. 44, 1973, p. 4622-4626.

[5] *Eisner, K.:* Prozesstechnologische Grundlagen zur Schockverfestigung von metallischen Werkstoffen mit einem kommerziellen Excimerlaser, Dissertation, Erlangen, 1998.

[6] *Hügel, H.:* Strahlwerkzeug Laser, Teubner Verlag, 1992.

On the Significance of the Die Design for Electromagnetic Sheet Metal Forming*

D. Risch, C. Beerwald, A. Brosius, M. Kleiner

Chair of Forming Technology, University of Dortmund, Germany

Abstract

Electromagnetic Forming is a high speed forming process using a pulsed magnetic field to form metals with high electrical conductivity, such as copper or aluminium alloys. During the process, typical pressure peaks up to 200 MPa and velocities in the range of 300 $^{m}/_{s}$ can be achieved. As significant process parameters the pressure maximum as well as the local and temporal varying pressure distribution have been identified.

As of a certain drawing depth and distance between workpiece and tool coil, the pressure does not act any longer on the workpiece, but the deformation process is still driven by the inertia forces. It has been found out that the velocity distribution within the sheet metal during the forming stages as well as at the time of impact with a die significantly influences the forming result. Additionally, a special undesired effect is the rebound behaviour of flat workpiece areas being in contact with the die. To investigate the influence capability of the die concerning this effect, the parameters stiffness and damping properties have been varied by means of simulation using a mechanical substitute model.

Keywords:

Electromagnetic sheet metal forming, Tool design, Parameter variation

1 Introduction

One of the major research field at the Chair of Forming Technology, University of Dortmund, is the process of electromagnetic sheet metal forming. This topic is, inter alia, investigated by the research unit 443 “Untersuchung der Wirkmechanismen der elektromagnetischen Blechumformung”, sponsored by the German Research Foundation (DFG). Main focus of this group’s activities is fundamental research with the aim to obtain

* *This work is based on the results of Forschergruppe FOR443; the authors would like to thank the German Research Foundation - DFG for its financial support*

a deeper understanding of the process and the interaction of the significant parameters. A long-term objective is to bring this innovative forming process towards industrial realisation. Besides the analysis of the free forming process, a second focus deals with shape forming, which means that a die is used in order to achieve a certain geometry. Here, one of the main aspects is the analysis and prediction of the interaction between workpiece and die.

2 Deformation process and relevant parameters observed at free forming operations

Electromagnetic sheet metal forming is an energy-based high speed forming process, forming metals with a high electrical conductivity by a pulsed magnetic field. The basic principle of this process is shown in Figure 1.

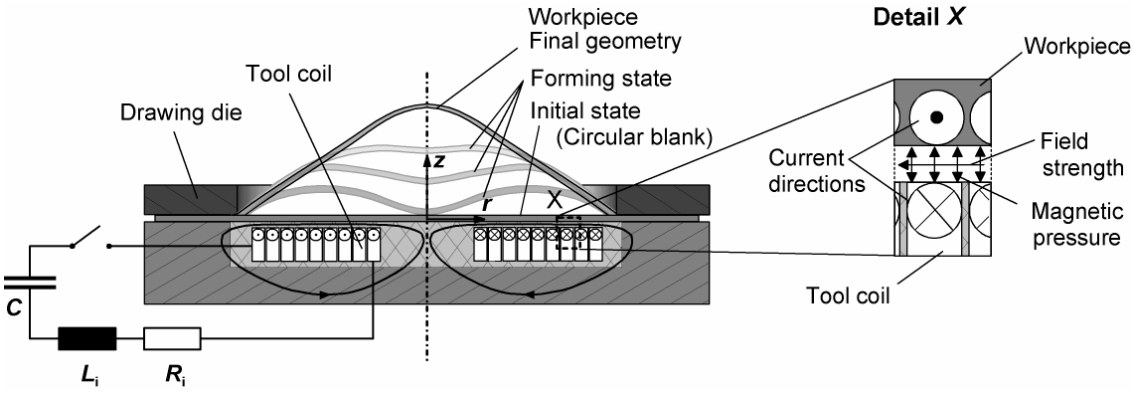

Figure 1: *Process principle [1]*

Closing the high-current switch effects a sudden discharge of the capacitor battery, thereby creating a highly damped sinusoidal current $I(t)$. The current causes a magnetic field $H(t)$ inducing a second current in the workpiece which is directed in the opposite direction of the coils current. As long as the workpiece is close to the coil, this induced current prevents the magnetic field from penetrating through the workpiece in z-direction. The energy density of the magnetic field within the gap between the sheet and the coil refers to a magnetic pressure p acting nearly orthogonal onto the workpiece's surface. If the yield point of the workpiece material is exceeded, plastic deformation occurs and the distance between workpiece and tool coil increases rapidly. Under the assumption that the magnetic field's local and temporal distribution is known the pressure can be calculated using the following equation [2]

$$p(r,z,t) = \frac{1}{2} \cdot \mu_0 \cdot H^2(r,z,t) \tag{1}$$

with
	p	magnetic pressure
	H	magnetic field
	μ_0	permeability constant
	r	radius
	z	coordinate in direction of the drawing depth
	t	process time

With regard to Figure 2b-c, the acting magnetic pressure depends on the local as well as on the temporal distribution, which reveals the complexity of the analysing electromagnetic sheet metal forming. Therefore, a finite element analysis is used to calculate the magnetic pressure, coupling two different software tools [3]. The first one, FEMM [4] is used for the determination of 2-dimensional harmonical magnetic fields. The second code, MARC, is used for the transient calculation of the forming process which is caused by the magnetic pressure. The calculated field distribution is used as input data in the transient mechanical simulation. The mechanical simulation stops when the deformation exceeds a defined value. In a next step, a new field distribution is determined with the formed workpiece geometry. This exchange is repeated until the magnetic pressure does not act any longer. In [5] the results of this coupled simulation have been compared with the results of a coupled simulation using a transient field analysis with EMAS instead of the harmonic field analysis with FEMM. Because of the similarity of the results the harmonic analysis will be preferred due to the less efforts regarding computation time.

Figure **2** shows the results of such a coupled simulation: there are some characteristic deformation stages from the mechanical simulation as well as the corresponding pressure of the electromagnetic simulation.

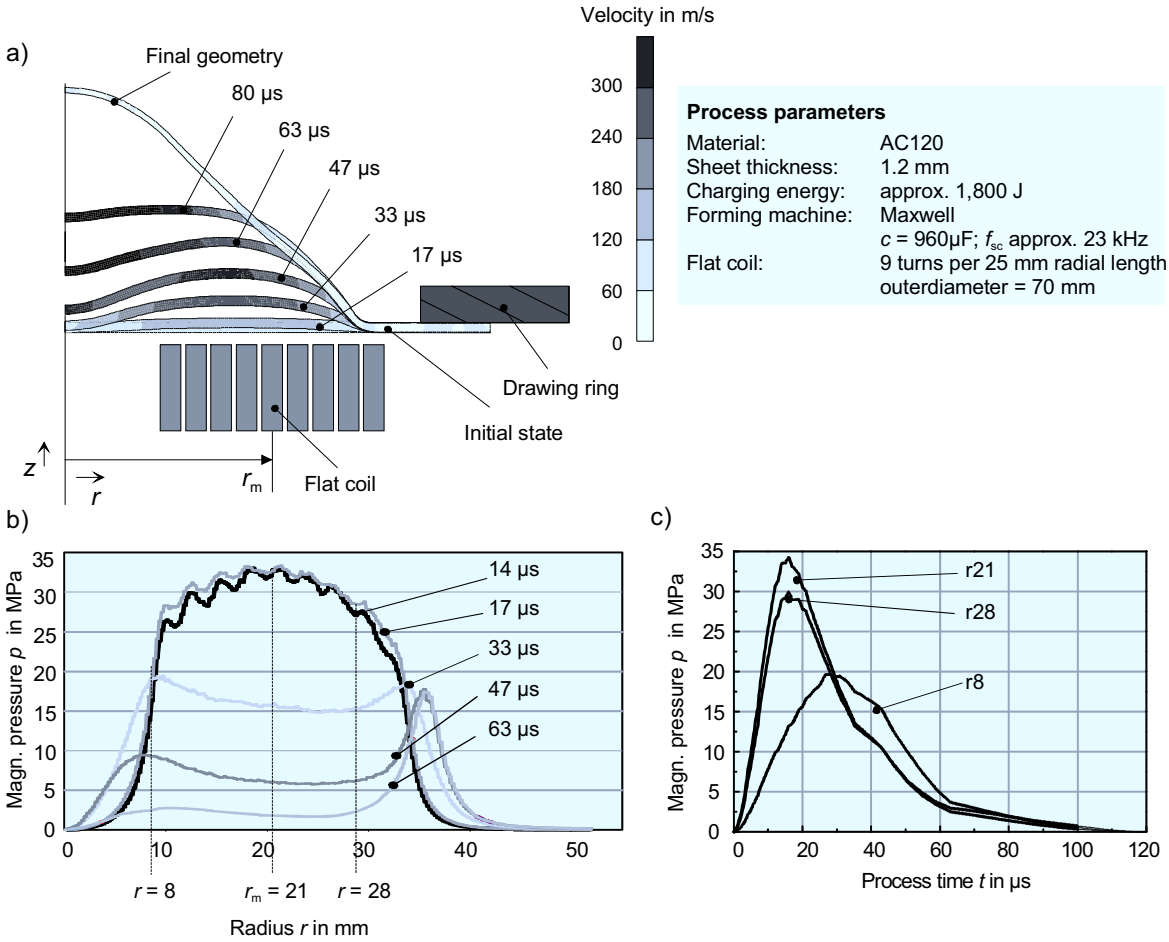

Figure 2: *Forming states and according local and temporal pressure distribution*

Figure 2a-b clearly shows the strong influence of the workpiece's movement on the pressure decrease. During the first stage, the maximum pressure occurs at position r_m, which refers to the medial coil radius where the movement starts. In contrast to this, there is no pressure in the centre of the coil. In the following deformation stages a continuously decreasing pressure can be observed due to the decreasing magnetic field strength with the increasing gap volume. It should be mentioned that the pressure decreases in a much shorter period than the coil current [1]. As a result of the inertia forces, the workpiece still moves on. These inertia forces act mainly in the area of r_m dragging the middle part ($r < r_m$) towards the drawing direction (positive z-direction). This effect causes a strong acceleration of the sheet metal centre which results in a large deformation. As soon as the workpiece leaves the influence area of the coil, only the inertia forces act on the sheet metal and a possible active influence on the movement is lost. But nevertheless, the responsible forces can be influenced by the relevant parameters charging energy and coil design as well as by the mass or the stiffness of the workpiece [1]:

- An increase of charging energy causes a higher pressure maximum which leads to a higher drawing depth, but to a higher velocity during the forming process as well.
- The pressure distribution will be created by the coil design. In particular the characteristic parameters are the inner and outer coil diameter as well as the winding density (number of turns per unit of length).

Starting from numerical analysis as described in [1], some experiments with different pressure distributions have been carried out to justify these assumptions. For example, Figure 3 shows the simulation results of a quite different pressure distribution compared to Figure 2. As expected, the workpiece deformation starts in those areas of the sheet where the winding is located. The other regions have to be accelerated by inertia forces. The example in Figure 3 shows how these acting forces can be distributed to influence the velocity distribution during the forming process.

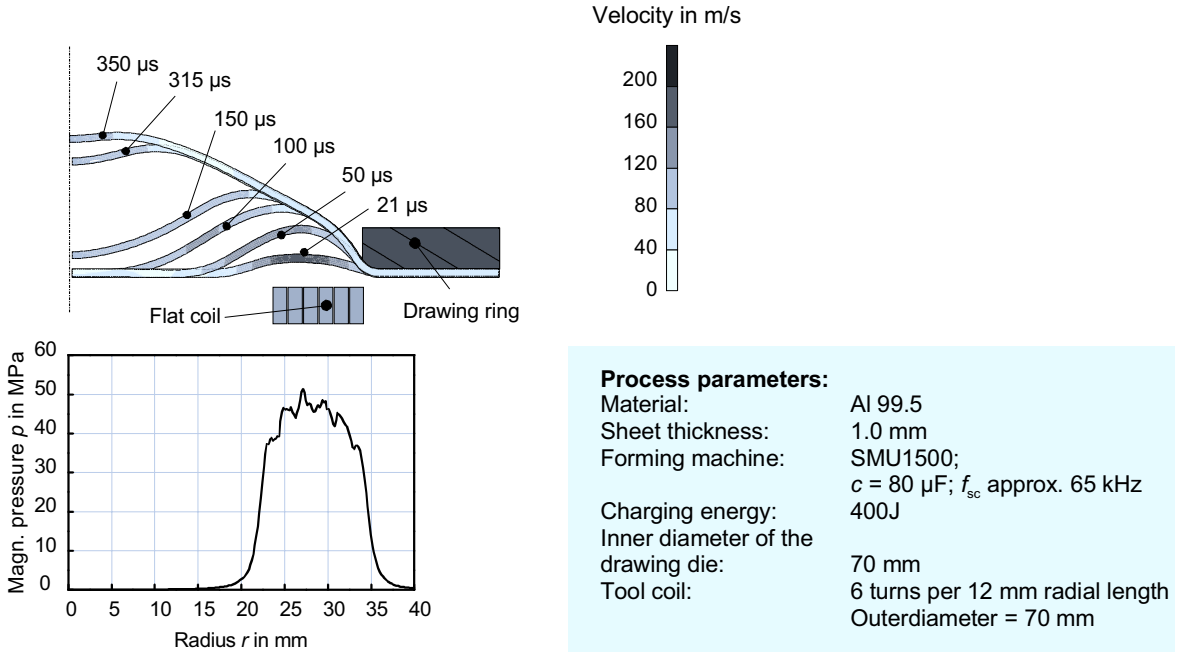

Figure 3: *Pressure distribution and according workpiece deformation*

The final geometry is completely different. The investigations have shown clearly that the forming result as well as the velocity distribution can be influenced by the pressure distribution. As a consequence, it seems to be useful to determine a matching pressure distribution by means of simulation for each forming task.

3 Typical effects and interactions at forming operations into a die

One research objective within the above mentioned research group is to achieve a given geometry using the electromagnetic sheet metal forming process. Therefore, tools like a die have to be used within this process. During the first stage by forming into a die, the workpiece passes through the same stages as in the free-forming process which means that the existing knowledge can be transferred for this special time slot. As already shown in Figure 2a, the workpiece has a very high velocity, especially in the middle area which reaches up to 300 $^{m}/_{s}$. This means that the workpiece locally has a very high kinetic energy. In the case of forming into a die, this energy must be transferred to the die when the workpiece movement is stopped by the die surface. This causes undesired effects, like for example,

- the generation of a strongly inhomogeneous velocity distribution in the sheet metal and
- the rebound-effect caused by the kinetic energy of the workpiece.

These two undesirable effects are discussed in the following.

3.1 Influence of the inhomogeneity of the velocity distribution

As known from the free-forming process, the velocity distribution in the sheet influences the forming process in a significant manner. Corresponding to different velocity distributions the workpiece passes through different geometrical forming stages. This behaviour causes a problem, if a tool is used to obtain the desired geometry. This should be explained by an example shown in Figure 4. Here, the simulation results with a spherical die using different charging energies are shown. In the case of the higher charging energy (see Figure 4b) the workpiece area A, where the maximum pressure dominates, has a very high velocity while area B still remains at its initial position. Later on, the faster area hits the die at first which causes an abrupt deceleration on the one hand. On the other hand, area B of the sheet material becomes very stiff due to the strain hardening as well as to the geometrical stiffness caused by the changed geometry. Due to these facts the inertia force which is the driving force during this process stage does not act any longer. Therefore, the centre of the workpiece (area B) is not being deformed anymore.

Contrary, in the case shown in Figure 4a, a lower charging energy influences the forming process in a positive manner. As a result of the lower energy, the forming velocity is lower at large. Additionally the velocity distribution is more homogenous which allows a better use of the inertia forces during a larger time period of the process. Thus, the geometry of the intermediate stages are less stiff and the sheet achieves the die geometry as desired.

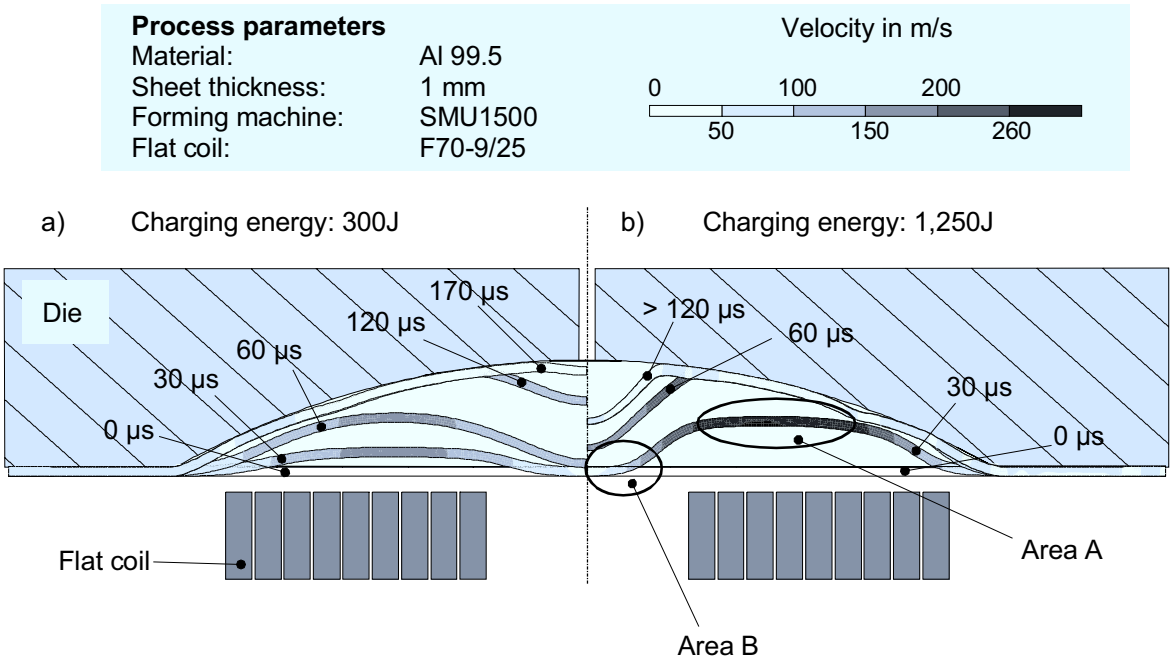

Figure 4: *Comparison of the velocity distribution depending on different charging energies*

These results are verified by according experiments. Figure 5 shows the contour (upper surface) of the workpiece measured with a Coordinate Measurement Machine (CMM). Compared to Figure 4, the simulation results are in good qualitative agreement with the performed experiments.

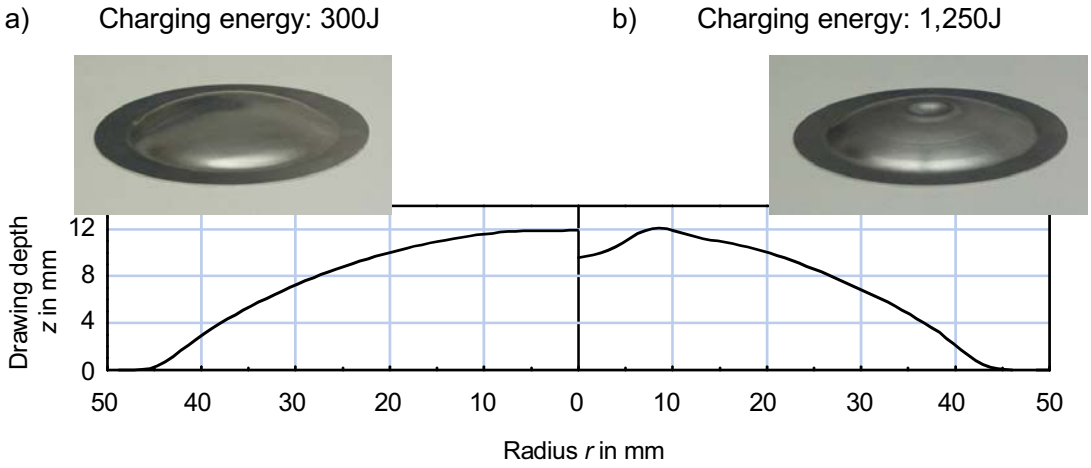

Figure 5: *Contour of the final geometry resulting from the experiments with different charging energies*

3.2 Rebound-effect caused by the kinetic energy

Due to its high velocity, the workpiece has a very high kinetic energy during the EMF process. This implies a difficulty when the workpiece contacts a die because at the time of impact the high kinetic energy should be transferred from the workpiece to the die. If the energy cannot be dissipated completely, the so called rebound-effect may occur. An

extreme example of this effect is shown in Figure 6, where those workpiece areas being in contact with the die has been thrown back into the direction of the tool coil.

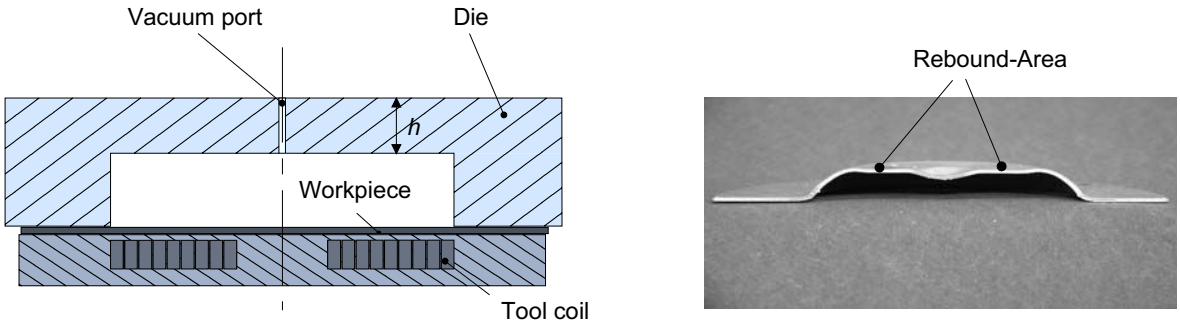

Figure 6: *Example of a workpiece geometry caused by the rebound-effect*

To regard the contact period of time more detailed, the coupled FEA as described in paragraph 2 has been used. For the qualitative interpretation of the simulation it was necessary to mesh the die completely. Additionally, it turned out that a very fine discretisation of the time domain is necessary to visualise the dynamic processes within the die. It could be observed how the energy transfer at the time of impact causes a deformation wave spreading out trough the die, analogue to an acoustic wave. In Figure 7 three stages of the spreading wave within the contact period are shown: the initiated deformation wave (a) spreads out through the die (b) until it is reflected on one of the die's surfaces (c) as indicated by the arrows.

Process parameters			
Die material :	Steel	Sheet material:	Al 99.5
Die's height *h*:	20 mm	Sheet thickness:	1.5 mm
Young's modulus *E*:	210,000 MPa	Forming machine:	SMU1500
Specific mass ρ:	7.81 g/cm³	Charging energy:	1,250 J

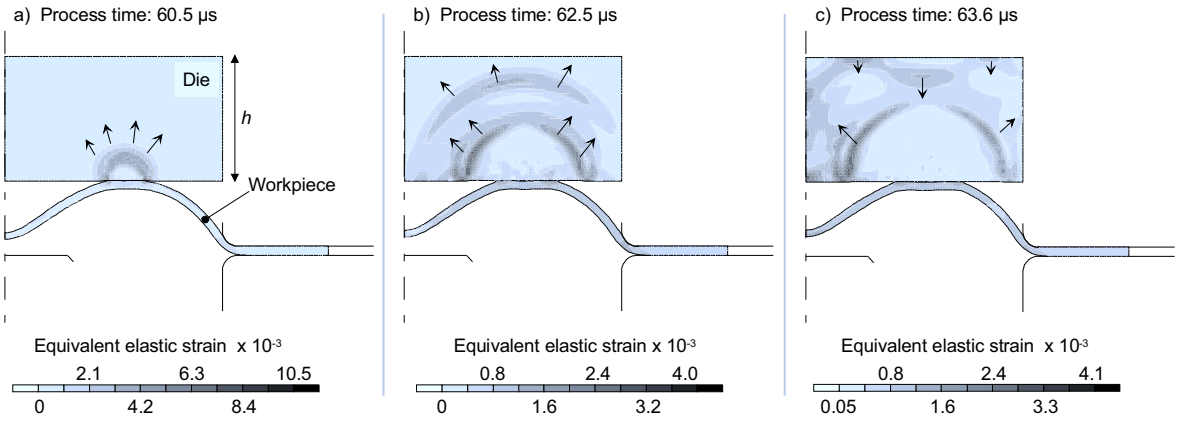

Figure 7: *Propagation of the deformation wave in the die during the contact period of time*

The impulses runtime depends on the sound velocity of the die material and can be estimated by

$$t_{run} = \frac{2 \cdot h \cdot \sqrt{\rho}}{\sqrt{E}} \qquad (2)$$

with	t_{run}	impulse runtime
	h	die's height (marked in Figure 6)
	E	Young's modulus
	ρ	density of the die's material

Because the contact time between workpiece and die, typically, is longer than the runtime of the deformation wave, the rebound-effect is feared to be intensified, if the backward impulse would be transferred to the sheet again. It could be regarded that the reflected wave usually crosses the incident wave which leads to favourable extinguishing effects. Nevertheless, the rebound-effect occurs. It should be mentioned that the considered example of a cylindrical die with a flat bottom is very sensitive to this effect, because the flat workpiece areas are not very stiff and the magnetic pressure does not act any more to support those sheet areas which are in contact with the die.

Following up the idea that the kinetic energy of the workpiece shall be dissipated at the contact with the die, the influence capability of the die properties has been investigated. Therefore the parameters stiffness and damping properties have been varied using a mechanical substitute model of the die. More precisely, a spring-dashpot-system has been used (see Figure 8a) to represent the die's physical behaviour without the need of a complete meshed die. In this way the number of degrees of freedom is reduced as well as the calculation time. In comparison to the completely meshed FE-model (see Figure 8b) now the stiffness of the spring C represents both, the material stiffness (Young's modulus) as well as the geometrical stiffness (for example, the height of the die). In the same way the damping coefficient η represents the material damping property as well as the constructive change, like for example the use of an additional shock absorber.

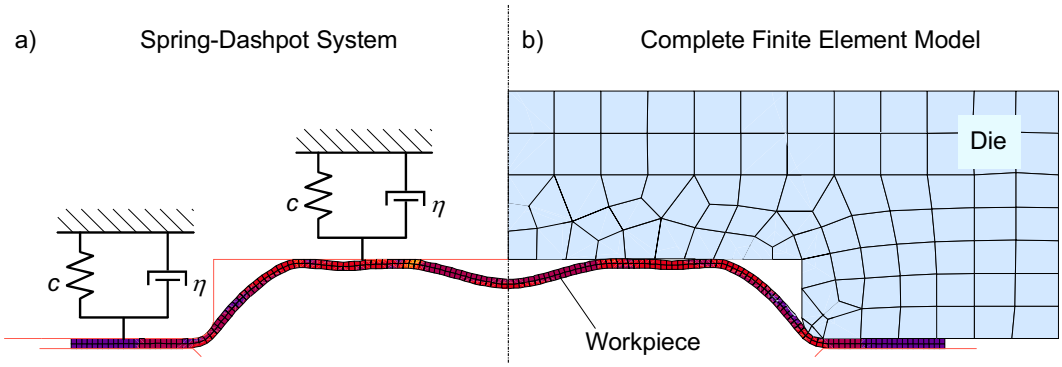

Figure 8: *Mechanical substitute: spring-dashpot system*

The parameter variation has been performed within a coupled simulation whereby the measured coil current was used as input. The cylindrical die geometry as well as thickness and diameter of the blank has been taken from the corresponding experiment. The parameters of the substitute die model have been varied starting with zero values for stiffness C and damping coefficient η. In Figure 9 an excerpt from the results is shown. It can be seen that for a constant spring stiffness an increase of the damping coefficient seems to improve the workpiece geometry up to an optimum followed again by a worse geometric accuracy if the damping will be increased further on: an optimal damping coefficient for a special spring stiffness seems to exist. On the other hand it is remarkable, that a flat bottom of the workpiece geometry can be achieved with best accuracy when the

stiffness is at comparable low values. A very low stiffness means that the die, particularly the bottom of the die, can be moved by the workpiece at the time of contact. In this case the kinetic energy of the workpiece will be obviously dissipated, but a realisation of this possibility is still a problematic point.

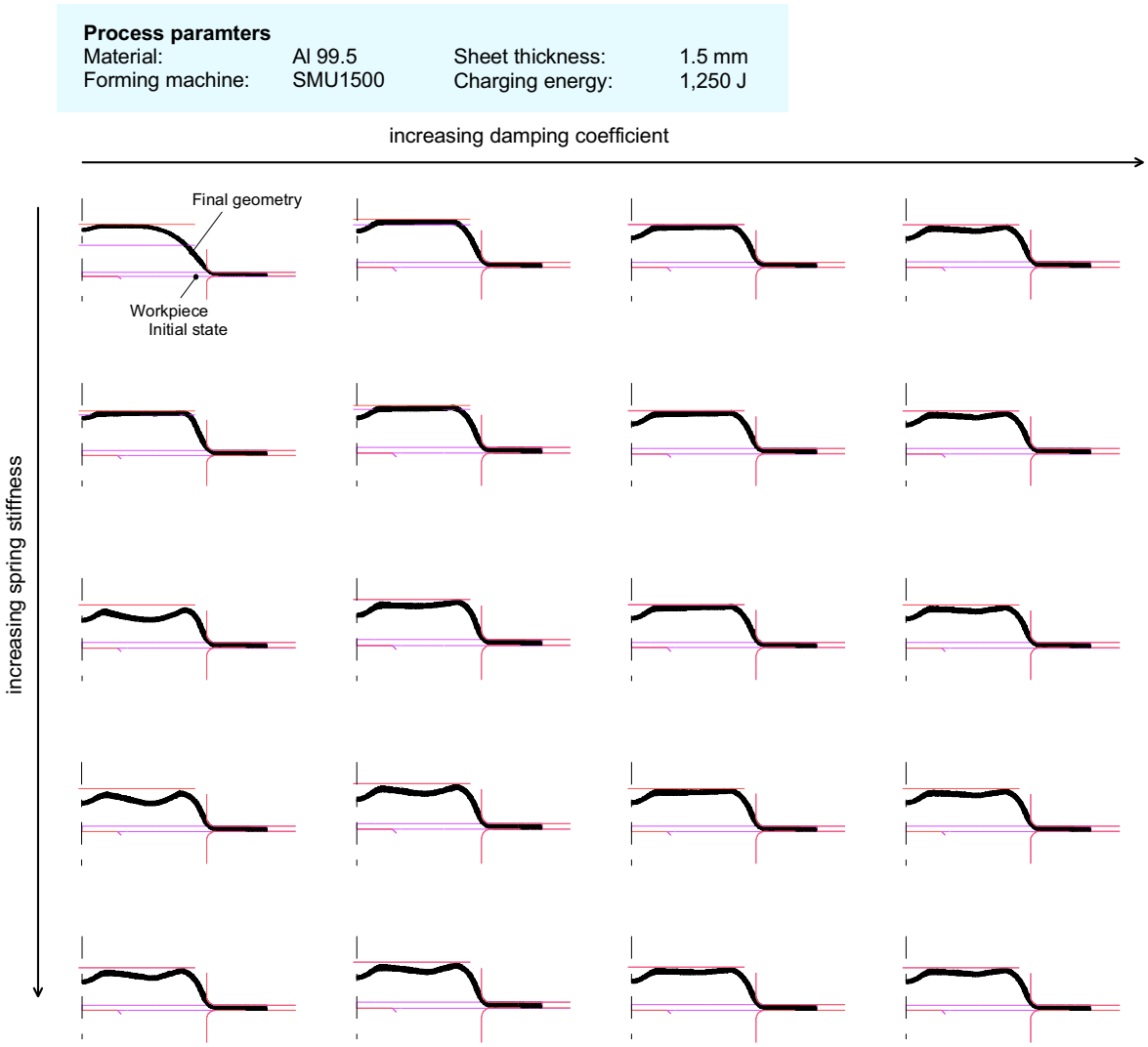

Figure 9: *Excerpt from the results of a parameter variation*

Furthermore, the parameter variation did not lead to a change of the significant shape of the workpiece, which occurs due to the inhomogeneous pressure distribution and the dimensions of the die. A better form filling can only be achieved at more process related geometries of the die, like e. g. by spherical, conical or other stiffening geometry elements, or by means of process combinations where an additional media is used to support the workpiece while it is in contact with the die. To determine such process related geometries the consequent use of the coupled simulation as well as further experimental investigations are necessary. Finally, as promising examples Figure 10 shows some workpieces without the described rebound-effect.

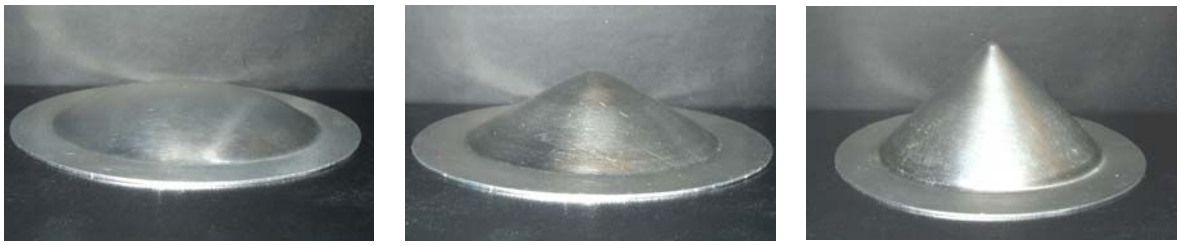

Figure 10: *Promising examples produced by forming into a die without the rebound-effect*

4 Summary

The investigation of the strongly interdependent working mechanisms of the electromagnetic sheet metal forming is the main objective of an interdisciplinary research group at the University of Dortmund. At the Chair of Forming Technology a special focus lies on the process and the tool design. Fundamental for this research work is the knowledge of the relevant process parameters, which have been identified in a first step on the basis of the free forming process. Here, the influence of the acting magnetic pressure and its distribution as well as the forming velocity and its distribution has been considered by examples.

A reliable simulation tool has been used as the basic requisite for first investigations of the interactions between the acting forces and the workpiece deformation as well as the interactions between the workpiece and the die at the time of impact. Undesired effects preventing the workpiece to get the desired shape are for example the inhomogeneous velocity distribution during the free forming stages as well as at the time of contact between workpiece and die. As a special case the so-called rebound-effect, where flat areas of the workpiece will be thrown back by the die surface, has been pointed out.

References

[1] *Beerwald, C.: Brosius, A.; Kleiner, M.; Psyk, V.:* Einfluss des magnetischen Druckes bei der elektromagnetischen Blechumformung. Proc. 2. Kolloq. Elektromagnetische Umformung, 28. Mai 2003, Dortmund, S. 77–85, ISBN 3000113762

[2] *Winkler, R.:* Hochgeschwindigkeitsbearbeitung – Grundlagen und technische Anwendungen elektrisch erzeugter Schockwellen und Impulsmagnetfelder. VEB-Verlag Technik, Berlin, p. 307-333, 1973

[3] *Kleiner, M.; Brosius, A.; Blum, H.; Suttmeier, F. T.; Stiemer, M.; Svendsen, B.; Unger, J.; Reese, S.:* Benchmark Simulation for Coupled Electromagnetic-Mechanical Metal Forming Processes. Production Engineering - Annals of the German Acad. Soc. for Prod. Eng. WGP, XI (2004) 1

[4] Foster-Miller Inc., FEMM, a free FEA software for magnetic field analysis by D. Meeker, Version 3.3 (17 Aug 03): http://femm.foster-miller.net (1st Mar 04).

[5] *Beerwald, C., Brosius, A., Homberg, W., Kleiner, M., Klocke, M.; Kulig, S.:* Extended Finite Element Modeling of Electromagnetic Forming. Proc. of the 10th Int. Conf. on Sheet Metal, 14.-16. April 2003, Jordanstown, UK, S. 559-566, ISBN 1859231713

Formability and Damage in Electromagnetically Formed AA5754 and AA6111*

J.M. Imbert[1], S.L. Winkler[1], M.J. Worswick[1], S. Golovashchenko[2]

[1] Dept. of Mech. Engineering, University of Waterloo, Waterloo, Ontario, Canada
[2] Ford Motor Company, Scientific Research Laboratory, Dearborn, MI

Abstract

This paper presents the results of experiments carried out to determine the formability of AA5754 and AA6111 using electromagnetic forming (EMF), and the effect of the tool/sheet interaction on damage evolution and failure. The experiments consisted of forming 1mm sheets into conical dies of 40° and 45° side angle, using a spiral coil. The experiments showed that both alloys could successfully be formed into the 40° die, with strains above the conventional forming limit diagram (FLD) of both alloys. Forming into the higher 45° cone resulted in failure for both materials. Metallographic analysis indicated that damage is suppressed during the forming process. Micrographs of the necked and fractured areas of the part show evidence that the materials do not fail in pure ductile fracture, but rather in what could be a combination of plastic collapse, ductile fracture and shear band fracture. The failure modes are different for each material; with the AA5754 parts failing by necking and fracture, with significant thinning at the fracture tip. The AA6111 exhibited a saw tooth pattern fractures, a crosshatch pattern of shear bands in the lower half of the part, and tears in the area close to the tip. Both areas showed evidence of shear fracture. This experimental study indicates that there is increased formability for AA5754 and AA6111 when these alloys are formed using EMF. A major factor in this increase in formability is the reduction in damage caused by the tool/sheet interaction.

Keywords:

Electromagnetic sheet metal forming, Damage, Formability

---

[*] *Funding from the Ontario Research and Development Challenge fund and Ford Motor Company is gratefully acknowledged. The authors thank V. Dmitriev for helping with the experiments.*

1 Introduction

The need to reduce vehicle weight has resulted in increased interest in aluminum alloys for automotive applications. A major factor affecting the application of aluminum alloys in automotive production is their relatively poor formability. This has led to an increased interest in electromagnetic forming (EMF).

Electromagnetic forming has been in use since the late 50's [1]. It has remained a niche manufacturing process mainly used for forming axisymmetric parts with limited sheet applications. Work has recently re-focused on electromagnetic sheet forming techniques. Balenethiram and Daehn [2,3] formed parts using electrohydraulic forming and found a significant increase in formability. Vohnout [4] studied hybrid conventional/EMF operations and found that difficult to form areas in aluminium stampings could be formed using hybrid methods. Oliveira and Worswick [5,6] performed free form and cavity fill EMF experiments with 1.0 and 1.6 mm AA5754 sheet and found increased formability in the cavity fill experiments, but no significant increase in the free form experiments. Golovashenko et al [7] performed electromagnetic and electrohydraulic forming on aluminium sheet and reported an increase of 10-15% in maximum displacement into the die when compared to quasi-static forming. It was also reported that forming into a die could result in increased formability. Recently, the present authors [8,9,10] reported an increase in formability of 1mm AA5754 sheet formed using EMF and proposed that this increase is caused by damage suppression due to the tool/sheet interaction. These conclusions were the result of experimental and numerical analysis of free form and conical (34º side angle) parts formed using a spiral coil. Free-formed samples did not show a significant increase in formability, while the parts formed into a die did.

This paper presents the results of experiments carried out to determine the formability of aluminium alloys AA5754 and AA6111 in an EMF operation, and the effects of the tool/sheet interaction on damage evolution. These alloys were chosen since they are currently used in automotive production. Formability was assessed by forming the alloys into 40 and 45° cones. Strain measurements were taken from the parts using the circle grid technique. Damage and fracture analysis was carried out to determine the effect of the tool/sheet interaction on damage. Optical micrographs showing damage and fracture surfaces are presented.

2 Experimental Procedure

2.1 Formability Experiments

The experiments consisted of forming 1mm sheet into conical dies of 40° and 45° side angle (100 and 90º included angle) using a spiral coil. A Magnepress [11] system with a maximum storage capacity of 22.5 kJ at 15 kV, capacitance of 200 μF and inductance of 230 nH was used. The conical cavity dies were made from tool steel hardened to 50 Rc. A vacuum port was provided to evacuate the air before each part was formed. Figure 1 shows a schematic of the experimental apparatus.

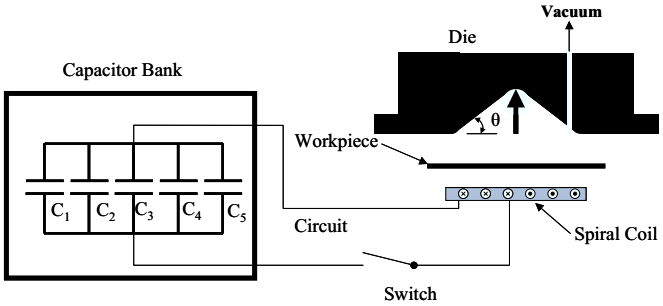

Figure 1: *Schematic of the experimental apparatus*

The material was cut into 165x165 mm (6.5"x 6.5") squares. The AA5754 was provided with a solid film lubricant which was removed. No lubrication was used in the experiments. Circle grids were used to measure the engineering strains. Grids with a nominal diameter of 2.5 mm were applied using electrochemical etching. The strains were measured in the rolling direction using a digital grid measurement system.

2.2 Damage Measurements

Metallographic investigations consisted of cold mounting sectioned specimens in epoxy resin, followed by grinding using 320, 600, 1200, and 4000 grit SiC paper and finally polishing using 3 μm and 1 μm diamond paste, and 0.05 μm colloidal silica suspension. 1392 x 1040 pixel, 8-bit grayscale micrographs of the prepared specimens were taken using an Olympus BH2-UMA optical microscope equipped with a Photometrics CoolSNAP CCD camera. A 20x objective lens was employed in combination with white light giving a resolution of 0.729 μm. The images obtained were analyzed using the Image-Pro Plus 5.0 software. The average percent area of voids was determined from void measurements acquired from a minimum of 15 images corresponding to a total analyzed area of approximately 2.0 mm^2.

3 Results

Safe parts were produced from both alloys with the 40º cone, with charge voltages of 8.0 kV for the AA5754 and 9.0 kV for the AA6111. All the parts formed with the 45º cone failed at charge voltages of 9.0 and 10.0 kV for AA5754 and AA6111, respectively. For the purposes of this work, a part that showed no indication of fracture or necking is considered safe; otherwise it is considered to have failed. Figure 2 and Figure 3 show AA5754 parts formed with the 40 and 45º cones, while Figure 4 and Figure 5 show those formed with AA6111. Three samples for each condition were formed; the ones shown are those that were used for metallographic analysis, unless otherwise noted.

Buckling was observed in all of the formed parts. In the AA5754 samples the buckling is localized in the area of the vacuum hole (Figure 3 B), whereas for AA6111 it was more evenly distributed (Figure 4, Figure 5). Buckling is currently attributed to the indentation produced on the sheet by the vacuum hole. Parts formed in previous experiments with a 34º cone die also showed a distinct indentation, but no buckling [9,10].

The failure modes are different for the two materials studied. AA5754 failed by necking which eventually led to fracture. AA6111 exhibited what appeared to be two distinct types of failure (Figure 5); however, closer examination revealed evidence that both failures were due to shear fracture. Details of the failure will be discussed in section 3.3, below.

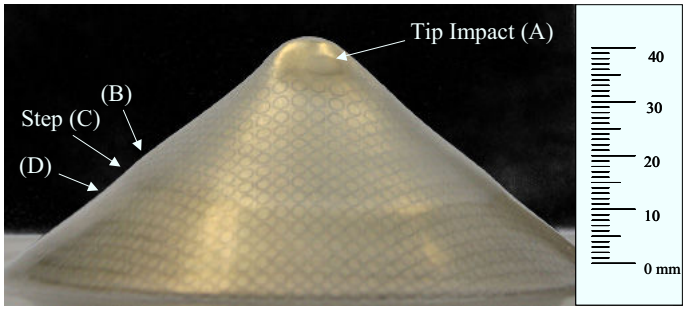

Figure 2: *AA5754 cone formed with the 40° die (8.0 kV)*

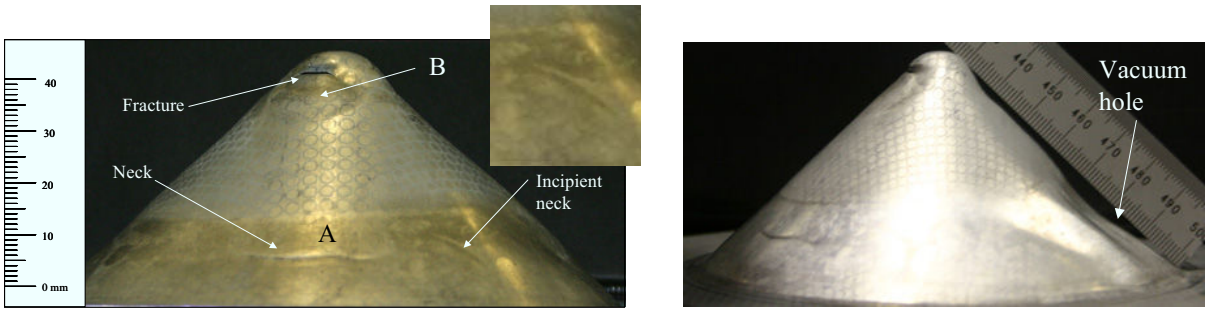

Figure 3: *AA5754 cone formed with the 45° die (9.0 kV). View I shows a neck in the area under the step and fracture near the tip. An incipient neck is shown in the inset. View II shows buckling in the area of the vacuum hole*

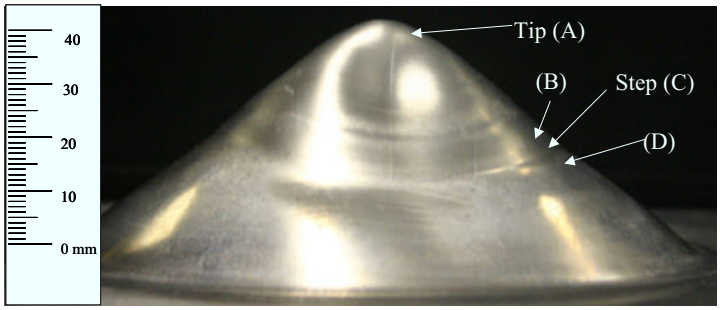

Figure 4: *AA6111 cone formed with the 40° die (9.0 kV). No tip impact was observed in the AA6111 parts*

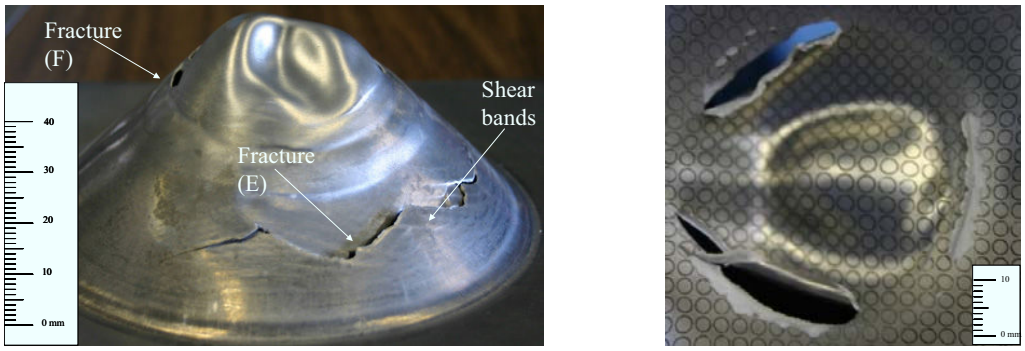

Figure 5: *AA6111 cone formed with the 45° die (10.0 kV). The fracture in the tip area is shown in B (Note that B is from a different sample than the one shown in A). The sample shown in A was used for metallographic analysis*

3.1 Formability Data

Figure 6 shows the measured strains for the safe and failed AA5754 parts. Strains above the conventional FLD were observed for the safe parts in the region below the step and the area of tip impact labelled A and D on Figure 2. The data for the failed AA5754 parts also shows very high strains under near plane strain conditions. The highest strains were recorded below the step and below the tip fracture, areas A and B in Figure 3. Figure 7 shows strain measurements for AA5754 samples free-formed with an open cavity die at 6.5 kV charging voltage with the same experimental apparatus [9]. In contrast to the current conical die results; the free-formed samples do not exhibit formability in excess to that obtained using conventional stamping methods.

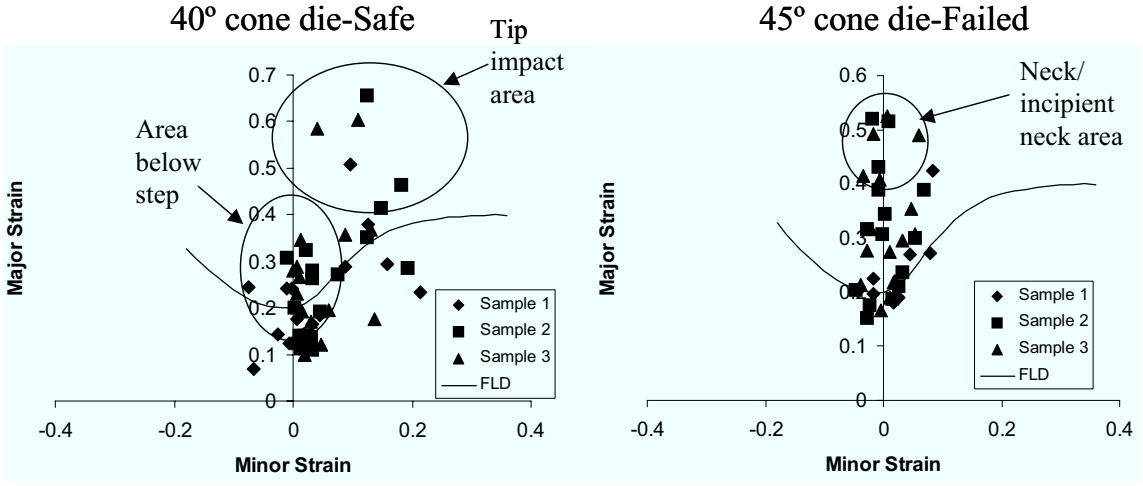

Figure 6: *Strain measurements in FLD format for the safe (left) and failed (right) parts. The curve represents a typical FLD for 1.0 mm AA5754 [12]*

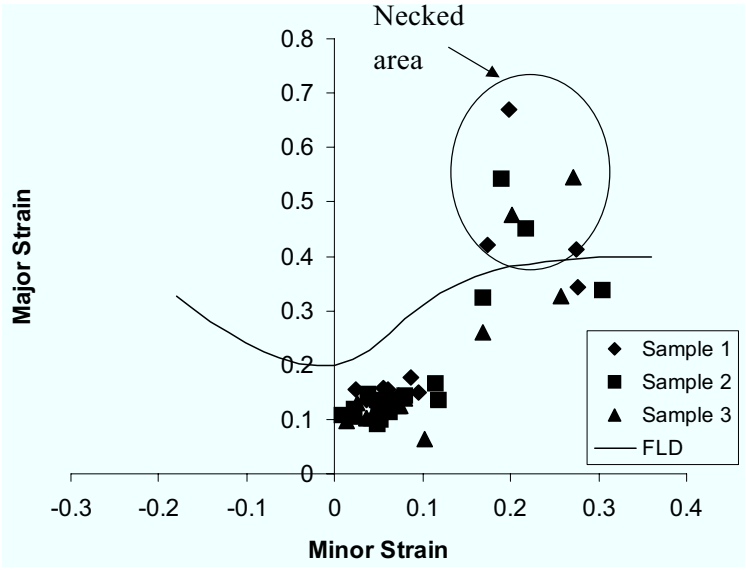

Figure 7: *Strain measurements for necked AA5754 free-formed samples formed using 6.5 kV charge voltage*

Figure 8 shows the strain measurements for the AA6111 safe and failed samples together with a conventional FLD curve. The highest strains were observed below the step for both the safe and failed parts. No impact at the tip of the part occurred, in contrast to the AA5754 parts. Data for the failed samples was taken away from the fracture surface where only incipient necking was present, and in the vicinity of the fracture where the grids were still intact. No strain measurements were taken in the tip region for the failed samples due to the condition of the samples (Figure 5 B). Visual inspection suggests that the strains in this area are significantly lower than the strains presented in Figure 8.

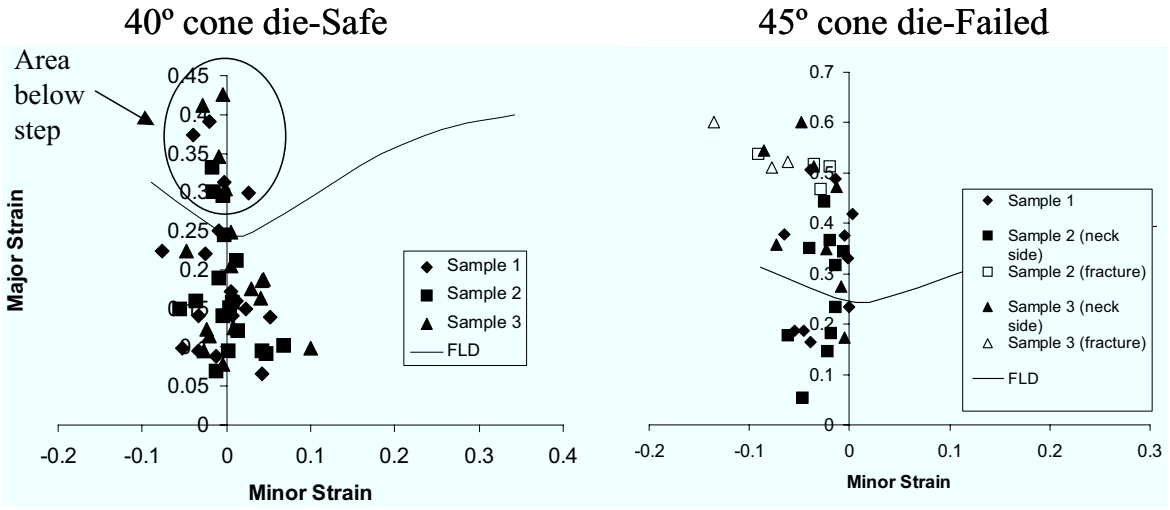

Figure 8: *Strain measurements in FLD format for the safe (left) and failed (right) parts. The curve represents a typical FLD for 0.9 mm AA6111 [12]. No FLD for 1 mm AA6111 sheet was available for publication*

Strains beyond the conventional forming limits were observed for both alloys. In conventional FLD's necking is considered as the forming limit. Using the same criterion the data for the failed samples could be considered as an upper limit of formability for these alloys. The data presented shows an increase in formability for the materials studied. In previous work, the present authors [8,9,10] have postulated that the increase in formability is the result of damage reduction produced by the tool/sheet interaction. The following sections will provide data to support this assertion.

3.2 Damage Measurements

Damage measurements are presented in Table 1 for the areas of highest observed damage. The safe parts for both materials exhibit the same damage trends with the highest damage being present in the tip and step areas. Neck measurements were not available for the AA6111, so measurements from the vicinity of the fracture surface are presented.

AA5754 as-received data **Percent area 2nd phase particles = 0.6** **Percent area porosity = 0.010**			
Location	Percent area porosity	e_1 strain (%)	Condition
40º sample			
Tip (A)	0.067	60	S
Above step (B)	0.011	19	S
Step (C)	0.021	22	S
Below step (D)	0.015	26	S
45º sample			
Neck	0.22	N/A	N
AA6111 as-received data **Percent area 2nd phase particles = 0.68** **Percent area porosity = 0.013**			
40º sample			
Tip (A)	0.14	12	S
Above step (B)	0.037	15	S
Step (C)	0.081	22	S
Below step (D)	0.05	30	S
45º sample			
Fracture (E)	0.32	N/A	F
Fracture (F)	0.065	N/A	F

Table 1: *Measured porosity for AA5754 and AA6111 samples. The data shown is for safe samples, except for the neck and fracture values. S = safe, N = necked and F = fractured. The locations of regions A-F are shown in Figures 2 to 5*

The formability data and the damage measurements obtained support the damage suppression theory. For AA5754, safe strains beyond the conventional FLD were recorded with the material showing little damage increase relative to the as-received condition, despite the large strains. The data for the cone experiments shows significantly lower dam-

age levels than the ones recorded in the free-formed case for similar strain levels. The area of the neck has an area porosity of 0.15% [9] for major and minor strains of 60% and 20%. This is significantly higher than the 0.067% area porosity for the tip area of the 40º part for major and minor strains of 60% and 10%. Similar data for free-formed AA6111 is currently being obtained.

The highest damage levels for the AA5754 parts were observed in the neck of the failed part, as expected. The fractures in the AA6111 showed two distinct trends, high levels of damage in the saw tooth fracture and relatively little damage in the fractures of the tip region (Figure 5). This is consistent with the higher strains observed in the area of the saw tooth fracture. Both areas show evidence of shear fracture as it will be shown in the following section.

More damage is present in the AA6111, which is consistent with the larger number of second phase particles present in the material, 0.68% area as opposed to 0.60% for AA5754.

3.3 Observed Failure

Micrographs of the fracture and necking of the part shown in Figure 3 are shown in Figure 9. It can be seen that the material thinned considerably before fracture in a manner more consistent with plastic collapse than with ductile fracture. The necked area shows voids elongated in the forming direction with significant thinning but relatively little damage. Large voids, similar to the ones present in the neck, could be the precursor to the rectangular feature present in the tip of the fracture surface. The material appears to thin considerably without a corresponding increase in damage. Thinning continues until the voids grow and coalesce to a size where the surrounding areas will either plastically collapse or fail in shear.

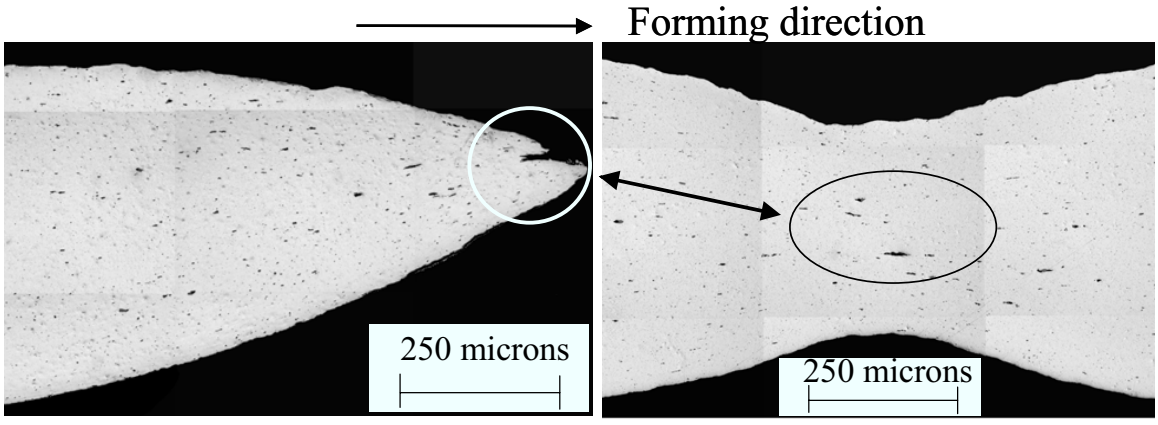

Figure 9: *Micrographs (200x) of the fracture and neck of a AA5754 part formed with the 45° die (Figure 3). Elongated voids, similar to the ones in the centre of the neck, could be the precursor of the rectangular feature present in the tip of the fracture*

Figure 10 shows micrographs of failures observed in AA6111 parts, which are markedly different from the failure observed in AA5754 parts. Both regions show the characteristics of ductile shear failure.

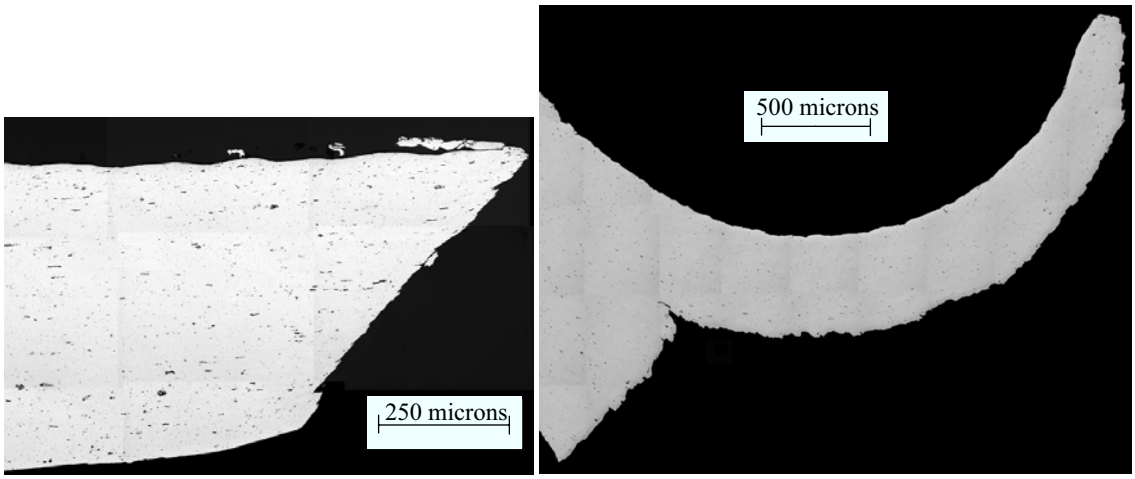

Figure 10: *Micrographs (200x) of the two fracture types observed in AA6111 parts formed with the 45° (Figure 5). Image A corresponds to the saw tooth fracture, while B corresponds to the fracture in the area of the tip (Figure 5)*

The failure modes present in the alloys are consistent with the proposed damage suppression theory during high rate forming. As damage is suppressed, ductile failure gives way to a combination of fracture modes. Although the alloys fail differently, both show evidence of fracture modes other than pure ductile failure. On-going microscopic and scanning electron microscope (SEM) analysis will help to determine the exact nature of the fracture.

4 Conclusions

Aluminum alloys AA5754 and AA6111 exhibit increased formability when formed using EMF. The damage measurements obtained support the theory that this increase is due to the suppression of damage caused by the tool/sheet interaction. The materials do not fail in pure ductile failure; rather, the failure modes seem to be a combination of plastic collapse, ductile failure, and shear localization. The failure modes for AA5754 and AA6111 in EMF are significantly different with the former showing significant thinning prior to fracture and evidence of what could be a combination of plastic collapse and ductile fracture, while the latter shows clear evidence of shear fracture. The vacuum hole has a significant effect on the quality of the formed parts, and its geometry and positioning are important considerations when designing EMF dies.

References

[1] *Wagner, H.J. and Boulger, F.W.:* High Velocity Metalworking Processes Based on the Sudden Release of Electrical of Electrical Energy. Memorandum prepared by the Battle Memorial Institute for the Defense Metals Information Center, 1960.

[2] *Balanethiram, V.S. and Daehn, G.S.:* Hyperplasticity: Increased Forming Limits at High Workpiece Velocity. Scripta Metall. et Mater., 30, 1994 pp. 515-520.

[3] *Balanethiram, V.S.:* Hyperplasticity: Enhanced Formability of Sheet Metals at High Workpiece Velocities. Ph.D. Thesis, The Ohio State University, 1996.

[4] *Vohnout, V.S.:* A Hybrid Quasi-Static/Dynamic Process for Forming Large Sheet Metal Parts From Aluminum Alloys. Ph.D. thesis, The Ohio State University, 1998.

[5] *Oliveira, D.A.:* Electromagnetic Forming of Aluminum Alloy Sheet: Experiment and Model. Masters of Applied Science thesis, University of Waterloo, 2002.

[6] *Oliveira, D.A. and Worswick, M.J.:* Electromagnetic Forming of Aluminum Alloy Sheet. J. Phys. IV France 110, EDP Sciences, Les Ulis, DOI: 10.1051/jp4:20030709, 2003, pp. 293-298.

[7] *Golovashchenko, S.:* Numerical and Experimental Results on Pulsed Tube Calibration. Proceedings of the TMS annual meeting “Sheet metal forming technology, M. Demeri ed., San Diego, Ca., 1999, pp. 117-127.

[8] *Imbert, J.M., Winkler, S.L., Worswick, M.J., Oliveira, D.A. and Golovashchenko, S.:* Damage Prediction in Aluminum Alloy Sheet Electromagnetic Forming. Proceedings of Plasticity’03 “The Tenth International Symposium on Plasticity and its Current Applications”, A. Khan ed., Quebec City, 2003, pp. 178-180.

[9] *Imbert, J.M., Winkler, S.L., Worswick, M.J., Oliveira, D.A. and Golovashchenko, S.:* The Effect of Tool/Sheet Interaction on Damage Evolution in Electromagnetic Forming of Aluminum Alloy Sheet. Submitted for publication, Dec. 2003.

[10] *Imbert, J.M., Winkler, S.L., Worswick, M.J., Oliveira, D.A. and Golovashchenko, S.:*Numerical Study of Damage Evolution and Failure in an Electromagnetic Corner Fill Operation. Proceedings of NUMIFORM04, Columbus, Ohio, June 2004. To be published.

[11] IAP Research Inc. 2003. Magnepress System product information. http://www.iap.com/2col.html.

[12] Data provided by Alcan *International.*

Improved Formability by Control of Strain Distribution in Sheet Stamping Using Electromagnetic Impulses

V. J. Vohnout, J. Shang, G. S. Daehn

Department of Materials Science and Engineering, The Ohio State University Columbus, OH, U.S.A

Abstract

Stamping failures consist of, broadly speaking, either tearing (excessive local strain energy) or wrinkling (insufficient or inappropriate local strain energy). Good parts are produced when the strain energy or plastic work is effectively distributed during the forming process such that tears and wrinkles are eliminated. The process window framed by tearing and wrinkling limits can be rather small for some materials, notably aluminum alloys. At present, there are no established methods of directly controlling the forming energy distribution within the tool during a stamping operation. All current commercial methods attempt plastic strain control at the sheet boundary by various binder geometries and pressure profiles. While improvements by active control of draw beads and binder pressure have led to improved stamping performance, these methods still broadly rely on tool geometry to set the energy distribution.

We have recently developed and demonstrated a method for more directly controlling the distribution of forming energy in a stamping operation based on an extension of electromagnetic (EM) impulse forming. We now have techniques for embedding and operating EM pulse actuator coils in stamping tools. These coils can be operated in a single high power pulse or as a series of lower energy pulses occurring several times during the forming stroke. A single high power pulse can provide the advantage of increased material forming limits of high velocity forming. However, applying a series of lower power pulses can increase forming limits without exposing the tooling and coil to large shock loads. Multiple pulses reduce the maximum strain levels by engaging more of the part material in the forming process which mimics (eliminates) the use of lubricants. Conventional production stamping rates are technically obtainable with proper integration of the EM impulse circuit with the forming press and tooling.

This paper focuses on the basic design approach of our multiple pulse technique and integrated process forming results. Comparisons to other augmented stamping processes as well as conventional stamping are presented in terms of both simple metrics, such as draw depth and strain distributions.

Keywords:

Deep drawing, Aluminum, Electro-impulse

1 Introduction

In conventional metal stamping a flat sheet of steel is transformed by the tooling geometry into a three dimensional part, such as an automotive fender, in a second or so. Stamping tools can be thought of as a type of lens that spatially directs energy from the press to the workpiece to generate the shape change. Press energy is absorbed by the sheet in the form of plastic work. The essential problem in sheet metal forming is that the energy is provided remotely (from the press as force and displacement through the tool) and this energy is focused by a passive but complex interaction between properties of the sheet and tool. In improving the ability to make a given part, stamping process augmentations are all attempts to better distribute the forming energy over the part (i.e., reducing strain localization). Even strain energy distribution is particularly important in aluminum alloy stampings due principally to the lack of strain rate hardening effect in these metals. We have developed a general approach to the problem of optimizing strain energy distribution in sheet metal stamping based on an overarching concept of integrating dynamic impulse events with conventional quasi-static processes. Detailed discussion of the fundamental aspects of this general approach and its various physical implementations have been published elsewhere [1-2]. Herein we will concentrate on a technique at the lower end of our hybrid process spectrum since it employs rather small impulse energies.

The most conventional methods employed to distribute strain energy are the use of lubricants and multiple sequential forming operations. Lubricants are one of the oldest means to help spread the press energy over the sheet, and thus augment the stamping process [3-4]. As the coefficient of friction between the part and die is reduced, the stress and strain distribution in the sheet is generally improved. However, lubricants must usually be removed before final part finishing and are often environmentally objectionable materials. The typical concept of multiple forming operations is to first draw and stretch the appropriate amount of sheet material into a precursor shape and then use other tools and operations to redirect press energy to more effectively form the detailed final shape [5-6]. The obvious drawback here is the increased cost and complexity of using multiple tools and presses. More recently developed methods attempt to improve stamping performance by independent active control of tool components. Some of the more successful methods, as reported in the available literature, are listed below. The performance of our method will be compared to the available performance data of these other methods.

- Active blankholder force control [7-8] - Restraining pressure on the sheet feeding into the die is controlled as a function of press stroke and, in some cases, location on the binder surface.
- Active draw bead penetration [9-10] - Draw bead height, and thus sheet feed control is varied as a function of press stroke.
- Ultrasonic vibration of tooling [11] - Ultrasonic generators are mounted in the stamping tools and tuned to change the effective friction between the sheet and tool in a controllable fashion.

2 Description of the New Process Approach

All of the approaches listed above essentially conform to the paradigm of remotely applying the forming energy and tweaking the boundary conditions to enable or improve the production of a given part. The present approach is based on the idea of delivering the deformation energy directly where it is required in the part. Figure 1 illustrates the desired effect on deformation energy distribution that is the goal of this new stamping method.

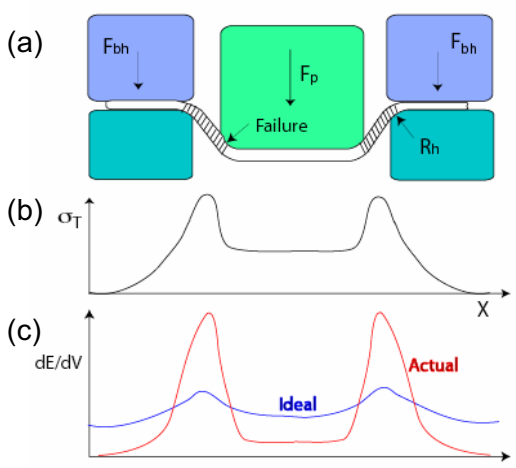

Figure 1:
(a) Schematic of a simple draw & stretch stamping operation.
(b) σ_T represents the tensile stress on the sheet.
(c) dE/dV represents the local dissipation of forming energy in an element of the sheet with change in volume swept by the punch in the sheet as a function of location in a typical (actual) and improved (ideal) metal forming situation.

Reliable generation of the ideal forming energy dissipation in a part should enable the economical production of lighter (smaller gage) components of the needed strength with fewer operations, while decreasing or eliminating the reliance on lubricants. The key enabler of this new method is the incorporation of EM actuator coils within otherwise relatively conventional stamping tools. Before describing this integrated approach it is worthwhile to review the essential elements of EM forming.

Electromagnetic forming is a process that has been well known since the 1960's, but has never seen very extensive use [12]. The basic experimental scheme is shown in Figure 2 where capacitor(s) with capacitance C_1 are charged to an operator specified voltage in the kilovolt range. These capacitors are connected to circuit with a primary coil that has an inductance L_1 and system resistance R_1. When the main switch is closed the current through the actuator produces a transient magnetic field that will induce eddy currents in the nearby metallic workpiece. The magnetic energy transfer is determined by the system coupling which is related to the mutual inductance, M, between the coil and workpiece. This process is governed by the classical coupled differential equations [13]:

$$\frac{d}{dt}\left(L_1 I_1 + M I_2\right) + R_1 I_1 + \frac{Q_1}{C_1} = 0\,;\ \frac{d}{dt}\left(L_2 I_2 + M I_1\right) + R_2 I_2 = 0 \qquad (1)$$

The currents in the actuator and metallic workpiece travel in opposite directions generating a natural electromagnetic repulsion. To calculate this precisely for a moving deforming 3-D situation problem is quite difficult, but the magnetic pressure can be approximated as [13]:

$$P_m = \frac{1}{A}\frac{dM}{dh} I_1 I_2 \tag{2}$$

where *A* is the area of the workpiece adjacent to the actuator. The spatial configuration of the coil directly controls the EM pressure distribution. The pressures attained can easily exceed the pressure needed to produce plastic deformation and can accelerate, within a few millimeters, the sheet to velocities of hundreds of meters per second. Process efficiency increases directly with increasing workpiece conductivity. Materials with lower conductivity, such as stainless steel, can be assisted by driver sheets or cladding of copper or aluminum. One important observation (not central to this paper) is that, at deformation velocities over about 50 m/s, the basic phenomenology of sheet metal forming is quite different than that in quasi-static forming. In particular, inertial effects in the workpiece can serve to dramatically increase the limit strains to values significantly greater than predicted by the standard forming limit diagrams. Our group at Ohio State, and others, have been actively investigating this area of velocity and strain rate effects in limit strains [14-18].

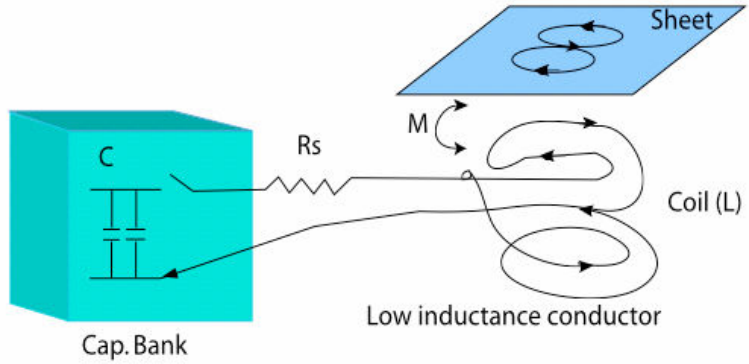

***Figure 2:**. Schematic diagram of electromagnetic forming of a sheet component*

2.1 Electromagnetically Assisted Incremental Stamping (EAIS)

This new approach to augmenting conventional production stamping (Figure 3) is conceptually simple. The primary goal is to provide forming energy to regions that are receiving too little strain or draw-in. Starting with the blankholder, the function of actuator 1b is to draw in the outer region of the blankholder surface taking advantage of the unbalanced forces over the surface and possibly to extend the material in the x-direction. The 'bubble' that 1b could form can be actively pulled into the die cavity using actuator 1a. These can be run sequentially to create what is in essence a controllable electromagnetic pump that can feed material into the die cavity. The function of actuators 2 and 3 is to stretch these regions essentially in the x-direction to provide the increase in line length needed to create the part.

The key idea is to energize the actuator coil many times where a small work increment is done in each cycle. In practice, it would not be a difficult matter to charge a group

of capacitors while loading a part and then discharge the capacitors sequentially as the punch moves into the die. There are no fundamental reasons this cannot accommodate a total part-to-part cycle time on the order of 5 or less seconds (as is typical in auto body panel stamping).

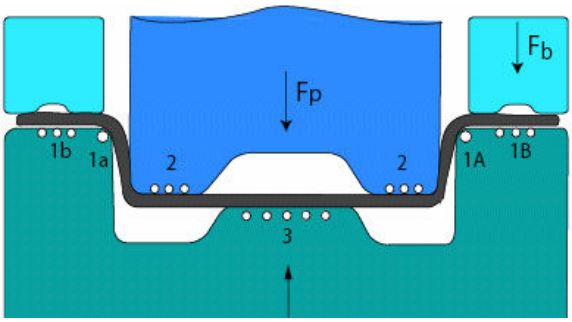

***Figure 3:**. Schematic of full implementation of electromagnetically assisted stamping: EM actuators are used to assist draw and stretch either by a single high energy pulse or incrementally with multiple low energy pulses*

2.2 Experimental Results of EAIS Trials

We carried out the first true hybrid electromagnetically assisted stamping operations by embedding EM actuators within conventional stamping tool and integrating the press and capacitor bank operations. These operations were performed using many relatively small EM impulses as opposed to the single high energy pulse used in our previous work [1-2]. An existing tool set for generically “difficult” pan part, originally developed by Hasida and Wagoner [7], was modified for these experiments. For the presented experiments only a single actuator coil was integrated in the tool set. A replicate punch was cast from a special iron filled epoxy. The punch face was then grooved to accept the actuator. Two simple configurations were tested. The first configuration (coil I) made a single loop around the punch face just inside the nose radius. Configuration II included additional path length in the center of the punch face. Each actuator coil was fabricated from 6 mm x 18 mm commercial copper bar bent to the appropriate configuration and inserted into the machined punch face groove. Figure 4 displays the photos of the cast punch inserted with the actuators I and II. The embedded actuators have demonstrated robust performance suffering no damage after well over 1000 shots.

The tooling was set up in an Interlaken computer controlled double acting hydraulic press. A flexible coaxial cable connected the capacitor bank to the actuator coil embedded into the punch. A Maxwell Magneform capacitor bank supplied the current pulses to the actuator. In the forming process, we set a constant blank clamp load at the level for best standard forming. The punch was then advanced a prescribed incremental distance and EM pulse discharged. The cycle was repeated until part failure occurred.

The typical result of forming is shown in Figure 5. The draw depth increased by 44% (from 4.4 cm to 6.35 cm). Figure 5 illustrates that the draw depth of the parts can be dramatically increased using the EAIS process and without any reliance on lubricants. This experiment verifies that the approach of placing forming energy where required, can dramatically increase the ability to make aggressive sheet metal parts. The effect of the embedded EM actuator coil is to produce tensile strain across the top surface of the part and tooling system constrains the part shape in the usual way.

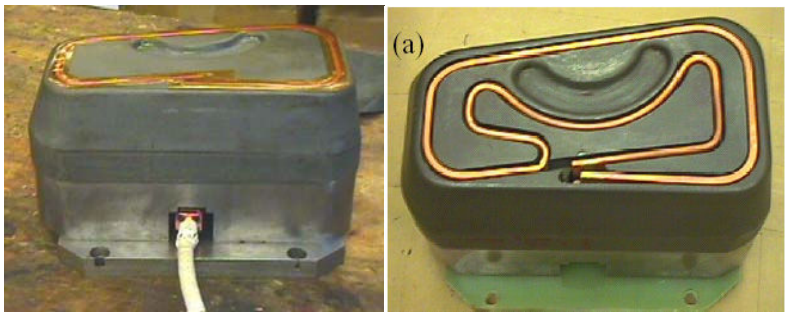

***Figure 4:**. Punch with Configuration I and II actuators (left and right).*

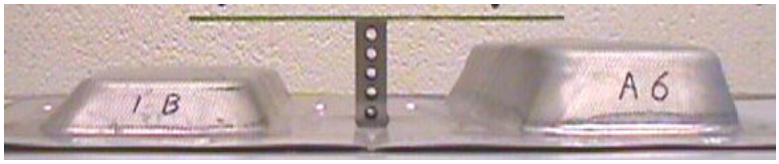

***Figure 5:** 6111-T4 aluminum formed conventionally (left) and using 22–5.4 kJ pulses, without lubrication (Draw depth increased from 4.4cm to 6.35 cm. Clamp load 35 k pounds, coil II used*

Figure 6 compares the strain distribution along the part longitudinal center between conventional forming and EAIS sheet forming. The electromagnetic energy added can produce much larger strain on the top surface of the part which allows a significantly deeper draw depth. In conventional forming, this area has little deformation because of the lock-out effect of friction between the sheet and tool at the punch nose radius. Now by the new EAIS approach, electromagnetic energy is delivered to this area generating an improved strain distribution and greater draw depth. In the case of Figure 5, draw depth increased by 44% (from 4.4 cm to 6.34 cm), and the average major strain of the top surface increased by 6.8 times (from 2.4% to 16%). The strains at walls change little because there is no electromagnetic energy delivered to those areas.

It should be noted that the conventional and EAIS process strain distributions shown in Figure 6 are for “as received” blank material. Trials investigating the effect of a medium weight oil showed that common blank oiling had little effect on the draw height (Figure 7). A special high performance blank lubricant might produce a greater effect generating a strain distribution somewhat similar to that of EAIS but of lower magnitude. Lubricants reduce the friction lock-out of material in a passive way that cannot produce the effect of direct application of deformation energy. The magnitude of the improvement available with EAIS would be very difficult to attain with the best lubricants even for simple axisymmetric, domed parts. The curious effect of lubrication reducing draw depth when employed in the EAIS process has not been thoroughly investigated as yet. Our current speculation is that oil lubrication provides a more air-tight seal between the punch and part that allows a higher vacuum to exist there. The vacuum between the punch and part restrains the local movement of the sheet away from the punch during the EM pulse event.

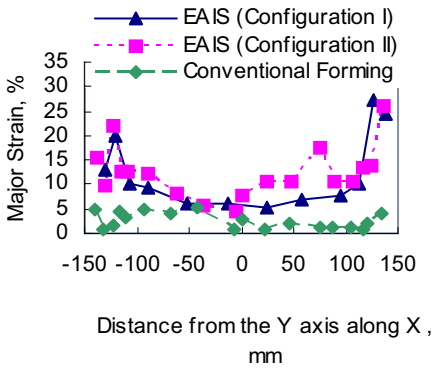

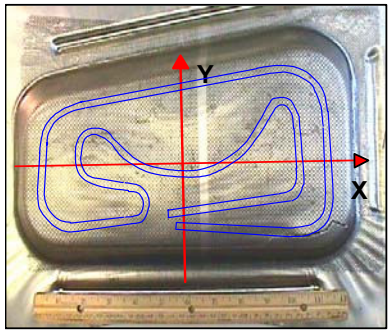

6111-T4, 1.0 mm thick actuator configuration II, path shown

Figure 6: *Comparison of strain distribution along the test part centerline between conventional forming and EAIS forming .*

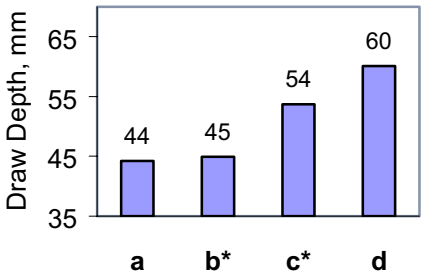

a - Conventional forming, no lubrication
b - Conventional forming with lubrication
c - EAIS process with lubrication
d – EAIS process , no lubrication
* two part average

Figure 7: *Effect of oil lubrication of part blanks on draw depth*

2.3 Effect of Process Parameters

The process parameters, such as clamp load, punch advance, and EM pulse energy, significantly effect the draw depth and the strain distribution as well as the propensity of the sample to wrinkle. For example, in the experiment of Figure 5 the punch was advanced incrementally 2.5 mm after each discharge pulse until the punch load reached about 156 kN. Then, the punch advance was reduced to a displacement of 1.3 mm after each pulse until failure. This protocol generated the greatest draw depth of the trials.

Aluminum stampings also experience greater problems with springback. An extension of the EAIS method can be envisioned to provide a means of controllable springback reduction. For actual parts the tooling could be designed to nearly bottom-out at the end of the forming sequence. In such tool sets a final pulse can be used to drive the workpiece material adjacent to the actuator against the die surface. With the proper pulse energy, a through thickness compressive plastic strain can be generated. EAIS actuator paths will generally run just inside the punch (male form) nose radius. A through thickness compressive straining of this region of the part will reduce the tendency of the part to open (springback) when released from the tooling. A variation of this technique has long been

used in conventional stamping (most safely using hydraulic presses) by precisely under sizing the punch nose radius with respect to the matching die radius and material thickness so as to generate the compressive “coining” strain at the punch nose radius when the tooling is bottomed. The EAIS implementation brings the added advantages of the reducing tool form precision, press loading, and the ability to tune the effect during production by simply changing pulse energy.

2.4 Required Design Methodology

The progress with the stretched and drawn pan show that this process basically does work. Forming depths can be increased by broadly moving deformation energy to areas of a part that would not otherwise plastically strain. The coil configuration used was chosen based largely on convenience, rather than on an analysis of the required energies or strains. We will seek to develop a formal design methodology based largely on the concept of mapping the required deformation energy onto the blank and then designing coils and schedules of punch advancement and pulse energy that will optimize the ability to make the part.

2.5 Comparison with other methods

The EAIS process as described here was specifically developed to increase formability of otherwise difficult aluminum alloy stamping. Ideally, we would like to make comparisons to other processes using 6111-T4. In all cases, results included baseline data for the non-augmented process so that an internally consistent, percent improvement figure of merit could be generated. Of the stamping augmentation methods compared with the EAIS process in Figure 8, two were found (A and E) that used the same material and gauge as the EAIS trials (6111-T4, 1.0 mm). To broaden the comparison, it was decided that other processes could be included since the data was normalized, in a sense, by the use of an internal percent improvement figure. A more rigorous comparison would require data from the application of the EAIS method to the other materials. EAIS experiments with materials such as steel have not yet been conducted, so the total applicability of this process is unknown. The reduction of the process efficiency with reduction of workpiece conductivity is known from the underlying physics and our previous work. Lower EM efficiency may, however, not be critical in the application of the EAIS method to cases where the available virtual anti-friction effect is of greatest benefit. Further, the use of highly conductive driver sheets or claddings may be an option for optimizing the performance of EAIS with lower conductivity sheet metals.

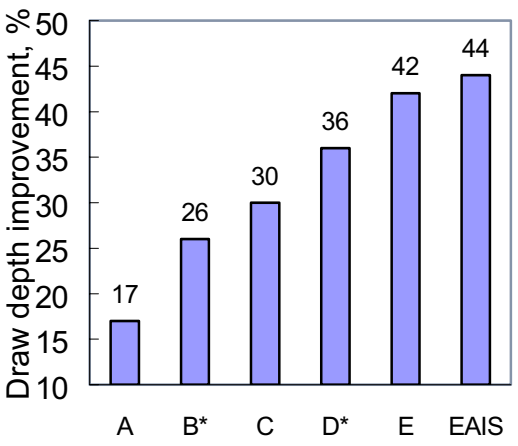

A) Ref. [9] Li, Rui: Active draw bead, Non-symmetric Al-6111-T4 parts with 1mm thickness, Clamp Load: 36.65kN
B*) Ref. [3] Zhang, Z.: Lubrication, Deep drawing cup test, using steel type 08F with 0.4mm thickness, LDR increases from 1.84 (dry) to 2.00 (lubrication)
C) Ref. [8] Obermeyer, E. J.: Segmented blankholders, aluminum alloy sheet cups
D*) Ref. [11] Takashi, J.: Ultrasonic vibration, deep drawing cups, average effect on SPCC (cold rolled steel), SPCE (cold rolled steel for deep drawing) and SUS304 (304 stainless steel) with a thickness of 0.5 mm.
E) Ref. [10] Bohn, M.: Active draw bead, Symmetric Al-6111-T4 parts with 1 mm thickness, Clamp load: 9.7 Mpa

Figure 8: *Comparison of draw depth improvement of several advanced stamping methods and EAIS with lubrication only (B) included for reference*

3 Conclusions

Electromagnetically Assisted Incremental Stamping (EAIS) may offer the following advantages:

- A reduced reliance on forming lubricants, or possibly their elimination. There are large spin-off benefits if lubricants can be eliminated. Equipment for application and removal would disappear, as would a waste stream. Lubrication also causes problems for joining (spot welding) and coating application, especially with aluminum alloys.
- Fewer forming steps and/or tools will be required to make a component of the same complexity. For somewhat different reasons this translates to much lower cost both in short run manufacture and mass production. Conversely parts of higher complexity and performance (such as possibly including ribs to increase section modulus) could be made on essentially the same tooling systems that made their less complex counterparts.
- The ability to directly fabricate stronger and less formable materials. This can reduce materials cost in addition to the obvious large benefit for automotive work of being able to reduce mass and increase vehicle performance.
- The same tools used to augment the forming process can be used to reduce springback. This provides improved dimensional tolerance, again reduces die development time, and can be used to compensate for differences in the hardness or thickness of incoming materials.

References

[1] *Vohnout,V.J.*: "A Hybrid Quasi-Static-Dynamic Process For Forming Large Sheet Metal Parts From Aluminum Alloys", Ph.D. Thesis, The Ohio State University, 1998, found at www.mse.eng.ohio-state.edu/~Daehn/vohnout/.

[2] *Daehn, G.S.; Shang, J.; Vohnout, V.J.*: Electromagnetically assisted sheet forming: enabling difficult shapes and materials by controlled energy distribution, Proceedings from Fourth MPMD, TMS, San Diego, 2003, p. 117-128, (2003).

[3] *Zhang, Z.; Chen, L.*: Study of the friction characteristics of lubricants and their affecting factors during drawing. J. of Mat. Proc. Tech. 63 (1997), p.144-147.

[4] *Wall, C.G.*: The laboratory evaluation of sheet-metal forming lubricants, Lubric Eng, 40, 139-147, (1984).

[5] *Peterson, D.A.*: "Progressive Dies: Principles and Practices of Design and Construction", SME, Dearborne, MI, (1994).

[6] *Goodwin, G.M.*: Applications of strain analysis to sheet metal forming in the press shop, SAE paper, No 680093, (1968).

[7] *Hashida, Y.; Wagoner, R. H.*: Experimental Analysis of Blank Holding Force Control in Sheet Forming, SAE Paper 930285, Sheet Metal Stamping Symposium, SAE SP-994, pp. 93-100, Warrendale, PA, (1993).

[8] *Obermeyer, M.; Majlessi, S.*: A review of recent advances in the application of blank-holder force towards improving the forming limits of sheet metal parts. Journal of Materials Processing Technology 75 (1998), p.222-234.

[9] *Li, Rui; Weinmann, Klaus J.*: Non-symmetric panel forming of AA 6111-T4 using active drawbeads, Proc. of TMS symposium , San-Diego, p.39-52 (1999).

[10] *Bohn, M.; Xu, S.; Weinmann, K.; Chen, C.; Chandra, A.*: Improving formability in sheet metal stamping with active drawbead technology. J.of Engineering materials and technology, Vol. 123, Oct., 2001, p.504-510.

[11] *Takashi, J.; Yukio, K.; Nobuyoshi, I.; Osamu, M; Eiji, M; Katsuhiko, I.; Hajime, H.:* An application of ultrasonic vibration to the deep drawing process, Journal of Materials Processing Technology 80–81 (1998), p.406–412.

[12] *Bruno, E.J.*, ed.: "High Velocity Forming of Metals", American Society of Tool and Manufacturing Engineers, Dearborne, MI, (1968).

[13] *Feynman, R.P.; Leightman, R.B.; Sands, M.L.* :"The Feynman Lectures on Physics", Addison-Wesley, Chapter 17, 2, (1989).

[14] *Wood, W.W.:* Experimental mechanics at velocity extremes, Exp. Mech., 19, 441, (1967).

[15] *Grady, D. E.; Benson*, *D. A.*,: Fragmentation of metal rings by electromagnetic loading., Experimental Mechanics: 393-400, (1983).

[16] R*egazzoni; G., Johnson; J.N., Follansbee, P.S.*: Theoretical study of the dynamic tensile test, J. Appl. Mech., 513, 519, (1986).

[17] *Wagoner, R. H.; Hu, X.; Daehn, G. S.; Ghosh S.*: The effect of inertia on tensile ductility, Metall. Trans., 1994, 25A, 2723-35.

[18] *Balanethiram, V. S.; Daehn, G. S.*: Hyperplasticity-increased forming limits at high workpiece velocities, Scripta Metall., 1994, 31, 515-520.

Pulsed Power Forming

Y. Livshitz, V. Shribman, A. Izhar O. Gafri

Pulsar Ltd., Yavne, Israel

Abstract

R&D and application work in the sphere of Pulsed Power Forming (PPF) is well known and has been documented since the 1960's, along with its advantages. Pulsed Power Forming applications, which have been developed at Pulsar Ltd over the last decade, are described in this paper.

Special equipment and tools for forming have been designed, developed, and manufactured, utilising pulsed magnetic fields. Theoretical and experimental research has been carried out to determine the magnetic field distribution in certain types of solenoids for diameters up to 600 mm. The software for mechanical pressure simulation and calculation has been carried out.

Research and application of forming by electrical discharge into liquid medium have been carried out with higher deformation than it has been attained by the classic processes.

Flat forming, cutting, and/or perforating of very thin materials (with thicknesses in the range of 0,1 up to 0,3 mm), such as aluminium, steel, stainless steel, nickel alloys, etc., have been made by applying high magnetic field with elastic medium.

In addition, forming and cutting of a steel tube with ~100 mm OD and a wall thickness up to 3 mm have been executed using direct high pulse magnetic field action. Aluminium tubes with OD ~100 mm and a wall thickness less than 0,5 mm have also been similarly processed.

Keywords

Forming, High Energy, Electrical Discharge

1 Introduction

Pulsed Power Forming (PPF) is a new technological application of pulsed power processes based on the use of high pulse current, created by the discharge of a capacitor battery through a load. This load may be a coil, a gap between electrodes, etc. PPF processes have been known for over 40 years and a lot of theoretical and experimental work has been carried out over the years. However, industrial utilisation of the process requires experimental work to determine the best electrical regime data as well as design

of the devices and equipment for each actual application with its accompanying industrial conditions.
Pulsar has performed much R&D work in this direction in order to solve actual problems on the way to industrial utilisation of the Pulsed Power Forming process.

Pulsar has developed a range of Pulse Current Generators (PCG) with parameters to cover a wide range of applications. Table 1 below presents a list of these generators:

Pulsar Model Type	Energy Storage kJ	Working Voltage kV max	Capacitance in microfarad	Self Frequency kHz
7.2/9	7.2	9	184	60
10/10	10	10	200	39
12.5/25	12.5	25	40	120
20	20	9	552	36
20Hf	20	25	64	100
30	30	6	1700	11
40	40	9	1104	22
100	100	25	320	65

Table 1: *Pulsar Pulse Current Generator Data*

Pulsed current generators have been used for many applications, including

- pulse forming by direct pulse magnetic field action,
- pulse forming by pulse magnetic action through an elastic medium.
- pulse forming by using underwater electrical discharge.

The forthcoming sections will define each of these methods.

2 Forming by direct action of pulse magnetic fields

There are two possibilities when using the direct action of pulse magnetic fields, as follows:

a) Forming of tubular shaped components with either/both external and internal pressure.

b) Forming of flat components.

It is well known that distribution of the magnetic field (or magnetic pressure) in the radial direction is very important for forming of flat details. It is a problem to control this distribution, especially for details with large dimensions.Another typical problem is the life time of the working coil. In this, it is well known, too, that single turn coils have an essentially longer lifetime than equivalent multi-turn ones .

Pulsar has developed the system for forming details with diameters up to 600 mm by using multi-turn (see Figure 1) as well as single turn coils. The single turn coils are connected with a PCG through a special matching transformer, which permits control of the magnetic field distribution. An example of magnetic field distribution in the radial direction for multi-turn coils is shown in Figure 2, and for the single turn coil system in

Figure 3. Pulsar has tested tubular as well as flat sheet options for forming by direct action of magnetic fields. Some results of this are illustrated in Figures 4 - 6.

2.1 Advantages and disadvantages for direct action

Advantages of direct magnetic pressure action are as follows:

a) Our experimental work has shown that forming by using direct magnetic field application is preferable for forming tubular shaped details, as it is a well known and documented process, especially for externally applied magnetic fields.

b) Forming of tubular shaped details with diameters less than ~100 mm using internally applied magnetic pressure is very difficult industrially, because of short lifetimes of the working coil for such dimensions.

c) Forming of flat details using the direct action of a magnetic field is a very suitable process for metals and alloys of high and medium electroconductivity, e.g. Cu, Al, and low carbon steels. The best results are obtained by using male rather than female dies. This is dictated by the fact that there is always a pressureless zone at the centre of the coil.

d) A system of single turn coils with matching transformers is the best option for industrial purposes as for control of magnetic field distribution as well as for long working coil lifetime.

Disadvantages of direct magnetic pressure action are as follows:

a) Results depend on the detail's material electroconductivity as well as on the material thickness. These determine the skin depth and process effectiveness in the final analysis.

b) It is very difficult to form flat details with small planar dimensions (less than 100 mm) due to coil's lifetime limitation.

3 Pulsed Power Forming by using magnetic field action through an elastic medium

Pulsed power forming by means of an elastic medium is also well known. Our R&D work has been directed to determine optimal regime data as well as optimal devices design. Here a system was designed with the intention of forming flat details with maximum planar dimensions of 100 mm diameter and material thickness in the range of 0,1 - 0,3 mm. This system consists of a multi-turn flat coil, a mechanical pressure concentrator, an elastomer punch, and a suitable holding device and matrix, etc.

Experimental work has been performed using a wide range of materials, including those suitable for traditional direct pulse forming such as Cu,Al, and low alloy steels as well as stainless steel, nickel alloys, etc. Three types of elastomer materials have been tested as well as the dependance of process effectivity on the type of die. The elastomers' modulus of elasticity (ME) was 38, 70 and 133 N/mm^2 with respective tensile strengths of 34, 38 and 45 MPa. It was determined that an elastomer of higher ME permits the use of an open die (without any constraining outer body).

An elastomer with lower modulus of elasticity can only be effectively used in a closed system due to its higher level of deformation under load. In general, a high ME elastomer is required for cutting processes, while elastomers with lower ME need to be used for forming processes. Devices are shown in Figure 7 and Figure 8.

3.1 Advantages and Disadvantages for the Elastic Medium

a) The elastic medium used permits the forming of materials independent of their electrical properties.

b) The elastic medium requires the use of an essentially lower current oscillation frequency, and therefore permits the use of Pulse Current Generators with low working voltage. Pulse current generators of 6 kV maximum working voltage have been used giving current oscillation frequency of about 5 kHz under load.

c) The industrial disadvantage of using an elastic medium is the medium's lifetime limitation, especially for cutting processes. This process has, for example, cut 1.5 mm diameter holes in the nickel alloy, Inconel 600 material of 0,27 mm thickness. However, elastic medium lifetime was about 500 pulses.

4 Underwater Discharge

Underwater high voltage discharge is an electrical pulsed power process using the liquid medium for transferring the pressure to the formed detail. The principle of high voltage electrical discharge for forming is also well known and a lot of work has been carried out, as well as patents, discribing the process. However, experimental work must be carried out to develop suitable industrial application requirements for the particular application.

Pulsar has passed along a part of this road on the way to forming details of plane dimensions up to 600 mm of materials including alloys of Al, steel, stainless steel, including DP steel etc., with thicknesses from 0,3 up to 1,5 mm.

The pulse maximum pressure in the liquid at the high voltage electrical discharge may be described by formula (1):

$$P_{max} = \rho \cdot \frac{a^2}{\tau^2} \tag{1}$$

Here:

$$a = \left[\frac{(\gamma - 1)}{(\pi \cdot \rho)} \cdot T^2 \cdot \frac{W}{L} \right]^{0.25} \tag{2}$$

W energy introduced into discharge, J

P density of the water at the moment of discharge. It may range from 1,05 up to 1,35 of initial density (this depends on pulse current amplitude), in kg/m3

T discharge duration, sec

γ = 0,26 effective adiabatic index for discharged plasma

L discharged distance, m

Energy introduced into discharge, *W*, depends on time needed for discharge forming and it may be essentially less than energy storage in the capacitor battery, especially at a charging voltage of less than ~10 kV. This means that higher working voltages provide more process effectivity. This is a contradiction because the high voltage battery has a lower capacitance, and thus a shorter discharge time than a low voltage capacitor battery. At the same time, details of greater dimensions (or the same with large mass) need a longer discharge time.

Our experiments show that for details of mass about 1 kg the first quarter of discharge period needs to be about 60 – 80 μsec. This means that discharge current oscillation needs to be about 3-5 kHz at the energy storage of about 30 kJ for steel of yield strength about 400 MPa. Typical formed samples are shown in Figures 9 and 10.

4.1 Advantages and Disadvantages for Underwater Discharge

Underwater electrical discharge is a very useful tool for the forming process which has the advantages inherent in other pulsed forming processes as well as the additional advantages as follows:

a) the possibility of achieving a very high pressure for a wide range of pulse durations.

b) process has a very high flexibility for adjusting the industrial Requirements.

c) process is very useful for forming the details of intricate shapes with or without axial symmetry.

d) disadvantages are that it is nessecary to change the water or to fill up the water after each pulse, which can take some additional time, and that the electrode lifetime is a very important problem. The former may be minimised by clever tooling design, and the latter problem with R&D work.

Figure 1: *Multi-Turn Coil*

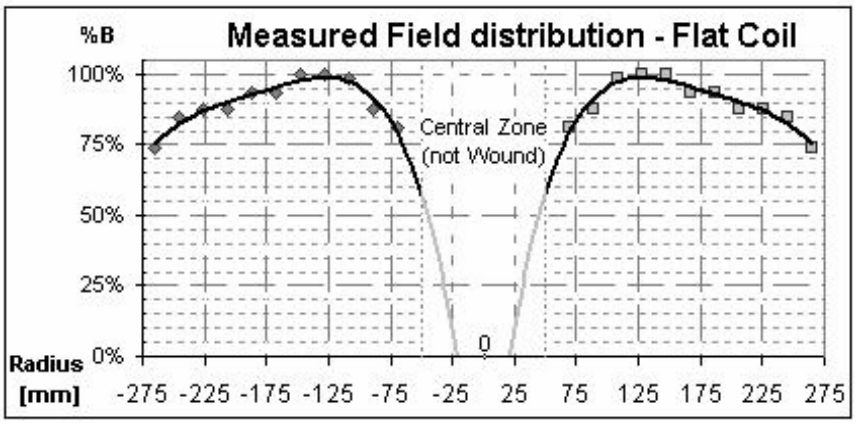

Figure 2: *Magnetic Field Distribution – Multi-Turn Coil*

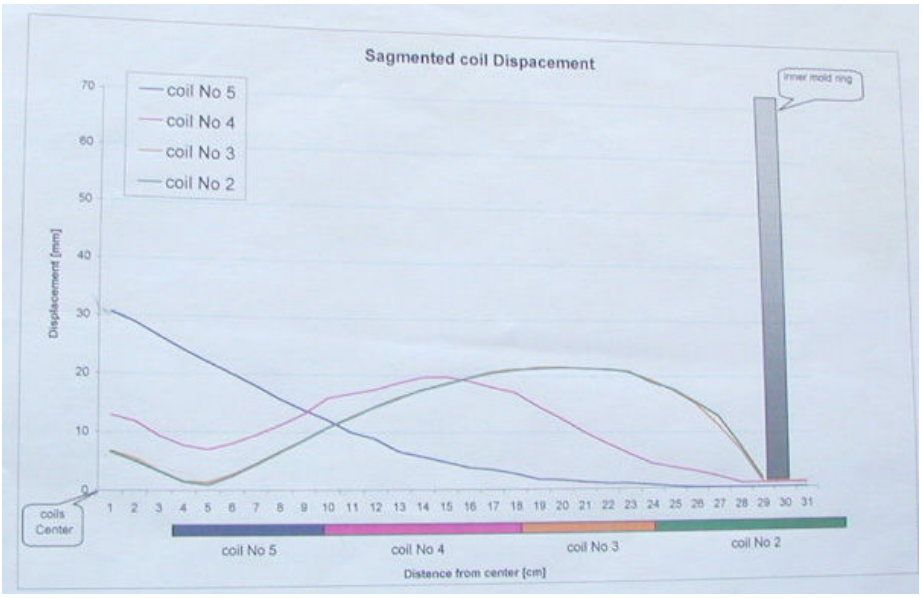

Figure 3: *Magnetic Field Distribution – Single Turn Coil*

Figure 4: *Tubular Forming 3 mm steel*

Figure 5: *Forming of 600 mm Al Antenna Disc*

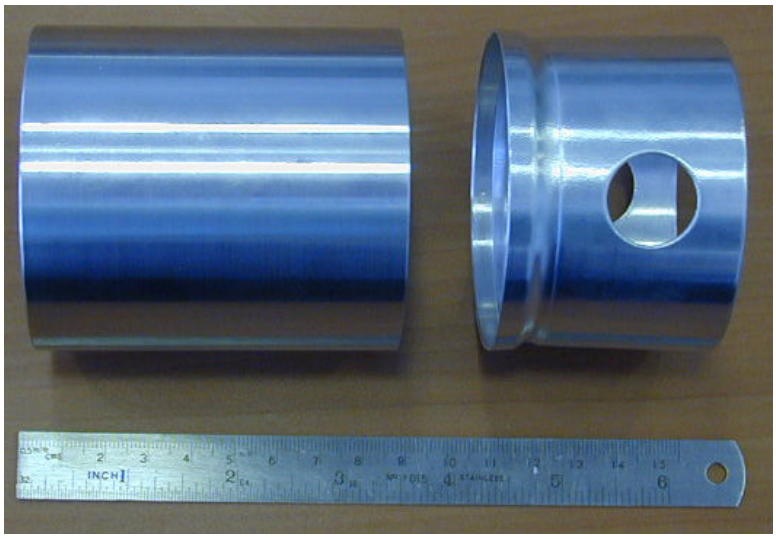

Figure 6: *Formed and Perforated Al Tube*

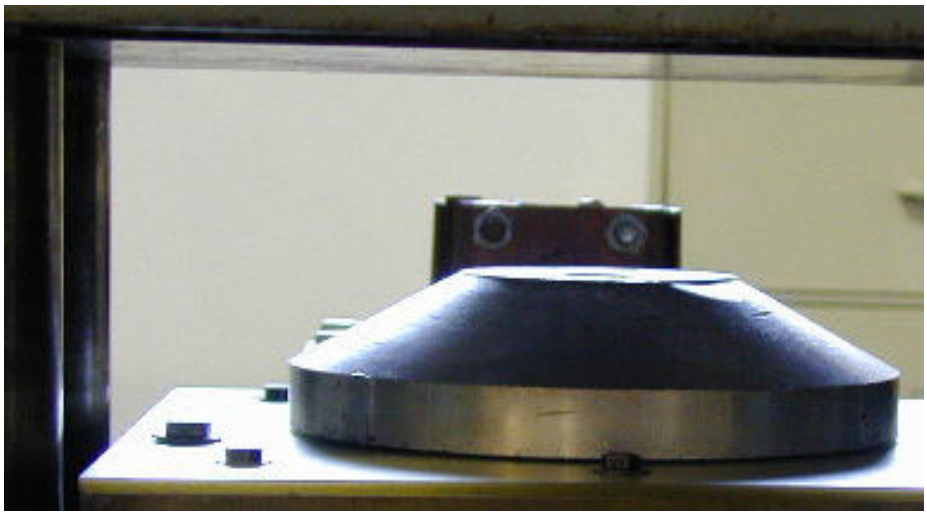

Figure 7: *Forming Device*

Figure 8: *Forming Die Assembly Device*

Figure 9: *Formed Stainless Steel*

Figure 10: *Formed Stainless Steel*

New Impulses in the Forming of Magnesium Sheet Metals*

E. Uhlmann, D. Jurgasch

Institute for Machine Tools and Factory Management, Technical University of Berlin, Germany

Abstract

Owing to growing demands by customers for comfort and safety in cars, the weight of the respective individual automobile increases constantly. Hence, the role of construction materials, such as aluminium and magnesium alloys in car body production becomes ever more important. Especially magnesium is highly attractive because of its small density, its positive mechanic-technological properties, and the ready availability as raw material.

It is known that magnesium has a reduced formability at room temperature and needs to be heated up to temperatures at around 300°C to be deformable with technologically useful forming rates. So therefore to form sheets made of magnesium alloys, the workpiece has to be heated previously. The idea of combining the processes "inductive heating" and "pulsed magnetic forming" led to the following research work. The aim was to develop a tool that combines both processes to be able to heat up the forming zone at the workpiece to a significant temperature and to form it afterwards without changing the tool.

However, in order to manufacture sheet metal components from magnesium innovative manufacturing technologies are necessary. The Institute for Machine Tools and Factory Management (IWF) carries out research and develops solutions in the field of pulsed magnetic forming.

Keywords:

Forming, Magnesium, Electrical Discharge Machining (EDM)

This work is based on the results of the research project "Pulsed Magnetic Flat Forming of Magnesium Sheets by Increased Forming Temperatures"; the authors would like to thank the DFG for their financial support

1 Introduction

The objective to reduce moved masses has led to the reinforced development of light metal alloys. Considering the limited amount of natural resources, growing environmental pollution, the necessity of energy saving, and the resulting ever stricter legal regulations, recyclable lightweight design materials are gaining increasing importance. Additionally, technology-oriented companies place ever more focus on the technological and economic potential of innovative materials. Therefore, it is especially in the vehicle industry that the tendency to novel concepts and solutions for weight reduction continues to be very significant despite the existing innovations in terms of constructive design and the increasing use of lightweight design materials.

As far as the fuel consumption of automobiles is concerned, the factors power, train, and vehicle mass play the most important role alongside the influencing parameters rolling and air drag. Since these values are very difficult to realise and have only a light effect on the consumption value in the case of the first three factors, the main focus is placed on further development work in reducing the vehicle mass. In the field of the drive train, the chassis, and a number of other functional components, the idea of lightweight design has consistently been realised using cast products on aluminum and magnesium basis. Therefore, a further potential of weight economy might be the car body shell [1].

At present, aluminum of a density of approx. 2,7 g/cm³ is the most frequently used functional metal in the production industry after steel with a density of approx. 7,8 g/cm³. Recent developments, such as car bodies made completely of aluminum, show that the ratio of lightweight design materials is clearly increasing in the automotive industry. Hereby, the basis is either a tubular grid frame, the so-called space frame, Figure 1, or an aluminum car body in the conventional self-supporting design, Figure 2.

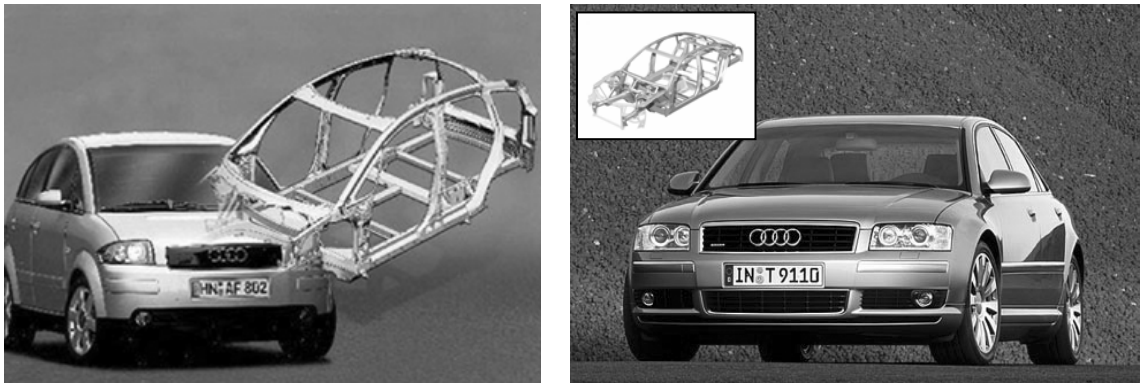

Figure 1: *Audi Space Frame® (ASF) in Audi A2 and Audi A8 [2]*

Figure 2: *Self-supporting aluminum car body in Jaguar XJ [3]*

2 Potentials of Magnesium Alloys

2.1 Technological and Economic Significance of Magnesium Alloys

With its specific mass of 1,8 g/cm³, magnesium is lighter by approx. 30 percent than aluminum, thus being the lightest metallic design material. Due to the high mass-specific solidity and rigidity characteristics, especially under bending and buckling stress, it has some weight advantages in the component of up to 60 and 25 percent, respectively, if compared to steel and aluminum [4]. Alongside their small density, the main advantages of magnesium alloys are good availability and good mechanical properties. Moreover, the excellent recycling potential of magnesium alloys entails an economical energy balance using comprehensive recycling systems. In comparison to the primary winning of aluminum requiring approx. 67,5 kWh/dm³ energy, magnesium shows a favorable energy demand of 63,0 kWh/dm³. If magnesium is recycled in the secondary way from magnesium scrap of the quality class 1 the balance can be further improved. Hereby, only five percent of the energy, used for the primary winning, are required [5].

Despite these advantages, magnesium alloys stay far behind other lightweight design materials in terms of their dissemination. The reasons are the unsatisfactory corrosion resistance of magnesium alloys, reservations in terms of the hazard potential, and the lack of suitable process technologies for the forming of magnesium sheets. It was not until the manufacture of “high purity“ (hp) magnesium alloys with small percentages of iron, copper, and nickel, that the corrosion resistance was considerably improved, enabling magnesium alloys to keep up with aluminum materials in this aspect, too [6].

Recent market analyses assume a growing European market for magnesium alloys of two-digit growth rates [7]. Within the period of 1990 to 1998, the consumption of magnesium in the automotive industry thus grew from 23.000 to more than 90.000 tons per year with an average growth rate of 20 percent. Today, cars usually contain around 3 kg of magnesium. Single cars of leading European producers, however, contain 5 to 7 times more. According to a US study, some automobile producers will use as much as 100 kg magnesium in their cars adhering to the objective to reduce the total weight of cars by 10 percent. This may suggest the growth potential to be expected for this material considering a world-wide production of 55 million cars per year [8].

Today, components from magnesium alloys are mainly produced by die casting, Figure 3.

Figure 3: *Inner door made from AM50 die cast (the newest VW Polo) [9]*

The production of components with large surfaces and, at the same time, thin walls is, however, limited by the required locking pressures and by the fluctuation of the material properties [10]. In order to avoid the disadvantages of die casting, sheet metal components of magnesium forgeable alloy should be produced by forming processes in the future. In contrast to primary forming, forming enables a homogeneous, fine-crystal material structure which has very few faults. In contrast to magnesium sheet components manufactured by die casting, the resulting advantages of those manufactured by forming are the higher elongation at fracture making them more suitable for the security field, small wall thicknesses to be realised in large car body components, and their higher potential of application for visible areas of the car body shell due to their smooth surface structure.

2.2 The Basis of the Forming of Magnesium forgeable Alloys

There are only a few recent investigations known on the machining of magnesium forgeable alloys by sheet forming processes. A crucial influencing parameter of the forming of magnesium forgeable alloys is the forming temperature.

Due to its hexagonal grid structure, magnesium is highly formable at ambient temperature. Investigations on the influence of temperature on the forming capacity, however, show that the form changing capacity of magnesium alloys jumps up at temperatures of T = 225°C [11], as further gliding planes are activated in this way.

For the above-mentioned reasons, nearly only tempered deep drawing tools are used for magnesium sheet forming. Through the variation of alloys, recent research projects are searching for possibilities to reduce the considerable cost factor. It is, however, rather questionable if the heating up of at least one of the tools (die or matrix) can be completely avoided for alloy systems ready for serial production [12].

2.3 Challenges to the Forming of Magnesium Alloys by Conventional Forming Processes

Independently of the fact whether the magnesium sheet is heated up externally, i. e. outside the forming tool or within it, the tempering of the forming tool cannot be avoided in any of the forming processes. This, however, implies some difficulties because the uneven heating up of the machine leads to a reduction of the guide clearance of the machine

tappet making it jam [5]. In order to avoid these negative effects, the tool must be completely thermally de-coupled from the machine by insulation layers and cooling elements.

Such a thermal de-coupling proves to be very complicated in practice. Additionally, investigations have shown that the heat transfer as a result of convection must also be considered for thermal de-coupling despite the use of heat insulating plates for the reduction of heat conduction between tool and forming machine [5].

3 Potentials of the Pulsed Magnetic Flat Hot Forming for the Lightweight Design

Due to the difficulties in the heating of the forming tools occurring during conventional forming processes, the goal of a topical research project promoted by the Deutsche Forschungsgemeinschaft (DFG) is to realise new possibilities for the forming of magnesium fine sheets. Hereby, impulse magnetic hot flat forming is an interesting possibility to consistently harness the potentials of this ultra light material.

3.1 The Process of Pulsed Magnetic Hot Flat Forming

Pulsed magnetic forming (PMF) is a non-contact technique where large forces can be imparted to a conductive metallic workpiece by a pure electromagnetic interaction. A significant amount of energy is stored in a bank of capacitors by charging to a high voltage. The charge is switched over low inductance conductive buswork through a coil acting as a tool so that large currents run through the coil.

The currents take the form of a damped sine wave and can be understood as a ringing Inductance-Resistance-Capacitance (LRC) circuit. The peak current is typically about 104 to 106 amperes and the time to peak current is on the orders of tens of microseconds. This creates an extremely strong transient magnetic field in the vicinity of the coil which induces eddy currents in any conductive material nearby.

These currents will generally be opposite in direction to the primary current. So the opposed fields in the coil and workpiece set up an electromagnetic repulsion between the coil and the workpiece. This electromagnetic force can produce stresses in the workpiece that are several times larger than the material flow stress. Ultimately, this can cause the workpiece to deform plastically and to be accelerated at velocities exceeding 100 m/s [13]. The process of pulsed magnetic forming for metal sheets is shown in Figure 4.

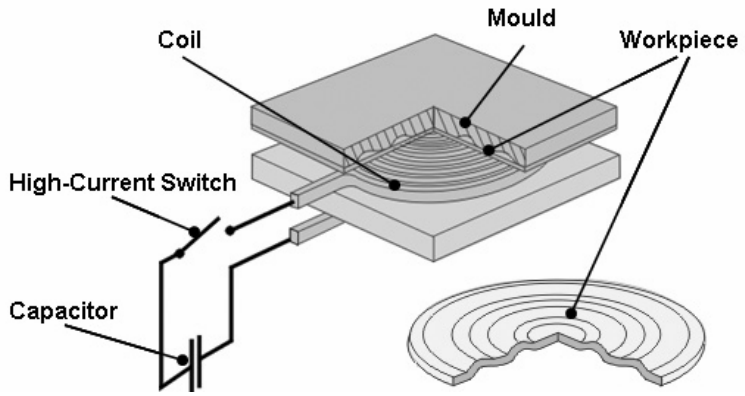

Figure 4: *Tool and workpiece by pulsed magnetic flat forming*

The small strain rate achievable on magnesium alloys in cold state is problematical for the application of the process for the pulsed magnetic flat forming. However, it is known from sheet metal forming that magnesium alloys can be deformed at temperatures of approximate 250°C to 300°C to sufficient strain rates [5].

A suitable solution for pre-heating the workpiece is to use inductive heating (IH), because the physical principles of both processes, inductive heating and pulsed magnetic forming, are close to each other. A combination of both processes was described for the first time in a patent from 1962, but it is unknown if it ever has been realised or investigated in an scientific way [14].

3.2 Former Investigations in Pulsed Magnetic Hot Forming of Magnesium Alloys

In the former USSR, basic investigations were done to form sheet metals and profiles with pulsed magnetic forming at high temperatures. The workpieces were previously heated up in an oven. This was tested at alloys of copper, steel, and magnesium. Especially for the investigated magnesium alloys, the results demonstrated a clearly increase of the formability at temperatures of 200°C to 250°C [15,16].
Other systematical experiments were carried out in Germany at the Technical University of Berlin. In this case, a tool which combines the processes of pulsed magnetic forming and inductive heating for thermally-supported-joining of magensium profiles was developed [17].

The investigations on thermally-supported-joining were carried out at a tube-core-joint. Here, a tube consisting of the technically relevant magnesium alloy AZ31 was compressed to an aluminium-core by using the combined compression-coil. The results of the investigations for pulsed magnetic hot joining showed that there is a distinctive potential for forming of magnesium alloys.

Joining by forming became possible for this material through pulsed magnetic hot forming. Those investigations proved that magnesium can be used in future lightweight designs not only in casted parts, but also in formed components like compressed tube-profiles [17].

4 Tool Principle and Developments

To utilise the potentials of the pulsed magnetic hot flat forming to turn magnesium sheets, it was necessary to develop an adequate tool which integrates the process of pulsed magnetic forming on the one hand and the inductive heating on the other hand.

4.1 Basic Reflections

The main problem was posed by the design layout of such a tool. Usually, coils used for both processes have to live up to completely different requirements in electro-technical, thermal, and mechanical terms. While in the case of a coil for pulsed magnetic forming, the mechanical stability is more important than its thermal stability. However, a coil for inductive heating has to be strongly cooled and is subject to only small mechanical strain [18].

Moreover, the requirements on both coils concerning the number of turns are very different to each other and can be changed only in narrow limits. For that reason it is not possible to use only one coil for the application of the two processes.

For the combination of both processes, it was necessary to develop a tool in which two separate coils focus on the same area of the workpiece. To realise this demand, it was inevitable to integrate a field former in the tool. Field formers are often used in pulsed magnetic forming, especially for compression. But also simply for the flat forming they have a lot of advantages:

- reduction of the process forces on the PMF-coil,
- possibility to integrate cooling channels in the field former,
- low-cost replacement,
- low-wear tool surface, and
- possibility to adjust the distribution of the magnetic pressure by changing the field former geometry.

Above all, the last reason to use field formers is the most important for the process of pulsed magnetic flat forming. That is why, because in the center of a directly working PMF-coil there is no magnetic pressure at all. A radial vectored force acts on each volume element of the workpiece and the coil if the orientation of the current density in the workpiece and the magnetic field between workpiece and coil are both at the same time, vertical and in parallel levels to each other. There are no conditions like this in the center of the coil.

4.2 Realisation of the tool conception

Figure 5 shows the princile of the combination of both processes “inductive heating” and “pulsed magnbetic flat forming”.

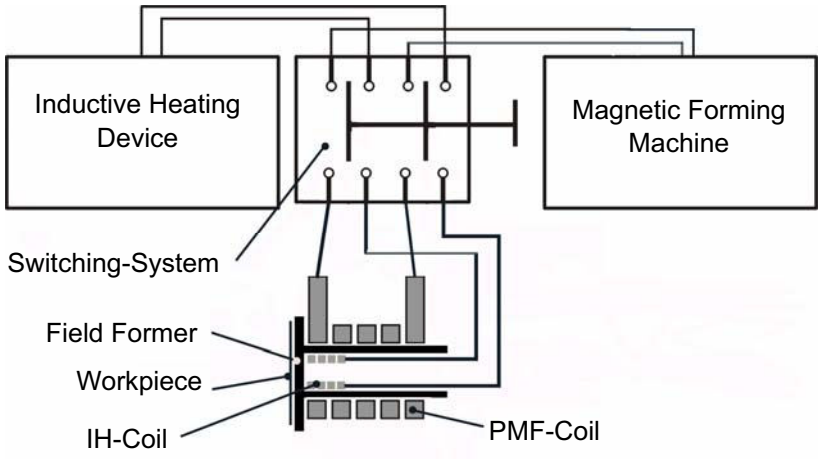

Figure 5: *Principle of process combination IH and PMF*

In this case, the coil for IH is situated at the inside of the field former, while the PMF-coil is placed at the outer circumferene of the field former, Figure 6. Both processes act on the

same area of the workpiece without changing the tool or movement. The coil for inductive heating and the field former are water-cooled, thus contributing to the cooling of the PMF-coil. The most important reason for using a cylindical PMF-coil instead of a spiral one is the enhanced possibility to integrate the amouring to increase the mechanical strength of this coil.

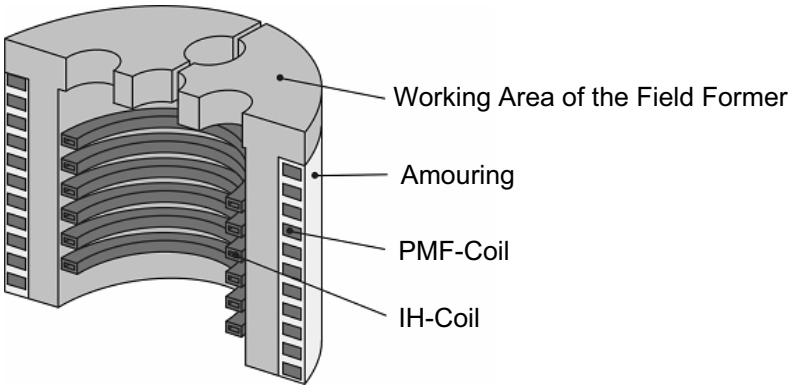

Figure 6: *Design of the combined tool*

This so-called combined coil was manufactured at the IWF and has already been successfully tested. The working area has a diameter of 96 mm. The IH-coil is fitted with five windings and the coil for pulsed magnetic forming has eight windings and an inner diameter of 110 mm.
Both coils are connected to the induction heating device and the magnetic forming machine via appropriate switches, which provide that the coil of the non-active process is electrically separated from its device. Figure 7 shows the experimental setup for the thermally supported pulsed magnetic flat forming.

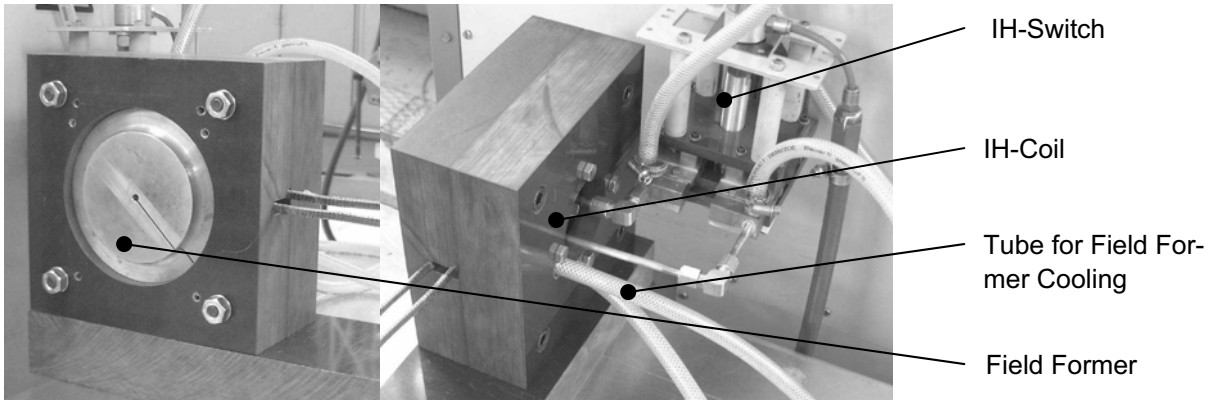

Figure 7: *Experimental setup with combined coil and peripheral equipment*

The investigations were carried out on magnesium sheets AZ31 with the measurements of 100 mm x 100 mm and a thickness of 1,0 mm. The first investigations were focused on the influence of the work area geometry of the field former on the temperature spreading in the workpiece during the heating process. Another object of investigation could be found in the connection of the field former geometry and the absolute and relative magnetic pressure within reach.

5 Results

In order to ascertain the possible temperature and the magnetic pressure, the investigations were carried out with two different field former geometries. They are called the 1Hole-Field former and the 5Hole-Field former, Figure 8.

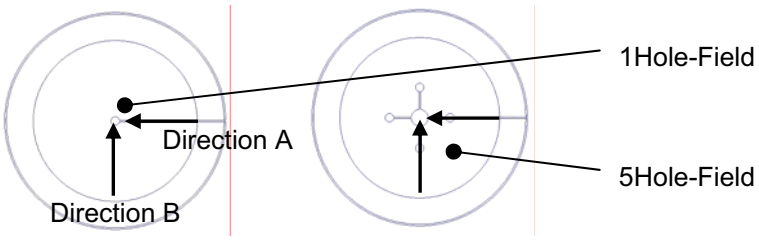

Figure 8: *Used field former geometries*

5.1 Results for the process of the inductive heating

For the two different geometries, there are different temperature maximums after a heating time of 20 s, Figure 9. There are differences up to 200°C.

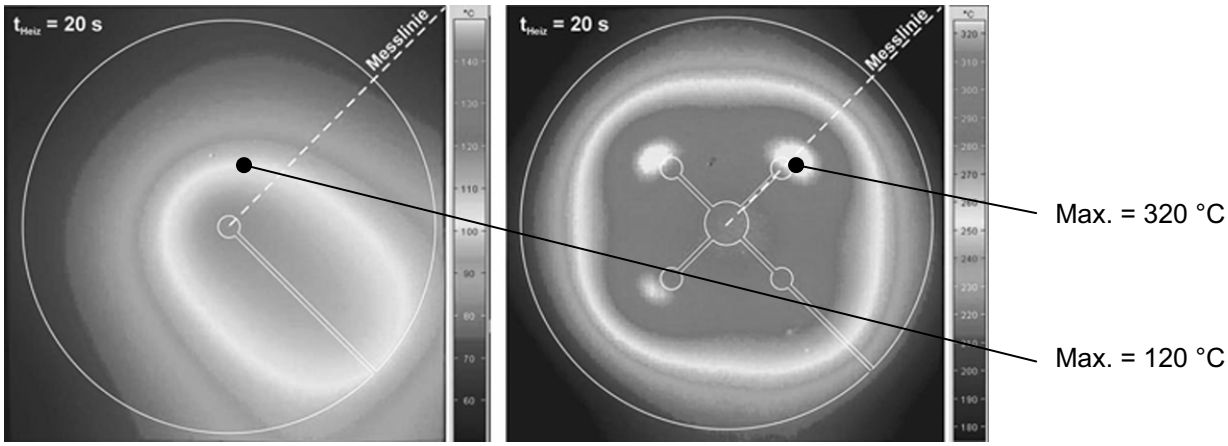

Figure 9: *Maximum and spreading of the heating temperature after 20 s heating*

So it is possible to carry out the process in a more efficient way by varying the geometry of the working area which is close to the workpiece. A first investigation shows that the number and the spot of the holes on the working area have a big influence on the efficiency of the process of inductive heating.

5.2 Results for the magnetic pressure within reach

For the magnetic pressure within reach, and thus for the maximum forming force, there also exists a connection between the number and the spot of the holes on the working area and the magnetic pressure. In the margin of the holes there are always the maximums of the magnetic pressure, Figure 10 and 11.
The measurings were done in two directions on the field former working area. The first measuring direction, the so-called “direction A”, was from the outer margin of the working area (-48 mm) along the field former slit to the center of the field former (0 mm) and be-

yond. Vertical to this orientation, the relative magnetic pressure in “direction B” was measured. Because of the symmetry of the working area in this direction it was only necessary to measure the pressure from the margin of the field former to the center of it, Figure 11.

It is evident that the maximums of the magnetic pressure are situated in both cases at the margin of the holes which are turned away from the slit. The reason for this can be found in high magnetic flow density at this point. At this point, the magnetic field is especially high, because the lines of electric flux get out of the small holes in the working area of the field former. There, they have to change their directions in a rectangular way, because the magnesium sheet acts like a shield. So a very high magnetic field between the workpiece and the field former working area gets a vertical orientation to the current density in the workpiece within a short way. This causes a maximum radial vectored force in this point.

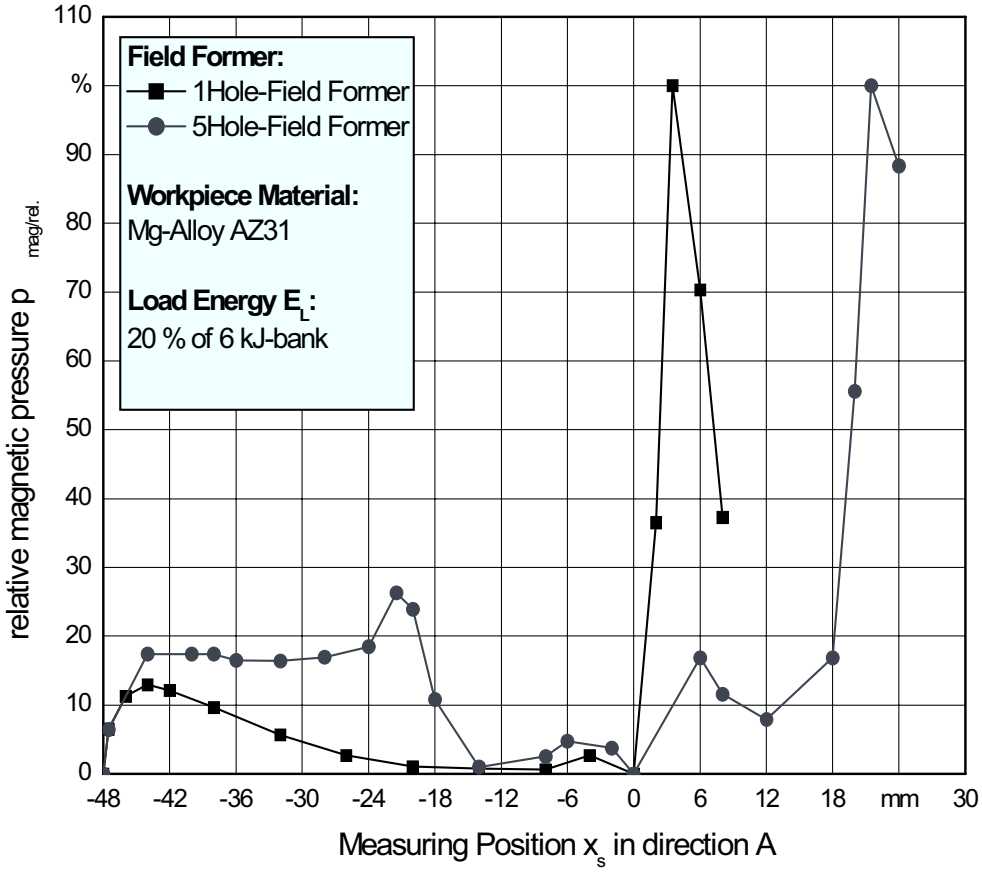

Figure 10: *Relative magnetic pressure in dependence on the working area geometry, Measuring direction A*

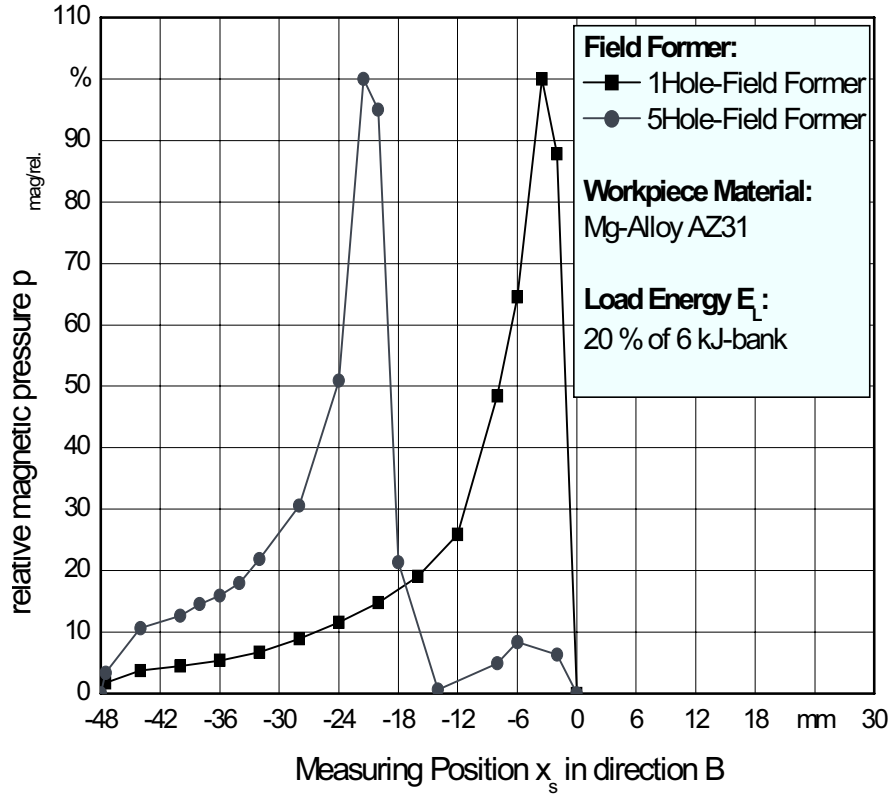

Figure 11: *Relative magnetic pressure in dependence on the working area geometry, Measuring direction B*

Further object of investigation was the finding of the absolute magnetic pressure in dependence on the load energy at one point on the working area of the field former. This point could be found during the measuring of the relative magnetic pressure. To compare the values of the 1Hole-Field former and the 5Hole-Field former, it was necessary to measure the absolute magnetic pressure at the point of the relative maximum. Figure 12 shows that the absolute magnetic pressure increases almost linear to the increase of the used load energy.

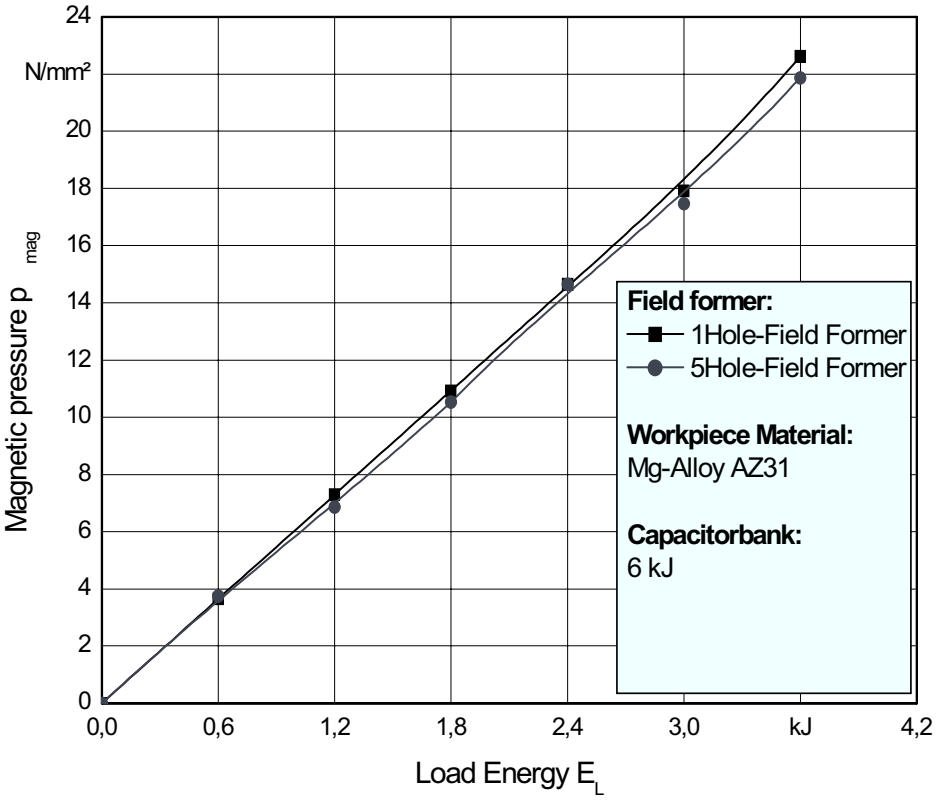

Figure 12: *Absolute magnetic pressure in dependence on the load energy, measuring point is the point of the maximum pressure within reach*

For both field formers the absolute magnetic pressure is almost identical by using the same load energy. This is important for future investigations. So it will be possible to generate an even spreading of magnetic pressure all over the working area of the field former by arranging the holes in the working area in a certain kind of way.

References

[1] *Friedrich, H.-E.:* Leichtbau und Werkstoffinnovationen im Fahrzeugbau. Automobiltechnische Zeitschrift - ATZ 2002, B. 104, H. 3, pp. 258 – 266.
[2] AUDI AG, 2004.
[3] Jaguar Ltd., Bromswick, U.K., 2004.
[4] Salzgitter Magnesium-Technologie GmbH, 2004.
[5] *Dröder K. G.:* Untersuchungen zum Umformen von Feinblechen aus Magnesiumknetlegierungen. Dissertation Universität Hannover 1999.
[6] *Winkler, P.-J.; Kellerer, H.:* Metallische Leichtbau-Werkstoffe für die Verkehrstechnik - Stand und Perspektiven Tagungsband zum Symposium Materialforschung - Neue Werkstoffe, 02.-04. November 1994.
[7] Fraunhofer Institut Werkstoffmechanik, Magnesium - Leichtbauwerkstoff im Automobilbau, Jahresbericht 1999.
[8] Neue Züricher Zeitung - Forschung und Technik, Nr. 87, 12.04.2000.
[9] Salzgitter AG, 2003.

[10] *Mertz, A.:* Karosserie-Strukturen aus Strangpressprofilen und Mg-Druckguss Tagungsband zum Seminar “Fortschritte mit Magnesium im Automobilbau“. Bad Nauheim, 11./12.02.1999.

[11] *Wilkinson, R. G.; Winter, D. B.:* Deep Drawing and Pressing of Magnesium Alloy Sheet, Sheet Metal Industries, 15 (1941) 8, pp. 1039 – 1042.

[12] *Bach, F.-W.; Kuhlmeyer, A.; Rossberg, A.; Schäperkötter, M.; Schaper, M.; Weber, J.:* Moderne Blechwerkstoffe für die Automobilindustrie; ein Vergleich. 10th Saxon Conference on Forming Technology SFU 2003 „International Conference on Accuracy in Forming Technology”. Fraunhofer Institut Werkzeugmaschinen und Umformtechnik (IWU) Chemnitz 2003, Tagungsband.

[13] *Daehn, G. S.:* Moderne Blechwerkstoffe für die Automobilindustrie; ein Vergleich. 10th Saxon Conference on Forming Technology SFU 2003 „International Conference on Accuracy in Forming Technology”. Fraunhofer Institut Werkzeugmaschinen und Umformtechnik (IWU) Chemnitz 2003, Tagungsband.

[14] *Alf, F.:* DE 1 157 320: Verfahren zur Verminderung der bei der Metallumformung durch Magnetfelder erforderlichen Kräfte. (1962) Deutsche Edelstahlwerke AG.

[15] *Lebedew, G. M.; Wislowa, L. S.; Isarowitsch, G. Z.; Skorobogatow, M. S.; Dmitriew, W. S.:* Technologische Kenndaten des Biegeumformens und Abkantens beim Magnetimpulsstanzen von erwärmten Werkstücken aus Magnesiumlegierungen. Kusnetscho-Schtampowotschnoe, N4, 1982, pp. 18 – 20.

[16] *Blevj, I. W.; Gorkin, L. D.; Himenko, L. T.:* Verformung von Metallen durch Impulsmagnetfelder mit erwärmten Werkstücken. Kusnetscho-Schtampowotschnoe, N7, 1984, pp. 6 – 8.

[17] *Uhlmann, E.; Hahn, R.:* Pulsed Magnetic Hot Forming of Magnesium Profiles. Production Engineering – Research and Development, Vol. 10, Issue 2, WGP e.V., Braunschweig 2003, pp. 87 – 90.

[18] *Uhlmann, E.; Hahn, R.:* Werkzeuge zur impulsmagnetischen Warmumformung. Fachtagung “Elektrische Energiewandlungssysteme”, 13. bis 14. März 2002, Otto-von-Guericke-Universität Magdeburg, pp. 277 – 282.

New Achievements in the Field of Impulse Processing Technologies

V. Vovk[1], V. Sabelkin[2]

[1]Otto-Von-Guericke University Magdeburg, Germany
[2]Instituto Mexicano del Petroleo, Mexico

Abstract

The outcomes of research in the field of application of high pressure in a process engineering are stated. The high pressure is created by impulsive sources of energy, such as explosion of condensed explosive substances and gaseous detonatable mixtures.

Application of high pressure created by explosion for technological processes of sheet forming parts from metal and non-metal materials is considered. In the latter case, the mechanical properties in the process polymerisation of composite materials in the outcome of the impulsive loading significantly rise. The impulsive high pressure has a significant impact on handling - compressing of powder materials, on manufacture of special products, foundry forms and ont destruction of rods in molten products.

Keywords:

Explosive forming, Impulse forming

1 Introduction

The review of existing methods of high impulse pressure deriving and practice of their technological application is given in the present work. The outcomes of an application of rigid and gaseous charges explosion for leaf forming of details and also for compaction discrete materials are stated. It is shown that a great expanding of the given technologies possibilities is possible at the expense of special dynamic effects. The use of impulse power sources is expedient for complicated items, which manufacturing by traditional methods is hardly hampered or generally is impossible.

2 High-Speed Processes

Various kinds and sources of energy are used for the realisation of technological processes of high-speed materials processing (Figure 1). With their help, impulses of high pressure with specific amplitude-temporary performances are received.

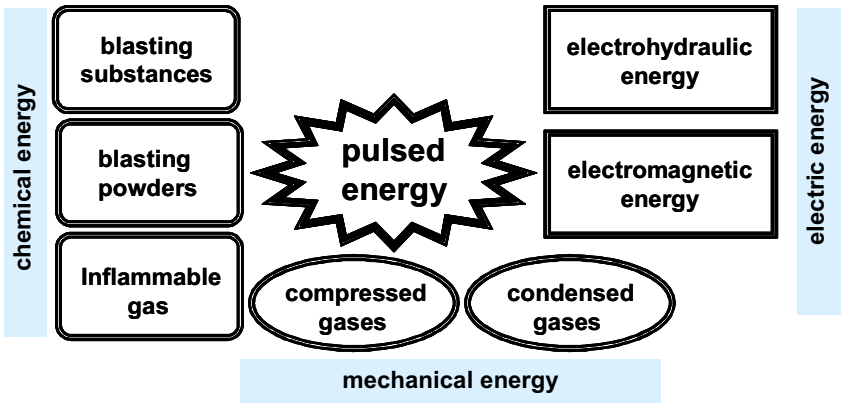

Figure 1: *Sources of impulse energy*

Blasting explosive substances was received the greatest application for the technological purposes. These substances have the highest specific accumulated energy. Depending on performances of impulse, the explosion can be used for the form modification, separation of a material, items mounting, covers plotting, and modification of materials properties (Figure 2)

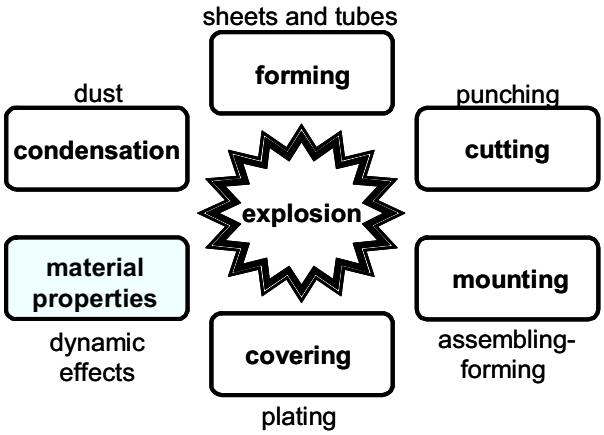

Figure 2: *Areas of explosion energy use*

The impulses of high intensity (explosion) are effective in operations of separation and over modification of materials properties (synthesis). For shaping operations try to use impulses with slanting performances. These impulses receive by damping explosive waves of pressure or by application of gaseous power sources.

3 Technologies of Explosive Forming

The schematic diagrams of explosive forming of a sheet details (Figure 3) and pipes (Figure 4) give submission about some variants of the process.

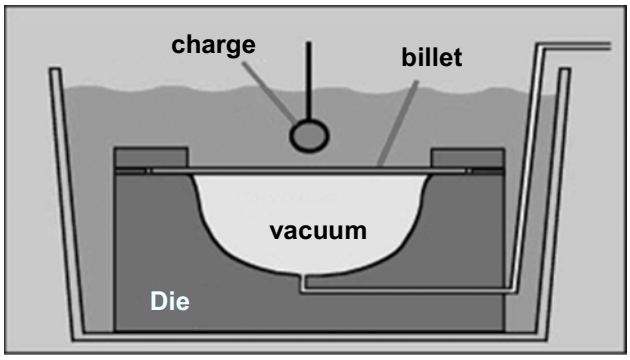

explosive forming of sheet metals

Figure 3: *Schematic diagram of leaf formings by explosion*

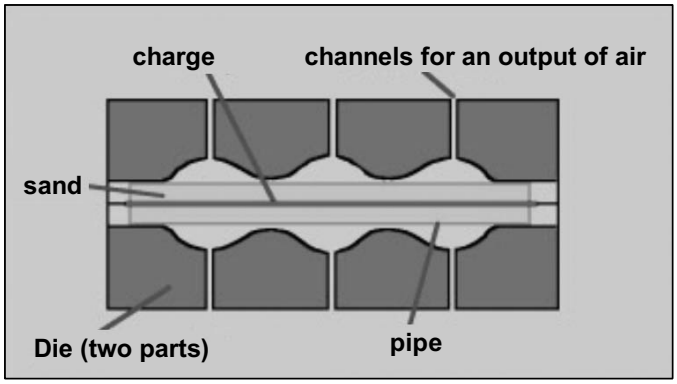

explosive forming of pipes

Figure 4: *Schematic diagram of pipes dispensing by explosion*

The charges of the simplest forms, such as spherical (Figure 3) or linear (Figure 4), are usually used, though for details with a local relief the application of complicated three-dimensional charges and certain sequences of their initiation (Figure 5) is justified.

Figure 5: *The complicated form charge in micropool to be destroyed*

The transmitting medium is as a rule liquid (Figure 3, 5) or discrete (Figure 4). Technical water is used as a liquid medium, and wetted sand is mainly used as a discrete medium. Other types of transmitting media, for example jelly-like and elastic, allow to control impulse performances over a wide range, however their application is limited because of a high seller's price and low stability.

Explosion forming is realised in stationary pools (Figure 6), in reusable pools (Figure 7), or in micropools to be destroyed (Figure 5).

Figure 6: *Stationary pool for explosion forming*

Figure 7: *Reusable microtank*

A main advantage of explosive forming is the use of simplified cheaper equipment. Equipment made of concrete, raw-wood, plaster, or simple-work alloys is widely used in practice of explosive forming. The surface quality of an equipment can be improved at the expense of covers from plastic masses and easily be changed on intermediate transitions by use of inserts from plasticines (Figure 8).

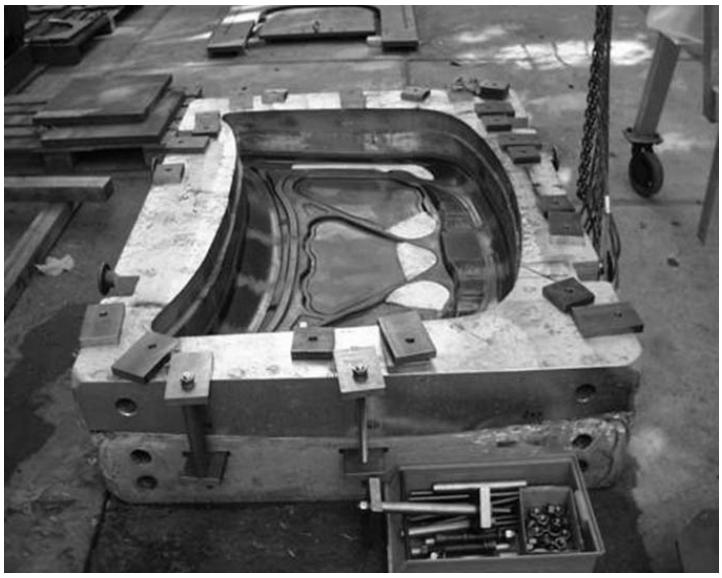

Figure 8: *An example of an equipment for explosive forming*

4 Outcomes

As a rule, explosive forming is effectively applied in small-scale and single production of details for a chemical mechanical engineering, power, aircraft building, and space technology.

Figure 9: *Details made by explosive forming*

The explosion forming gives good outcomes in the prototype manufacturing in the motor industry, too. The application of the simplified equipment, the possibility of forming of a different thickness billets from various materials on the same equipment is especially attractive to the designers which are developing new models of cars.

Figure 10: *The prototypes of details for motor industry*

Apart from traditional cold explosion forming, works on hot sheet metal details forming from low-ductile titanium alloys are conducted. By combined effect of dynamic pressure and thermal effects it is possible to receive details with unique properties.

Figure 11: *Details from low-deformable alloy stamped in a hot condition by explosion*

The experimentally established effects of significant increase of titanium alloys plasticity show that the phenomenon of "superplasticity" is exhibited not only over very small, but also over high velocities of a strain.

5 Alternative Power Sources

Despite of all advantages mentioned above, the application of blasting explosive substances is connected to special safety requirements. Therefore, impulse technologies based on alternate power sources, such as compressed gases and combustible gas mixtures, develop still faster. The use of combustible and compressed gases is possible in usual industrial conditions, though realised impulses are lower than over explosion. Within the framework of the programme DFG research of hydroimpulse forming processes, which is the perspective for the introduction under traditional production is carried out [1] During hydroimpulse forming the pressure in a transmitting medium forms by impact of the previously dispersed skew body. A schematic diagram and appearance of a unit for hydroimpulse forming are shown in Figure 12.

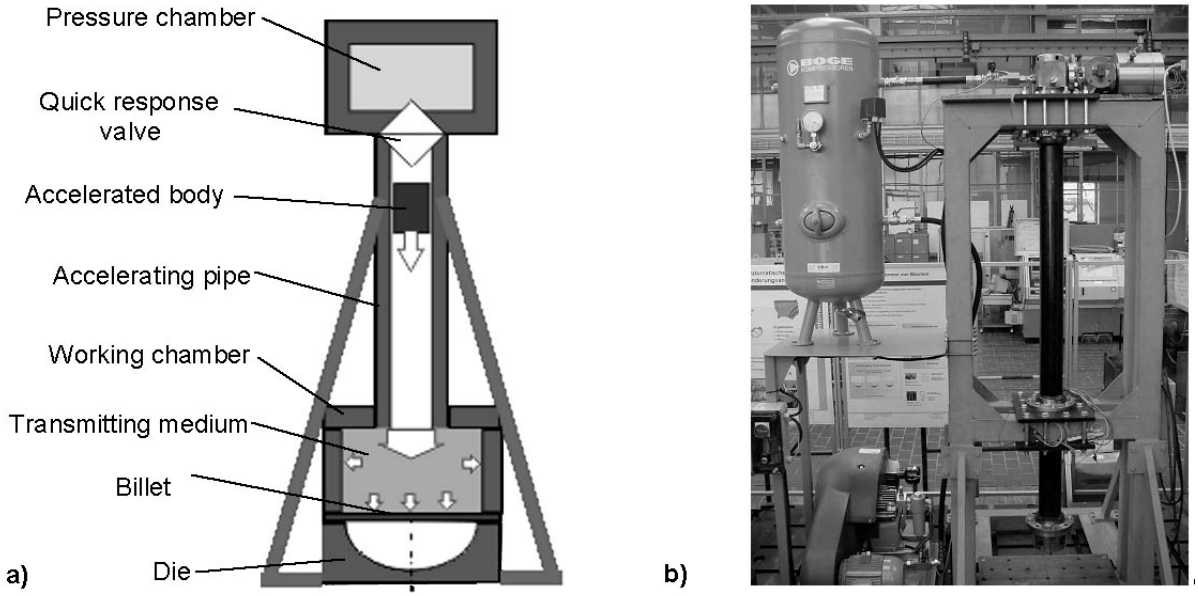

Figure 12: *Schematic diagram a) and appearance b) of a unit for hydroimpulse forming*

The hydroimpulse forming is effective for manufacturing small dimensions details with open (Figure 13) and closed (Figure 14) outlines.

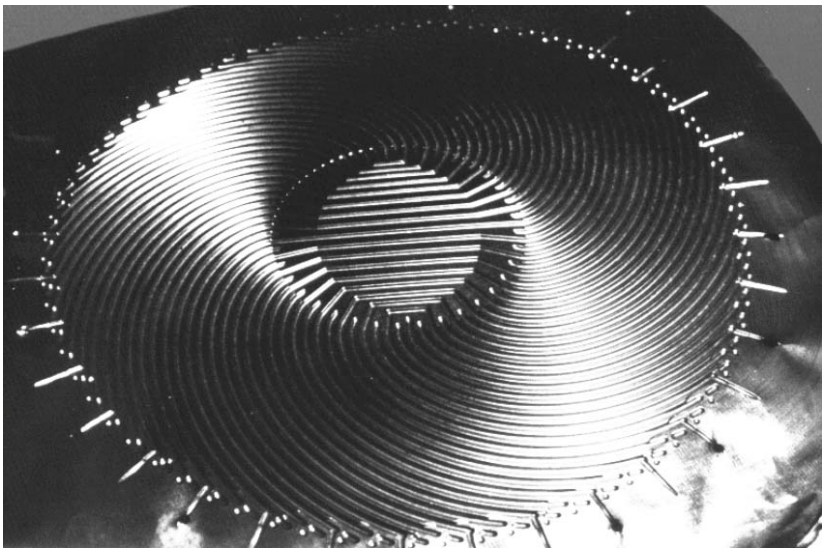

Figure 13: *A details of the heat exchanger*

Figure 14: *An equaliser*

Other rather perspective source of impulse energies are the combustible gas mixtures. Possessing lower denseness of energy and velocity of a detonation than blasting explosive substances, the mixtures of combustible gases are optimum for forming shaping operations and compaction of powders (see [2,3] for more details).

The equipment for forming gas-explosive (Figure 15) can be used in a usual technological cycle, and the process is easily automised.

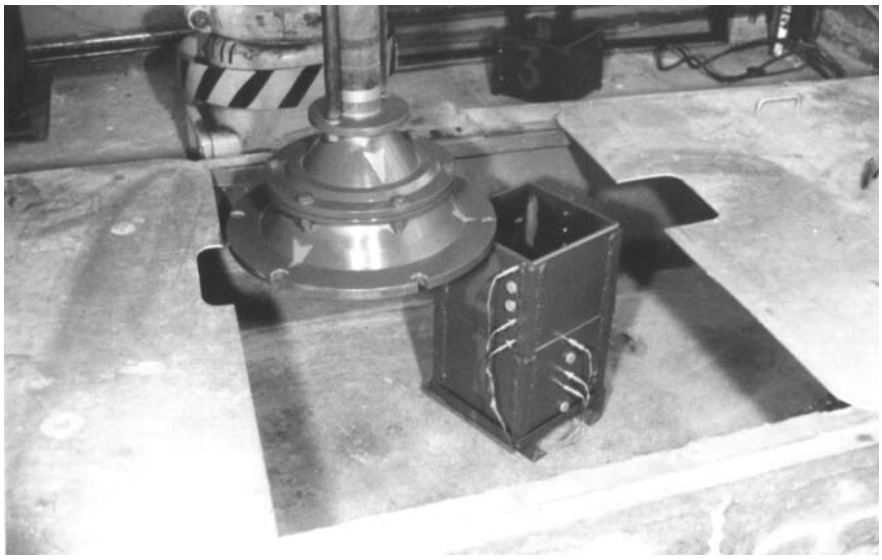

Figure 15: *An example of the equipment for gas-explosive forming*

6 Calculation of Impulse Forming Parameters

The approximate calculation of impulse forming parameters is carried out on the basis of a power technique for a required charges and explosion distances evaluation [4]. The detail FEM-account with allowance of material dynamic characteristics, thermal effects, inertial forces, friction over high velocities, and also cavitational and wave effects in a transmitting medium is executed with the help of the AUTODYN programme [5]. All main objects of a technological circuit (a detail, billet, technological process, equipment, and equipment) are analysed, too.

7 Conclusions

The impulse forming has the greatest advantages in manufacturing of the prototypes and single items, whose production by traditional methods is complicated or impossible. The dynamic character of a behavior of forming process results in origin of special effects, which can be used for rising deforming ability of used materials. The use of various power sources allows to select the optimal impulse in correspondence with technological process.

References

[1] *Vovk, V. Stroppe, H. Taran, V.:* Untersuchungen zum Duktilitaets- und Festigkeitsverhalten ausgewaehlter Staehle und Al-Legierungen bei hohen Deformationsgeschwindigkeiten. In Tagungsband Elektodynamisches Impulsumformen. Dortmund 2001.

[2] *Sabelkin V.P., Krivtsov V.S.:* Concept of Development of Technological Processes for Aerospace Equipment Parts Manufacture with Application of Impulsive Sourses

of Energy. - Proc. IV Ukraine-Russia-China Symp. on Space Sci. & Techn., Kiev, Sept. 12-17, 1996, Vol.2, p.639.

[3] *Sabelkin V.P., Borisevich V.K., Vovk V.T.:* Industrial Application of Impulsive High Pressures in Sheet Forming with Parameters Optimization. - Proc. XI Int. AIRAPT Conf. on High Pressures in Engineering and Science, Kiev, 1987, Vol.3, p. 299-301

[4] *Herold, K.P. Vovk, V. Taran, V. Vovk, A.:* Explosive forming of high-strength sheet material. 10-th International conference Sheet Metal, Ulster, E; 14-16. April, 2003

[5] *Vovk, V. Taran, V. Vovk, A.:* Hidro-impulse forming of sheet metals. VI International Forging Conference Metal forming. 23 – 24 Oktober 2002. Gramado – RS, RS Brasil, S. 158-162.

Methods of Increase of Ductility in Explosion Shaping of High-Strength Sheet Material

V. Vovk, V. Taran, A. Vovk

Otto-Von-Guericke University Magdeburg, Germany

Abstract

The outcomes of research on the increase of ductility of low-ductile materials are indicated in this work. Dynamic effects of increase of materials ductility and special technological methods are used to obtain by a method of explosive forming high-strength details. On the one hand, these methods are based on the increase of stability of the shaping process. On the other hand, they are based on the use of mass forces for additional submission of a material from a flange. The features of explosive forming also allow for an effective application of a universal equipment with special inserts from plastic mixture.

Keywords:

Explosive forming, Impulse forming

1 Introduction

The decrease of weight with simultaneous increase of automobile and aircraft details strength and reliability requires a more and more broad use of the new complicated form constructions from high-strength materials. The high-strength materials have as a rule deferred ductility, which makes the manufacturing of the details with complicated geometry by traditional methods difficult. The problem is decided by the application of forming during some transitions with intermediate thermal treatments, or by the application of methods of forming in a hot condition. Both variants essentially complicate technological process and increase its cost. Besides sheet materials with the previously created stratified structure the heat up to the temperature of the transformation phase is unacceptable. For prototypes and small series manufacturing the method of explosive forming offers new possibilities and technological methods.

2 Technological Methods

It is known that a number of materials, including high-strength ones, shows on high velocities large ductility [1]. The increase of ductility is observed in the limited range of deforma-

tion velocities. The further velocity increase again results from the material blistering. Therefore, it is very important during the designing of technological process not only to take into account dynamic material properties instead of a static one, but also to correctly select a velocity of loading. The velocity of loading is determined by a type of a source of impulse energy used (Figure 1) and by the amplitude-time characteristics of the impulse (Figure 2).

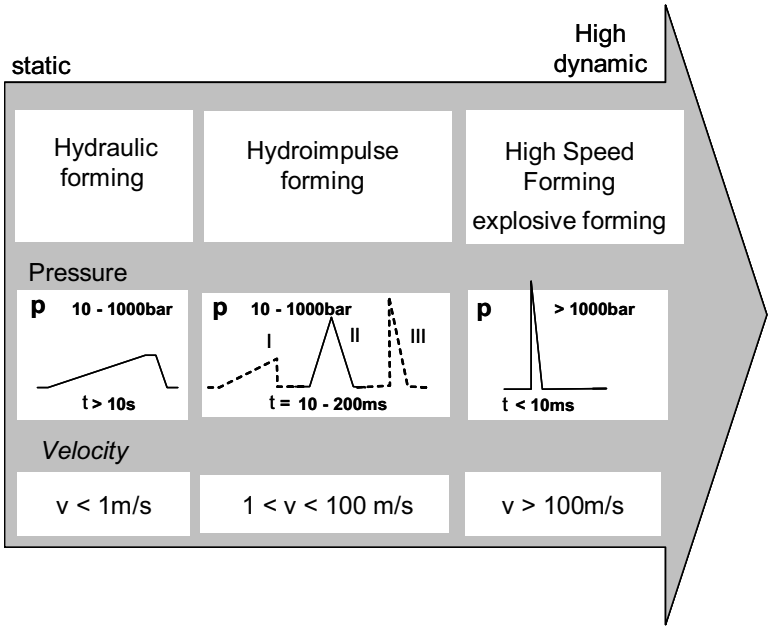

Figure 1: *Systematisation of impulse power sources*

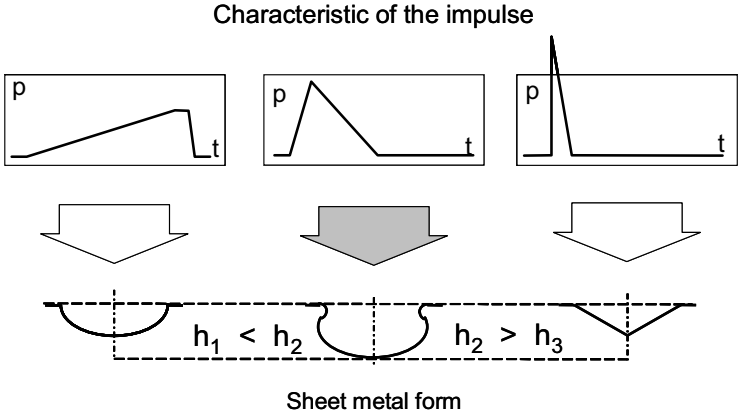

Figure 2: *Influence of impulse characteristics*

When an optimum velocity of deformation is selected it is possible to realise a deep draw-forming of details from materials which are difficult to deform during one technological transition (Figure 3).

Figure 3: *The reservoir from a material Dual-Stahl RVS 1.4462 stamped by explosion (size 280 x 380 mm; 1,8 mm thickness)*

Despite of a high velocity of a strain and connected to it local heating of a material, the initial stratified structure is saved in a material down to destruction during of large plastic deformations (Figure 4).

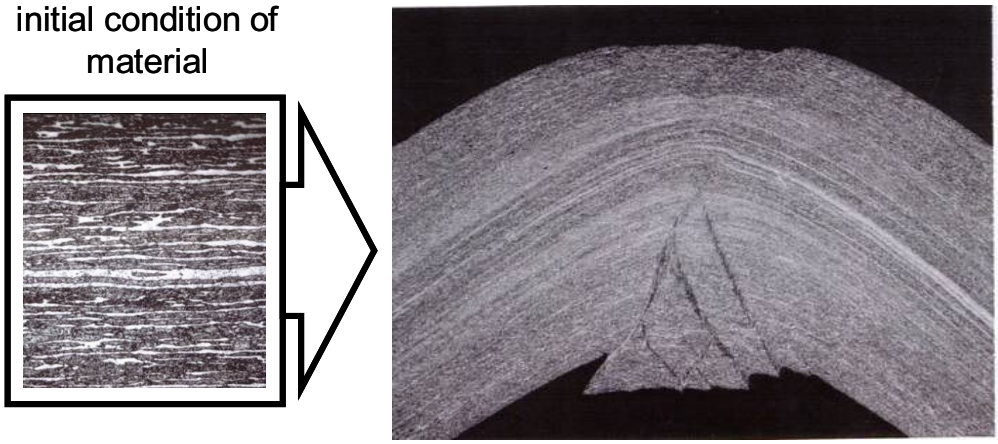

Figure 4*: A structure of a material RVS 1.4462 before and after explosion forming*

During the explosion forming a problem of dynamic loss of stability and formation of tucks acquires special significance. For providing a stable high-strength material shaping, it is necessary to create very large stretching gains in a sheet. If it fails to be made with the help of traditional methods there is the need to resort to special technological methods. Made-up closure of a billet outline with the purpose of increasing its stability is one of them. This method means that the nonclosed flat shells are stamped pairwise, using the billet of the closed cylindrical form. In Figure 5 the example of a flat shell with a radius of a curvature 6,5 m from a high-strength material GLARE® is shown. This material is a stratified aggregate from aluminium A2024 reinforced by fiber glass. Its deformation by traditional methods is very hard.

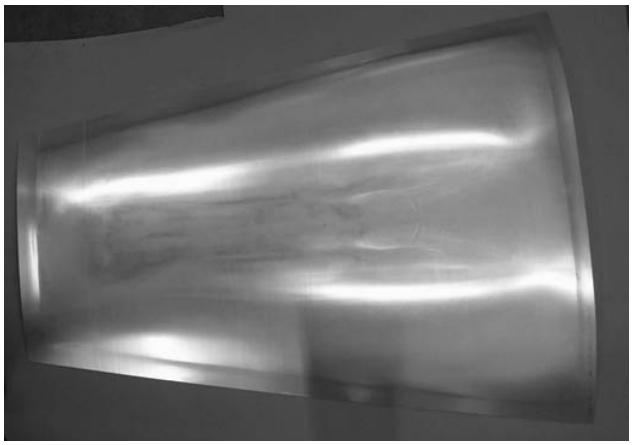

Figure 5: *A flat shall from a material GLARE®*

For manufacturing such details it is expedient to use a method of made-up closure of an outline. The billet for simultaneous forming of several details represents the cylinder. After dispensing the cylindrical billet by explosion in an equipment (Figure 6) and deriving of a preformed material, the details of a double curvature can be cut out from it.

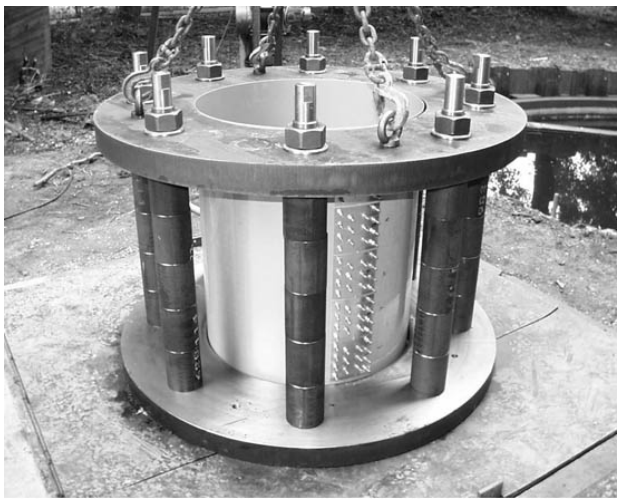

Figure 6: *A closed outline billet and equipment for its dispensing by explosion*

The given technological method is used for forming flat details from very thin sheets. It is effective for holding of free flanges of billet and prevention of crimps formation.

During the manufacturing of details with large depth of s relief, the high-strength material reaches the limit of its deformable abilities. The depth of a relief as a rule is unequal and hardly located. Therefore, simultaneously with a shortage of material in the most deep places there is a problem of "wasting material " in places with small depth of a relief. The technological methods indicated below are directed on the control of a material streaming during an explosion forming.

The method of made-up breaking of an outline and forming of the closed details from billets of the nonclosed form is used for dispensing of rigid envelopes and profiles when material is insufficient for a full detail's molding. The ring frame (Figure 7) is formed by explosion from a nonclosed billet with an overcloak of an additional material.

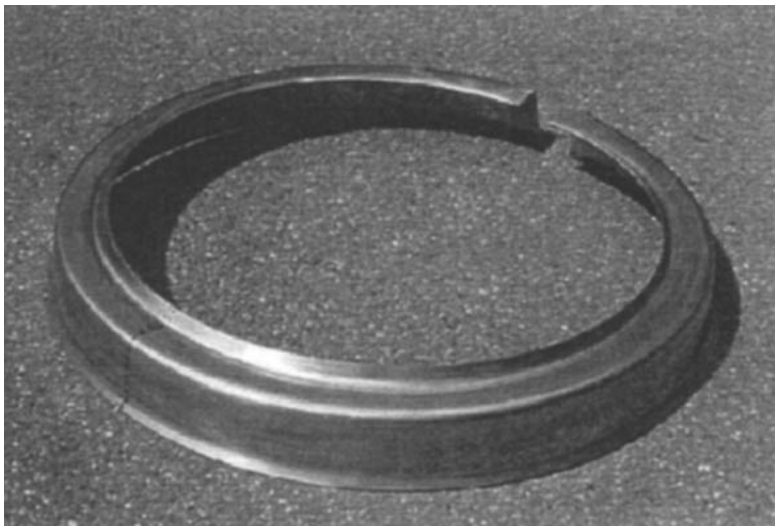

Figure 7: *A ring frame from a material A2024 T3*

The method of a forced gathering of a material on an additional relief will be realised with the help of special inserts in a technological equipment (Figure 8). During the explosive forming these inserts can be executed from soft ductile materials due to a high velocity of deformation. They save the form during of impact with billet and deform it. The inserts are deleted on consequent technological transitions. Gathered on inserts the additional material is used for a main contour shaping.

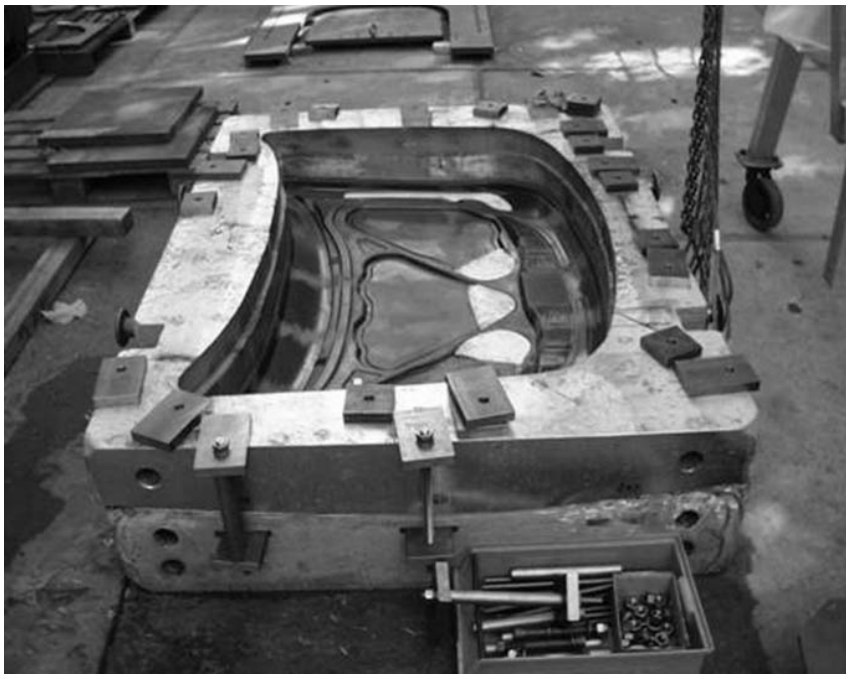

Figure 8: *An equipment for explosion forming with technological inserts from plasticines*

The dynamic character of details deformation during the explosion forming allows to use a technological method that is specific only for high-speed processes. pressure of explosion and force of friction about an equipment The dispersed up to large velocities billet as a whole and its separate sites are acted by explosion pressure and force of friction about an

equipment together with the mass forces. The mass forces are used for additional pushing of a flange (Figure 9) and thus for improving the conditions of deformation [2].

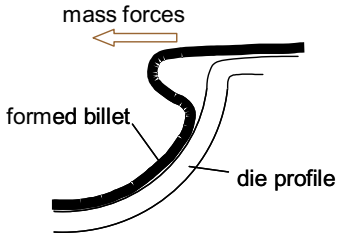

Figure 9: *The scheme of submission of a flange at the expense of mass forces*

At the expense of the given technological method use it is possible to obtain details of the unique form for one technological transition (Figure 10).

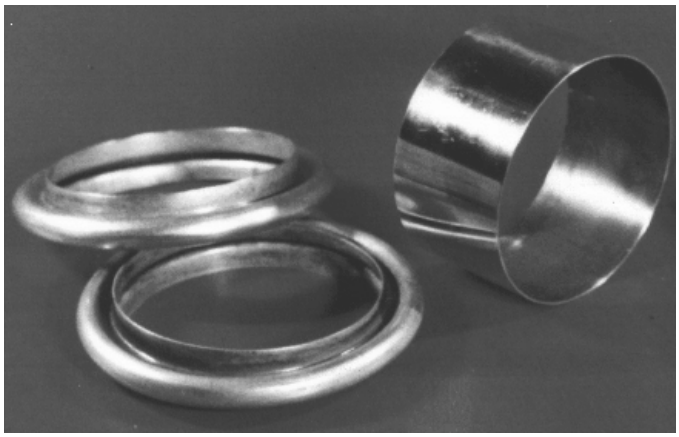

Figure 10: *An equaliser of a torus form obtained from cylindrical billet*

3 Conclusions

The use of special technological methods during the explosion forming allows to expand the possibilities of a technique and mould complicated details from high-strength materials successfully. The optimum selection of amplitude-time performances of an impulse provides the maximum use of the materials deformation ability. The additional stretching gains are created and stability of the shaping process is increased by the closing an outline of sheet billet. Thus, it is possible to stamp details of a very small curvature. The redistribution of a material in correspondence with the depth of a detail's relief is achieved by special inserts and control of a field of a load.

References

[1] *Herold, K.P. Vovk, V. Taran, V. Vovk, A.:* Explosive forming of high-strength sheet material. 10-th International conference Sheet Metal, Ulster, E; 14-16. April, 2003

[2] *Vovk, V. Taran, V. Vovk, A.:* Hidro-impulse forming of sheet metals. VI International Forging Conference Metal forming. 23 – 24 Oktober 2002. Gramado – RS, RS Brasil, S. 158-162.

SESSION 4

TOOLS & EQUIPMENT

Optical Position and Time Resolved Measurement of Magnetic Field Distribution in High Speed Metal Forming

R. Merte, D. Peier, J. Teunissen

Institute of High Voltage Engineering, University of Dortmund, Germany

Abstract

In the area of the position and time resolved measurement of the magnetic field distribution in small gaps between workpieces and coils in high-speed sheet metal forming optical sensors are predestined to be integrated into the very small geometries of experimental setups.

Optical sensors for current measurement based on the magneto-optic Faraday effect are well known for a long time. This effect can also be used for the direct measurement of magnetic fields. For the use in electromagnetic high-speed metal forming applications, only very small field probes are probable. The measurement of axial symmetric fields can be achieved with two connected fibres with different Verdet constants. They solve the problem with the not given measurement value, which occurs by the use of only one fibre because of its closed integral domain. A continuous time signal of the magnetic field can be calculated for discrete regions.

Likewise, it is possible to employ miniature fibre-optic magnetic field point sensors for the field determination in the gap of an electromagnetic high-speed forming device. It is necessary to examine the influence on the polarisation state and the intensity of the light in a fibre. There are two different sensors shown in this paper. One is based on a piece of flint glass fibre spliced between two polarising fibres, and the other sensor arrangement consists of two glued SiO_2 blocks.

A workbench for assembling of fibre-optic sensors using the splice technology has been constructed and will be presented.

First trial measurements of the magnetic field, compared to the causing current, show the functionality of these kinds of optical sensors and are discussed under the aspect of optimisation.

Keywords:

Miniaturization, Probe, Optical Fibre Sensor

1 Introduction

The use of optical sensors is of high interest in the area of the position and time resolved measurement of the magnetic field distribution in small gaps between workpieces and coils in electromagnetic high-speed metal forming devices. Among the typical advantages, like an inherent potential separation, they offer the possibility of integration into places with very small geometric boundary conditions.

Electromagnetic high-speed metal forming, e.g. for the use in the automobile industry, is an excellent method for forming a lot of materials, like alloys, which cause problems in classic low speed processes. The principle of a sheet metal forming device consists of a large capacitor bank, which gets loaded to a voltage of between 5 kV and about 20 kV. The charged capacitors are connected by a high-speed switch to a flat coil with a small amount of windings. The resulting transient current in the work-coil has an amplitude of some 10 kA and induces eddy currents in the workpiece. The result of the interaction of these currents is a force which accelerates the workpiece extremely fast and forms it in some microseconds.

Although electromagnetic forming is widely used for cylindrical forming the mechanisms in high-speed sheet metal forming are not well investigated up to now. For modelling this process, it is desirable to get information about the position- and time resolved distribution of the magnetic field in the gap between the workpiece and the forming coil during the forming process. This gap is given by the insulation foil which is needed because of the very high electrical field strength between workpiece and coil. Because of the small gap and the high field strength the use of small potential free optical sensors is compulsory.

2 Current measurement by use of Faraday effect

Fibre optic current sensors are well known for a long time [1]. They use the magneto-optic Faraday effect, whose functional principle is illustrated in Figure 1.

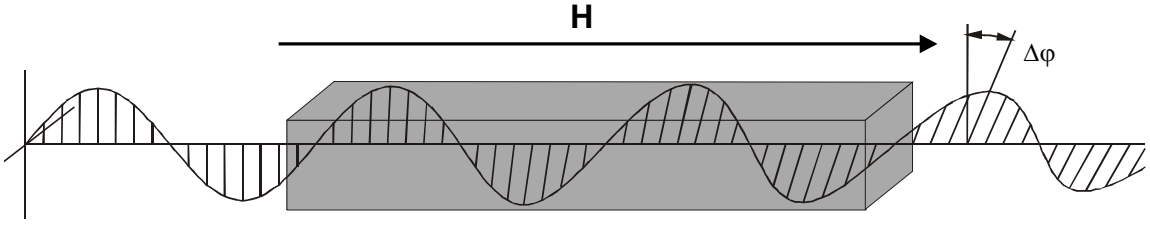

Figure 1: *Functional principle of Faraday effect*

An applied longitudinal magnetic field induces circular birefringence in the optical material. Therefore, a linear polarised light wave, propagating through the material, will receive a change in its polarisation angle $\Delta\varphi$ according to Equation 1, where k_V is called the Verdet constant.

$$\Delta\varphi = k_V \int_{c(\vec{s})} \vec{H} d\vec{s} \tag{1}$$

The Verdet constant of typical standard fibres is about $4.6 \cdot 10^{-6}$ A^{-1}. Special fibres can reach much higher sensitivities (flint glass fibre at 820 nm: $2.1 \cdot 10^{-5}$ A^{-1}). If a closed loop with n windings is formed around a conductor the resulting angle is proportional to the current in the wire (Equation 2).

$$\Delta\varphi = k_V \cdot n \cdot I \tag{2}$$

With an appropriate test setup and evaluation unit a potential free current sensor with high immunity against electromagnetic interference can be realised. Measurements of high impulse currents with such a device are shown in Figure 2.

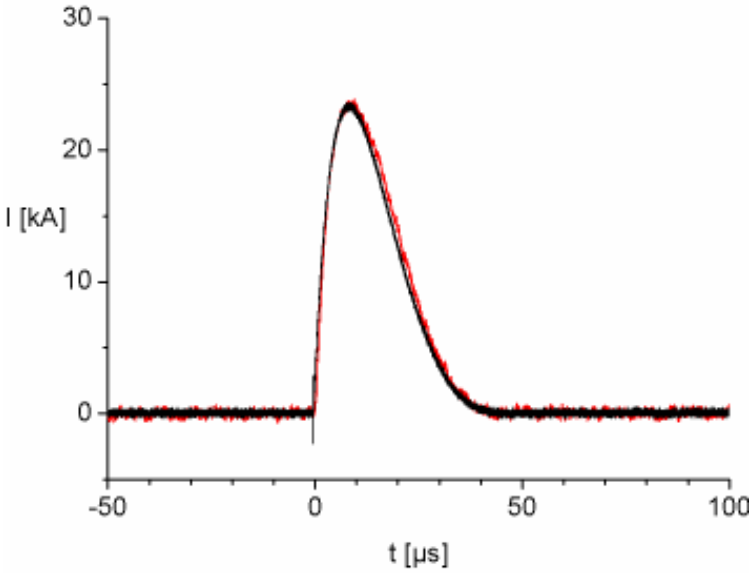

Figure 2: *Conventional and fibre-optic impulse current measurement at an optimised high current source [2]. The curves match within line width*

As an optimised shunt is used for comparison, there is no visible difference between the optical and the conventional measured signal.

3 Position resolved measurement of a symmetrical magnetic field with a distributed fibre sensor

Besides the standard application of current measurements the Faraday effect can also be used for direct measurements of magnetic fields. The time and position resolved field distribution between a workpiece and the windings of the coil of an electromagnetic high speed metal forming device is of special interest as it is the source for the resulting forces during the forming process. Regarding the electromagnetic and dimensional conditions at a typical setup (Figure 3) only non-conductive miniature field probes are applicable.

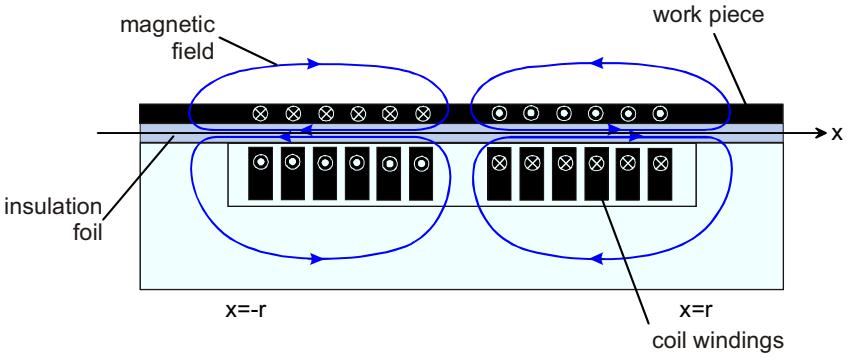

Figure 3: *Field configuration of a setup for electromagnetic high-speed metal forming. The insulation foil has a thickness of 600 µm, the radius r is 35 mm*

Measurements with only one fibre put into the gap would only give a time dependant integral value of the axial component of the magnetic field, but not a position resolved measurement. An axially symmetric magnetic field (Equation 3) would not even give a measurable value because of the compensating terms within the integral (Equation 4).

$$H_x(x) = -H_x(-x) \tag{3}$$

$$\Delta\varphi = \int_{-r}^{r} H_x(x)\cdot dx \cdot k_V = \int_{0}^{r} -H_x(x)\cdot dx \cdot k_V + \int_{0}^{r} H_x(x)\cdot dx \cdot k_V = 0 \tag{4}$$

Connecting two fibres with different Verdet constants (Figure 4) could solve this problem, so that the field's effect on one part of the sensor fibre is not fully compensated by the other part.

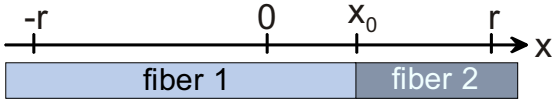

Figure 4: *Composite fibre sensor with different Verdet constants*

In a perfect symmetric magnetic field, where the axial component propagates along the fibre and is restricted to the area inside the coil (i.e.± r), it is possible to get a position and time resolved information about the magnetic field strength by pulling the fibre through the field along the x-axis (Equation 5).

$$\Delta\varphi = \int_{-r}^{x_0} H_x(x)\cdot dx \cdot k_{V1} + \int_{x_0}^{r} H_x(x)\cdot dx \cdot k_{V2} = \int_{x_0}^{r} H_x(x)\cdot dx \cdot (k_{V2} - k_{V1}) \tag{5}$$

The local resolution is determined by the distance between two measurement points as illustrated in Figure 5.

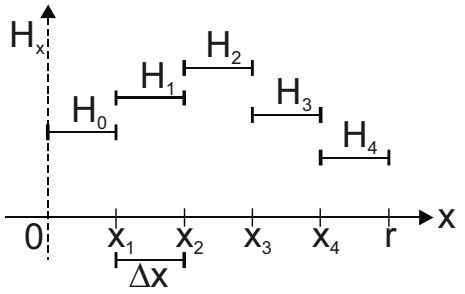

Figure 5: *Principle of field distribution with discrete values*

For a simple calculation of the respective fields, consecutive measurements beginning at the edge of the coil (here x_4) have to be carried out. The time and position resolved field distribution follows Equation 6.

$$\Delta\varphi = \int_{x_4}^{r} H_x(x) \cdot dx \cdot (k_{V2} - k_{V1}) = H_4 \cdot \Delta x \cdot (k_{V2} - k_{V1}) \Leftrightarrow H_4 = \frac{\Delta\varphi}{\Delta x \cdot (k_{V2} - k_{V1})}. \quad (6)$$

The values for the next step (here x_3) depend on the new measurement and the previously calculated field strengths (Equation 7).

$$\Delta\varphi = H_3 \cdot \Delta x \cdot (k_{V2} - k_{V1}) + H_4 \cdot \Delta x \cdot (k_{V2} - k_{V1}) \Leftrightarrow H_3 = \frac{\Delta\varphi}{\Delta x \cdot (k_{V2} - k_{V1})} - H_4. \quad (7)$$

So, a continuous time signal of the magnetic field can be calculated for discrete regions. In case of a not perfect axial symmetrical field this method would only give approximated values, thus a miniature magnetic field point sensor would be advantageous.

4 Miniature fibre-optic magnetic field point sensors

There are several optical point sensors suggested in the literature, but none of them is usable in the special case of field determination inside the small gap of an electromagnetic high-speed forming device because of their saturation field strength (about 20 Tesla have to be measured) or dimensions. Nevertheless, the functional principle keeps the same, similar to that of the current sensor. Linear polarised light is entering a sensitive fibre or crystal with a defined angle and is subject to circular birefringence. After passing through the optic material, the rotation of the polarisation angle is converted into a variation of the light's intensity.

The polarisation state in standard multimode fibres is affected by the magnetic field. As the magnetic field is not restricted to the area between the coil-windings and the workpiece, stray fields at the edge of the coil have to be taken into account as well. Hence, special precaution is necessary for the connection of the sensor itself with the light source and the photoreceiver. Preliminary investigations show that the polarisation state and the intensity of light is not affected by a magnetic field if a special polarising fibre is used. Another possibility is to use a depolarised light source and polarising surfaces at the sensor's boundaries.

The dimensions of the sensing fibre/crystal are of special interest as they determine the local resolution of the sensor on the one hand, and its implementability on the other. Microscope photos from two assembled sensors are shown in Figure. 6.

a)

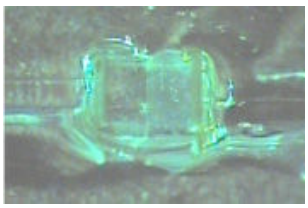

b)

Figure 6: *Miniature magnetic field sensors. a) Multimode fibres (200/220 µm SiO_2) with glued crystals (1 mm × 500 µm SiO_2) with polarising surfaces. b) Polarising fibres (3M FS-PZ-4611) with spliced piece of flint glass fibre (HOYA LBF-850, 1 mm long) and protective cover*

One sensor consists of two crystal blocks with an edge length of 500 µm each. Both blocks have a polarising surface glued to a multimode fibre. The other sensor consists of a small piece of flint-glass fibre which is spliced between two polarising fibres.

5 Assembling of polarimetric fibre sensors

As the mode field diameter of a single mode fibre at 820 nm is about 6 µm, it is very difficult to connect two fibres with minimal loss. Only the use of splicing technology seems to succeed. If polarising or polarisation maintaining fibres are used they have to be spliced with defined angles in addition. Consequently, a workbench had to be constructed which makes it possible to build polarimetric fibre sensors with suitable effort (Figure 7).

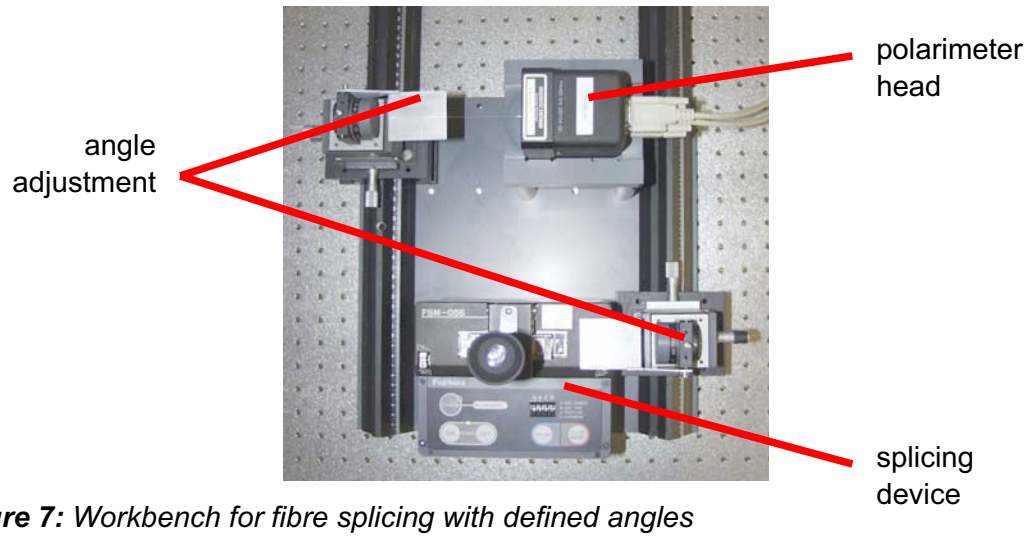

Figure 7: *Workbench for fibre splicing with defined angles*

A left and a right rail carry rotateable holding fixtures which guide the end of a fibre. The fibre is placed in front of a computer-controlled polarimeter. The holding fixture can be rotated until the desired orientation is indicated by the polarimeter. After that, the holding fixture is moved to the splicing device where the fibre end will be fixed. After translating the polarimeter, the same procedure is repeated for the other fibre end.

6 First field measurements

First trial measurements of the magnetic field have been carried out with the described flint glass fibre sensor at a device for electromagnetic high speed metal forming. The sensor has been placed in the gap between the coil and an alloyed workpiece. The recorded signals are presented in Figure 8.

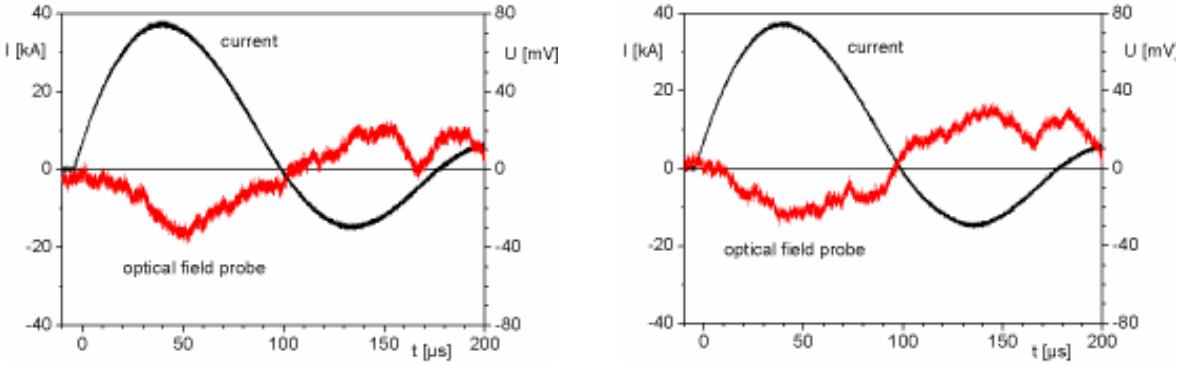

Figure 8: *Measurements of the magnetic field in the gap between a fixed workpiece and the coil of an electromagnetic high-speed metal forming device (Maxwell Magneform 7000) with the sensor from Figure 6b at position x = 20 mm*

Due to the high field strength the sensor could not be calibrated before, so only the measured voltages from the evaluation unit are given. The transient current, which is conducted through the coil, causes a magnetic field. Together with the induced eddy currents in the workpiece a resulting field configuration is generated as indicated in Figure 3. Hence, the pattern of the magnetic field signal does not have to be equal to the applied current which is shown in Figure 8, too. Since consecutive measurements show different signals the following reasons are taken under consideration: The field configuration might be very sensitive to small changes or mechanical coupling may disturb the sensor.

Restrictions to the sensor placement are given by the need to put a dielectric layer between the electrodes for electrical insulation and mechanical stability. An incorporated fibre cannot be moved unless there is a small gap with fluid or gas between the fibre's coating and the insulating foil. Another aspect is that fibre implementation has to be done with respect to vibration during metal forming. The fibre must not be exposed to strain or stress, as these components induce birefringence by their own. So an optimised mechanical setup is essential for further investigations with various optical sensors.

7 Conclusion

Miniaturised fibre-optic magnetic field probes are a promising technology for the experimental determination of the magnetic field in a 600 µm gap with an extremely high field strength. First measurements with a specially assembled sensor prove the principle functionality and show great potential for further research.

8 Acknowledgement

We would like to acknowledge the contribution of Mr. M. Willsch from the Siemens AG, who assembled some of the used sensors.

References

[1] *Helmig, C.; Peier, D.; Teunissen, J.:* Optical Current Sensor Using Two Flint Glass Fibers as Sensing Element. 14th International Conference on Optical Fiber Sensors. Venezia, Italy, 2000, p.520-523, SPIE Vol. 4185.

[2] *Kempen, S.; Peier, D.:* An optimized high current impulse source. 1st International Conference on High Speed Forming. Dortmund, Germany, 2004.

The Potential for Electromagnetic Metal Forming for Plane (Car Body) Components

R. Neugebauer, P. Blau, H. Bräunlich, M. Pfeifer

Abstract

Classical quasi-static technologies of sheet metal forming are not the only domain of the Fraunhofer Institute for Machine Tools and Forming Technology (IWU). It also delves into techniques for high-energy rate forming, such as gas generator technology, and it will be dedicating greater efforts to electromagnetic metal forming. Electromagnetic metal forming processes major potential for innovation and development in manufacturing car-body components since the benefits to be derived from this technique (such as extending the limitations of forming, enhancing spring back behavior, and delivering a high degree of flexibility in production) have this sector's key problems in mind.

The Fraunhofer Institute for Machine Tools and Forming Technology focuses its research on coming up with technology, tool and plant strategies suitable for manufacturing medium-sized and large car-body components. There are two technological directions that IWU targets in this field of research. First of all, given the existing technical and physical process constraints, it is studying the possibilities of large-scale and partial deformation since both directions are of importance for the targeted products. However, these two approaches have very different requirements for designing and tools. The first approach forms components without preforming. Several forming steps are required for mapping typical car-body component shapes either with serial workstations or a flexible tool system. The partial electromagnetic metal forming approach means using integrated plant components, i.e. combining conventional press equipment with a magnetic forming plant. This can tap a potential that encompasses the technological benefits mentioned above while hiking productivity and scaling down the expenditures for investing in equipment.

Keywords:

Electromagnetic metal forming, Sheet metal, Forming, Accuracy, Calibration, Deep drawing

1 Introduction

The car body is one of the most important components, meaning that it has a major bearing on quality. The trend towards increasing perfection in automobile engineering (not just quality in terms of appearance, but also physical quality) means that car body engineering

is subject to an ever-increasing demand for new ideas. In this domain, it is the application of new materials and joining technologies that force spring back behavior in conventional forming techniques into a continually limited tolerance range, making it virtually unmanageable. This directly results in reduced deformation reproducibility combined with dwindling production stability. The pressure to produce higher-quality cars is accompanied by the pressure exerted to scale down costs, forcing companies to constantly augment the efficiency of their manufacturing processes. These costs include not only personnel, but first and foremost the expenditures for plant equipment that jeopardise modern production technologies. Electromagnetic metal forming, from the techniques of high-energy rate forming, is the main process that promises the potential for providing relief from the aforementioned problems.

2 The Potential of Electromagnetic Metal Forming

In contrast to quasi-static forming techniques, the essential benefits to be derived from the electromagnetic metal forming technique for manufacturing car body components are:

- it achieves higher deformation ratios since its strain rates are in the range of the hyperplasticity of the material,
- the component has little spring back or none at all, meaning high dimensional accuracy,
- the process can be well reproduced and automated,
- it is inert to instability (folds and dents),
- the material has a high degree of strain hardening,
- it is a contactless process, meaning less surface damage, and
- it is environmentally compatible.

Fraunhofer IWU made a comparison of the investment expenditures with a conventional press line and an adequate electromagnetic metal forming plant for manufacturing a large-scale car-body component. It indicated an essential advantageous of cost ratio. The major cost difference is a result of the different plant equipment, while tools and automatic equipment were postulated to be at similar rates. Furthermore, we may also expect additional savings from the costs for tools.

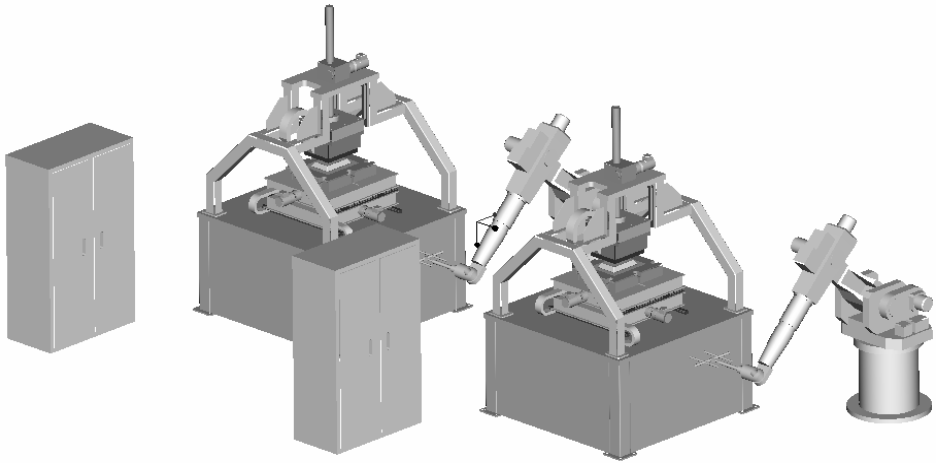

Figure 1: *A study for integrating electromagnetic metal forming plants in production lines*

Previously, process application was mainly restricted to producing and joining smaller rotation-symmetrical components (such as pipes and sections), and electromagnetic metal forming is applied in simplified sheet metal processing for embossing operations. However, this technology has not been applied to manufacturing larger-scale formed sheet parts either in terms of process design or plant equipment or in a scientific sense or in practice. Hence, after decades of stagnation in the field of electromagnetic metal forming, there are good prospects for furthering this process since new and important electrical and electronic developments have emerged and complex technical conditions (i.e., new materials) and economic conditions (i.e., scaling down costs) are exerting greater force on manufacturers to search for ways to augment efficiency. This is the reason the Fraunhofer IWU is concentrating its research work in electromagnetic metal forming on coming up with technology, tool and plant strategies suitable for manufacturing medium-sized and large-scale car-body components (Figure 2) due to its major potential for saving and the process benefits to be derived. The entire assortment of car body components is included in our deliberations:

- class-A exterior components (such as the roof and exterior door sheet metal),
- interior car body components (such as the interior door sheet metal and floor sheet metal), and
- structural components (such as side members, crossmembers and the A-, B- and C-columns).

In addition, the present range of electromagnetic metal forming processes has the technological and physical peculiarity of implementing the deformation by reducing wall thickness. However, if this process is applied to car-body components with rigidity and safety functions there are tight restrictions in terms of maximum material thinning. Thus, one of the concentrations of our study will be to calculate the effect that any strain hardening has on compensating for these factors and formulating new compensation strategies.

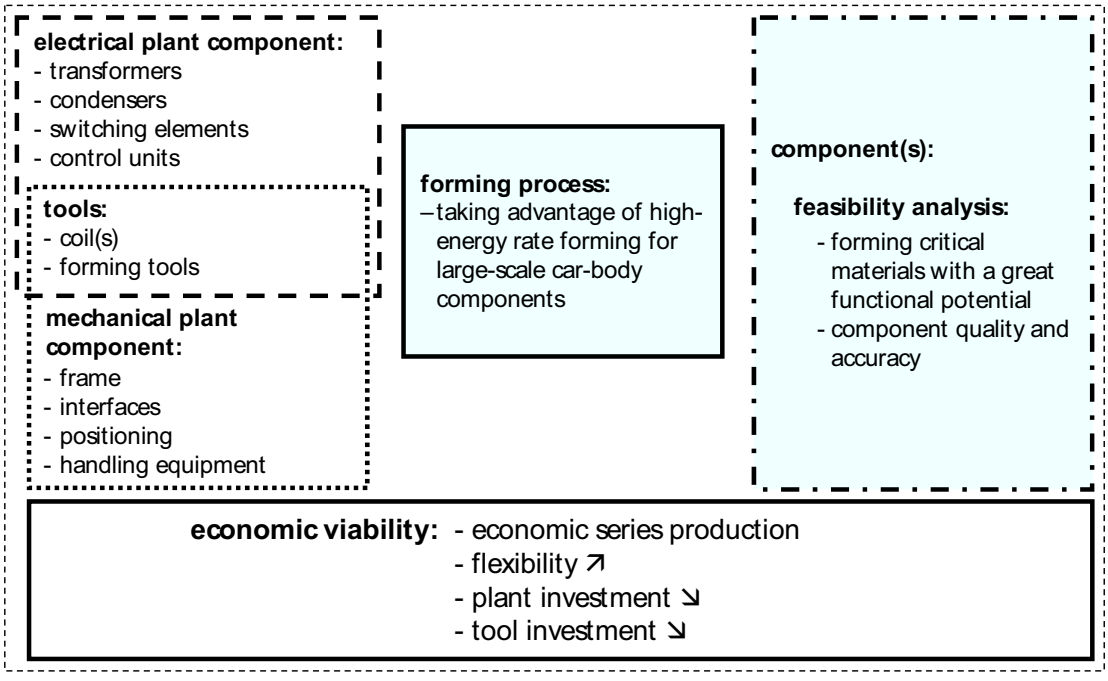

Figure 2: *The Fraunhofer IWU's concentration in electromagnetic metal forming*

3 New Technological Strategies

We can break down our technological strategies into two areas:

- electromagnetic metal forming of complete components (Figure 3) and
- partial electromagnetic metal forming of individual form elements in an integrated plant strategy (Figure 5).

The first step taken by the Fraunhofer IWU is to investigate the possibilities and potential of electromagnetic metal forming of complete components excluding the preforming process. However, several forming steps are required for mapping typical car-body component shapes that could be done with serial workstations or a flexible tool system (for instance, multicoil systems with coil and/or workpiece positioning) (Figure 3). To implement this project, the Fraunhofer IWU is presently developing and building a 100 kJ trial plant for its own studies. It will be available in the 3rd quarter of 2004 and it will be dedicated to creating the basic forming, plant engineering, and tool conditions for manufacturing large-scale car-body components. The greatest challenge will be designing the coil, and Figure 3 shows two coil designs out of a series of different possibilities. The most efficient design is forming with a coil and a discharging process, although designs with segmented coils and readjusting the coil would probably be more suitable for forming complete car-body components.

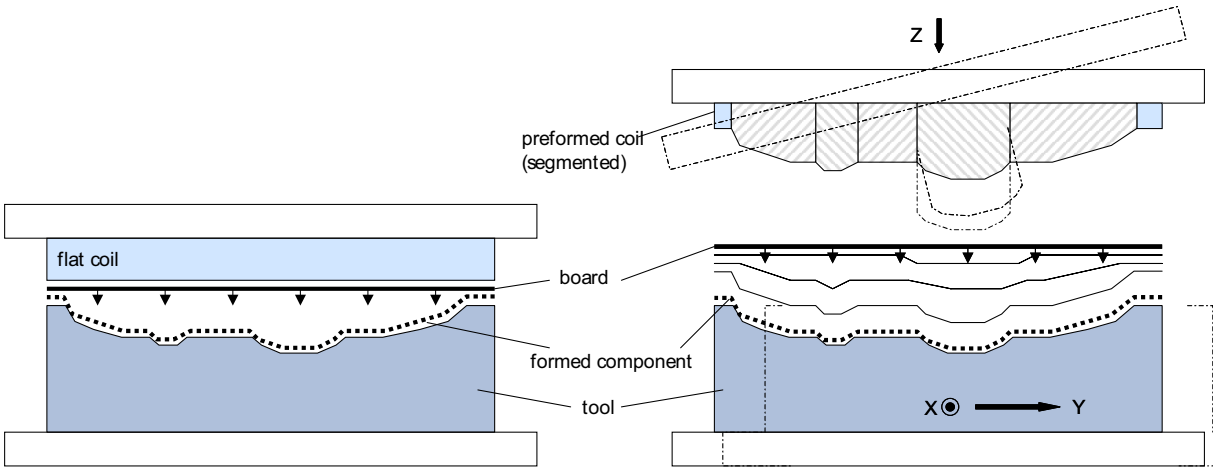

Figure 3: *Electromagnetic metal forming of complete components*

The following detailed procedure is planned:

- calculating the limitations of forming/potential of electromagnetic metal forming as compared with conventional deformation of plane components. Our strategy to study the criteria and influences exerted on thin-sheet components and sandwich structures, such as the maximum potential deformation, deformation distribution, minimum radiuses, the thickness of sheet metal, and the material,
- adapting this process to plane components (basic forms, such as beads and shape elements including possibilities for controlling the material flow),
- ways to solve the problem of scaling this process to large components, and
- streamlining plant and tool designs (i.e., scaling down the number of forming steps) for specific industrial applications in car body component manufacturing.

Given the high productivity of mechanical forming plants, the Fraunhofer IWU is planning other projects for studying the constraints of electromagnetic metal forming in connection with integrating it into conventional forming plants (Figure 4 and Figure 5).

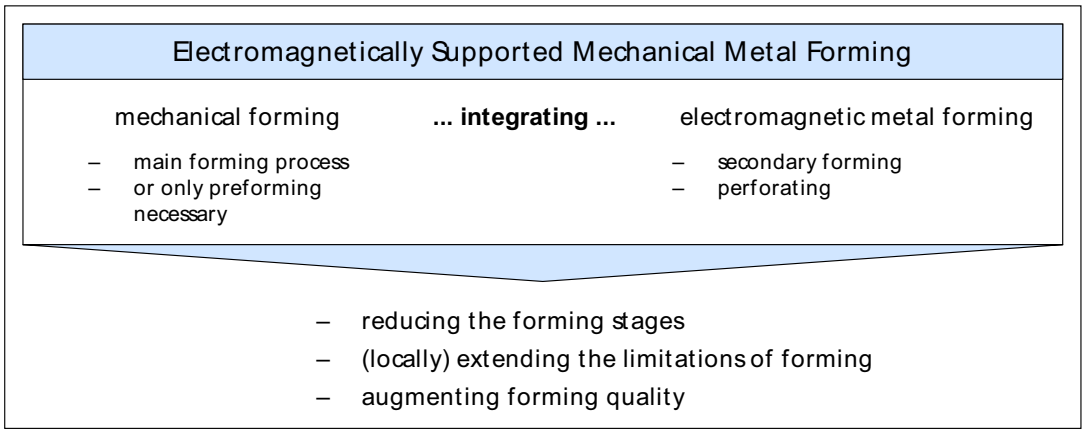

Figure 4: *The strategy for integrating magnetic forming plants into conventional forming plants.*

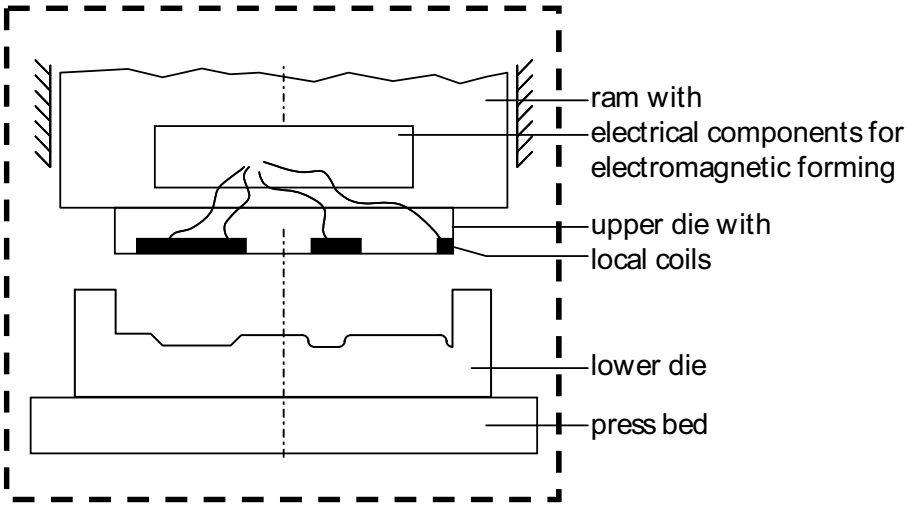

Figure 5: *The principle of partial electromagnetic metal forming while integrating it into a conventional pressing design*

These targets will have the following effects:

- reducing the number of forming steps,
- (locally) extending the limitations of forming while
- augmenting forming quality.

These two approaches have very different requirements for plant and tool design. First of all, since the transmission lengths between the magnetic forming plant and coil are limited (i.e., minimising losses), these two plants have to be positioned very close to one another. This poses the question of system compatibility, for instance in the control units. Then, the problem of how the discharging process can be synchronised for the slide motion has to be resolved (i.e., with a control mechanism or mechanical coupling). However, what is

crucial for delivering a reproducible final result is discharging at a defined and very small interval from the lower tool where the drive characteristics of the press figure prominently. There are also design restrictions in terms of other plant components required, such as for ventilating the forming tools. The additional components will either have to be installed in the moving slide or at great transmission lengths depending upon which of the tools (the lower or the upper tool) is engineering for taking up the coils. A final aspect is integrating the coils into the deep-drawing tool while bearing wear criteria in mind where we will have to study whether and under what circumstances magnetic forming would be possible where material has a major influence (such as radiuses in the exterior range of geometry).

4 Conclusions

Electromagnetic metal forming offers major potential for enhancing the economic viability of the manufacturing process of forming components while extending the limits of forming technology. This potential can particularly be seen when we apply this technique to plane components (i.e., special car-body components). This is the reason why the Fraunhofer IWU has dedicated its efforts to applying the electromagnetic metal forming technique to plane components.

Design and Adaptation of EMF Equipment – From Direct Acting Multi-turn Coils to Separable Tool Coils for Electromagnetic Tube Compression

A. Henselek, M. Beerwald, C. Beerwald

Poynting GmbH, Dortmund, Germany

Abstract

Since the electromagnetic forming (EMF) becomes more and more accepted within industrial manufacturing, the methods engineer has to deal with the choice of matching equipment as to perform the task of production in the best possible way. At the present time several manufacturers offer EMF-machines with different characteristics, whereby the machines consist of a pulse power generator and an exchangeable tool coil. The storable energy, the current capability and a high short circuit frequency enable the engineer to adapt tool coils for an optimised pressure course.

In the following some aspects of how to dimension direct acting tool coil properties for the EM compression process will be considered. Basically the use of multi-turn coils is advantageous for a good matching. But in a lot of cases the use of a fieldshaper is necessary. It will be shown how the design of a tool coil system including a fieldshaper influences the pressure course. A special case is the application of EM compression in closed spaceframe structures for which a separable tool coil is required. A separable compression coil with non-welding contact elements will be presented.

Keywords:

Electromagnetic forming, Tube compression, Tool design

1 Introduction

Investigations and developments in the field of electromagnetic forming (EMF) can be traced back to the early 1960s. But the increasing use of aluminium alloys in car manufacturing in the last ten years inspired a renewed and strong interest in the commercial application of this special high speed forming process. This forebodes the EMF process to become widely accepted within industrial manufacturing in the near future. At present, the most common application is the EMF of tubular aluminium components, especially for joining, but also for pre-forming or calibrating operations.

The most simple and well-known process type is the EM compression of tubular workpieces with good electrical conductivity: In this case the tool coil is located around a tubular workpiece and the sudden discharge of a capacitor bank through the tool coil causes a fast increasing axial magnetic field inside the coil. Due to the skin effect the magnetic field strength H decreases in the workpiece wall. Thus, it penetrates through the workpiece wall dependent on the frequency, the electrical conductivity, the wall thickness, and the radius of the workpiece [1]. The energy density of the magnetic field, which is equivalent to the acting magnetic pressure p (see equation (1)), is most efficient if the field is completely shielded by the current which will be induced in the workpiece wall.

$$p(t,z) = ½ \cdot \mu_0 \cdot H^2(t,z) \tag{1}$$

$$H(t,z) = w \cdot I(t) \cdot k_H(z) , \tag{2}$$

where w is the so called density of winding (number of turns per unit length) and k_H is a function describing the axial field distribution on the surface of the workpiece [2].

The principle of using the energy density of an extremely strong pulsed magnetic field for a non-contact type of forming operation places additional demands on the interdisciplinary understanding of the methods engineer: this includes a minimum fundamental knowledge of the Maxwell's theory to estimate the acting magnetic pressure, as well as some knowledge of the workpiece's forming behaviour under high speed conditions to determine the demands on the magnetic pressure. The strong dependencies and interactions between electrodynamics, acting forces, and forming behaviour of the workpiece complicate the choice of matching EMF equipment to fulfil a defined forming task in the best possible way. In the following, the design and dimensioning of EM compression coils will be treated more detailed under the aspect of an efficient energy use.

2 Significant characteristics of the EMF equipment

In general, the EMF process and its associated mechanisms are determined by the induced current in the workpiece, and therefore by the coil current as the responsible source. Figure 1 shows the equivalent circuit diagram including the core components of an EMF-system for tube compression which typically consists of a pulse power generator and an exchangeable tool coil. The pulse power generator, mainly consisting of a capacitor bank and a high current switch, has to be constructed in a low-inductive way (L_{inner} should be much smaller than the coil inductance) to realise an efficient use of the capacitors energy as a high current through the tool coil. The sudden close of the high current switch in this resonant circuit leads to a damped oscillating current $I_1(t)$ through the tool coil. The workpiece can be seen as a single shorted secondary turn of a transformer, in which the current $I_2(t)$ will be induced. Additionally, by the arrangement of tool coil and workpiece, especially by the gap volume in between, a leakage inductance L_{leak} will be caused.

During the deformation process with the increasing volume of the gap, the leakage inductance increases. This results in an evident change of frequency of the coil current, as shown in Figure 1.

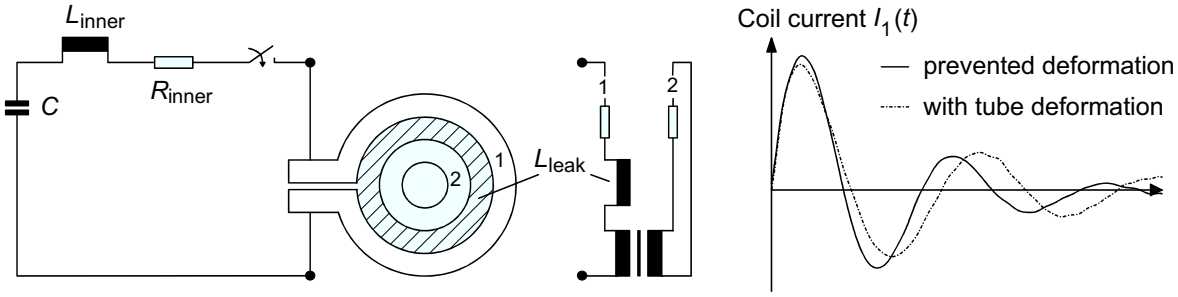

***Figure 1**: Equivalent circuit of an EMF machine with compression coil (1) and tubular workpiece (2)*

The parameters of the equivalent circuit diagram determine the frequency of the discharge, whereas the lower the inductance of the whole coil-workpiece-system, the higher the frequency. The maximum possible frequency is limited by the short circuit frequency which is mainly determined by the capacity and the inner inductance of the pulse power generator (without tool coil and workpiece). This is a significant characteristic of EMF-machines which is typically in the range of 20 to 100 kHz.

The other descriptive parameters of the machines are the maximum charging energy of the capacitors, which is defined by the capacity and the maximum charging voltage, and the maximum current, which is mainly limited by the capacitors and the high current switches. New developments in the field of high current switches are today of common interest because the well-known ignitrons, which are known as being robust against overload, are controversial due to the expected restrictions concerning the use of mercury [3].

The storable energy, the current capability, and a high short circuit frequency enable the engineer to adapt tool coils for an optimised current, field and pressure course (according to the relationship in equation (1) and (2). On the other hand, these characteristics of the pulse generator are dependent on the manufacturer and the machine costs (either as investment costs or as costs in consequence of wear lifespan).

3 Adaptation of direct acting multi-turn compression coils

Since the beginnings of working with the EMF process the design and realisation of durable and efficient tool coils, which have to resist magnetic fields of above 20 T, have been problematic. Up to now, the use of low efficient single turn coils is prevalent in order to obtain high mechanical stability. Their low inductance compared to the inner inductance of the pulse power generator leads to lower efficiency. This particularly concerns tool coils for small workpiece diameters, which hence should be realised as multi-turn coils.

The realisation of such multi-turn compression coils requires a strong reinforcement by a non-conductive high strength material with good damping quality. For these purposes we successfully use a composite that consists of para-aramid fibre (Kevlar) and an epoxy resin. Additionally, for the industrial use of these compression coils it is necessary to overcome the poor thermal conductivity of the composite. Therefore, copper parts are skilfully placed within the reinforcement and can be connected with a water cooling system. A more detailed description is given in [4, 5].

Regarding the efficiency of the process, it is necessary to design the tool coil according to the forming task, but also in accordance with the properties of the pulse power generator. The forming task defines the dimension of the workpiece to be formed and therefore the inner coil diameter and the coil length. The minimum gap width between tool coil and workpiece is defined by the required thickness of the insulation material and by a comfortable handling of the workpiece. Principally, it should be as small as possible to reduce the initial leakage inductance. If the coil diameter and axial length is fixed the number of turns is the essential parameter to determine the optimum inductance of the tool coil. The influence of this parameter is shown in Figure 2 for an aluminium tube ø12 mm x 1 mm, a coil length of 15 mm and a coil diameter of ø13.4 mm. To determine an optimised number of turns, the capacitor discharge in the equivalent circuit diagram has been calculated neglecting the workpiece deformation. This calculation has been performed for two different pulse power generators to show that the optimum number of turns is dependent on the generators characteristics. Interesting in this context is the obvious low efficiency of single-turn coils for both of the generators.

Furthermore, it is conspicuous that for a pressure maximum of 150 MPa with the optimum number of turns the generator with the higher short circuit frequency (generator A) needs less charging energy. Additionally, the required current maximum is less, because due to equations (1) and (2) a higher density of winding results in the same field strength and this means nearly in the same pressure maximum.

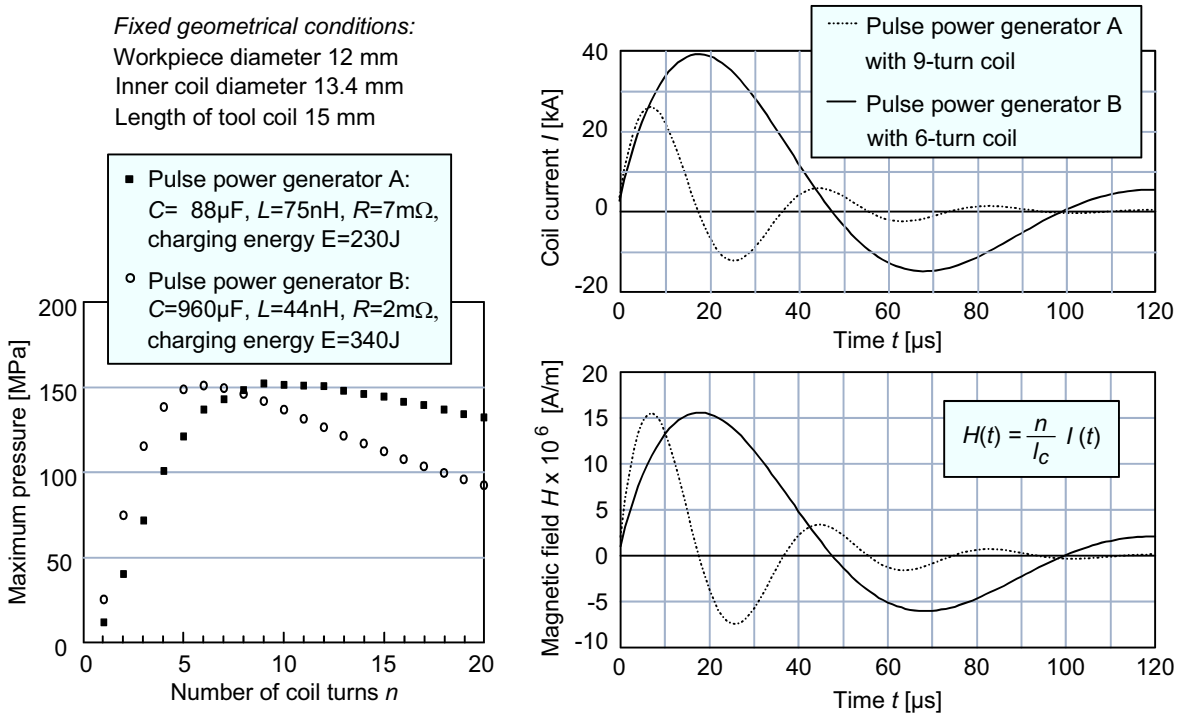

***Figure 2**: Adaptation of the coil turns dependent on the machine characteristics*

Which current course is most suitable depends on the forming task. The current course directly influences the pressure course, which is essentially described with the parameters pressure maximum, pressure rise time, and duration of the acting pressure pulse, resp. the working frequency. Investigations at the Chair of Forming Technology of the University of Dortmund have shown that in the case of EM compression of aluminium tubes the

increase of stiffness due to the reduction of diameter during the forming process causes the compression process to be finished within the first pressure pulse. Therefore, the shape of the pressure over time curve influences the forming behaviour of the tubes. It could be observed that, for example, an increasing pressure rise time causes an increase of the forming velocity, and with an increasing forming velocity an improved roundness of the workpiece could be achieved [6]. Another advantage of a higher forming velocity can be seen in the case of joining operations, where a higher forming velocity of a tubular component results in a higher kinetic energy at the time of impact with an inner joining partner.

Furthermore, the duration of the pressure pulse, resp. the first half cycle duration of the coil current should not exceed the duration of the forming operation. In Figure 3, the measured coil currents of the adapted tool coil with 9 turns are shown as well as the current shape of an unfavourable coil with 27 turns. The latter demonstrates the case when the current still increases although the deformation is finished. In the diagrams the duration of the compression process is marked with grey columns, whereas the reduction of the diameter is limited by a mandrel with a diameter of 8 mm. This leads to an over-consumption of energy as well as to unnecessary high current loads of the generator components.

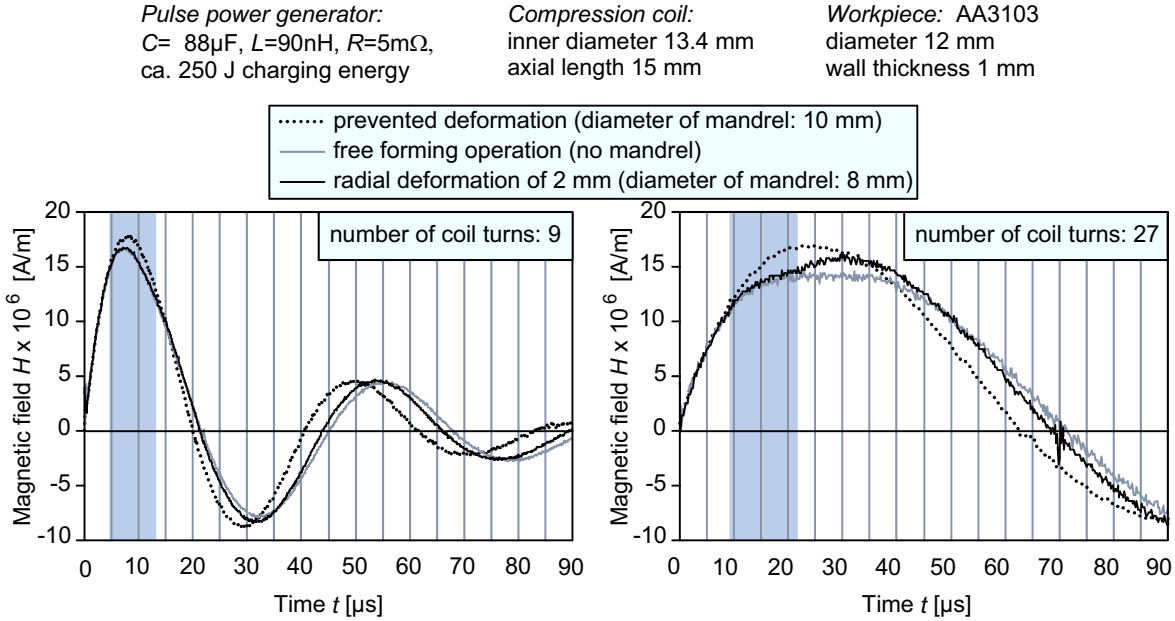

Figure 3: *Different current over time curves for a joining example with different direct acting compression coils*

Recapitulating, from the point of view of the efficiency the dimensioning of tool coils has to be adapted with regard to the EMF machine properties, but within the limiting conditions resulting from the forming task. As the considered workpiece example shows, the required charging energy for such small tubes is very low. This is because the required energy depends on the dimension of the workpiece surface to be loaded with magnetic pressure. On the other hand, the required working frequency for the considered small tube should be comparable high, because the duration of the forming process is very short. Finally, it should be mentioned that also by the capacitance of the pulse generator the working

frequency can be influenced. Thus, the methods engineer has the best chances to adjust a desired pressure course with the tool coil if the pulse power generator can be used in a modular way, with switchable energy segments.

4 Energy considerations in the use of fieldshapers

Many forming tasks require the use of a fieldshaper, for example if a tube is to be assembled on both of its ends with fittings like shown in Figure 4. The geometry of the fittings does not allow the use of a matching direct acting tool coil, because the minimum required coil diameter is contrary to the requirement of a small gap between tool coil and workpiece. A possible solution consists in a two-part fieldshaper. Due to the skin effect the induced current in the fieldshaper flows near to its surface, so that in both fieldshaper parts there are closed loop currents as it is indicated by the arrows in Figure 4. The current at the inner edge of the field shaper, which is close to the workpiece, determines the acting magnetic pressure.

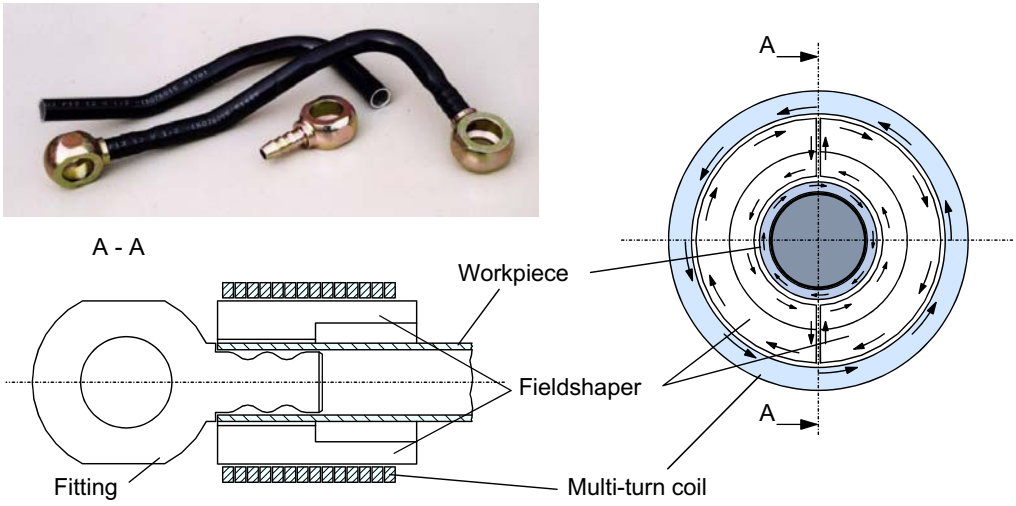

***Figure 4**: Joining example requiring the use of a multi-part fieldshaper*

Regarding the multi-turn coil and the fieldshaper together as the tool coil system, the gap volume to be filled with magnetic field energy leads to an additional leakage inductance in comparison to a direct acting coil. Consequently, more charging energy is needed and the current over time curve changes to lower frequencies.

Nevertheless, to achieve a high pressure pulse in the forming zone by low charging energies, normally the effect of field concentration by the geometrical design of the fieldshaper will be used: the current per length *H* at the outer surface of the fieldshaper is determined by the coil turns per length and will be concentrated at the inner surface of the fieldshaper by the length of an edge which is close to the workpiece, while the residual length is far away from the workpiece. If there are no restrictions concerning the dimensions of the multi-turn coil, it is possible to achieve very high concentrating factors for the magnetic field as well as for the acting magnetic pressure. But the higher the concentrating factor the higher the local mechanical load on the inner edge of the fieldshaper, and this leads to a more massive construction finally resulting in a larger coil diameter.

While the optimum energy efficiency depends on geometrical boundary conditions of the application, a desired pressure rise time and pulse duration depend on the electrical properties of the EMF machine and on the total inductance of the system consisting of multi-turn coil, fieldshaper, and workpiece. As an example, the setup of Figure 4 shall be considered in the following:

Because of the geometry of the fitting, a minimum coil diameter of 25 mm is required. The fieldshaper has to transform the magnetic field to the tube diameter of 12 mm and a length of 15 mm (similar to the forming area considered in chapter 3). Here, the multi-turn coil should be as small as possible and has been chosen at a winding diameter of 26 mm and a winding length of 27 mm. According to the dimensioning of a matching direct acting compression coil as shown in chapter 3, an inductance of about 0.225 µH should be realised with the fieldshaper setup. The dimensioning can be executed, for example with the help of the simulation software FEMM, a free finite element code for magnetic field analysis [7]. Here, the resulting number of coil turns was 7. To compare this tool coil setup with the direct acting tool coil, nearly the same diameter reduction has been performed as with the magnetic field which is shown in Figure 3 (left diagram). Instead of 250 J with the 9-turn direct acting coil, a charging energy of 750 J was necessary with the fieldshaper. The measured coil current is shown in Figure 5. Due to the reduction of the workpiece diameter during the forming operation, the gap volume increases, but will not influence the coil current as much as in the case of direct acting coils. Additionally to the higher charging energy, the required coil current is about 45 kA (instead of 28 kA with the direct acting coil). With regard to the current load of the switch and the capacitors of the pulse generator, the number of turns has been increased to 14 (corresponding total inductance: 1.14 µH). As shown in Figure 5, the current maximum then is clearly reduced, but on the other hand the duration of the first half wavelength seems almost too long relative to the duration of the forming process.

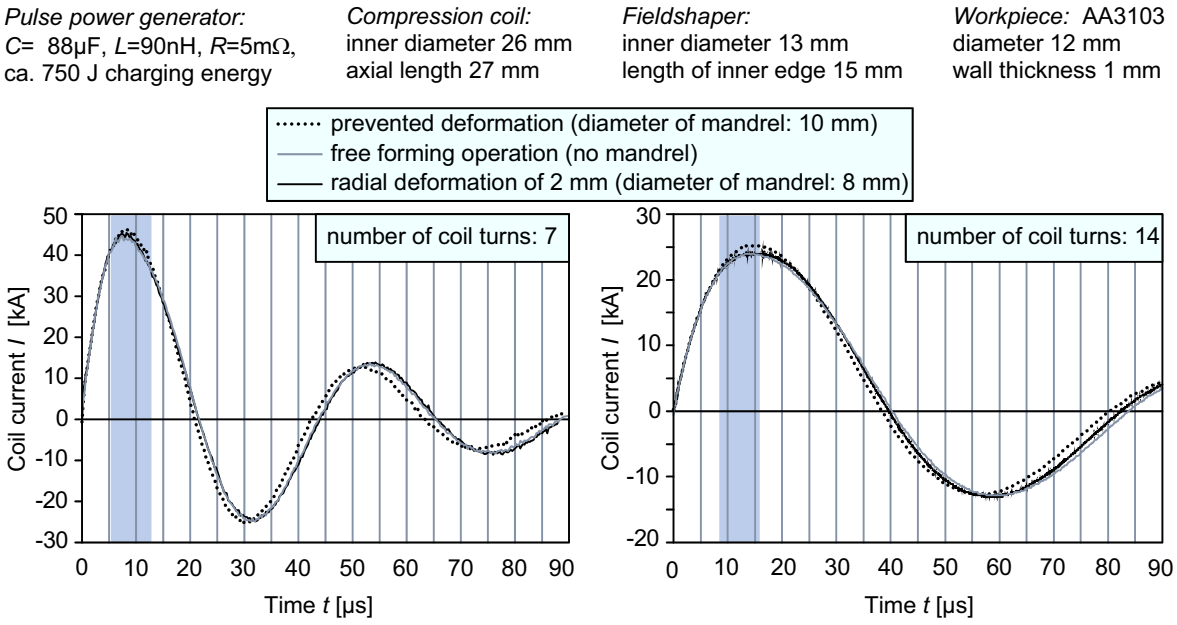

Figure 5: *Coil currents of different tool coils combined with the same fieldshaper*

Additionally to the geometric boundary condition of each case of application, the properties of the pulse power generator significantly influence the optimum design of the tool coil system. While the forming velocity and the duration of the forming process determine the optimum inductance of the tool coil system (maximum number of turns, coil diameter, and coil length), the current capability limits the minimum permissible number of coil turns. Furthermore, the efficient use of fieldshapers requires a pulse generator with a sufficient high short circuit frequency. The worst case concerning the efficiency would be if the temporal demands lead to a use of a single turn coil, because the concentrating effect mainly bases on the possibility of using multi-turn coils.

5 Example of a realized separable compression coil

A special case is the application of EM compression for joining operations in closed spaceframe structures as often required in the automotive industry. Therefore, the use of a separable tool coil is unavoidable.

To understand the difficulties in the realisation of a separable compression coil, let us consider a single turn coil consisting of two parts which are directly coupled to the high current pulse generator: a desired magnetic pressure inside the coil of about 200 MPa requires a magnetic field strength of 18×10^6 A/m (= 18 kA/mm). With the skin depth in copper of about 0.5 mm for the typical impulse length of 10 to 40 µs, the current density in the coil will be more than 30 kA/mm^2. This would certainly cause a welding procedure in the contact zone of the two coil parts. Our experimental investigations with CuBe-springs have shown that it is possible to avoid welding at a current per unit length lower than 5 kA/mm. But this corresponds only to a magnetic pressure of 15 MPa, which is too low for the forming process. So it is necessary to realise a current carrying geometry which concentrates the field strength in the forming zone.

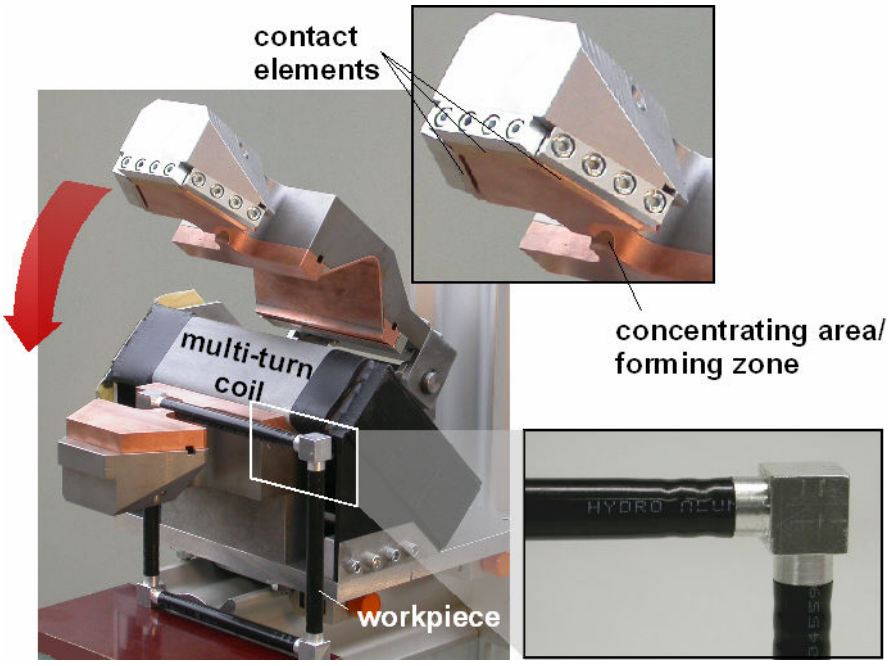

Figure 6: *Separable compression coil with non-welding contact elements and joining example (closed frame structure)*

Figure 6 shows such a separable coil with non-welding contact elements [4, 8]: the single turn coil consists of two parts which are inductively coupled to a long multi-turn coil. The length of this multi-turn coil is nearly the same as the minimum required length of the contact elements. Due to the increasing amount and complexity of the current-carrying geometry an unavoidable additional leakage inductance occurs. It is therefore very important to adapt the number of turns as good as possible to the pulse generator and to compensate the corresponding energy losses with a concentrating factor.

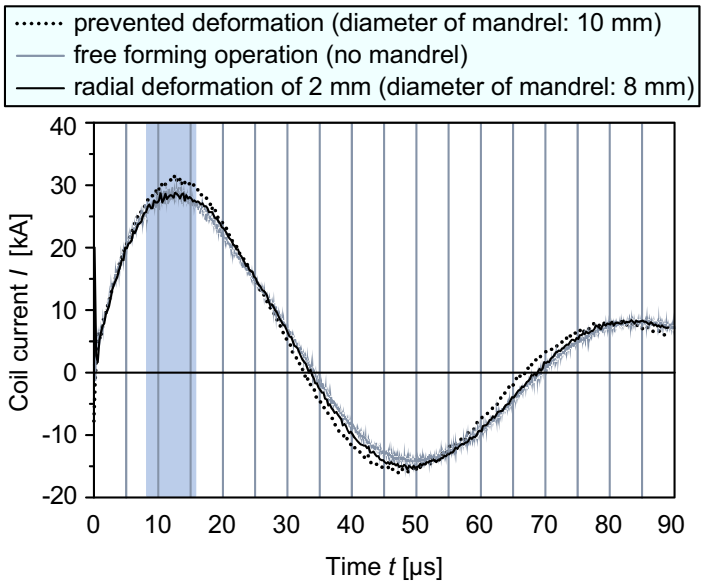

Pulse power generator:
C= 88µF, *L*=90nH, *R*=5mΩ,
ca. 900 J charging energy

Separable compression coil:
diameter of the forming zone 13.4 mm
axial length of the forming zone 15 mm

Workpiece: AA3103
diameter 12 mm
wall thickness 1 mm

Figure 7: *Measured current over time curves of the separable compression coil*

Figure 7 shows that it is possible to achieve an adapted current over time behaviour with the same pulse generator as it has been used with the matching direct acting coil (chapter 3) as well as with the coil-fieldshaper-tool (chapter 4). For a similar diameter reduction of the abovementioned 12 mm x 1 mm aluminium tube 900 J charging energy is necessary and the current is within the required specifications (described in chapter 4).

6 Summary

As the most common and well suited application of the EMF process the compression of tubes has been considered. It can be used e. g. for joining, calibrating, or pre-forming operations. Due to the forming task the optimum pressure pulse has to be defined and then to be realised by the EMF equipment. In the case of tube compression the pressure maximum and rise time influence the forming velocity as well as the desired final geometry and properties of the workpiece. Additionally, the engineer should turn attention to the efficient use of the pulse generators energy by a good matching between the duration of the deformation process and the duration of the pressure pulse.

The shape of the pressure over time behaviour is directly related to the course of the magnetic field strength which finally is determined by the current through the tool coil. The latter depends strongly on the parameters of the EMF equipment consisting of the pulse power generator and an exchangeable tool coil. In most cases it should be possible to adjust a desired pressure course by the coil design, more precisely by its number of turns.

The limiting factors are the short circuit frequency and the current capability of the pulse generator. Vice versa, a pulse generator with switchable energy segments can be used to match the pressure pulse for a given coil-workpiece arrangement.

This is regardless of the tool coil being a direct acting multi-turn coil or a single-turn coil coupled to the generator by a multi-turn coil, like in the case of using a fieldshaper or a separable compression coil.

References

[1] *Kaden, H.:* Wirbelströme und Schirmung in der Nachrichtentechnik. Springer-Verlag, Berlin, Göttingen, Heidelberg 1959, pp 76-79.

[2] *Beerwald, C.; Brosius, A.; Homberg, W.; Kleiner, M.; Wellendorf, A.:* New aspects of electromagnetic forming. Proceedings of the 6th International Conference on the Technology of Plasticity, Erlangen, 1999, ISBN3-540-66066-6, Volume III, pp. 2471-2476.

[3] *Henselek A.:* Anlagenkonzept für die industrielle Anwendung der Elektromagnetischen Umformung. Proceedings Kolloquium Elektromagnetische Umformung 2001, Dortmund, 2001, ISBN3-00-008122-4, pp 39-44.

[4] *Beerwald, H.:* Contribution to the generation of pulsed magnetic fields up to 25 T for industrial applications especially electromagnetic metal forming systems. Proceedings of the 7th International Conference on Optimization of Electrical and Electronic Equipment (OPTIM 2000), Brasov, May 2000.

[5] *Beerwald, H.:* Mehrwindungsspule zur Erzeugung starker Magnetfeldimpulse. Patent DE 100 20 708 C2.

[6] *Psyk, V.; Beerwald, C.; Homberg, W.; Kleiner, M.:* Electromagnetic compression as preforming operation for tubular hydroforming parts. Proceedings of International Conference on High Speed Forming “ICHSF 2004”, Dortmund, 2004.

[7] Foster-Miller Inc., FEMM, a free FEA software for magnetic field analysis by D. Meeker, Version 3.3 (17 Aug 03): http://femm.foster-miller.net (1st Mar 04).

[8] *Beerwald, H.; Beerwald, M.; Henselek, A.:* Teilbare Einwindungsspule zur Erzeugung starker Magnetfeldimpulse, Patentapplication DE 199 19 301.

An Optimised High Current Impulse Source

S. Kempen, D. Peier

Institute of High Voltage Engineering , University of Dortmund, Germany

Abstract

Starting from a predefined 8/20 µs impulse current, the design and construction of an impulse current source is derived. In the first step an equivalent circuit is defined that meets exactly the predefined impulse current. In the next step the components that are required to realise the equivalent circuit diagram are chosen and modelled by their equivalent circuit diagrams. As far as the components do not show ideal behaviour, the stray parameters of the components are determined by calculation and measurement. Further on, the construction parameters for the geometric structure of the plant are derived from the equivalent circuit diagram of the entire impulse generating network. Finally it is shown that the measured current of the realised impulse current generator meets exactly the desired predefined impulse current.

Keywords:

Impulse current source, Electromagnetic high-speed forming, Optimisation

1 Introduction

During a high-speed forming process the workpiece has to be fed with the forming energy $W_{form}(t)$ following ideally a certain time function. This function is determined by the material parameters of the workpiece and by the desired forming result. In the case of the electromagnetic high speed forming the required forming energy $W_{form}(t)$ is provided by a time variable magnetic field $B_{form}(t)$. Co-action between the magnetic field $B_{form}(t)$ and the eddy currents in the workpiece result in Lorentz forces causing the forming process. The interrelation between the desired forming result and material parameters on the one hand, and the therefore required time dependent magnetic field $B_{form}(t)$ on the other is matter of the actual research activities.

The time variable magnetic field $B_{form}(t)$ can be generated by a defined time variable current $i(t)$ flowing through a forming coil which operates as part of an impulse-generating electric network. A schematic drawing of the setup is given in Figure 1. The impulse-generating network consists of an energy storage device which is discharged over impulse forming circuit elements initiated by a certain circuit breaker. Thereby, the forming coil is one of the impulse forming circuit elements. After the desired magnetic field $B_{form}(t)$,

and therewith the current $i(t)$, have been defined, an optimised high current impulse source can be designed.
At present, the impulse current $i(t)$ for an optimised forming result can not be specified. It is the matter of actual research. Alternatively, a standardised 8/20 µs impulse current is used to demonstrate the design method for an optimised impulse current source anyhow. This current is a common used test impulse in the field of electrical power engineering. Typical peak values range from 5 kA to 100 kA. The curve progression is exactly defined in [1] and simulates the load type due to switching operations in power lines and indirectly impact of lightning strokes. The time characteristic of this impulse may be also similar to

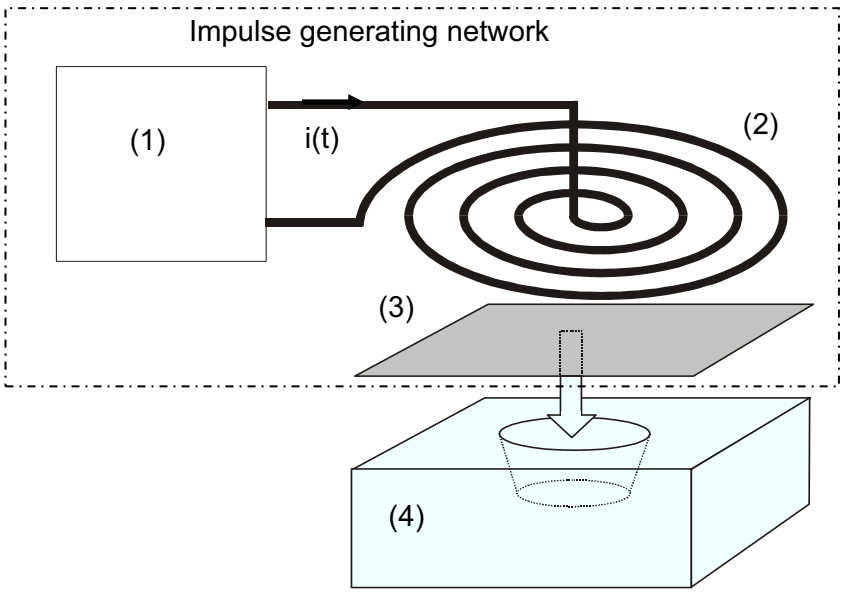

Figure 1: *Schematic drawing of a plant for electromagnetic high-speed forming. The main parts of the plant are: Impulse forming network with energy storage device and circuit breaker (1), forming coil (2), workpiece (3), cavity (4)*

the time characteristic of impulse currents used for electromagnetic high speed forming.

2 Definition of the equivalent circuit diagram according to the desired impulse characteristic

2.1 Definition of the standardised 8/20µs impulse current

The standardised 8/20µs impulse current [1] possesses a characteristic which rises in a very short time period from zero to the peak value î and falls back to zero following an exponential or aperiodic sinusoidal time characteristic (Figure 2). The curve is characterised by the virtual front time T_1 and by the virtual time to half value T_2. In the case of the 8/20 µs impulse current, T_1 amounts 8 µs and T_2 amounts 20 µs. The curve can be analytically approximated by Equation (1).

$$i(t) = i_0 \cdot e^{-t/\tau_1} \cdot \sin\left(\frac{t}{\tau_2}\right) \tag{1}$$

Attention should be paid to the fact that there is no oscillation, under- or over-shooting in the progression of the curve.

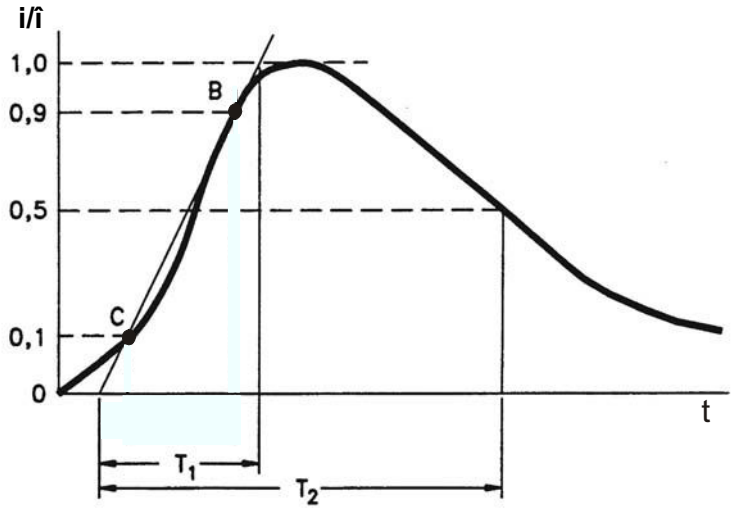

Figure 2: *Definition of the standardised exponential impulse current [1]: T_1: virtual front time, T_2: virtual time to half value, î: current peal value*

2.2 Structure of the equivalent circuit diagram

The structure of an impulse generating electrical network can be derived from the impulse describing equation. The sinusoidal term in Equation (1) leads to the demand for two energy storage devices of different type. Therefore, the resulting circuit is able to oscillate. To avoid these undesired oscillation of energy between the two storage devices, a damping device has to be part of the circuit. The damping function is represented by the exponential term in Equation (1). These conclusions lead to a basic equivalent circuit with a least 4 elements including a switch. The different types of energy storage devices are displayed by a capacitance and an inductivity. At the beginning, the only known element of the circuit is the forming coil which is displayed mainly by its inductivity. Damping devices are displayed by resistances. The catenation of the elements leads to the series resonant circuit (Figure 3).

Further on, it has to be decided which of the both energy storage devices has to be carried out as the primary energy storage device. According to the duality principle it would be possible to choose either the inductivity *L* or the capacitance *C* as the primary energy storage device [2]. With regard to the demand of calculability of all components, including the switch, the choice of the capacitance as primary energy storage device is advantageous. In the case that for the primary energy storage an inductivity would be chosen, a properly defined non ideal behaviour of the switch is required. The switch be-

haviour determines mainly the rise in current in this case [2]. This would make the calculability and the later construction of the switch extremely difficult. In the case that the capacitance is chosen to be the primary energy storage, the switch behaviour is approximately ideal. Therefore, the capacitance *C* is chosen to be the basic energy storage device in this case. So the charging circuit is carried out as a DC voltage source which is connected over a charging resistance R_L to the capacitance (Figure 3). The task of the charging resistance is to decouple the two circuit loops.

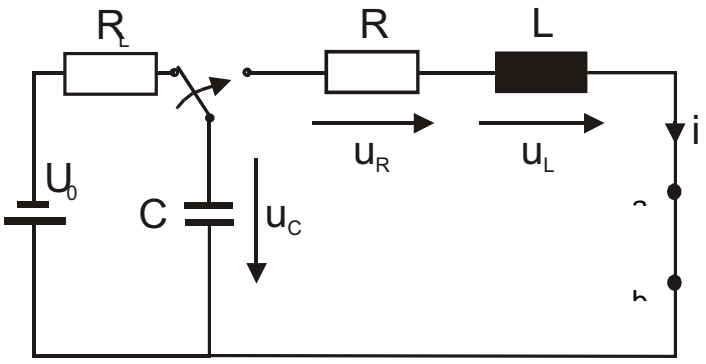

Figure 3: *Basic equivalent circuit diagram of the impulse current source with charging circuit*

The equivalent circuit represents graphically the differential equation of the electric network. In the present case, the circuit is described by a linear 2nd order differential equation for the current *i*(*t*).

$$\frac{d^2 i}{dt^2} + \frac{R}{L} \cdot \frac{di}{dt} + \frac{1}{LC} \cdot i = 0 \tag{2}$$

Equation (1) displays the periodic damped solution for this differential equation. It appears if the network parameters comply with condition (3)

$$R < 2 \cdot \sqrt{L/C} \tag{3}$$

To avoid undesired oscillation of the current, the circuit resistance *R* has to be carried out in the way that the circuit operates in, or at least near the aperiodic limiting case which results if the circuit parameters comply with Equation (4).

$$R = 2 \cdot \sqrt{L/C} \tag{4}$$

The voltage U_0 of the source determines the initial condition of the capacitance. It is assumed that the circuit breaker only is switched at the time t_0 after the charging current has become zero, and so the initial voltage of the capacitance is $U_C = U_0$, although there is a charging resistor R_L between the source and the capacitance.

2.3 Calculation of parameters in the equivalent circuit diagram

The desired 8/20 µs impulse current can be analytically described by Equation (1) as mentioned. In the first step, the parameters i_0, τ_1 and τ_2 have to be fixed. Therefore, the

analytic current function has to be fitted to the standardised 8/20 µs current impulse (Figure 2). For a 17,3 kA – 8/20 µs impulse current the curve fitting results in the values: i_0 = 86,0 kA, τ_1 = 9,071 µs, τ_2 = 0,1586 µs

In the next step, the circuit parameters R, C, L, and the operation parameter U_0 have to be calculated from the impulse current parameters. The special solution of the differential equation leads to the following equations which assign the interrelation between the current parameters and the circuit parameters.

$$i_0 = \frac{U_0}{L \cdot \sqrt{\frac{1}{LC} - \frac{R^2}{4L^2}}} \tag{5}$$

$$\frac{1}{\tau_1} = \frac{R}{2L} \tag{6}$$

$$\frac{1}{\tau_2} = \sqrt{\frac{1}{LC} - \frac{R^2}{4L^2}} \tag{7}$$

With (5,6,7), a system of three implicit equations with four unknowns is given. For the solution of the system of equations, a further condition to one of the parameters has to be fixed by a technical boundary condition. This might be, for example, the capacitance of the available impulse capacitors. In the present case, the capacitance is fixed to the value of C = 74,7 µF. After this, a system with three equations and three unknowns remains. The solution of the equation system leads to the following set of circuit parameters: U_0 = 4,5 kV, L = 830 nH, R = 183 mΩ

By fixing one of the circuit parameters, the following further aspects should be taken into account:

- maximum available and economic charging voltage
- required forming energy plus electrical and mechanical losses
- compliance with condition (3,4)

Hence, the free parameter can be used to optimise the system under the mentioned aspects.

3 Design and construction of the impulse current source

The realisation of the calculated equivalent circuit to an impulse current generator construction which meets exactly the desired current function demands that the equivalent circuit displays all of the electric properties of the construction, including the electric properties of the components. From this it follows that the electrical properties of the components and the structure of the plant have to be known.

3.1 Structure of the impulse current source and choice of components

From the demand that the electrical properties of the construction have to be known follows that it has to be possible to calculate the electrical properties from the geometric data of the structure. The choice of the structure determines significantly the inductivity of the

structure. The relatively low value of the calculated inductivity (L= 830 nH) and the consideration that the other required components bring additional inductivity into the circuit (e.g. the forming coil) lead to the demand of an overall low inductive plant structure. In reference to the great storage capacitance (C = 74,7 µF) the stray capacitances of a geometric structure are negligible. The requirements of low inductivity and calculability lead to a coaxial geometric structure which is carried out as weir. The geometry data of the structure is determined in the way that the inductivity of the coaxial weir structure displays the desired inductivity of the calculated equivalent circuit together with the inductivity of the other required components.

Other required components are the capacitive energy storage, damping resistance, a current measurement resistor, circuit breaker, and the forming coil.

For the realisation of the capacitive energy storage, certain impulse capacitors are needed. With regard to the mentioned demands the most important criterion in choosing the capacitors is a self-inductance which is as small as possible. The entire required capacitance should be displayed by several capacitors which can be arranged to a circular structure. Parallel connection of these capacitors reduces additionally the resulting inductivity of the storage. In the present case, 10 impulse capacitors with a nominal capacitance of C = 7,74 µF are used (Figure 4). They can operate up to a maximum charging voltage of U_{LMax} = 24 kV and have therefore each a maximum stored energy of 2,15 kJ.

The required value of the damping resistor is in the range of 100 mΩ. During a discharge it has to absorb the energy

$$W = R_{Damping} \int i^2(t)dt \tag{8}$$

This leads to an extreme warming of the resistor material. Also the damping resistor should be constructed as low inductive as possible. In this case, it is realised by parallel connection of two or more carbon rods for arc lamps (Figure 5). The resistance value can be adjusted by varying the length and the number of the rods. With regard to the high voltages which have to be expected during the high current discharge, the design of the carbon rod connecting electrodes is optimised for high voltage application.

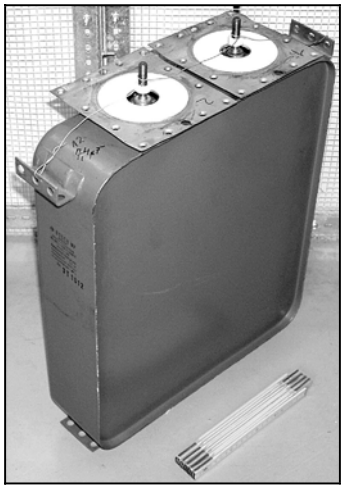

Figure 4: *Impulse capacitor with C_N = 7,47 µF*

Figure 5: *Damping resistor with 2 carbon rods*

Figure 6: *Vacuum circuit breaker tube*

The current $i(t)$ flowing through the test object, which is the forming coil in this case, is detected with a coaxial foil measurement resistor. The shunt resistor is designed to be able to absorb the entire energy stored in the capacitor battery without bringing out irreversible damage to the resistor in the case of failure.

For starting the transient discharge in the circuit, one or more circuit breakers are needed. The use of only one central circuit breaker has the advantage that difficulties with isochronous switching do not have to be expected. Taking the operating parameters of the impulse current source into account, the switch has to be designed for high current applications and should have a sufficiently high isolation voltage. Further, the switching behaviour should be preferably ideal. Therefore, a vacuum circuit breaker is chosen (Figure 6). It can be opened pneumatically and can be closed by an electric trigger signal.
The design and the properties of the forming coil are described in [3].

3.2 Electric properties of the components and the geometric structure

The electrical behaviour of the impulse capacitors can be modelled by the equivalent circuit diagram in Figure 7. The time parameters of the equivalent circuit elements are determined by measuring of the charge and discharge characteristics with different resistors in series to the capacitor. The most important parameter is the value of the series inductivity which amounts L_C = 228 nH. The value of series resistance is very small (several of 10 µΩ) in comparison to the required circuit resistance. In order to that it can be neglected for modelling the impulse generating network. The value of the parallel resistance R_{C2} determines the self discharging time constant of the capacitor. The time constant amounts several 10 minutes so that it can also be neglected.

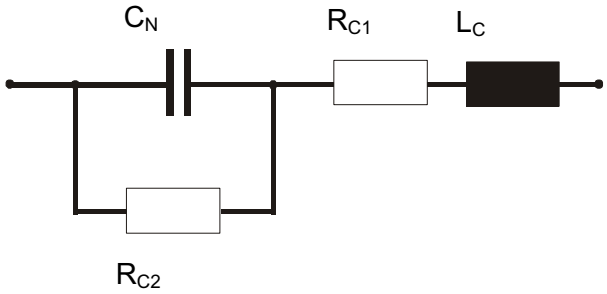

Figure 7: *Equivalent circuit diagram of an impulse capacitor [4]*

The required circuit resistance amounts R = 183 mΩ. It is primary built by the resistances of the shunt and the damping resistor. Additionally, the relevance of the parasitic resistances of the forming coil, the impulse capacitors, and the structure itself have to be considered. In the present case, the circuit resistance is built by the damping resistor ($R_{Damping}$ = 182,8 mΩ) and the shunt resistor (R_{Shunt} = 0,185 mΩ). In comparison to this, the other components have negligible values of their parasitic resistances. Due to their construction the damping resistor and the shunt resistor can be modelled as quasi ideal ohmic resistances. The experimental determined bandwidth of the shunt amounts B = 2 MHz.

For calculating the current $i(t)$, the vacuum circuit breaker can be modelled as an ideal switch. In the opened state the resistance is in the range of several 100 MΩ and in the closed state the resistance amounts only a few mΩ. The breakdown time of a vacuum circuit breaker amounts a few nanoseconds. For calculating the voltage rise at the forming

coil or at another test object in the circuit, the time and path length depending capacity $C_{Switch}(t,s)$ of the vacuum circuit breaker has to be considered. It determines the voltage rise at the test object before the voltage at the circuit breaker breaks down.

The required inductivity, which has to be displayed by the coaxial weir structure of the impulse generator, can be calculated by differencing the unavoidable inductivities in the circuit from the required circuit inductivity.

$$L_{Structure} = L - \sum L_{Components} \tag{9}$$

In the present case results a value of $L_{Structure}$ = 0,81 µH. The required geometric data of the coaxial structure can be estimated by the inductivity of a coaxial cable [5] where *d* is the diameter of the inner conductor and *D* the diameter of the outer conductor

$$\frac{L'}{nH/cm} = 2 \cdot ln\frac{D}{d} \tag{10}$$

Together with demands to the maximum possible diameter of the plant due to the limited available area in the laboratory a height of *h* = 1m results.

3.3 Design and construction of the impulse current generator

Figure 8 shows the resulting coaxial 100 kA- impulse current generator without charging circuit and without forming coil. The impulse capacitors at the bottom are arranged in a ¾ - circle. A 90 degree opening in the circle is needed to handle test objects in the centre of the plant. The capacitors ground terminals are connected low inductively with the circular basic earth plane. In the centre of the bottom plate the shunt resistor is mounted. The high voltage connectors of the capacitors are connected over copper tubes (length: 1 m) to the low inductive circular top plate. In the centre of the top plate the vacuum circuit breaker is mounted. Under the circuit breaker follows the damping resistor. Between the lower connector of the damping resistor and the connector of the shunt resistor the test object or a forming coil can be mounted. The horn structure that can be seen in the photography in the centre above the bottom plate displays a coaxial ohmic- capacitive voltage divider with high frequent termination. It can be used to measure the voltage at a test object with high bandwidth (*B* = 8 MHz).

Figure 8: Coaxial 100 kA- impulse current generator with capacitive energy storage and without charging circuit

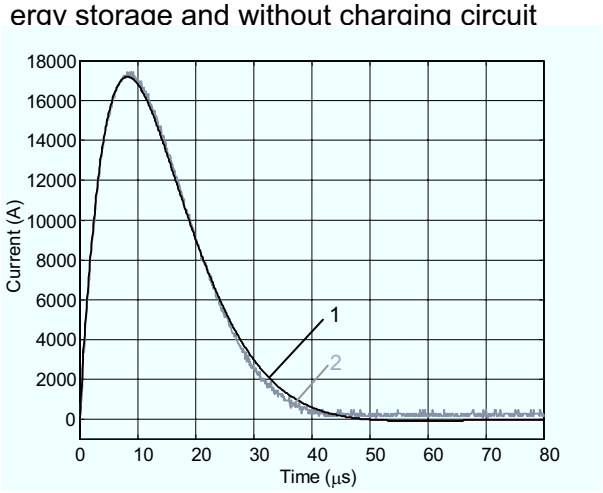

Figure 9: *Measurement (curve 2) and calculation (curve 1) of the 8/20 µs impulse current output*

3.4 Verification of function

To verify the correct design and function of the impulse current source, the capacitor battery is charged to a voltage U_0 = 4,5 kV and discharged over a short circuit instead of the test object (without forming coil in the circuit). It is measured by the shunt resistor. The expected current can be calculated by (1,5,6,7) using the following circuit parameters:

R = 183 mΩ	(damping resistor and shunt)
L = 830 nH	(accumulated inductivities in the circuit)
C = 74,7 µF	(capacitance of the capacitor battery)

The measured and the calculated currents are plotted in Figure 9. It can be seen that both curves have nearly identical progressions. The time typical constants T_1 and T_2 meet exactly the desired values of the standardised 8/20 µs impulse current.

4 Conclusion

For high electromagnetic high-speed sheet forming an impulse current source is needed which supplies the forming coil with a certain impulse current. The design of an impulse current source can be performed in two steps. In the first step, an equivalent circuit is defined that meets exactly the predefined progression of a desired impulse current. In the second step, the equivalent circuit diagram is realised with real components. The example of a standardised 8/20 µs impulse current shows that it is possible to design a impulse current source which meets exactly the progression of a predetermined impulse current. The precondition for such a design is that the electrical properties of the geometric structure and of all used components are precisely known, or that their behaviour is quasi ideal. Only then it is possible to derive an interrelation between the construction parameters and the desired electrical parameters of the equivalent circuit.

References

[1] IEC 60060-1: 1989-11-00: “High-voltage test techniques; Part 1: General definitions and test requirements”.

[2] *Braunsberger, U.:* “Über die Verwendung induktiv gespeicherter Energie zur Hochstromimpulserzeugung”, Dissertation, TU Braunschweig, 1978.

[3] *Winkler, R.:* „Hochgeschwindigkeitsbearbeitung“, 1. Auflage, VEB Verlag Technik, Berlin 1973.

[4] *Zinke, O.; Seither, H.:* „Widerstände, Kondensatoren, Spulen und ihre Werkstoffe“, 2. erw. u. neubearb. Auflage, Springer-Verlag Berlin – Heidelberg –New York 1982.

[5] *Meinke,H.; Gundlach, F. W.:* „Taschenbuch der Hochfrequenztechnik“, 3. verbesserte Auflage, Springer-Verlag, Berlin – Heidelberg - New York 1968.